



TURKISH JOURNAL OF ENGINEERING

EDITOR IN CHIEF

Prof. Dr. Murat YAKAR
Mersin University Engineering Faculty
Turkey

CO-EDITORS

Prof. Dr. Erol YAŞAR
Mersin University Faculty of Art and Science
Turkey

Prof. Dr. Cahit BİLİM
Mersin University Engineering Faculty
Turkey

Assist. Prof. Dr. Hüdaverdi ARSLAN
Mersin University Engineering Faculty
Turkey

ADVISORY BOARD

Prof. Dr. Orhan ALTAN
Honorary Member of ISPRS, ICSU EB Member
Turkey

Prof. Dr. Armin GRUEN
ETH Zurich University
Switzerland

Prof. Dr. Hacı Murat YILMAZ
Aksaray University Engineering Faculty
Turkey

Prof. Dr. Artu ELLMANN
Tallinn University of Technology Faculty of Civil Engineering
Estonia

Assoc. Prof. Dr. E. Çağlan KUMBUR
Drexel University
USA

TECHNICAL EDITORS

Prof. Dr. Roman KOCH
Erlangen-Nurnberg Institute Palaontologie
Germany

Prof. Dr. Hamdalla WANAS
Menoufyia University, Science Faculty
Egypt

Prof. Dr. Turgay CELIK
Witwatersrand University
South Africa

Prof. Dr. Muhsin EREN
Mersin University Engineering Faculty
Turkey

Prof. Dr. Johannes Van LEEUWEN
Iowa State University
USA

Prof. Dr. Elias STATHATOS
TEI of Western Greece
Greece

Prof. Dr. Vedamanickam SAMPATH
Institute of Technology Madras
India

Prof. Dr. Khandaker M. Anwar HOSSAIN
Ryerson University
Canada

Prof. Dr. Hamza EROL
Mersin University Engineering Faculty
Turkey

Prof. Dr. Ali Cemal BENİM
Duesseldorf University of Applied Sciences
Germany

Prof. Dr. Mohammad Mehdi RASHIDI
University of Birmingham
England

Prof. Dr. Muthana SHANSAL
Baghdad University
Iraq

Prof. Dr. Ibrahim S. YAHIA
Ain Shams University
Egypt

Assoc. Prof. Dr. Kurt A. ROSENTRATER
Iowa State University
USA

Assoc. Prof. Dr. Christo ANANTH
Francis Xavier Engineering College
India

Prof. Dr. Bahadır K. KÖRBAHTI
Mersin University Engineering Faculty
Turkey

Assist. Prof. Dr. Akın TATOGLU
Hartford University College of Engineering
USA

Assist. Prof. Dr. Şevket DEMİRCİ
Mersin University Engineering Faculty
Turkey

Assist. Prof. Dr. Yelda TURKAN
Oregon State University
USA

Assist. Prof. Dr. Gökhan ARSLAN
Mersin University Engineering Faculty
Turkey

Assist. Prof. Dr. Seval Hale GÜLER
Mersin University Engineering Faculty
Turkey

Assist. Prof. Dr. Mehmet ACI
Mersin University Engineering Faculty
Turkey

Dr. Ghazi DROUBI
Robert Gordon University Engineering Faculty
Scotland, UK

JOURNAL SECRETARY

Aydin Alptekin
aydinalptekin@mersin.edu.tr

TURKISH JOURNAL OF ENGINEERING (TUJE)

Turkish Journal of Engineering (TUJE) is a multi-disciplinary journal. The Turkish Journal of Engineering (TUJE) publishes the articles in English and is being published 4 times (January, April, July and October) a year. The Journal is a multidisciplinary journal and covers all fields of basic science and engineering. It is the main purpose of the Journal that to convey the latest development on the science and technology towards the related scientists and to the readers. The Journal is also involved in both experimental and theoretical studies on the subject area of basic science and engineering. Submission of an article implies that the work described has not been published previously and it is not under consideration for publication elsewhere. The copyright release form must be signed by the corresponding author on behalf of all authors. All the responsibilities for the article belong to the authors. The publications of papers are selected through double peer reviewed to ensure originality, relevance and readability.

AIM AND SCOPE

The Journal publishes both experimental and theoretical studies which are reviewed by at least two scientists and researchers for the subject area of basic science and engineering in the fields listed below:

- Aerospace Engineering
- Environmental Engineering
- Civil Engineering
- Geomatic Engineering
- Mechanical Engineering
- Geology Science and Engineering
- Mining Engineering
- Chemical Engineering
- Metallurgical and Materials Engineering
- Electrical and Electronics Engineering
- Mathematical Applications in Engineering
- Computer Engineering
- Food Engineering

PEER REVIEW PROCESS

All submissions will be scanned by iThenticate® to prevent plagiarism. Author(s) of the present study and the article about the ethical responsibilities that fit PUBLICATION ETHICS agree. Each author is responsible for the content of the article. Articles submitted for publication are priorly controlled via iThenticate® (Professional Plagiarism Prevention) program. If articles that are controlled by iThenticate® program identified as plagiarism or self-plagiarism with more than 25% manuscript will return to the author for appropriate citation and correction. All submitted manuscripts are read by the editorial staff. To save time for authors and peer-reviewers, only those papers that seem most likely to meet our editorial criteria are sent for formal review. Reviewer selection is critical to the publication process, and we base our choice on many factors, including expertise, reputation, specific recommendations and our own previous experience of a reviewer's characteristics. For instance, we avoid using people who are slow, careless or do not provide reasoning for their views, whether harsh or lenient. All submissions will be double blind peer reviewed. All papers are expected to have original content. They should not have been previously published and it should not be under review. Prior to the sending out to referees, editors check that the paper aim and scope of the journal. The journal seeks minimum three independent referees. All submissions are subject to a double blind peer review; if two of referees gives a negative feedback on a paper, the paper is being rejected. If two of referees gives a positive feedback on a paper and one referee negative, the editor can decide whether accept or reject. All submitted papers and referee reports are archived by journal Submissions whether they are published or not are not returned. Authors who want to give up publishing their paper in TUJE after the submission have to apply to the editorial board in written. Authors are responsible from the writing quality of their papers. TUJE journal will not pay any copyright fee to authors. A signed Copyright Assignment Form has to be submitted together with the paper.

PUBLICATION ETHICS

Our publication ethics and publication malpractice statement is mainly based on the Code of Conduct and Best-Practice Guidelines for Journal Editors. Committee on Publication Ethics (COPE). (2011, March 7). Code of Conduct and Best-Practice Guidelines for Journal Editors. Retrieved from http://publicationethics.org/files/Code%20of%20Conduct_2.pdf

PUBLICATION FREQUENCY

The TUJE accepts the articles in English and is being published 4 times (January, April, July and October) a year.

CORRESPONDENCE ADDRESS

Journal Contact: tuje@mersin.edu.tr

CONTENTS

Volume 7 – Issue 4

ARTICLES

The effect of Cumin Black (<i>Nigella Sativa L.</i>) as bio-based filler on chemical, rheological and mechanical properties of epdm composites Ahmet Güngör.....	279
A review of friction stir welding parameters, process and application fields Emre Kaygusuz, Filiz Karaömerlioğlu, Serhat Akıncı.....	286
A comparative study to estimate the mode I fracture toughness of rocks using several soft computing techniques Ekin Köken, Tümay Kadakci Koca.....	296
Temperature series analysis of the Hirfanli Dam Basin with the Mann-Kendall and Sequential Mann-Kendall tests Utku Zeybekoglu.....	306
A numerical study on the low-velocity impact response of hybrid composite materials Uzay Gezer, Bünyamin Demir, Yusuf Kepir, Alper Gunoz, Memduh Kara.....	314
Machine learning-based lung cancer diagnosis Mahmut Dirik.....	322
Modeling of daily groundwater level using deep learning neural networks Mohammed Moatasem Othman.....	331
Bentonite and polymeric support fluids used for stabilization in excavations Muhammad Shahbaz Akhtar.....	338
Laboratory modeling and analysis of slopes of different geometry under the effect of precipitation Mert Takci, Inci Develioglu, Hasan Firat Pulat, Hasan Emre Demirci.....	349
Comparison of commodity prices by using machine learning models in the COVID-19 era Sena Alparslan, Tamer Uçar.....	358



The effect of Cumin Black (*Nigella Sativa L.*) as bio-based filler on chemical, rheological and mechanical properties of epdm composites

Ahmet Gungör*¹ 

¹Sabancı University, Faculty of Engineering and Natural Sciences, Türkiye

Keywords

EPDM
Cumin Black
Bio-based filler
Waste Assessment
Rubber

Research Article

DOI: 10.31127/tuje.1180753

Received:27.09.2022

Revised: 12.11.2022

Accepted:16.11.2022

Published:27.02.2023



Abstract

One of the significant problems of our time and future is environmental pollution. There are many factors that cause environmental pollution and the main concerns are waste material. Since production, consumption and service activities have increased with rapid industrialization and increasing population. Waste assessment is a process that includes minimization, separate collection at source, intermediate storage, pre-treatment, the establishment of waste transfer centers, recovery and disposal when necessary, which are qualified as outputs as a result of activities such as production, application and consumption. The purpose of waste assessment is to ensure the process of wastes generated by human action without harming the environment and human health. In this context, re-evaluation of agricultural and aquaculture products that turn into waste after being used as a product is important both in terms of economic and environmental pollution. Herein, the use of cumin black pulp, which is waste at the end of black seed oil production, as a bio-based filler material in ethylene-propylene diene rubber (EPDM) was examined. Accordingly, the effects of cumin black pulp added to the EPDM matrix at different content on the rheological, mechanical and crosslinking degree of EPDM were determined. With the use of 10 phr cumin black pulp, the mechanical and rheological properties of EPDM and the degree of crosslinking increased. The tensile strength and elongation at break of the EPDM/CB composites increased up to 11 MPa and 480% with the addition of 10 phr CB, respectively. In addition, it was revealed that the vulcanization parameters were also enhanced. Consequently, it has been concluded as a result of the analysis that the waste cumin black pulp can be used as a filling material in the EPDM matrix. Thus, it has been seen that a product in the state of waste can be recovered and become an economic value.

1. Introduction

Rubber is a significant material with a multi-purpose and wide range of uses and it is a polymeric material obtained naturally from the tree sap of some plants or artificially produced from petroleum and alcohol [1]. Rubbers are widely used in many industrial applications [2]. For example, rubber is the main component of the low-pressure hoses of the wheels and the car body connections in the automotive industry. In addition, fuel and brake hoses, windshield wipers, transmission belts, gaskets, axle bellows, radiator and air hoses, door and window profiles, oscillation and vibration wedges, and insulation elements are other examples of rubber materials used in the automotive industry [3-5].

Rubbers differ from other polymeric materials due to their unique characteristics. In the unstressed state,

rubbers are amorphous and elastic over glass transition temperatures, conversely, plastics are crystalline and are used under glass transition temperatures to maintain their stability [6]. Rubbers gain a significant elasticity at room temperature due to the elongation properties of the molecular chains that are in the form of a ball [7]. Under the influence of high temperature and deforming forces, they show viscous flow and can be shaped under suitable conditions. In addition, with increasing temperature, the fluidity of the material increases and they exhibit a thermoplastic behavior [8,9].

The use of rubber in daily life increased with Charles Goodyear's discovery of vulcanization in 1843. Goodyear and Hancock added sulfur to the rubber to eliminate the difficulties in use such as softening of the rubber in the heat and embrittlement in the cold medium, and heated

* Corresponding Author

(ahmet.gungor21@gmail.com) ORCID ID 0000-0002-8319-1652

Cite this article

Gungor, A. (2023). The effect of Cumin Black (*Nigella Sativa L.*) as bio-based filler on chemical, rheological and mechanical properties of epdm composites. Turkish Journal of Engineering, 7(4), 279-285

rubber up to 130-140°C after shaping, and this process is called vulcanization [10,11].

Terpolymer EPDM, which is one of the synthetic rubber types, is synthesized by the polymerization reaction of diene together with ethylene and propylene. With the participation of diene in the reaction, a double bond, that is, unsaturation occurs in the chain [12]. This chemical modification allows curing with sulfur as well as peroxides and mixing with other polymers [13]. Since the unsaturation is in the side group in EPDM, the olefinic segments are saturated [13]. Therefore, EPDM-based products are rubbers with very high resistance to oxygen, ozone and chemicals [14]. Since EPDM is nonpolar, it is resistant to polar chemicals. While EPDM is resistant to acids and bases, it is not resistant to oils and is highly affected by aromatic, aliphatic and chlorinated hydrocarbons [15].

Depending on the physical properties desired in the field of use as a final product, there are various additives and fillers with different properties in the composition of rubber-based materials, as well as some natural or synthetic polymers, and these substances are added to the unvulcanized mixture in a certain amount in the rubber dough preparation process [16]. Fillers are added to the composition to improve the physical properties of the product, give a specific functionality to the product, or reduce the unit cost [17]. One of the most commonly used filling materials in the rubber industry is carbon black and it improves mechanical properties of rubbers. In addition, the use of carbon black causes an increase in hardness, breaking strength and electrical conductivity and a decrease in elastic modulus after vulcanization in rubbers [18].

Despite all these advantages it provides to rubber materials, it has been determined that carbon black is a genotoxic material, and its use as a filling material is very harmful for both employees and the environment [19,20]. For this reason, in recent years, the use of bio-based filling materials has been emphasized in the rubber industry instead of filling materials such as carbon black, which are known to be harmful, considering both the sustainable environment and employee health. For this purpose, natural components such as walnut shell, fish scale, peanut shell, which are in the form of waste, can be used as filling material [21]. Thus, both a waste material is evaluated and the negative effects caused by carbon black can be minimized.

Cumin black (*Nigella sativa L.*), a flowering plant, mostly grows in Asia, the Middle East and the Mediterranean. Cumin black, which has a peppery flavor, is used as a spice in Indian and Middle Eastern. It is consumed in powder form or oil is obtained by squeezing the seeds [22,23]. Today, cumin black is a valuable product used in spice, functional food, herbal drug preparations, health and cosmetics sectors [24]. Turkey is one of the leading countries in black seed production due to its suitable climate and land conditions. The composition of the seed contains 30-45% fixed oil, 0.01-0.5% essential oil, 20-30% protein, alkaloid bitter substances and saponins [25]. Due to its high oil content, black seed oil production has been increasing in recent years. After the black seed oil is obtained, the remaining pulp is generally used as animal feed [25].

In this study, the use of cumin black pulp, which is waste after black seed oil production, in EPDM rubber was examined. To the best of our knowledge, the use of cumin black pulp, which is waste as a result of cumin black oil production, as a biodegradable filling material in EPDM has not been found in the literature. In this direction, cumin black pulp was added to the EPDM matrix in different amounts and its effect on the rheological, mechanical and chemical properties of the final product was examined.

2. Method

The cumin black pulp (CB) was obtained from a local cumin black seed oil producer. Before the use of CB, a filler material, it applied some pre-treatment. In this regard, cumin black pulp is washed with de-ionized water to remove the impurities. The cleaned CB was dried in an oven at 50 °C. The dried CB was milled and then sieved with different mesh-sized sieves. CB particles below 250 micrometers were used throughout the study. In the second step, the unvulcanized EPDM compound and CB were mixed with a Kneader-type closed mixer until a homogeneous dough is obtained at 60 °C. After that, the obtained compound was compressed in a two-roll mill [14].

Table 1. The recipe applied for the synthesis of EPDM and EPDM/CB composite materials

Materials	Function	Amount (phr)
KELTAN 9650Q	Rubber	100
Carbon Black	Filler	1
Zinc Oxide	Activator	1.5
Mineral Oil	Lubricant	32
Stearic Acid	Activator	1
TAC/50	Coagent	1
Perkadox	Crosslinker	5
Cumin Black pulp (CB)	Biobased	0-5-10-15
(OCB-5CB-10CB-15CB)	Filler	

In characterization studies, the effects of CB added to the EPDM matrix as a bio-based filling material at different rates on the rheological, mechanical and chemical properties of the material were investigated.

The rheological properties and vulcanization parameters of EPDM and EPDM/CB composite materials were determined with a moving die rheometer (MDR) device. A universal mechanical testing machine (Shimadzu AGS-X) was used to determine the mechanical properties. 2mm EPDM samples were cut into dog bone shapes by ASTM D412 standard and all mechanical analyzes were performed in accordance with ASTM D412 standard.

The crosslinking density of EPDM and EPDM/CB composites was determined by the Soxhlet extraction method. The crosslinking density of the prepared composites was calculated via Equation 1, where w_i is the initial weight of the composite and w_f is the final weight of the composite. Hexane was used as solvent throughout the experiment and the extraction process were carried out at 75 °C.

$$Gel\ Content, \% = w_f/w_i * 100 \quad (1)$$

The crosslinking degree was also calculated by swelling test. The EPDM and EPDM/CB composites were prepared 1cm x 1cm with a thickness of 2 mm and the toluene was utilized. The swelling ratio was determined by Equation 2.

$$Swelling\ Ratio, \% = (w_f - w_i)/w_i * 100 \quad (2)$$

3. Results and Discussion

In this study, the use of cumin black pulp, which is waste after cumin black seed oil production, a filling material in EPDM rubber was investigated. Accordingly, different amounts of CB particles as bio-based filling materials were added to the EPDM matrix and the effects of the amount of CB on the rheological, mechanical and chemical properties of the composite material were investigated.

3.1. Rheological properties

Vulcanization is the process of crosslinking long rubber chains to form a three-dimensional elastic structure. The vulcanization process can usually occur with the help of sulfur or sometimes with a different chemical such as peroxide. Vulcanization is a chemical process that improves the physical properties of elastomer mixtures. On the other hand, rheology is the science of the flow and deformation of matter. Shear stress deals with the relationships between shear deformation and time. It covers the study of the mechanical properties of gases, liquids and solids. Therefore, characterization of rheological properties and vulcanization parameters has important in the evaluation of rubber materials [26,27].

Torque curves of EPDM and EPDM/CB composite materials produced are shown in Figure 1. As seen in Figure 1, the torque values of the material increase up to 10 phr CB content. However, a significant decrease is observed in the torque value of the synthesized composite material when the amount of CB used is above 10 phr. Increasing the amount of CB may cause a decrease in the homogeneity of the rubber mixture, which can lead to the formation of void regions (fail points) in the rubber matrix. These fail points may cause the torque values of CB15 to decrease under the applied stress actuation.

In Table 2, the vulcanization parameters of the synthesized EPDM and EPDM/CB composite materials are tabulated. The effect of CB added into the EPDM matrix on t_{s2} , t_{90} and $M_H - M_L$ values was investigated in the evaluation of vulcanization parameters.

Table 2. Vulcanization parameters of EPDM and EPDM/CB composite materials

Samples	t_{s2} (sec)	t_{90} (sec)	$M_H - M_L$ (N.m)
0CB	38.92	95.86	11.85
5CB	40.12	93.87	12.17
10CB	43.81	90.24	13.41
15CB	34.53	101.63	11.26

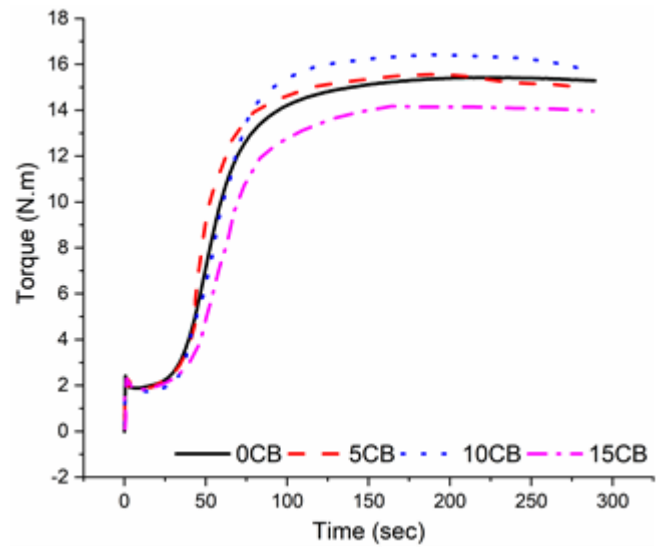


Figure 1. Torque curves of EPDM and EPDM/CB composite materials

The M_L and M_H values represent the minimum and maximum torque, respectively. M_L value is the smallest torque value at which vulcanization starts and is related to mixing conditions. The M_H value is related to properties such as tensile, tear and rupture strength. t_{s2} time is the scorch time of the rubber mixture. Scorch time refers to the time to start vulcanization. The short scorch time causes the rubber to cure prematurely. When there is an early curing problem, shape stability and workability decrease and the mechanical properties of rubber decrease. Therefore, it is desirable for the t_{s2} value should be long. The t_{90} value is the time it takes for 90% of the EPDM to cure. 90% is the optimum curing time. If the vulcanization process is completed before reaching the t_{90} time, deformation of the rubber and a decrease in mechanical properties may occur.

When the effect of CB on t_{s2} is examined, it is seen that CB added up to 10 phr increases the flux time of the rubber. The t_{s2} time of the material is significantly reduced when the amount of CB used is above 10 phr. At t_{90} values, a similar trend is observed for t_{s2} time. In addition, the optimum curing time of the rubber decreases until the use of 10 phr CB. With the increasing amount of filler material, an increase in the optimum curing time is also observed. Furthermore, when the torque difference values ($M_H - M_L$) related to the crosslinking degree of rubber materials were examined, the highest torque difference value was obtained in the CB10 sample. Considering the vulcanization parameters, it is concluded that the addition of CB until 10 phr positively affects the vulcanization parameters of the material. Thus, it has been understood that waste CB particles can be used as a bio-based filler in the EPDM rubber.

3.2. Tensile properties

In the preparation of rubber materials, the production of high mechanical properties for the area to be used is one of the most important parameters. Therefore, the characterization of the mechanical properties of rubber materials is significant for the

evaluation of the rubber material. In this study, the effects of bio-based CB particles used as filler material on the mechanical properties of EPDM were investigated and the analysis results were given in Figure 2-4. Tensile strength, elongation at break, hardness and toughness (energy) properties of EPDM and EPDM/CB composites were taken into account in the evaluation of mechanical properties.

In Figure 2, the effects of CB on the tensile strength and elongation at break values of the prepared samples are given. Tensile strength is the maximum amount of load the polymer can tolerate without breaking when two forces applied to the polymer in the same way but in opposite directions. When the applied force overcome the tensile strength of the polymeric material, rupture happens in the polymeric material [28]. When the tensile strengths of EPDM and EPDM/CB samples were examined, it was observed that the tensile strength of the material increased up to CB10 sample, while the CB0 and CB5 samples gave similar results. In parallel with the increase in the amount of CB used, the tensile strength also decreased. On the other hand, elongation at break is the rate of elongation of the material at full break during the tensile test applied to the material. The elongation value is usually expressed as a percentage, so it is not a value dependent on the unit area over which the force is applied. As can be seen from Figure 2, CB used as filler material increased the elongation at break of the material and an elongation value of approximately 500% (CB10) was reached. The results of elongation at break and tensile strength results are similar to each other, and it is revealed that the mechanical properties increase with the use of 10 phr CB in both analyzes.

The effects of CB on the toughness and hardness of the prepared composites are given in Figure 3 and Figure 4, respectively. Toughness refers to the total energy absorbed by the material until it deforms. Toughness is an engineering property that matters when it comes to a material's ability to withstand an impact without breaking. The toughness of a material is equal to the area under the stress-strain graph of the material [29]. As can be seen in Figure 3, it is seen that CB used as a bio-based filling material increases the toughness values of EPDM by up to 10 phr CB content. Therefore, it has been concluded that CB added to the EPDM matrix increases the ductility of the produced composite materials. With the addition of more than 10 phr of CB to the EPDM matrix, the ductility of the EPDM composite decreased and it became a more brittle material.

Hardness is the resistance of a material against a hard object immersed in its surface, and it is of great importance as the hardness values are directly related to the strength of the materials [30]. Figure 4 shows the effect of the amount of CB used as a bio-based filler on the hardness of EPDM composites. Compared to Neat EPDM (0CB), EPDM with different CB content had a reduction in hardness values. In parallel with the increase in the amount of CB added to the EPDM matrix, the hardness values also decreased, that is, the material is in a softer form and therefore its resistance to the applied force decreases.

When the mechanical analysis results were evaluated, it was concluded that the tensile properties of the

material increased in the use of CB, which is used as a filling material, up to 10 phr. On the other hand, the use of CB above 10 phr decreased the mechanical properties., It is understood that the optimum amount of CB is 10 phr considering the mechanical analysis results. In addition, the results of the mechanical and rheological analysis are compatible with each other. It is also understood that CB can be used in the EPDM matrix as a bio-based filler material.

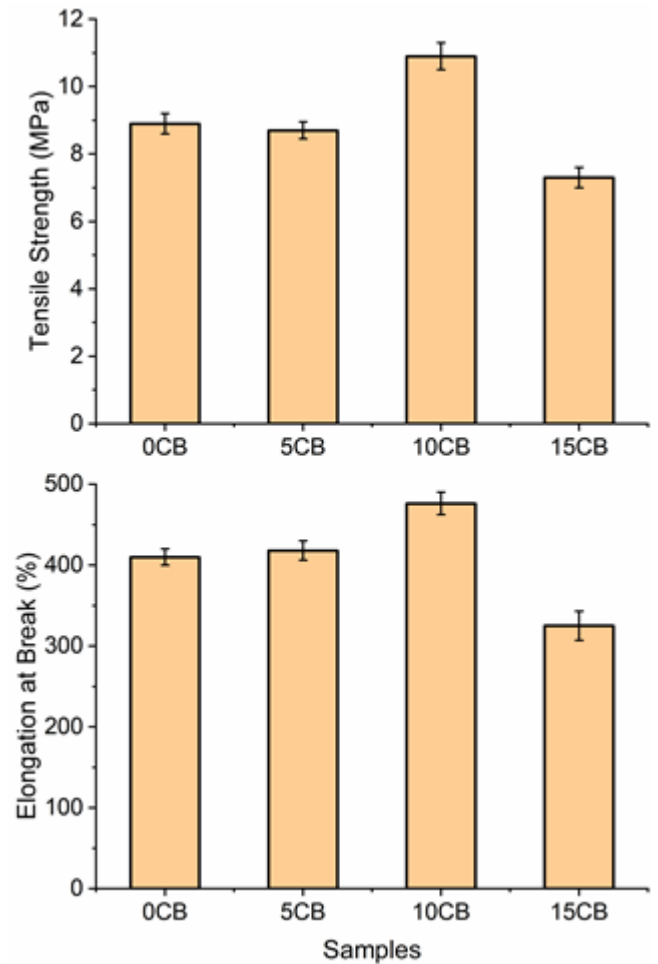


Figure 2. Tensile strength and elongation at break values of EPDM and EPDM/CB composite materials

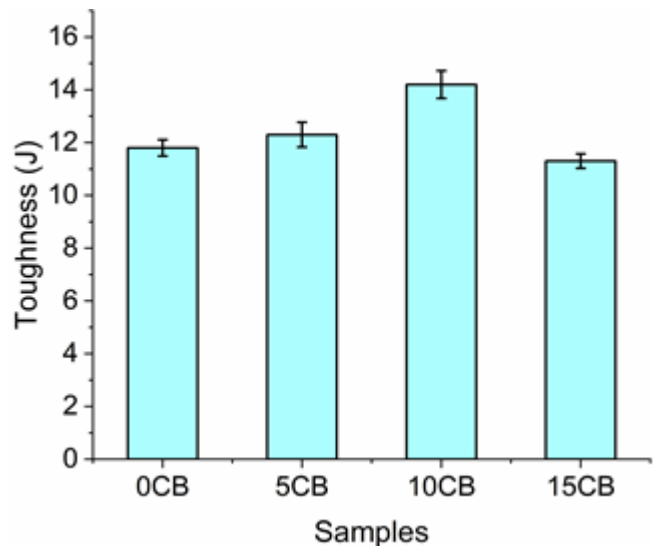


Figure 3. Toughness values of EPDM and EPDM/CB composite materials

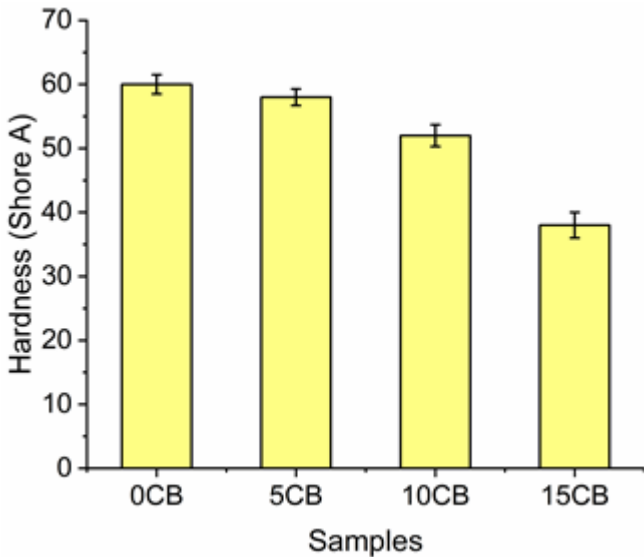


Figure 4. Hardness values of EPDM and EPDM/CB composite materials

3.3. Gel content and swelling ratio of EPDM composites

The gel content (crosslinking density) of rubber materials is directly related to their mechanical properties and is therefore an important analysis method for the evaluation of the material. In general, the traditional Soxhlet extraction method and swelling ratio analysis are frequently used to determine the gel content of rubber materials [30].

Figure 5 shows the effect of the amount of CB used as a bio-based filler on the gel content of EPDM composites. Gel content was calculated using Equation 1. Accordingly, the mass change during the extraction process was taken into account. The high gel content of the rubber material indicates that the mass loss will be less. As can be seen in Figure 5, the gel content of the material increased with the addition of up to 10 phr of CB and the highest gel content was reached in the CB10 sample at about 86.5%. With the increasing amount of CB, the gel content decreased significantly.

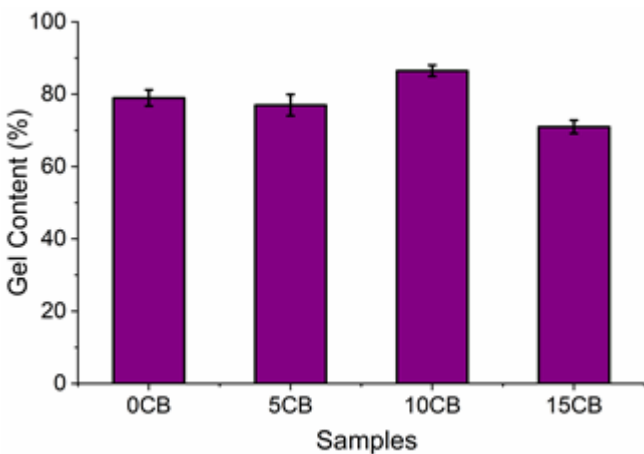


Figure 5. Gel content of EPDM and EPDM/CB composite materials

Figure 5 shows the effect of the amount of CB used as a bio-based filler on the swelling ratio of EPDM composites. Swelling ratio analysis also gives

information about the gel content of the rubber material. The higher the gel content of the rubber material, the less water it absorbs into its structure and the less it swells. As seen in Figure 6, the swelling ratio of the samples decreased with the addition of CB. The highest swelling ratio was reached in the CB15 sample and about 180%, while the lowest swelling ratio was calculated as 105% in the CB10 sample.

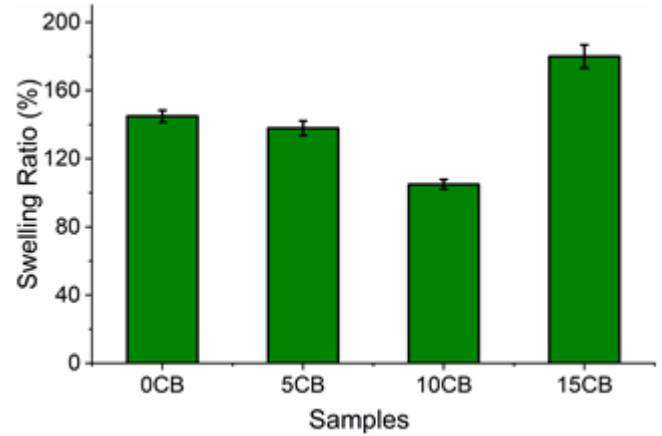


Figure 6. Swelling ratio values of EPDM and EPDM/CB composite materials

According to the gel content and swelling ratio analysis results, it was understood that the sample with the highest crosslink density was the CB10 sample using 10 phr CB. Gel content and swelling ratio analysis also support each other. In addition, the results of the crosslink density analysis are also compatible with the mechanical analysis results. Accordingly, composite material with high crosslink density and mechanical properties was synthesized by using 10 phr CB. The mechanical properties of the material have also decreased considerably due to the reduced crosslink density with the use of 15 phr CB.

4. Conclusion

Carbon black, which is one of the filler materials frequently used in the rubber industry, is a very harmful material in terms of both the environment and employee health, despite the superior mechanical properties it provides. For this reason, many research is carried out on the use of bio-based fillers to replace carbon black or to reduce the carbon black used per unit of rubber weight. The selection of bio-based filler materials, especially the selection of waste products, provides a great advantage with regard to both economic and sustainable environments. Herein, as a result of the production of cumin black oil, which is frequently used and consumed in our country, the waste cumin black pulp was added to the EPDM matrix at different weight ratios as a bio-based filler material. The effect of added CB particles on the rheological, mechanical and chemical properties of the produced composite material was investigated. MDR analysis shows that CB added up to 10phr increases the torque values and t_{s2} time of the material and decreases the t_{90} time. From the mechanical analysis results, it was understood that the EPDM sample (CB10) containing 10 phr CB was the optimum sample considering the tensile

strength, elongation at break and toughness values. In addition, both the gel content and swelling analysis results are in accordance with the rheological and mechanical analysis results and show that the sample with the highest crosslink density in both analyzes is EPDM containing 10 phr CB. As a result of the characterization studies, it is evaluated that the waste CB can be used as a bio-based filling material in EPDM and rubber materials. The use of waste materials such as CB as filling material in the rubber industry is a very important gain in terms of both economic and environmental pollution.

Conflicts of interest

The authors declare no conflicts of interest.

References

1. Vijayaram, T. R. (2009). A technical review on rubber. *International Journal on Design and Manufacturing Technologies*, 3(1), 25-37.
2. Wang, G., Li, A., Zhao, W., Xu, Z., Ma, Y., Zhang, F., ... & He, Q. (2021). A review on fabrication methods and research progress of superhydrophobic silicone rubber materials. *Advanced Materials Interfaces*, 8(1), 2001460. <https://doi.org/10.1002/admi.202001460>
3. Shit, S. C., & Shah, P. (2013). A review on silicone rubber. *National academy science letters*, 36(4), 355-365. <https://doi.org/10.1007/s40009-013-0150-2>
4. Güngör, A., Akbay, I. K., & Özdemir, T. (2019). EPDM rubber with hexagonal boron nitride: A thermal neutron shielding composite. *Radiation Physics and Chemistry*, 165, 108391. <https://doi.org/10.1016/j.radphyschem.2019.108391>
5. Da Maia, J. V., Pereira, F. P., Dutra, J. C. N., Mello, S. A. C., Becerra, E. A. O., Massi, M., & da Silva Sobrinho, A. S. (2013). Influence of gas and treatment time on the surface modification of EPDM rubber treated at afterglow microwave plasmas. *Applied surface science*, 285, 918-926. <https://doi.org/10.1016/j.apsusc.2013.09.013>
6. Legge, N. R. (1987). Thermoplastic elastomers. *Rubber Chemistry and Technology*, 60(3), 83-117. <https://doi.org/10.5254/1.3536141>.
7. Ginder, J. M., Nichols, M. E., Elie, L. D., & Tardiff, J. L. (1999, July). Magnetorheological elastomers: properties and applications. In *Smart Structures and Materials 1999: Smart Materials Technologies* (Vol. 3675, pp. 131-138). SPIE. <https://doi.org/10.1117/12.352787>
8. Suo, Z. (2010). Theory of dielectric elastomers. *Acta Mechanica Solida Sinica*, 23(6), 549-578. [https://doi.org/10.1016/S0894-9166\(11\)60004-9](https://doi.org/10.1016/S0894-9166(11)60004-9)
9. Heinrich, G., Klüppel, M., & Vilgis, T. A. (2002). Reinforcement of elastomers. *Current opinion in solid state and materials science*, 6(3), 195-203. [https://doi.org/10.1016/S1359-0286\(02\)00030-X](https://doi.org/10.1016/S1359-0286(02)00030-X).
10. Datta, R. N. (2008). Rubber-curing systems. In *Current Topics in Elastomers Research* (pp. 415-462). CRC Press. <https://doi.org/10.1201/9781420007183-14>
11. Kruželák, J., Sýkora, R., & Hudec, I. (2017). Vulcanization of rubber compounds with peroxide curing systems. *Rubber chemistry and technology*, 90(1), 60-88. <https://doi.org/10.5254/RCT.16.83758>
12. Greene, J. P. (2021). Elastomers and Rubbers. *Automotive Plastics and Composites; Elsevier: Amsterdam, The Netherlands*, 127-147. <https://doi.org/10.1016/b978-0-12-818008-2.00016-7>.
13. Stelescu, M. D., Manaila, E., & Craciun, G. (2013). Vulcanization of ethylene-propylene-terpolymer-based rubber mixtures by radiation processing. *Journal of Applied Polymer Science*, 128(4), 2325-2336. <https://doi.org/10.1002/app.38231>
14. Akbay, İ. K., Güngör, A., & Özdemir, T. (2017). Optimization of the vulcanization parameters for ethylene-propylene-diene termonomer (EPDM)/ground waste tyre composite using response surface methodology. *Polymer Bulletin*, 74, 5095-5109. <https://doi.org/10.1007/S00289-017-2001-7>
15. Ravishankar, P. S. (2012). Treatise on EPDM. *Rubber chemistry and technology*, 85(3), 327-349. <https://doi.org/10.5254/rct.12.87993>
16. Abdul Salim, Z. A. S., Hassan, A., & Ismail, H. (2018). A review on hybrid fillers in rubber composites. *Polymer-Plastics Technology and Engineering*, 57(6), 523-539. <https://doi.org/10.1080/03602559.2017.1329432>
17. Zhang, Y., Ge, S., Tang, B., Koga, T., Rafailovich, M. H., Sokolov, J. C., ... & Nguyen, D. (2001). Effect of carbon black and silica fillers in elastomer blends. *Macromolecules*, 34(20), 7056-7065. <https://doi.org/10.1021/MA010183P>
18. Wang, M. J., Gray, C. A., Reznik, S. A., Mahmud, K., & Kutsovsky, Y. (2003). Carbon black. *Kirk-Othmer Encyclopedia of Chemical Technology*. <https://doi.org/10.1002/0471238961.0301180204.011414.a01.pub2>
19. Chaudhuri, I., Fruijtier-Pölloth, C., Ngiewih, Y., & Levy, L. (2018). Evaluating the evidence on genotoxicity and reproductive toxicity of carbon black: a critical review. *Critical reviews in toxicology*, 48(2), 143-169. <https://doi.org/10.1080/10408444.2017.1391746>
20. Di Ianni, E., Jacobsen, N. R., Vogel, U. B., & Møller, P. (2022). Systematic review on primary and secondary genotoxicity of carbon black nanoparticles in mammalian cells and animals. *Mutation Research/Reviews in Mutation Research*, 108441. <https://doi.org/10.1016/J.MRREV.2022.108441>
21. Mokhothu, T. H., John, M. J., & John, M. J. (2016). Bio-based fillers for environmentally friendly composites. *Handbook of Composites from Renewable Materials; Vijay, KT, Manju, KT, Michael, RK, Eds*, 243-270. <https://doi.org/10.1002/9781119441632.ch10>
22. Butt, M. S., & Sultan, M. T. (2010). Nigella sativa: reduces the risk of various maladies. *Critical reviews*

- in food science and nutrition*, 50(7), 654-665. <https://doi.org/10.1080/10408390902768797>
23. Hanafy, M. S. M., & Hatem, M. E. (1991). Studies on the antimicrobial activity of *Nigella sativa* seed (black cummin). *Journal of ethnopharmacology*, 34(2-3), 275-278. [https://doi.org/10.1016/0378-8741\(91\)90047-H](https://doi.org/10.1016/0378-8741(91)90047-H)
24. Ahmad, A., Husain, A., Mujeeb, M., Khan, S. A., Najmi, A. K., Siddique, N. A., ... & Anwar, F. (2013). A review on therapeutic potential of *Nigella sativa*: A miracle herb. *Asian Pacific journal of tropical biomedicine*, 3(5), 337-352. [https://doi.org/10.1016/S2221-1691\(13\)60075-1](https://doi.org/10.1016/S2221-1691(13)60075-1)
25. Nergiz, C., & Ötles, S. (1993). Chemical composition of *Nigella sativa* L. seeds. *Food chemistry*, 48(3), 259-261. [https://doi.org/10.1016/0308-8146\(93\)90137-5](https://doi.org/10.1016/0308-8146(93)90137-5)
26. Akiba, M. A., & Hashim, A. S. (1997). Vulcanization and crosslinking in elastomers. *Progress in polymer science*, 22(3), 475-521. [https://doi.org/10.1016/S0079-6700\(96\)00015-9](https://doi.org/10.1016/S0079-6700(96)00015-9)
27. Coran, A. Y. (2003). Chemistry of the vulcanization and protection of elastomers: A review of the achievements. *Journal of Applied Polymer Science*, 87(1), 24-30.
28. Smith, T. L. (1963). Ultimate tensile properties of elastomers. I. Characterization by a time and temperature independent failure envelope. *Journal of Polymer Science Part A: General Papers*, 1(12), 3597-3615. <https://doi.org/10.1002/POL.1963.100011207>
29. Smith, T. L. (1964). Ultimate tensile properties of elastomers. II. Comparison of failure envelopes for unfilled vulcanizates. *Rubber Chemistry and Technology*, 37(4), 792-807. <https://doi.org/10.5254/1.3540378>
30. Ermilov, A. S., & Nurullaev, E. M. (2012). Mechanical properties of elastomers filled with solid particles. *Mechanics of composite Materials*, 48(3), 243-252. <https://doi.org/10.1007/S11029-012-9271-9>



© Author(s) 2023. This work is distributed under <https://creativecommons.org/licenses/by-sa/4.0/>



A review of friction stir welding parameters, process and application fields

Emre Kaygusuz*¹, Filiz Karaömerlioğlu^{2,3}, Serhat Akıncı³

¹Bingol University, Pilot University of Central Coordination Unit, Türkiye

²Mersin University, Engineering Faculty, Electrical Electronics Engineering, Türkiye

³Mersin University, Nanotechnology and Advanced Materials, Türkiye

Keywords

Friction Stir Welding
FSW
Application
Welding Al Alloys

Review Article

DOI: 10.31127/tuje.1107210

Received: 21.04.2022

Revised: 25.10.2022

Accepted: 21.11.2022

Published: 27.02.2023



Abstract

It is important to join materials for systems that require high-performance and to minimize the defects that may occur during this joining. Welding is the most common way for joining materials but for lightweight and similar/ dissimilar materials, Friction Stir Welding preferable for its high-performance joining properties. Lightweight and durable materials such as aluminum alloys are widely used in sectors such as defense industry, aerospace industry, automotive industry, and high-speed train manufacturing. Some of these materials cannot be welded by conventional methods due to their high thermal conductivity and low melting point. In welding processes, material properties are expected to be as close as possible to base material. Friction stir welding (FSW) is a joining method that provides welding below the melting point of materials that cannot be welded by conventional methods or where the welding process causes the mechanical structure of the material to deteriorate. In this study, Friction Stir Welding process, advantages and disadvantages and application fields of Friction Stir Welding were examined.

1. Introduction

The industrial revolution has been an important turning point in the history of humanity, where new materials have been developed. New materials have played a major role in the development of technology used in land, air, sea and space studies due to their low cost and durability. The 20th century has witnessed the growth in engineering works and development of the materials [1]. While this expansion in the material range allows engineers to design specific parts and equipment, it has also created new situations where different materials are used in the construction. Combining parts made of different materials in terms of chemical, thermal, physical and mechanical properties also created difficulties. Mechanical joining has been a suitable method for many of the different materials. However, the need for high-performance construction has paved the way for welded joints to replace mechanical joints such as rivets and bolts. The use of welding construction has gained great importance especially in the realization of structures where lightness comes to the fore [2].

Welding is the metallurgical joining process of two metal parts to produce a single piece. This joining is the leading way of obtaining monolithic structures and is often accomplished with the use of heat and/or pressure. According to the chemical composition of the main material, fusion welding or solid-state welding is used in welded joining. In fusion welding method, which is based on melting the base metal parts to be welded in the welded area using heat, filler metal is added to the molten area to increase the strength in the joint. Electric arc, electric current or gas mixtures are used in the melting process in the welding zone of the parts to be joined. If the melting process in the welded joint is carried out with an electric arc, it is expressed as arc welding. The heat released from the resistance of the parts held together under pressure against the electric current passing through the contact surfaces, and the bonding provided by the melting process formed on the contact surface constitute the source of resistance [3].

If the hot flame required to melt the metal parts to be joined and the filling material, if used, is provided by combustible gas and oxygen, it is called a gas source. In

* Corresponding Author

(emre_kygsz@windowslive.com) ORCID ID 0000-0001-9356-2149
(filizkrm@mersin.edu.tr) ORCID ID 0000-0002-4677-4365
(serhatakinci1903@gmail.com) ORCID ID 0000-0002-8597-6189

Cite this article

Kaygusuz, E., Karaömerlioğlu, F., & Akıncı, S. (2023). A review of friction stir welding parameters, process and application fields. Turkish Journal of Engineering, 7(4), 286-295

recent years, electron beam and laser are also used for melting in the weld zone in welded joints. If melting in the welding zone is carried out using an electron beam, it is referred to as electron source, if melting using laser, it is expressed as laser source. In welded joining, electron welding and laser welding are superior to other fusion welding methods by forming a small melt pool and narrower heat affected zone (HAZ). Fusion welding methods are most widely used in welded joining of metallic materials. However, welded joining of metallic materials with high thermal and electrical conductivity coefficients, such as copper and aluminum, by fusion welding methods, is carried out under special conditions. In joining, welding methods in which only pressure or pressure and heat are applied together without melting are called solid state welding. When the two-part surfaces are pressed together under high temperature below the melting temperature, the parts are combined by solid state diffusion. This source in solid state is called diffusion welding. The parts are placed on top of each other and moderate pressure is applied, and the jointing, which uses high frequency sound waves to create vibration motion parallel to the part contact surfaces, is called ultrasonic welding method. Welded joining of parts with the help of heat released from friction between two surfaces is expressed as friction welding. Solid state welding methods are used successfully in welded joining of many metallic materials, especially copper and aluminum, which are problematic to be joined by fusion welding methods. Numerous scientific studies have been conducted using solid-state welding methods for welded joining of the same type of materials. In recent years, welded joining of different types of metallic materials has been carried out with the friction stir welding method, which is one of the solid-state welding techniques.

Solid state welding methods include one of the oldest welding methods in the world, such as forging [4]. The katana swords used by the ancient Japanese Samurai were also produced with forging welding (forged steel) [5]. Pressure and/or heat are used in solid state welds, but the effect of heat does not melt the parts and softens them [6].

The FSW method can be applied for the similar or dissimilar materials, materials which have different melting points and non-ferrous materials [7].

Singh et. al. [8] studied microstructure and mechanical behavior of friction-stir-welded magnesium alloys: as-welded and post weld heat treated conditions. The tensile strength, elongation and efficiency improved by 8.8%, 32.4%, and 3.8% after post weld heat treatment at the stir zone. Hardness of the stir zone reduced by 12.95% after heat treatment [8]. 1400 r/min tool rotation speed and 25 mm/min tool traverse feed rate were found suitable for FSW of dissimilar magnesium alloys.

Singh et. al. [9] studied investigation on the microstructure and mechanical properties of a dissimilar friction stir welded joint of magnesium alloys.

Cakan et. al. [10] applied FSW method to dissimilar pure copper and the aluminum alloy AA7075-T6 plates. A maximum tensile strength of 224 MPa obtained at 660

rpm tool rotation speed and, 32 mm/min traverse speed with same tool geometry.

Singh et. al. [11] studied influence of post welding heat treatment on the microstructure and mechanical properties of friction stir welding joint of AZ31 Mg alloy. Tensile strength and elongation of FSW joint were 145.4 ± 4.9 MPa and $9.5 \pm 0.9\%$, in their study. Tensile strength and elongation of the joint were improved by 4.74% and 15.78% after PWHT [11].

Wang et. al. [12] studied FSW and heat treatment of 7050 Aluminum Alloy. With T74 heat treatment after welding, the tensile strength of weld increased by over 12% [12].

Prasad et. al. [13] investigated mechanical properties of AA6061T6 and AA6351T6 plates joined by friction stir welding. They used vertical milling machine for FSW and 5 mm thickness Al plates. FSW process applied with different pin geometries, tool rotational speed and traverse speeds. 167.95 MPa ultimate tensile strength and 92 RHN maximum microhardness value obtained [13].

Singh et. al. [14] investigated the influence of holding time on the characteristics of friction stir welded dissimilar magnesium alloy joints during PWHT (post welding heat treatment). They applied post weld heat treatment after FSW to magnesium alloys AZ31 and AZ91 to improve characteristics and performance of welded joints. For microhardness performance, at 60 min PWHT holding time, researchers got smoother microhardness profile. PWHT joints had the highest impact energy of 4.2 J for 30 min [14].

Su et. al. [15] applied double sided(DS) FSW (compared with single sided (SD)) to 6063-T6 aluminum alloy with thickness of 10mm. 92 MPa fatigue strength obtained at DS FSW, and 76 MPa fatigue strength obtained at SS FSW [15].

Singh et. al. [16] studied influence of PWHT on FSW joint of AZ61 Mg alloy. After PWHT, the microhardness in the stirring zone was reduced approximately 16% and the percentage elongation of the weld joint was increased by 18.5%. The microstructure of the welded zone improved [16].

Hunt et. al. [17] studied a generalized Method for In-Process Defect Detection in Friction Stir Welding. In their study, it is mentioned that the welding speed is expected to be faster for FSW method, in the industry. The challenging part of the faster welding speed at FSW method, is to produce defect-free welded zone. In their study, when FSW applied to aluminum blanks at 1500 to 3000 mm/min traverse speed, their methodology succeed to detect defects and lower the cost of NDE (non-destructive evaluation) in the industry [17].

In this study, FSW application, advantages and disadvantages and usage areas of friction stir welding were examined.

2. Principle of FSW

In the FSW process, the temperature is generated by the friction between the rotating tool and the material surface, as shown in Figure 1. Materials softening along the welding line are mixed and combined with each other by giving the rotating tool a forward movement along the

material surface [19]. During this process, parameters such as the rotational speed of the rotating tool, the traverse speed, the geometry of the tool, the tilt angle of the tool, the force applied by the tool to the material and the fixation of the material affect the structure of the weld. In addition, the direction of rotation of the rotating tool (determines the advancing side and retreating side of the weld shown in Figure 1) is an effective parameter for the FSW process. Tool shoulder geometries used for friction stir welding shown in Figure 2. Examples of tools with different pin geometries are shown in Figure 3.

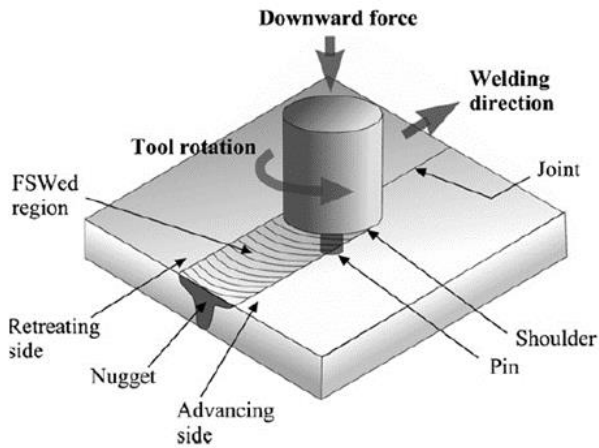


Figure 1. Schematic representation of the Friction Stir Welding process [18]

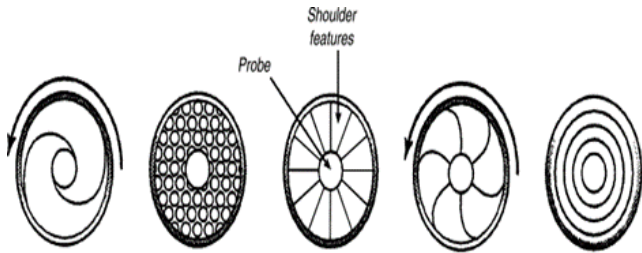


Figure 2. Tool shoulder geometries, viewed from underneath the shoulder (Copyright© 2001, TWI Ltd) (after Thomas et al. [20])



Figure 3. Examples of tools with different pin geometries [21]

2.1. Parameters of friction stir welding

The parameters that are effective in the FSW process are divided into three groups as indicated in Figure 4, these are:

- a) Tool geometry: Shoulder profile, pin profile, shoulder and pin diameter, shoulder and pin material.
- b) Welding parameters: traverse speed, rotational speed, tilt angle, etc.
- c) Other parameters: Workpiece properties, tool size, workpiece size, tool material [22]

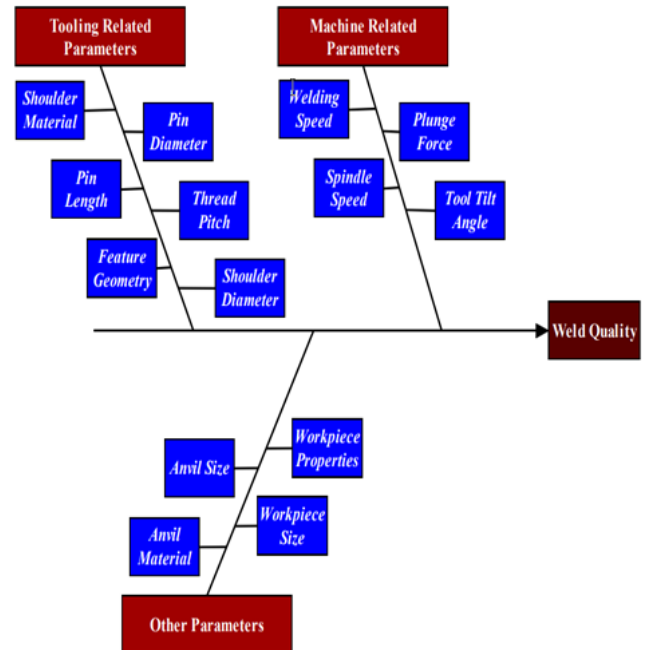


Figure 4. Parameters in the friction stir welding process [22]

2.2. Tool geometry

Tool geometry is one of the important factors to consider when joining using the FSW method. As seen in Figure 5, the tool with different geometries performs many functions such as generating heat, mixing, cutting the joint line, breaking the oxide layers, creating forging pressure and adding material to the joint. At the same time, the geometry of the tool must be able to meet the force and torque values that occur during the joining process and must be compatible with the plunge depth [23].

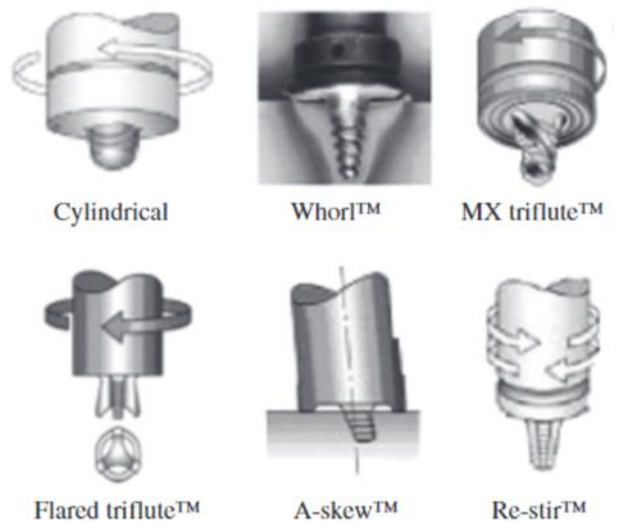


Figure 5. Tools used in the FSW method [24]

Whereas older tool designs consisted of straight, featureless shoulders and cylindrical or threaded pins, some of the earliest design innovations today were developed by Thomas et al. [20]. These innovations were the Flared-Triflute™ and Skew-Stir™ sets, indicated in Figure 5, designs aimed at increasing the degradation of the interfacial oxide layer and increasing the ITAB width especially in thrust welds [20, 23]. The Welding Institute (TWI) designed the Trivex™ tool shown in Figure 6, which can reduce process forces and are relatively easy to manufacture [23]. Studies on tool design and development focused on welded joining of many materials, especially in the welding of aluminum alloys, continues increasingly [23].



Figure 6. Trivex tool, designed by TWI [25]

Zhao et al. [26] investigated the effects of pin geometry on material flow in AA2014 butt welding. Elangovan and Balasubramanian [27] investigated the effects of AA2219 butt welds of straight cylindrical, conical cylindrical, toothed cylindrical, square and triangular profile pins on microstructure, tensile strength and microhardness. Scialpi et al. [28] investigated the effect of shoulder geometry on microstructure, strength and microhardness in butt welds of AA6082 material. The shoulder part of the tool usually includes geometries consisting of a cavity and a corner. Liu et al. [29] investigated the effects of varying shoulder and pin sizes on the microstructure and mechanical properties of 6061-T651 butt welds. It was stated that cracks formed in the low hardness region of the weld, an increase in the tensile strength of the weld area was observed with the increase in the feed rate, and the changes in the tool dimensions did not affect the welding performance.

Sorensen and Nielsen [30] designed a convex hollow shoulder assembly with spiral pins, which offers lower process forces and the ability to work with zero degree tilt angle. Longhurst [31] used a straight screw shoulder design shown in Figure 7. He stated that the shoulder design, which allows 0° axis angle, minimizes burr formation. He emphasized that the choice of pin geometry is also extremely important, along with the shoulder design, to strengthen the mix of the workpiece.

Muthu and Jayabalan [32], studied the effects of helical, flat conical and flat conical screw pin profiles on

plates joined by FSW method. They reported that they obtained better mechanical properties with the use of flat conical pin profile in the study using AA1100 series aluminum and pure copper.

Hassanifard et al. [33] employed various Friction Stir Welding (FSW) tools to investigate mechanical properties of Al 6061-T6 joints. Tensile properties of aluminum joint samples were improved as cone angle increased from 0° to 20° through different welding tools [33].

In the FSW process, the rotation speed, the traverse speed, the tool plunge force on the workpiece and the tilt angle between the tool and the workpiece constitute the welding parameters. With the rotation of the tool, the mixed material moves from the front to the back of the pin. It is extremely important for the welded joint to rotate the tool at the appropriate speed, to advance the rotating tool along the welding line at the appropriate speed, to contact the shoulder of the rotating tool to the welded parts to generate heat.



Figure 7. Tool with hollow spherical shoulder and cylindrical threaded pin [23]

The tool, which rotates faster than expected, generates more heat than necessary in the weld area, causing turbulent flow in the weld seam area. This creates micro-scale voids in the mixing zone, resulting in a decrease in strength. The low rotational speed causes not enough heat to be produced to ensure the bond, which produces a weak bond and low strength value [34–36]. Suresha et al. [37] stated that tool rotation speed is the most effective parameter on the mechanical properties of the weld when joining AA7075 aluminum alloy plates using the FSW method [22].

3. Advantages and disadvantages of friction stir welding

Advantages of friction stir welding:

- Good material mixing and seamless bonding around the interfaces [38].
- A non-consumable tool is used in the joining process performed with the FSW method [20].
- FSW can be applied as fully automatic welding process [39].
- Shielding gas and filler wire are not using at FSW method [40].
- Welding of alloys such as light and durable Aluminum 7075-T6 series, which are known as non-weldable, can be welded with FSW [41].
- Dissimilar materials can be welded [42].

- Performing the welding process at low temperature prevents welding defects such as porosity, wormholes and crack formation [43].
- FSW is a solid-state welding process [44].
- FSW is environmentally friendly [45].
- Lightweight materials such as titanium, magnesium and composite materials can be welded [46–48].
- FSW can be applied as a portable joining process [49].

The disadvantages of FSW are:

- High cost robotic systems are needed in complex geometry joints [39].

- Initial investment cost is higher than some of conventional methods [50].
- Additional apparatus is required for fixing process [51].
- Since the joining of materials with the FSW method is a solid state welding process, abrasions may occur on the rotating tool and pin during the joining of the material [52].

According to Table 1, for Al 6082 T6 alloy, mechanical properties of MIG, TIG and FS welded materials shows close values. For pure copper plates, FS welded materials shows better mechanical properties than TIG welding and mechanical properties closer to BM values.

Table 1. Comparison of material properties of FS welded, TIG and MIG Welded Materials (BM: Base Material, TS: Tensile Strength, UTS: Ultimate Tensile Strength)

Material	Yield Strength (MPa)	UTS/ TS (MPa)	Elongation (%)	References
Al 6082 T6 (BM)	291	317 (TS)	11.3	[53]
Al 6082 T6 MIG-pulse	147	221 (TS)	5.2	[53]
Al 6082 T6 TIG	145	219 (TS)	5.4	[53]
Al 6082 T6 FSW (low traverse speed)	150	245 (TS)	5.7	[53]
Pure Copper (BM)	68	212 (UTS)	28.1	[54]
Pure Copper TIG	53	168 (UTS)	12.3	[54]
Pure Copper FSW	70	194 (UTS)	22.8	[54]

4. Friction stir welding applications

4.1. Defense industry

The FSW method is used in the defense industry, in the manufacture of armored boxes, turrets and structural parts. FSW method is used for joining materials like Al 7075-T651 rolled sheet metal for structural applications in defensive areas like military [55].

Defense industry applications using the FSW method:

- FSW method can be used in light military tanks manufactured using high strength aluminum alloys.
- Military bridges and amphibious personnel carriers.
- Titanium light field howitzers [56].

There is wide interest in the defense industry in using aluminum alloys for survivability related applications. Aluminum alloys have a low density compared to existing solutions and Al alloys are relatively cost-effective compared to other light armor materials such as titanium. FSW method is preferred for welding defense industry lightweight materials, as it has nearly similar properties to the base material and provides higher strength. tank body prototype manufactured by the FSW method are shown in Figure 9.

4.2. Aerospace industry

In 1995, NASA had to use light and durable aluminum-lithium alloy material in the external fuel tank of the spacecraft. However, since these materials are difficult to weld, the fuel tanks are combined with the

FSW method [58]. The NASA SLS launch rocket produced by the FSW method is shown in Figure 10.



Figure 9. A prototype of a tank body manufactured with the FSW method [57]



Figure 10. NASA SLS launch rocket produced by the FSW method [61]

Aluminum alloys are frequently used in the aero plane industry as well as in the aerospace industry.

Parts of the fuselage structure of the Eclipse 500 private plane welded by the FSW method is shown in Figure 11 [59]. In the outer panel design of aircraft fuselages, beams riveted to the outer panel surface are used. This leads to sealing problems. FSW technology is applied to the outer panel designs of airframes, increasing the production speed and optimizing the stress, fatigue and corrosion values of the structure [60].



Figure 11. Demonstration of joined parts of the fuselage structure of Eclipse 500 private plane using FSW method [62]

4.3. Marine industry

Aluminum panels formed by aluminum extrusion are used in the shipbuilding industry in the shipbuilding industry, honeycomb panels, decks, helipads and some ship partitions are manufactured with FSW technology. With FSW method, modular manufacturing of ships is possible, the assembly process is accelerated, weight savings are achieved and maintenance needs are reduced [63]. FBFSW (Floating Bobbin Friction Stir Welding) technology developed for shipbuilding can be combined with a portable apparatus developed for FSW process [64]. Portable friction stir welding devices for marine applications are shown in Figure 12 and Figure 13. Portable friction stir welding (PFSW) devices can be used for repairing ships and manufacturing parts in field.

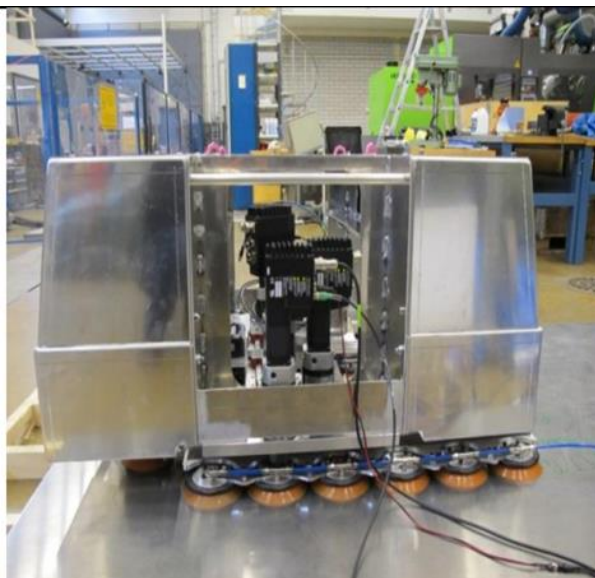


Figure 12. Portable friction stir welding device named Mobi-weld system [64]

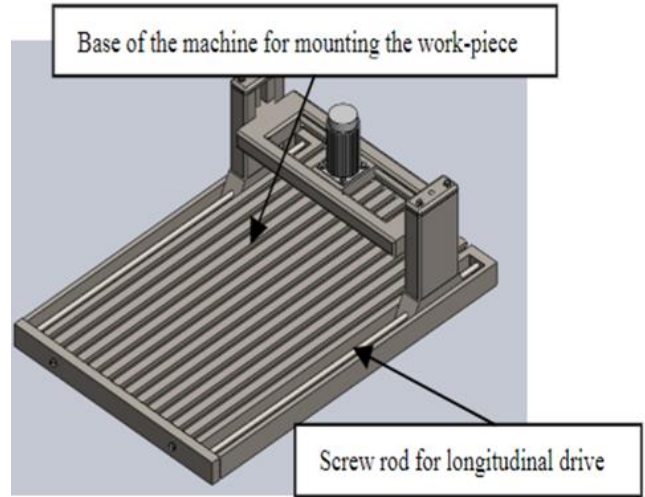


Figure 13. Portable Friction Stir Welding Device design [65]

4.4. Automotive industry

FSW and FSSW (Friction Stir Spot Welding) technology are used by manufacturers and suppliers in the automotive industry. Lightweight structures is using in Automobile components for fuel economy and meeting reduction in emissions regulation [66]. Automobile components joined with FSW are shown in Figure 14. Nowadays, aluminum is used in the cooling components of electric vehicles due to its being light weight and its thermal performance, and with the FSW method, which is the most ideal joining method for aluminum parts, is used in these parts.

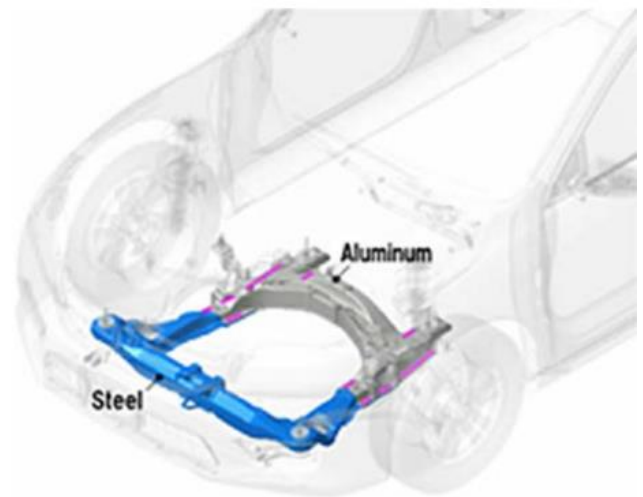


Figure 14. Friction stir spot welded dissimilar aluminum and steel sub-frame Honda Accord 2003 [67]

4.5. Railway industry

In railway industry lightweight materials can be joined with FSW method. FSW robot system for high-speed trains is shown in Figure 15.

5. Conclusion

In recent years, space travel has been on the agenda, high-speed trains have become widespread, electric

vehicles have begun to replace internal combustion engines, and developments in the field of maritime have increased the demand for light, high-strength and fast-manufacturable parts. The main materials for these fields are Aluminum 2xxx, 5xxx, 6xxx and 7xxx series materials, which are difficult or impossible to combine with conventional methods. The FSW method was a method for joining aluminum materials, but can now be used for steel, titanium and titanium alloys that need to be joined at higher temperatures.

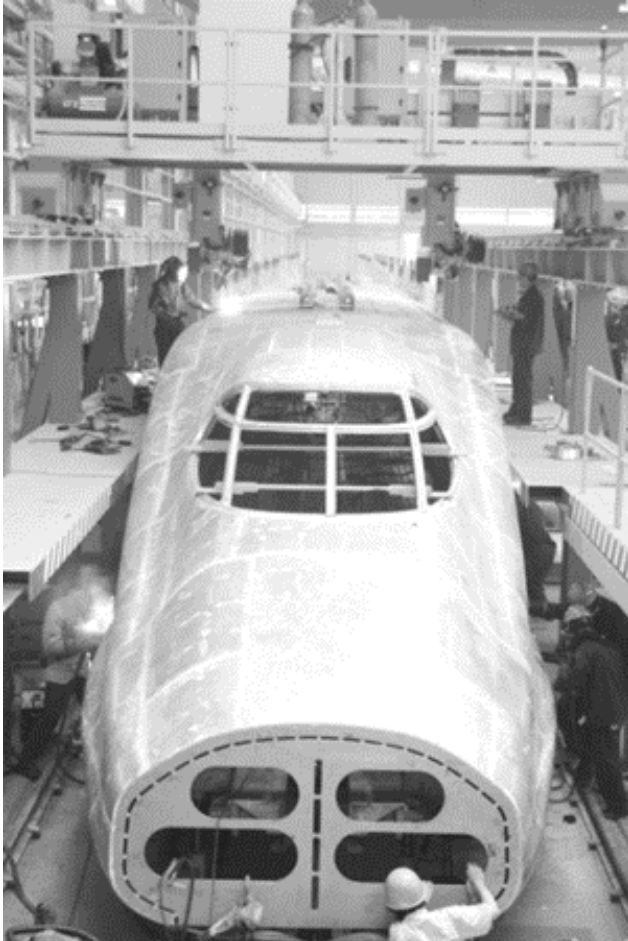


Figure 15. FSW robot system for high speed trains [68]

Friction Stir Welding method has a cost advantage besides its features such as preventing welding defects and enabling the possibility of welding, eliminating the need for filler material and being able to be applied faster. With increasing production amount, the FSW method is less costly than a conventional welding method such as MIG [69].

One of the advantages of friction stir welding over laser welding, which can be considered as an alternative, is that its parameters (rotational speed, welding traverse speed, tilt angle, axial force, probe and shoulder profile [70] are easy to apply, the laser source needs cooling and it is difficult to provide a stable energy flow. FSW technology is becoming widespread with the spread of robotic systems (for welding complex geometries), decreasing in initial investment costs, the widespread use of portable systems in repair and manufacturing, minimizing welding defects and the increasing need for lightly different materials. Additionally, FSW method is the most suitable method for combining the cooling

systems and battery systems of electric vehicles and hybrid cars. Welding dissimilar materials, plastics, ceramics, composite materials as well as steel with the FSW method is possible with the studies carried out today. The FSW method stands out as a strategic technology that is becoming widespread nowadays.

Author contributions

Emre Kaygusuz: Methodology, Writing-Reviewing, Writing-Original draft preparation. **Filiz Karaömerlioğlu and Serhat Akinci:** Writing-Reviewing and Editing.

Conflicts of interest

The authors declare no conflicts of interest.

References

1. Kutz, M. (2006). *Materials and Mechanical Design*. John Wiley & Sons.
2. Kumar, N., Mishra, R. S., & Yuan, W. (2015). *Friction stir welding of dissimilar alloys and materials*. Butterworth-Heinemann.
3. Norrish, J. (1992). *Advanced welding processes*. Springer Science & Business Media. <https://doi.org/10.1533/9781845691707.218>
4. Cooper, D. R., & Allwood, J. M. (2014). The influence of deformation conditions in solid-state aluminium weld strength. *Journal of Materials Processing Technology*, 214(11), 2576-2592. <https://doi.org/10.1016/j.jmatprotec.2014.04.018>
5. Duarte, A., Queirós, G. W., Sanchez, L. G., de Salazar, J. M. G., & Portal, A. J. C. (2018). Welding by Hot Forging of Two Carbon Steels for the Manufacture of Spanish and Japanese Weapons. *Journal of Material Sciences & Engineering*, 7(446), 2169-0022.
6. Djurdjanovic, M. B., Mijajlovic, M. M., Milcic, D. S., & Stamenkovic, D. S. (2009). Heat generation during friction stir welding process. *Tribology in industry*, 31(1&2), 8.
7. Verma, S., Kumar, V., Kumar, R., & Sidhu, R. S. (2022). Exploring the application domain of friction stir welding in aluminum and other alloys. *Materials Today: Proceedings*, 50, 1032-1042. <https://doi.org/10.1016/j.matpr.2021.07.449>
8. Singh, K., Singh, G., & Singh, H. (2019). Microstructure and mechanical behaviour of friction-stir-welded magnesium alloys: As-Welded and post weld heat treated. *Materials Today Communications*, 20, 100600. <https://doi.org/10.1016/j.mtcomm.2019.100600>
9. Singh, K., Singh, G., & Singh, H. (2019). Investigation on the microstructure and mechanical properties of a dissimilar friction stir welded joint of magnesium alloys. *Proceedings of the Institution of Mechanical Engineers, Part L: Journal of Materials: Design and*

- Applications, 233(12), 2444–2454. <https://doi.org/10.1177/1464420719865292>
10. Cakan, A., Ugurlu, M., & Kaygusuz, E. (2019). Effect of weld parameters on the microstructure and mechanical properties of dissimilar friction stir joints between pure copper and the aluminum alloy AA7075-T6, 61(2), 142–148. <https://doi.org/10.3139/120.111297>
 11. Singh, K., Singh, G., & Singh, H. (2021). Influence of post welding heat treatment on the microstructure and mechanical properties of friction stir welding joint of AZ31 Mg alloy. *Proceedings of the Institution of Mechanical Engineers, Part E: Journal of Process Mechanical Engineering*, 235(5), 1375–1382. <https://doi.org/10.1177/0954408921997626>
 12. Wang, T., Feng, Z., & Wang, R. (2022). Study on Friction Stir Welding and Heat Treatment of 7050 Aluminum Alloy. In B. Duan, K. Umeda, & C. Kim (Eds.), *Proceedings of the Eighth Asia International Symposium on Mechatronics* (pp. 196–202). Singapore: Springer Nature Singapore.
 13. Prasad, K. A., Chand, A. A., Kumar, N. M., Narayan, S., & Mamun, K. A. (2022). A Critical Review of Power Take-Off Wave Energy Technology Leading to the Conceptual Design of a Novel Wave-Plus-Photon Energy Harvester for Island/Coastal Communities' Energy Needs. *Sustainability*, 14(4), 2354. <https://doi.org/10.3390/su14042354>
 14. Singh, K., Singh, G., & Singh, H. (2022). The influence of holding time on the characteristics of friction stir welded dissimilar magnesium alloy joints during post welding heat treatment. *Proceedings of the Institution of Mechanical Engineers, Part L: Journal of Materials: Design and Applications*, 14644207221106576. <https://doi.org/10.1177/14644207221106576>
 15. Su, M., Qi, X., Xu, L., Feng, Q., Han, Y., & Zhao, L. (2022). Microstructural and mechanical analysis of 6063-T6 aluminum alloy joints bonded by friction stir welding. *Journal of Materials Science*, 57(31), 15078–15093. <https://doi.org/10.1007/s10853-022-07541-w>
 16. Singh, K., Sehgal, A. K., Singh, G., & Singh, H. (2022). Influence of PWHT on FSW joint of AZ61 Mg alloy. *International Conference on Latest Developments in Materials & Manufacturing*, 60, 2217–2221. <https://doi.org/10.1016/j.matpr.2022.03.117>
 17. Hunt, J. B., Mazzeo, B. A., Sorensen, C. D., & Hovanski, Y. (2022). A Generalized Method for In-Process Defect Detection in Friction Stir Welding. *Journal of Manufacturing and Materials Processing*, 6(4), 80. <https://doi.org/10.3390/jmmp6040080>
 18. Elatharasan, G., & V.S., S. kumar. (2013). An Experimental Analysis and Optimization of Process Parameter on Friction Stir Welding of AA 6061-T6 Aluminum Alloy using RSM. *Procedia Engineering*, 64. <https://doi.org/10.1016/j.proeng.2013.09.202>
 19. Khalaf, H. I., Al-Sabur, R., Abdullah, M. E., Kubit, A., & Derazkola, H. A. (2022). Effects of Underwater Friction Stir Welding Heat Generation on Residual Stress of AA6068-T6 Aluminum Alloy. *Materials*, 15(6), 2223. <https://doi.org/10.3390/ma15062223>
 20. Thomas, W. M., Johnson, K. I., & Wiesner, C. S. (2003). Friction Stir Welding – Recent Developments in Tool and Process Technologies. *Advanced Engineering Materials*, 5(7), 485–490. <https://doi.org/10.1002/adem.200300355>
 21. Ahmadi, H., Arab, N. B. M., Ghasemi, F. A., & Farsani, R. E. (2012). Influence of Pin Profile on Quality of Friction Stir Lap Welds in Carbon Fiber Reinforced Polypropylene Composite. *International Journal of Mechanics and Applications*, 2(3), 24–28. <https://doi.org/10.5923/j.mechanics.20120203.01>
 22. Verma, S., Gupta, M., & Misra, J. P. (2016). Friction Stir Welding of Aerospace Materials: A State of Art Review. In B. Katalinic (Ed.), *DAAAM International Scientific Book* (1st ed., Vol. 15, pp. 135–150). DAAAM International Vienna. <https://doi.org/10.2507/daaam.scibook.2016.13>
 23. Gibson, B. T., Lammlein, D. H., Prater, T. J., Longhurst, W. R., Cox, C. D., Ballun, M. C., ... Strauss, A. M. (2014). Friction stir welding: Process, automation, and control. *Journal of Manufacturing Processes*, 16(1), 56–73. <https://doi.org/10.1016/j.jmapro.2013.04.002>
 24. He, X., Gu, F., & Ball, A. (2014). A review of numerical analysis of friction stir welding. *Progress in Materials Science*, 65, 1–66. <https://doi.org/10.1016/j.pmatsci.2014.03.003>
 25. Bhardwaj, N., Narayanan, R. G., Dixit, U. S., & Hashmi, M. S. J. (2019). Recent developments in friction stir welding and resulting industrial practices. *Advances in Materials and Processing Technologies*, 5(3), 461–496. <https://doi.org/10.1080/2374068X.2019.1631065>
 26. Zhao, Y. H., Lin, S. B., Qu, F. X., & Wu, L. (2006). Influence of pin geometry on material flow in friction stir welding process. *Materials science and technology*, 22(1), 45–50. <https://doi.org/10.1179/174328406X78424>
 27. Elangovan, K., & Balasubramanian, V. (2008). Influences of tool pin profile and welding speed on the formation of friction stir processing zone in AA2219 aluminium alloy. *Journal of Materials Processing Technology*, 200(1–3), 163–175. <https://doi.org/10.1016/j.jmatprotec.2007.09.019>
 28. Scialpi, A., De Filippis, L. A. C., & Cavaliere, P. (2007). Influence of shoulder geometry on microstructure and mechanical properties of friction stir welded 6082 aluminium alloy. *Materials and Design*, 28(4), 1124–1129. <https://doi.org/10.1016/j.matdes.2006.01.031>
 29. Liu, F. C., & Ma, Z. Y. (2008). Influence of tool dimension and welding parameters on microstructure and mechanical properties of friction-stir-welded 6061-T651 aluminum alloy. *Metallurgical and Materials Transactions A: Physical Metallurgy and Materials Science*, 39(10), 2378–2388. <https://doi.org/10.1007/s11661-008-9586-2>
 30. Sorensen, C., & Nielsen, B. (2009). Exploring Geometry Effects for Convex Scrolled Shoulder, Step Spiral Probe FSW Tools. In *The Materials Society Annual Meeting* (pp. 85–92).

31. Longhurst, W. R. (2009). Force Control of Friction Stir Welding, 229.
32. Muthu, M. F. X., & Jayabalan, V. (2016). Effect of pin profile and process parameters on microstructure and mechanical properties of friction stir welded Al-Cu joints. *Transactions of Nonferrous Metals Society of China*, 26(4), 984-993. [https://doi.org/10.1016/S1003-6326\(16\)64195-X](https://doi.org/10.1016/S1003-6326(16)64195-X)
33. Hassanifard, S., Ghiasvand, A., Hashemi, S. M., & Varvani-Farahani, A. (2022). The effect of the friction stir welding tool shape on tensile properties of welded Al 6061-T6 joints. *Materials Today Communications*, 31, 103457. <https://doi.org/10.1016/j.mtcomm.2022.103457>
34. Azimzadegan, T., & Serajzadeh, S. (2010). An investigation into microstructures and mechanical properties of AA7075-T6 during friction stir welding at relatively high rotational speeds. *Journal of Materials Engineering and Performance*, 19(9), 1256-1263. <https://doi.org/10.1007/s11665-010-9625-1>
35. Dinaharan, I., & Murugan, N. (2012). Optimization of friction stir welding process to maximize tensile strength of AA6061/ZrB 2 in-situ composite butt joints. *Metals and Materials International*, 18(1), 135-142. <https://doi.org/10.1007/s12540-012-0016-z>
36. Heidarzadeh, A., Khodaverdizadeh, H., Mahmoudi, A., & Nazari, E. (2012). Tensile behavior of friction stir welded AA 6061-T4 aluminum alloy joints. *Materials and Design*, 37, 166-173. <https://doi.org/10.1016/j.matdes.2011.12.022>
37. Suresha, C. N., Rajaprakash, B. M., & Upadhy, S. (2011). A Study of the Effect of Tool Pin Profiles on Tensile Strength of Welded Joints Produced Using Friction Stir Welding Process. *Materials and Manufacturing Processes*, 26(9), 1111-1116. <https://doi.org/10.1080/10426914.2010.532527>
38. Guo, J., Gougeon, P., & Chen, X. G. (2012). Microstructure evolution and mechanical properties of dissimilar friction stir welded joints between AA1100-B4C MMC and AA6063 alloy. *Materials Science and Engineering: A*, 553, 149-156. <https://doi.org/10.1016/j.msea.2012.06.004>
39. Mendes, N., Neto, P., Simão, M. A., Loureiro, A., & Pires, J. N. (2016). A novel friction stir welding robotic platform: welding polymeric materials. *The International Journal of Advanced Manufacturing Technology*, 85(1), 37-46. <https://doi.org/10.1007/s00170-014-6024-z>
40. Shah, S., & Tosunoglu, S. (2012). Friction Stir Welding: Current State of the Art and Future Prospects, 7.
41. Goloborodko, A., Ito, T., Yun, X., Motohashi, Y., & Itoh, G. (2004). Friction Stir Welding of a Commercial 7075-T6 Aluminum Alloy: Grain Refinement, Thermal Stability and Tensile Properties. *Materials Transactions*, 45, 2503-2508. <https://doi.org/10.2320/matertrans.45.2503>
42. Murr, L. E. (2010). A Review of FSW Research on Dissimilar Metal and Alloy Systems. *Journal of Materials Engineering and Performance*, 19(8), 1071-1089. <https://doi.org/10.1007/s11665-010-9598-0>
43. Albannai, A. I. (2020). Review the common defects in friction stir welding. *International Journal of Scientific & Technology Research*, 9(11), 318-329.
44. Mahoney, M. W., Rhodes, C. G., Flintoff, J. G., Bingel, W. H., & Spurling, R. A. (1998). Properties of friction-stir-welded 7075 T651 aluminum. *Metallurgical and Materials Transactions A*, 29(7), 1955-1964. <https://doi.org/10.1007/s11661-998-0021-5>
45. Swarnkar, A., Kumar, R., Suri, A., & Saha, A. (2016, December). A review on Friction Stir Welding: An environment friendly welding technique. In *2016 IEEE Region 10 Humanitarian Technology Conference (R10-HTC)* (pp. 1-4). IEEE. <https://doi.org/10.1109/R10-HTC.2016.7906807>
46. Liu, H. J., Zhou, L., Huang, Y. X., & Liu, Q. W. (2010). Study of the key issues of friction stir welding of titanium alloy. In *Materials Science Forum* (Vol. 638, pp. 1185-1190). Trans Tech Publications Ltd. <https://doi.org/10.4028/www.scientific.net/MSF.638-642.1185>
47. Singh, K., Singh, G., & Singh, H. (2018). Review on friction stir welding of magnesium alloys. *Journal of Magnesium and Alloys*, 6(4), 399-416. <https://doi.org/10.1016/j.jma.2018.06.001>
48. Kumar, N., Das, A., & Prasad, S. B. (2020). An analysis of friction stir welding (FSW) of metal matrix composites (MMCs). *Materials Today: Proceedings*, 26, 2650-2656. <https://doi.org/10.1016/j.matpr.2020.02.558>
49. Dos Santos, J. F., Staron, P., Fischer, T., Robson, J. D., Kostka, A., Colegrove, P., ... & Schreyer, A. (2018). Understanding precipitate evolution during friction stir welding of Al-Zn-Mg-Cu alloy through in-situ measurement coupled with simulation. *Acta Materialia*, 148, 163-172. <https://doi.org/10.1016/j.actamat.2018.01.020>
50. Strand, S. (2003, September). Joining plastics-can friction stir welding compete?. In *Proceedings: Electrical Insulation Conference and Electrical Manufacturing and Coil Winding Technology Conference (Cat. No. 03CH37480)* (pp. 321-326). IEEE. <https://doi.org/10.1109/EICEMC.2003.1247904>
51. Doos, Q. M., & Wahab, B. A. (2012). Experimental study of friction stir welding of 6061-T6 aluminum pipe. *International Journal of Mechanical Engineering and Robotics Research*, 1(3), 143-156.
52. Campanelli, S., Casalino, G., Casavola, C., & Moramarco, V. (2013). Analysis and Comparison of Friction Stir Welding and Laser Assisted Friction Stir Welding of Aluminum Alloy. *Materials*, 6(12), 5923-5941. <https://doi.org/10.3390/ma6125923>
53. Taban, E., & Kaluç, E. (2007). Comparison between microstructure characteristics and joint performance of 5086-H32 aluminium alloy welded by MIG, TIG and friction stir welding processes. *Kovove Materialy*, 45, 241-248.
54. Lin, J. W., Chang, H. C., & Wu, M. H. (2014). Comparison of mechanical properties of pure copper welded using friction stir welding and tungsten inert gas welding. *Journal of Manufacturing Processes*, 16(2), 296-304. <https://doi.org/10.1016/j.jmappro.2013.09.006>

55. Ikumapayi, O. M., & Akinlabi, E. T. (2019). Efficacy of α - β grade titanium alloy powder (Ti-6Al-2Sn-2Zr-2Mo-2Cr-0.25Si) in surface modification and corrosion mitigation in 3.5% NaCl on friction stir processed armour grade 7075-T651 aluminum alloys—insight in defence applications. *Materials Research Express*, 6(7), 076546. <https://doi.org/10.1088/2053-1591/ab1566>
56. Wells, M., Roopchand, B., Montgomery, J., & Gooch, W. (1998). Titanium Applications and R&D for Army Ground Systems TMS Non-Aerospace Applications of Titanium.
57. Burgess, V., & Rickert, R. (2019). Investigation in Friction Stir Welded Aluminum Alloy 2139-T8 for Hull Structure Applications, 27.
58. Ding, J., Carter, B., Lawless, K., Nunes, A., Russell, C., Suites, M., & Schneider, J. (2006). A Decade of Friction Stir Welding R and D at NASA's Marshall Space Flight Center and a Glance into the Future. NTRS - NASA Technical Reports Server, (20080009619).
59. Sergeeva, E. V. (2013). Friction stir welding in aerospace industry. *The Paton Welding Journal*, 5, 56-60.
60. Srubar, M. (2021). Application of friction stir welding in aircraft structures.
61. Ding, J., Michael, F., & Sowards, J. W. (2020). To the Moon, Mars, and Beyond: NASA's Space Launch System. *Welding Journal*, 60.
62. Leon, J. S., Bharathiraja, G., & Jayakumar, V. (2020). A review on Friction Stir Welding in Aluminium Alloys. *IOP Conference Series: Materials Science and Engineering*, 954(1), 012007. <https://doi.org/10.1088/1757-899x/954/1/012007>
63. Singh, P., Biswas, P., & Kore, S. D. (2019). Influence of Traverse Speed in Self-Reacting FSW of AA6061-T6. *Journal of Ship Production and Design*.
64. Martin, J., & Wei, S. (2015). Friction Stir Welding Technology for Marine Applications (pp. 217-226). <https://doi.org/10.1002/9781119093343.ch24>
65. Renish, R. R., Pranesh, M. A., & Logesh, K. (2018). Design and analysis of a portable friction stir welding machine. *Materials Today: Proceedings*, 5(9, Part 3), 19340-19348. <https://doi.org/10.1016/j.matpr.2018.06.293>
66. Kayode, O., & Akinlabi, E. T. (2019). An overview on joining of aluminium and magnesium alloys using friction stir welding (FSW) for automotive lightweight applications (Vol. 6). IOP Publishing. Retrieved from <https://doi.org/10.1088/2053-1591/ab3262>
67. Kusuda, Y. (2013). Honda develops robotized FSW technology to weld steel and aluminum and applied it to a mass-production vehicle. *Industrial Robot: An International Journal*, 40(3), 208-212. <https://doi.org/10.1108/01439911311309889>
68. Lee, S. C. (2013). Technologies for Robotized Welding of Big Aluminium Structures with Tolerances for High Speed Trains. *Journal of the Korean Welding and Joining Society*, 31(1), 33-37. <https://doi.org/10.5781/KWJS.2013.31.1.33>
69. Mononen, J., Sirén, M., & Hänninen, H. (2003). Cost Comparison of FSW and MIG Welded Aluminium Panels. *Welding in the World*, 47(11-12), 32-35. <https://doi.org/10.1007/BF03266406>
70. Gite, R. A., Loharkar, P. K., & Shimpi, R. (2019). Friction stir welding parameters and application: A review. *Materials Today: Proceedings*, 19, 361-365. <https://doi.org/10.1016/j.matpr.2019.07.613>



© Author(s) 2023. This work is distributed under <https://creativecommons.org/licenses/by-sa/4.0/>



A comparative study to estimate the mode I fracture toughness of rocks using several soft computing techniques

Ekin Köken ^{*1}, Tümay Kadakci Koca ²

¹Abdullah Gul University, Nanotechnology Engineering Department, Türkiye

²Muğla Sıtkı Koçman University, Geological Engineering Department, Türkiye

Keywords

Mode-I fracture toughness
Uniaxial compressive strength
Brazilian tensile strength
Soft computing techniques

Research Article

DOI: 10.31127/tuje.1120669

Received: 24.05.2022

Revised: 06.09.2022

Accepted: 23.10.2022

Published: 27.02.2023



Abstract

Fracture toughness is an important phenomenon to reveal the actual strength of fractured rock materials. It is, therefore, crucial to use the fracture toughness models principally for simulating the performance of fractured rock medium. In this study, the mode-I fracture toughness (K_{Ic}) was investigated using several soft computing techniques. For this purpose, an extensive literature survey was carried out to obtain a comprehensive database that includes simple and widely used mechanical rock parameters such as uniaxial compressive strength (UCS) and Brazilian tensile strength (BTS). Several soft computing techniques such as artificial neural network (ANN), adaptive neuro-fuzzy inference system (ANFIS), gene expression programming (GEP), and multivariate adaptive regression spline (MARS) were attempted to reveal the availability of these methods to estimate the K_{Ic} . Among these techniques, it was determined that ANN presents the best prediction capability. The correlation of determination value (R^2) for the proposed ANN model is 0.90, showing its relative success. In this manner, the present study can be declared a case study, indicating the applicability of several soft computing techniques for the evaluation of K_{Ic} . However, the number of samples for different rock types should be increased to improve the established predictive models in future studies.

1. Introduction

Fracture toughness is defined as a stress intensity factor (SIF) in fracture mechanics [1]. It also characterizes the resistance of materials against crack development. In terms of rock mechanics, it is a fundamental concept that provides a physical framework for understanding many processes associated with rock fractures. In a typical brittle material, three types of stress-strain states have been documented. Figure 1 shows a schematic plot of failure stress versus fracture toughness. For low toughness materials, brittle fracture is the governing failure mechanism, and critical stress varies linearly with fracture toughness, which is calculated using Equation 1 [2].

$$K_I = \sigma \sqrt{\pi a} \quad (1)$$

Where a is the radius of the crack plate, σ is the tensile stress causing the fracture in the material.

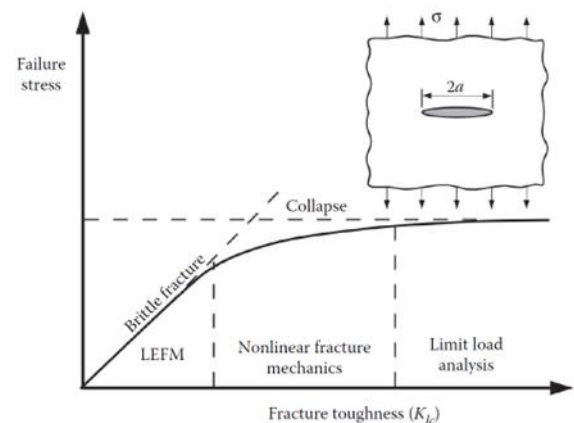


Figure 1. Effect of fracture toughness on the governing failure mechanism in a typical brittle material (LEFM: Linear elastic fracture mechanics, $2a$: diameter of the crack plate, σ : tensile stress triggering fracture development) [2]

* Corresponding Author

^{*}(ekin.koken@agu.edu.tr) ORCID ID 0000-0003-0178-329X
(tumaykoca@gmail.com) ORCID ID 0000-0002-6705-9117

Cite this article

Köken, E., & Koca, T. K. (2023). A comparative study to estimate the mode I fracture toughness of rocks using several soft computing techniques. Turkish Journal of Engineering, 7(4), 296-305

When the fracture toughness of the rock material increases, the principles of nonlinear fracture mechanics and limit load analysis are valid for the evaluation of various fracture types.

Based on modern rock mechanics and rock engineering approaches, three types of fracture toughness models have been identified, which are illustrated in Figure 2. Mode I fracture toughness (K_{IC}), where the principal load is applied normally to the crack plane, tends to open the crack. Mode II fracture toughness (K_{IIc}) corresponds to in-plane shear loading and tends to slide one crack face concerning the other. Mode III fracture toughness (K_{IIIc}) refers to out-of-plane shear. A cracked body can be loaded in any one of these modes, or a combination of two or three modes [2].

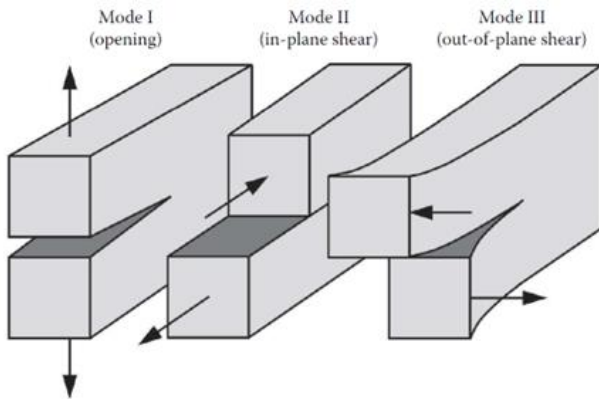


Figure 2. Three fracture toughness models in fracture mechanics [2]

Extensive scientific works have been carried out on the fracture toughness of rocks from different engineering geological aspects [3–12]. In these studies, the effects of elevated temperature, microwave treatment, and heating-cooling cycles on fracture toughness and the methods to determine the fracture toughness of rocks have been profoundly investigated. Regarding rock mechanics practices, the most common method to determine fracture toughness is based on using Brazilian disks with definite notches and cracked Chevron-notched Brazilian discs [13–21].

However, the determination of fracture toughness in the laboratory is laboring due to the requirement of special sample preparation and complicated testing procedures. Hence, several theories have been postulated to estimate the fracture toughness of rocks. Some empirical relationships to estimate the K_{IC} of rocks is listed in Table 1. However, the empirical relationships in Table 1 are valid for small-scale datasets or they represent a specific area of interest. Therefore, Pappalardo [22] described the regression-based predictive models as site-specific and he claimed that they have some limitations in dealing with larger datasets with different rock origins. To deal with larger datasets with different rock origins, soft computing tools would enable one to establish comprehensive predictive models. Based on a comprehensive literature survey, only two studies by Guha Roy et al. [23] and Afrasiabian and Eftekhari [24] proposed some soft computing-based predictive models for the evaluation of K_{IC} for different rock types (Table 2).

Table 1. Empirical relationships to estimate the K_{IC} of different rock types

Equation	R ²	Units	Ref.
$K_{IC} = 3.510^{-4} V_p^{-0.18}$	0.64	V_p in m/sec	
$K_{IC} = 4.28 \times 10^{-3} UCS + 1.05$	0.30	UCS in MPa	[5]
$K_{IC} = -0.50n_e + 1.70$	0.36	n_e in %	
$K_{IC} = -0.332 + 0.00036V_p$	0.96	V_p in m/sec	
$K_{IC} = 0.0006147V_s - 0.5517$	0.95	V_s in m/sec	[25]
$K_{IC} = 0.02150E_d + 0.2468$	0.93	E_d in GPa	
$K_{IC} = 3.2962\gamma_d - 7.8974$	0.48	γ_d in kN/m ³	
$K_{IC} = 0.0093SHV^{1.2464}$	0.35	SHV and SH in numerical digits	
$K_{IC} = 0.0126SH + 0.3644$	0.28		
$K_{IC} = -0.5304\ln(BAV) + 2.5345$	0.61	BAV in cm ³ /50cm ²	[26]
$K_{IC} = 0.0408\exp(0.0384ISI)$	0.37	ISI in %	
$K_{IC} = 0.1331PLI + 0.3921$	0.59	PLI in MPa	
$K_{IC} = 0.4075\exp(0.1427BTS)$	0.71	BTS in MPa	
$K_{IC} = 0.1013UCS^{0.5038}$	0.36	UCS in MPa	
$K_{IC} = 0.0037\exp(0.0022\rho_d)$	0.54	ρ_d in kg/m ³	
$K_{IC} = 0.45V_p - 0.58$	0.55	V_p in km/sec	[27]
$K_{IC} = 0.90V_s - 1.06$	0.60	V_s in km/sec	

Explanations: V_p : P wave velocity, V_s : S wave velocity,

E_d : Dynamic Young modulus, UCS: Uniaxial compressive strength, n_e : Effective porosity, γ_d : Dry unit weight, SHV: Schmidt hammer rebounding number, SH: Shore hardness, BAV: Böhme abrasion value, ISI: Impact strength index, PLI: Point load index, BTS: Brazilian tensile strength, ρ_d : Dry density

Table 2. Soft computing-based predictive models to estimate K_{Ic} for different rock types

Data analysis method	R^2		Independent variables	n	Ref.
	Training	Testing			
ANN	0.87	0.91	BTS, V_p , V_s	45	[23]
FIS	N.R	0.92			
ANFIS	N.R	0.97			
GEP	0.88	0.57	UCS, BTS	60	[24]
	0.88	0.76	UCS, E		
	0.86	0.75	BTS, E		
	0.86	0.87	UCS, BTS, E		

Explanations: BTS: Brazilian tensile strength, V_p : P wave velocity, V_s : S wave velocity UCS: Uniaxial compressive strength, BTS: Brazilian tensile strength, E: Young Modulus, ANN: Artificial neural networks, FIS: Fuzzy inference system, ANFIS: Adaptive neuro-fuzzy inference system, GEP: Gene expression programming, N.R: Not reported.

It is clear to figure out that using soft computing tools for the evaluation of K_{Ic} for different rock types has not been much studied. For this reason, the present study aims to build comprehensive predictive models for the evaluation of K_{Ic} using several soft computing tools and also to find out their superiority over one another.

For this purpose, artificial neural network (ANN), adaptive neuro-fuzzy inference system (ANFIS), gene expression programming (GEP), and multivariate adaptive regression spline (MARS) were adopted as the data analysis methods. The datasets were compiled from various published literature, and they are transformed into a comprehensive database for soft computing analyses.

As a result, four robust predictive models have been developed as a function of the UCS and BTS of rock material. The robustness of the models was evaluated by the coefficient of determination (R^2) values.

The details and mathematical formulations behind the proposed models are also given in this study to let users implement them in their work more efficiently.

The present study, in this manner, can save time and provide accurate and practical information on the K_{Ic} of

different rock types and understand the physical interaction between the input parameters and the K_{Ic} . The predictive models established in this study could also be integrated into rock mechanics applications such as hydraulic fracturing and drilling and blasting in fractured rock medium.

2. Data documentation

A comprehensive literature survey was conducted to compile quantitative data on the K_{Ic} for different rock types. Unfortunately, a significant number of previous studies could not have been regarded due to a lack of information on physical and mechanical rock properties, which are so important as input parameters. As a result of the literature survey, a database composed of 60 cases including the UCS and BTS of rocks was developed (Table 3). Before involving the database in the soft computing analyses, the database was randomly divided into the training (70/100) and testing (30/100) parts. The soft computing analyses were first conducted using the training parts of the database then the models were verified using the testing part.

Table 3. Datasets employed in soft computing analyses

Rock type	UCS (MPa)	BTS (MPa)	K_{Ic} (MPa m ^{0.5})	n	Reference
Limestone	105.0	2.3	0.40	1	[3]
Shale	12.0–16.0	0.86–1.07	0.15–0.22	2	[10]
Gabbro	132.5	11.1	1.97	1	[11]
Granite	151.0–157.4	9.7–12.0	1.60–1.70	3	[18]
Limestone, Travertine, Marble, Trachyte, Basalt	43.3–145.9	3.3–9.6	0.60–1.80	15	[26]
Sandstone, Shale, Basalt, Tonalite	33.0–145.2	5.4–19.4	0.30–3.50	6	[27]
Basalt, Syenite	148.6–222.	11.10–13.20	1.35–1.70	2	[28]
Sandstone, Limestone	32.3–144.9	2.7–8.5	0.30–0.90	3	[29]
Granite, Diorite, Marble, Sandstone, Limestone	40.0–219.0	5.0–15.0	1.10–3.80	6	[30]
Granite	173.0–259.0	7.9–12.8	1.26–1.71	3	[31]
Diorite	211.0	14.9	3.8	1	[32]
Granite, Diorite	165.0–224.0	10.0–14.5	1.00–25.0	2	[33]
Diorite	165.0	14.8	3.30	1	[34]
Sandstone	32.0	3.6	0.28	1	[35]
Andesite, Marble	52.3–82.8	5.1–7.0	0.56–0.94	2	[36]
Marble	52.3–75.3	4.7–5.9	1.15–1.22	3	[37]
Pegmatite, Gneiss	105.0–123.0	10.0–14.0	1.9–3.1	3	[38]
Limestone, Rhyolite, Granite	55.0–240.0	10.7–12.2	0.80–1.21	3	[39]
Travertine	26.1–29.6	4.9–5.3	0.54–0.59	2	[40]

Explanations: UCS: Uniaxial compressive strength, BTS: Brazilian tensile strength, K_{Ic} : Mode 1 Fracture toughness, n: Number of samples

Before performing the soft computing analyses, simple correlations of the considered variables were revealed by Pearson's correlation coefficient (r) and Spearman rho values, which are listed in Table 4. Accordingly, the UCS is moderately associated with the K_{IC} , whereas the BTS is highly correlated with the K_{IC} .

Therefore, these two independent variables can be readily selected as input parameters in soft computing analyses.

Table 4. Correlations of independent variables for the evaluation of K_{IC} for different rock types

Indicator	UCS	BTS
Pearson's correlation coefficient, r	0.595	0.829
Spearman rho value	0.689	0.811

3. Data analysis methods

3.1. Adaptive neuro-fuzzy inference system (ANFIS)

Considering many advantages, researchers have used ANFIS to build various predictive models that are many used in engineering geological problems [41–43]. The advantage of the ANFIS is that it practices a hybrid learning process to estimate the premise and consequent parameters [44].

In most ANFIS models, Sugeno fuzzy reasoning algorithm is primarily adopted based on numerous membership functions. Based on this information, the ANFIS analyses were carried out in the MATLAB

environment in this study. The UCS and BTS of rocks were selected as input parameters for the evaluation of K_{IC} (Figure 3a). For each input parameter, three triangular membership functions were identified (Figure 3b, 3c). Then, nine different if-then rules were developed in the context of ANFIS analyses (Figure 3d). Finally, the ANFIS model structure was completed (Figure 3e) for interpretation. The if-then rules employed in the ANFIS analyses are listed in Table 5.

Table 5. If-then rules established in the ANFIS analyses

Rule	Description
1	If UCS is in(1) and BTS is in(1) then K_{IC} is 0.1889
2	If UCS is in(1) and BTS is in(2) then K_{IC} is 0.7836
3	If UCS is in(1) and BTS is in(3) then K_{IC} is 11.09
4	If UCS is in(2) and BTS is in(1) then K_{IC} is 0.4918
5	If UCS is in(2) and BTS is in(2) then K_{IC} is 1.747
6	If UCS is in(2) and BTS is in(3) then K_{IC} is 3.206
7	If UCS is in(3) and BTS is in(1) then K_{IC} is 8.582
8	If UCS is in(3) and BTS is in(2) then K_{IC} is 0.2904
9	If UCS is in(3) and BTS is in(3) then K_{IC} is 6.43

3.2. Artificial neural networks (ANN)

ANN can analyze the data, learn and save the experience-based knowledge, and utilize it in future predictions [45, 46]. This parallel distributed learning algorithm is applicable to many problems, from social sciences to applied sciences. In most ANN models, a feed-forward backpropagation algorithm is adopted.

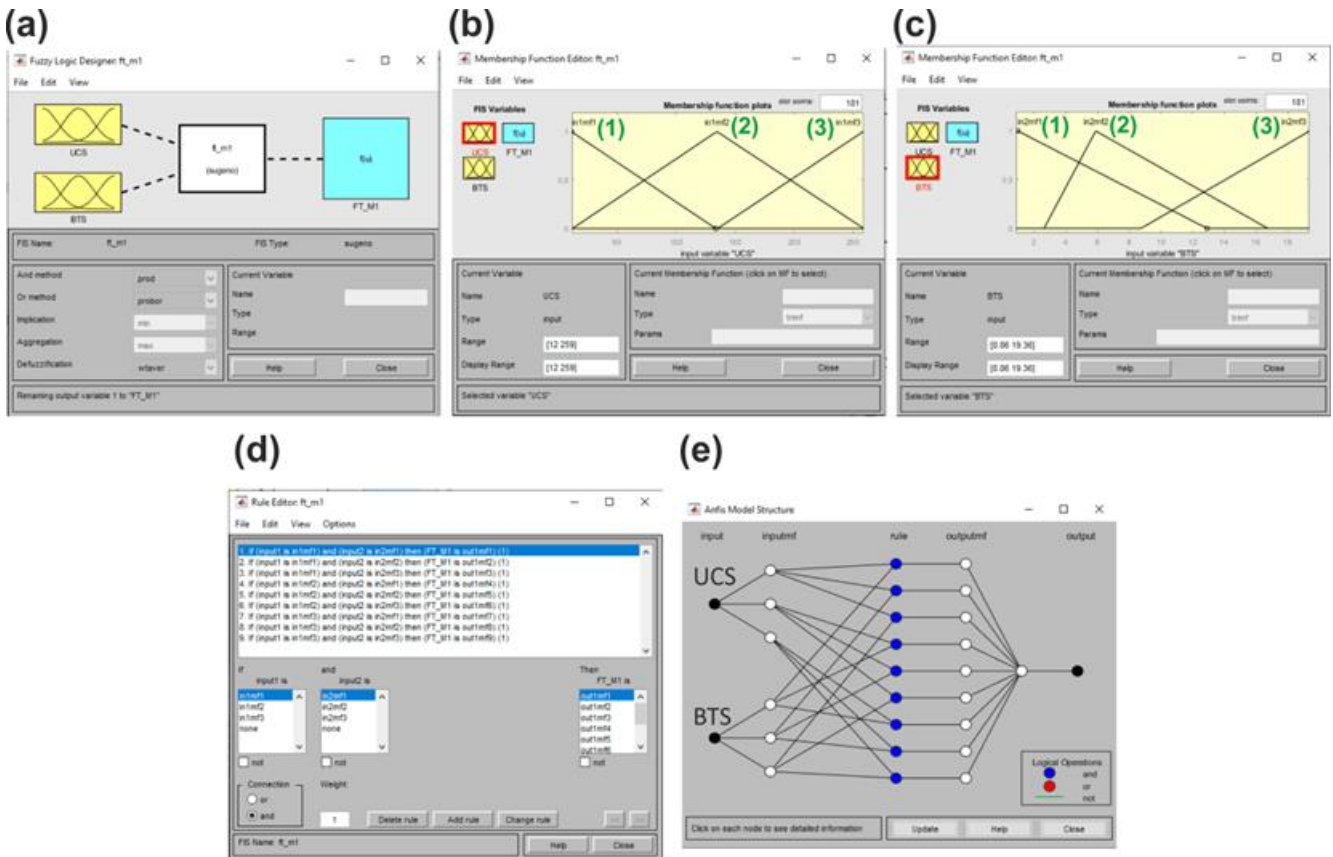


Figure 3. ANFIS outputs a) Input parameters b) UCS membership functions c) BTS membership functions d) If-then rule viewer e) ANFIS model structure

In this study, several ANN analyses were performed using the neural network toolbox (nntool) in the MATLAB environment. The novel ANN-based predictive model was introduced with definite mathematical equations using the weights and biases extracted from the ANN analyses. The ANN architecture adopted in this study is illustrated in Figure 4.

The UCS and BTS of rocks were adopted as input parameters. Six different hidden layers were developed in the ANN analyses and finally, a robust ANN model was developed to estimate the K_{IC} of rocks.

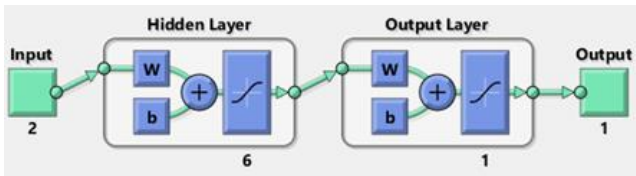


Figure 4. ANN architecture adopted in this study.

Before performing the ANN analyses, the database was normalized between -1 and 1 using Equation 2. As a result of the ANN analyses, K_{IC} can be estimated using Equation 3. The subfunctions of Equation 3 were determined based on the deterministic approach described by Das [47] and they are listed in Table 6.

$$V_n = 2 \left(\frac{x_i - x_{\min}}{x_{\max} - x_{\min}} \right) - 1 \quad (2)$$

where x_i is the relevant parameter to be normalized, x_{\min} , and x_{\max} are the minimum and maximum values in the dataset (Table 3).

$$K_{IC(ANN)} = 1.778 \tanh \left(\sum_{i=1}^6 x_i - 0.547 \right) + 1.9177, R^2 = 0.90 \quad (3)$$

Table 6. Subfunctions of the proposed ANN model

$x_1 = 2.9235 \tanh(9.6091 {}^n UCS - 4.0477 {}^n BTS - 3.5939)$
$x_2 = -2.8967 \tanh(12.2927 {}^n UCS - 5.7981 {}^n BTS - 4.9622)$
$x_3 = 0.39318 \tanh(-4.2588 {}^n UCS + 9.8239 {}^n BTS + 3.9321)$
$x_4 = 0.91735 \tanh(5.1937 {}^n UCS - 2.3084 {}^n BTS + 2.1721)$
$x_5 = -0.47452 \tanh(-1.0616 {}^n UCS - 13.8607 {}^n BTS + 5.3417)$
$x_6 = 0.85583 \tanh(-1.958 {}^n UCS + 1.2956 {}^n BTS - 0.55962)$
Normalization functions
${}^n UCS = 0.0081 UCS - 1.0972$
${}^n BTS = 0.1081 BTS - 1.093$

3.3. Gene Expression Programming (GEP)

The GEP is an evolutionary-based algorithm that produces an explicit mathematical formulation series

between dependent and independent variables. The GEP was first developed by Ferreira [48], and for the past two decades, the GEP has gained popularity among researchers in various engineering fields.

In the context of the GEP models, the number of chromosomes, head sizes, and gene sizes were assigned to 10, 7, and 3, respectively. The linking function was the multiplication and root means squared error (RMSE) was regarded as the fitness function. As a result of GEP analyses, sub-expression trees are given in Figure 5. These sub-expression trees are also listed in Table 7 as mathematical formulations.

Table 7. Mathematical equations of the sub-expression trees

$$x_1 = \frac{(-1.694 + (1 - BTS))}{2} \times \min \left(\exp(-3.702); \frac{1}{UCS} \right)$$

$$x_2 = \min(BTS; (-0.552 - UCS)) + \min(UCS; BTS) + BTS$$

$$x_3 = \min \left(\frac{-1.851 + BTS}{2}; \frac{1}{BTS} \right) \times \exp(-4.378) \times 2BTS$$

Based on the GEP model, the K_{IC} can be estimated using Equation 4 as follows:

$$K_{IC(GEP)} = 0.9415 \prod_{i=1}^3 x_i + 0.0721, R^2 = 0.73 \quad (4)$$

3.4. Multivariate adaptive regression spline (MARS)

The MARS was firstly proposed by Friedman [49] as a nonparametric regression method, which can be perceived as a hybrid linear model. There are two important parts in typical MARS models. One is the forward pass and the other one is the backward pass. In the forward pass, MARS models are initiated with constant terms, which are called basis functions (BFs). On the other hand, in the backward pass, the BFs are connected with linear regression models. In this study, a novel MARS model was introduced to estimate the K_{IC} of rocks.

The MARS analyses were performed using the software R and the established MARS model is given as Equation 5. The BFs of the MARS model are listed in Table 8.

Table 8. BFs of the established MARS model

Basis functions	Equation
BF2	$\max(0; 11.18 - BTS)$
BF3	$\max(0; BTS - 9.57)$
BF5	$\max(0; BTS - 10.22)$
BF10	$\max(0; UCS - 144.9)$

$$K_{IC(MARS)} = 2.00 - 0.192BF2 - 1.336BF3 + 1.671BF5 + 0.0027BF10, R^2 = 0.75 \quad (5)$$

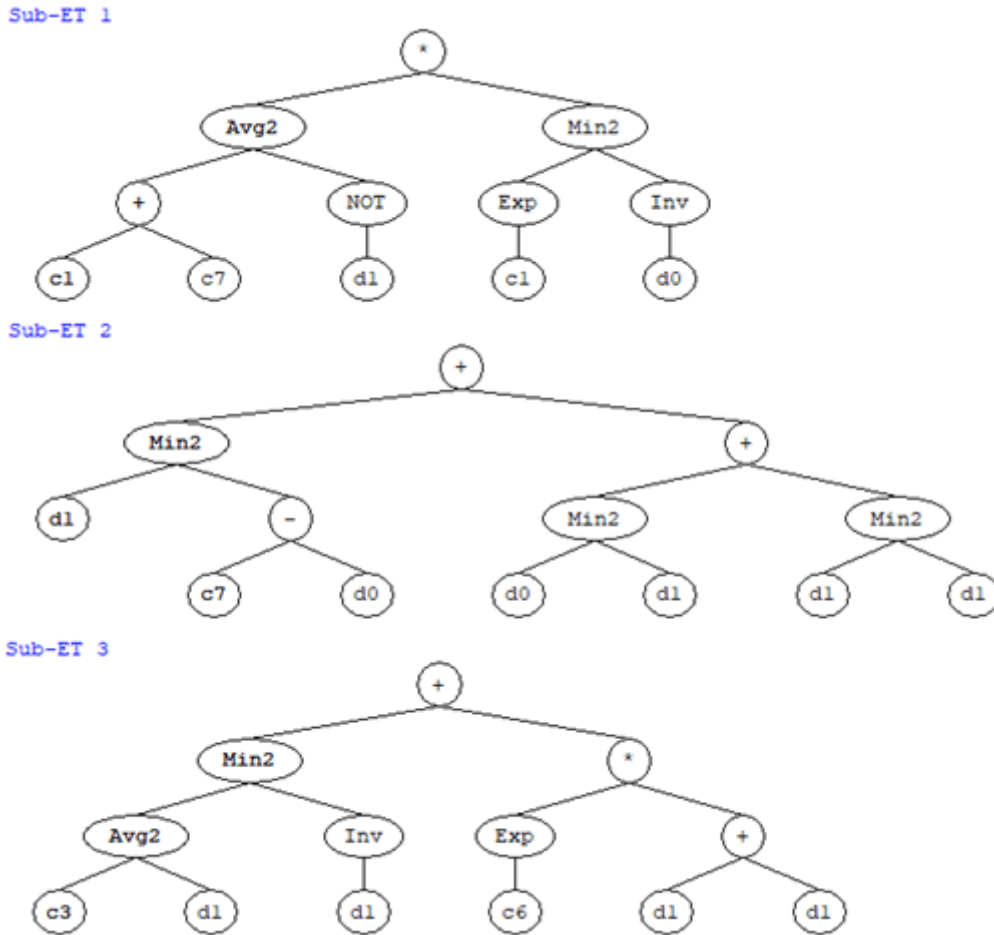


Figure 5. Sub-expression trees of the established GEP model (d0: UCS, d1: BTS, g1c1: -3.702, g1c7: 2.008, g2c7: -0.552, g3c3: -1.851, g3c6: -4.378)

4. Discussion

Simple regression models to estimate the K_{IC} of compiled rock types are illustrated in Figure 6. Accordingly, the BTS of rocks is highly associated with the K_{IC} . However, simple regression models are not enough for precise estimations. Therefore, soft computing analyses were performed to estimate K_{IC} values with intended accuracy. As a result of the soft computing analyses based on the database collected from rock mechanics test results (Table 3) presented in the literature by some researchers, four robust predictive models were developed to estimate the K_{IC} for different rock types. The predicted K_{IC} values by this study versus K_{IC} values compiled from the literature are plotted in Figure 7 for each model. Accordingly, the predicted and measured K_{IC} values are in good agreement which shows the model's relative success. The correlation of determination value (R^2) for the ANFIS, ANN, GEP, and MARS models was found to be 0.86, 0.90, 0.73, and 0.75, respectively (Figure 7).

The soft computing analysis results obtained from the present study indicated that the ANN model (Equation 3) is found to be the best predictive model for the evaluation of K_{IC} . This finding indicated the strong learning ability and adaptivity of the ANN methodology.

The soft computing models presented better R^2 values than most of the regression models proposed in the literature except for the regression models proposed

by Zhixi et al. [25]. Because the regression models of these researchers were developed using 13 cases composed of several sandstone samples.

As it is well known, if the sample size decreases and it is distributed more evenly, the regression models may have a better prediction performance.

When comparing the performance of the established soft computing models with the ones previously proposed by Guha Roy et al. [23] and Afrasiabian and Eftekhari [24], it is clear to state that the proposed ANN model is better than the GEP models proposed by Afrasiabian and Eftekhari [24]. Nevertheless, the GEP model in this study was not as successful as the GEP model proposed by Afrasiabian and Eftekhari [24]. The reason for this phenomenon may be interpreted as the structure of the GEP model being quite different.

On the other hand, the proposed models presented a lower performance than the models proposed by Guha Roy et al. [23]. The reason for this phenomenon can be attributed to the fact that the dataset used in this study involves different rock types unlike the dataset of Guha Roy et al. [23] and also input parameters that were integrated into the soft computing analyses are different. It is certain that as the variety of the rock types increases, the model performances may decrease.

However, it can be claimed that the BTS of rocks can be a correlative parameter for the evaluation of K_{IC} . The Pearson's correlation analysis results also support this phenomenon (Table 4).

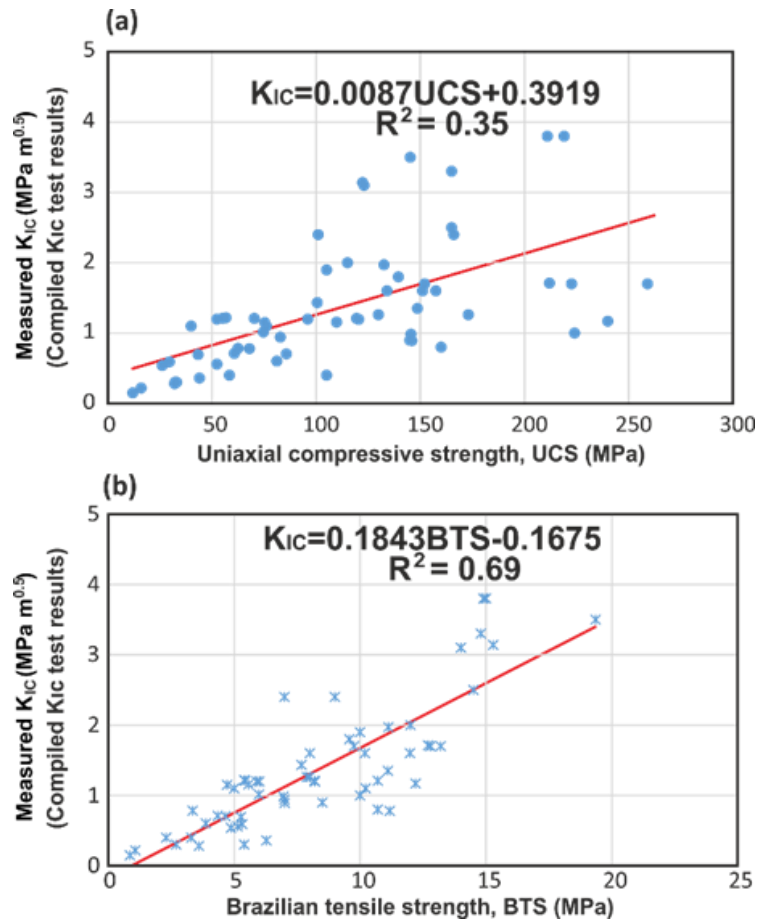


Figure 6. Simple regression models for the evaluation of K_{Ic} based on different rock properties
a) UCS b) BTS

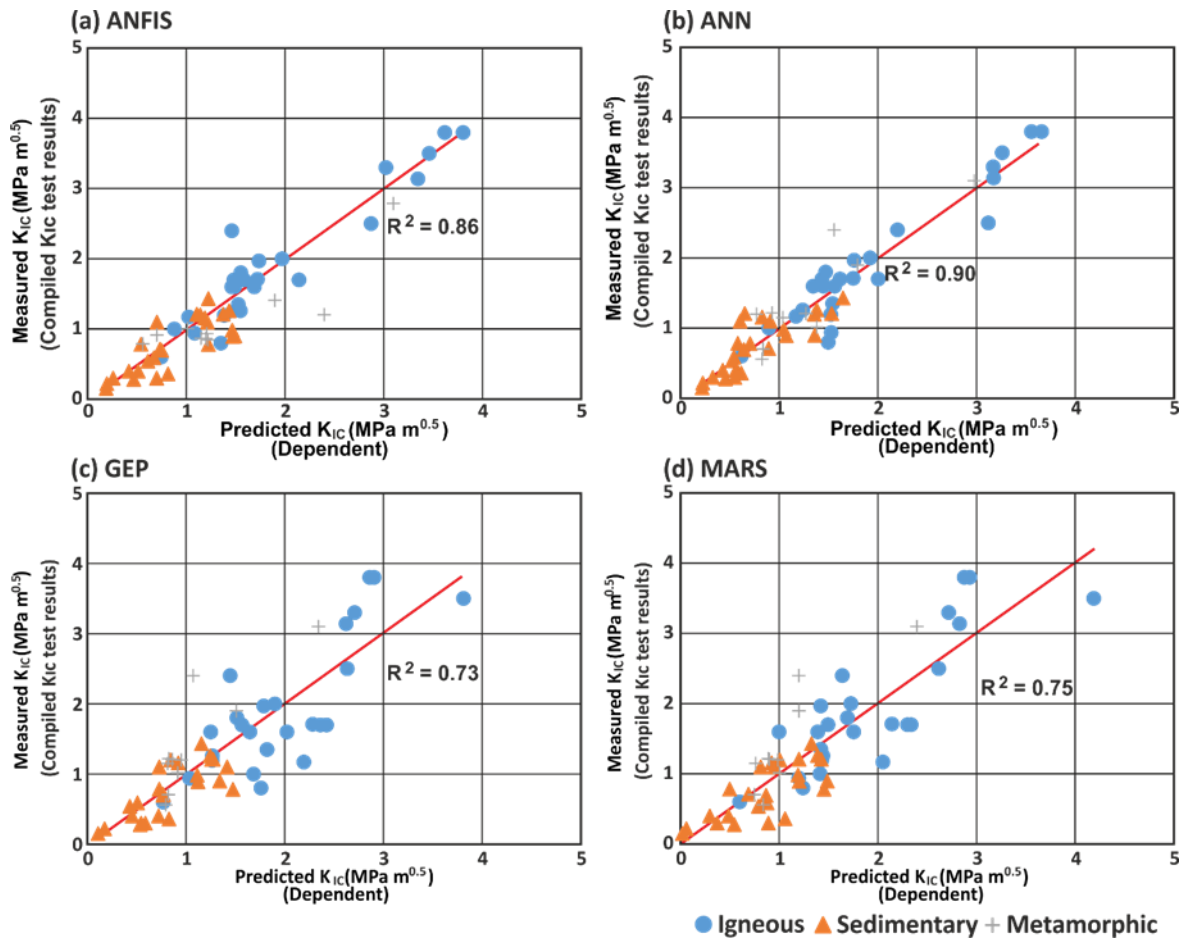


Figure 7. Predicted and measured K_{Ic} values for the established models a) ANFIS b) ANN c) GEP d) MARS

On the other hand, the use of MARS models has not been previously used for estimating the K_{IC} for a wide range of rock types. It was found that although the MARS and GEP models provide lower performances than the ANFIS and ANN models, they might have the potential on estimating the K_{IC} .

Overall, the findings obtained from the present study and the ones from the previous studies indicated that the UCS, BTS, V_p , and V_s can be used to estimate the K_{IC} of rocks. In this study, only UCS and BTS of rocks were adopted since they are the most commonly measured parameters in engineering geological projects.

Since the ANN model was found to be the best predictive model among the models established in this

study, an example of calculating the proposed ANN model was given as follows:

Example 1:

Case study 1 (Data was obtained from Reference 3)

UCS: 105.0 MPa, BTS: 2.3 MPa

Normalized values:

$$"UCS = 0.0081 \otimes 105.0 - 1.0972 = -0.2467$$

$$"BTS = 0.1081 \otimes 2.3 - 1.093 = -0.84437$$

Subfunctions:

$$x_1 = 2.9235 \tanh (9.6091 \otimes -0.2467 - 4.0477 \otimes -0.84437 - 3.5939) = -2.88438$$

$$x_2 = -2.8967 \tanh (12.2927 \otimes -0.2467 - 5.7981 \otimes -0.84437 - 4.9622) = 2.88494$$

$$x_3 = 0.39318 \tanh (-4.2588 \otimes -0.2467 + 9.8239 \otimes -0.84437 + 3.9321) = -0.39214$$

$$x_4 = 0.91735 \tanh (5.1937 \otimes -0.2467 - 2.3084 \otimes -0.84437 + 2.1721) = 0.91110$$

$$x_5 = -0.47452 \tanh (-1.0616 \otimes -0.2467 - 13.8607 \otimes -0.84437 + 5.3417) = -0.47452$$

$$x_6 = 0.85583 \tanh (-1.958 \otimes -0.2467 + 1.2956 \otimes -0.84437 - 0.55962) = -0.70559$$

$$K_{IC(ANN)} = 1.778 \tanh (-2.88438 + 2.88494 - 0.39214 + 0.91110 - 0.47452 - 0.70559 - 0.547) + 1.9177 = 0.43138 MPa m^{0.5} \text{ (Measured } K_{IC} = 0.40 MPa m^{0.5})$$

5. Conclusion

In this study, the K_{IC} of different rock types has been examined using ANN, ANFIS, GEP, and MARS methodologies. For this purpose, a comprehensive literature survey was conducted to compile such datasets for the implementation of the above-mentioned analysis methods. Consequently, 60 cases composed of the K_{IC} , UCS, and BTS of rocks from various published literature were considered. Based on the UCS and BTS of rocks, four robust predictive models have been developed.

Even though the ANN, ANFIS, and GEP models have been studied before for the evaluation of K_{IC} , the MARS model has not been used to estimate the K_{IC} of rocks.

Among these techniques, the ANN model (Equation 3) presented the best prediction performance. Contrary to the published literature, the GEP model has the lowest prediction capability with an R^2 of 0.73 for the evaluation of K_{IC} . The details and mathematical framework of the proposed models were introduced in this study to let users implement them more efficiently. The present study, in this context, can be declared a case study, indicating the applicability of several soft computing techniques for the evaluation of K_{IC} . However, the number of samples for different rock types should be increased to improve the established predictive models in future studies. Last but not least, it is important to note that the adopted techniques to estimate the K_{IC} of rocks may have some uncertainties due to their operational flow and the expert knowledge of the physical relationship between the input and output parameters.

Author contributions

Ekin Köken: Conceptualization, Methodology, Software, Writing-Original draft preparation
Tümay Kadakci Koca: Writing-Original draft preparation, Validation, Editing.

Conflicts of interest

The authors declare no conflicts of interest.

References

- Dai, F., Wei, M. D., Xu, N. W., Zhao, T., Xu, Y. (2015). Numerical investigation of the progressive fracture mechanisms of four ISRM-suggested specimens for determining the mode I fracture toughness of rocks. *Computers and Geotechnics*, 69, 424-441.
- Anderson, T. L. (2017). *Fracture mechanics: fundamentals and applications*. Fourth edition, CRC Press, 680 pp, ISBN: 978-1-4987-2813-3.
- Al-Shayea, N. A., Khan, K., & Abduljauwad, S. N. (2000). Effects of confining pressure and temperature on mixed-mode (I-II) fracture toughness of a limestone rock. *International Journal of Rock Mechanics and Mining Sciences*, 37(4), 629-643.
- Dwivedi, R. D., Soni, A. K., Goel, R. K., & Dube, A. K. (2000). Fracture toughness of rocks under sub-zero temperature conditions. *International Journal of*

- Rock Mechanics and Mining Sciences, 37(8), 1267-1275.
5. Chang, S. H., Lee, C. I., & Jeon, S. (2002). Measurement of rock fracture toughness under modes I and II and mixed-mode conditions by using disc-type specimens. *Engineering Geology*, 66(1-2), 79-97.
 6. Alber, M., & Brardt, A. (2003). Factors influencing fracture toughness K_{IC} from simple screening tests. *International Journal of Rock Mechanics and Mining Sciences*, 5(40), 779-784.
 7. Al-Shayea, N. A. (2005). Crack propagation trajectories for rocks under mixed mode I-II fracture. *Engineering Geology*, 81(1), 84-97.
 8. Nasser, M. H. B., Mohanty, B., & Robin, P. Y. (2005). Characterization of microstructures and fracture toughness in five granitic rocks. *International journal of rock mechanics and mining sciences*, 3(42), 450-460.
 9. Mahanta, B., Singh, T. N., & Ranjith, P. G. (2016). Influence of thermal treatment on mode I fracture toughness of certain Indian rocks. *Engineering Geology*, 210, 103-114.
 10. Brevik, N. Ø. (2016). Experimental study of fracture toughness in sedimentary rocks, Master's thesis, Norwegian University of Science and Technology, Department of Petroleum Engineering and Applied Geophysics, 144.
 11. Pakdaman, A. M., Moosavi, M., & Mohammadi, S. (2019). Experimental and numerical investigation into the methods of determination of mode I static fracture toughness of rocks. *Theoretical and Applied Fracture Mechanics*, 100, 154-170.
 12. Ge, Z., Sun, Q., Xue, L., & Yang, T. (2021). The influence of microwave treatment on the mode I fracture toughness of granite. *Engineering Fracture Mechanics*, 249, 107768.
 13. Kuruppu, M. D. (1997). Fracture toughness measurement using chevron notched semi-circular bend specimen. *International journal of fracture*, 86(4), L33-L38.
 14. Wang, J. J., Zhu, J. G., Chiu, C. F., & Zhang, H. (2007). Experimental study on fracture toughness and tensile strength of a clay. *Engineering Geology*, 94(1-2), 65-75.
 15. Zhou, Y. X., Xia, K., Li, X. B., Li, H. B., Ma, G. W., Zhao, J., ... & Dai, F. (2012). Suggested methods for determining the dynamic strength parameters and mode-I fracture toughness of rock materials. *International Journal of Rock Mechanics and Mining Sciences*, 49, 105-112.
 16. Erarslan, N., & Williams, D. J. (2012). The damage mechanism of rock fatigue and its relationship to the fracture toughness of rocks. *International Journal of Rock Mechanics and Mining Sciences*, 56, 15-26.
 17. Kuruppu, M. D., Obara, Y., Ayatollahi, M. R., Chong, K. P., & Funatsu, T. (2014). ISRM-suggested method for determining the mode I static fracture toughness using semi-circular bend specimen. *Rock Mechanics and Rock Engineering*, 47(1), 267-274.
 18. Sabri, M., Ghazvinian, A., & Nejati, H. R. (2016). Effect of particle size heterogeneity on fracture toughness and failure mechanism of rocks. *International Journal of Rock Mechanics and Mining Sciences*, 81, 79-85.
 19. Wei, M. D., Dai, F., Liu, Y., Xu, N. W., & Zhao, T. (2018). An experimental and theoretical comparison of CCNBD and CCNSCB specimens for determining mode I fracture toughness of rocks. *Fatigue & Fracture of Engineering Materials & Structures*, 41(5), 1002-1018.
 20. Wong, L. N. Y., & Guo, T. Y. (2019). Microcracking behavior of two semi-circular bend specimens in mode I fracture toughness test of granite. *Engineering Fracture Mechanics*, 221, 106565.
 21. Wu, S., Sun, W., & Xu, X. (2022). Study on Mode I Fracture Toughness of Rocks Using Flat-Joint Model and Moment Tensor. *Theoretical and Applied Fracture Mechanics*, 103403.
 22. Pappalardo, G. (2015). Correlation between P-wave velocity and physical-mechanical properties of intensely jointed dolostones, Peloritani mounts, NE Sicily. *Rock mechanics and rock engineering*, 48(4), 1711-1721.
 23. Guha Roy, D., Singh, T. N., & Kodikara, J. (2018). Predicting mode-I fracture toughness of rocks using soft computing and multiple regression. *Measurement*, 126, 231-241.
 24. Afrasiabian, B., & Eftekhari, M. (2022). Prediction of mode I fracture toughness of rock using linear multiple regression and gene expression programming. *Journal of Rock Mechanics and Geotechnical Engineering*, <https://doi.org/10.1016/j.jrmge.2022.03.008>
 25. Zhixi, C., Mian, C., Yan, J., & Rongzun, H. (1997). Determination of rock fracture toughness and its relationship with acoustic velocity. *International Journal of Rock Mechanics and Mining Sciences*, 34(3-4), 49-e1.
 26. Şengün, N., Altındağ, R. (2010). Kayaçların kırılma tokluğu (Mod-I) ile fiziko-mekanik özellikleri arasındaki ilişkilerinin değerlendirilmesi. *Yerbilimleri*, 31(2), 127-139.
 27. Guha Roy, D., Singh, T. N., Kodikara, J., & Talukdar, M. (2017). Correlating the mechanical and physical properties with mode-I fracture toughness of rocks. *Rock Mechanics and Rock Engineering*, 50(7), 1941-1946.
 28. Jian-An, H., & Sijing, W. (1985). An experimental investigation concerning the comprehensive fracture toughness of some brittle rocks. In *International Journal of Rock Mechanics and Mining Sciences & Geomechanics Abstracts (Vol. 22, No. 2, pp. 99-104)*. Pergamon.
 29. Singh, R. N., & Sun, G. X. (1989). The relationship between fracture toughness hardness indices and mechanical properties of rocks. *Nottingham University Mining Department Magazine;(UK)*, 41.
 30. Backers, T. (2004). Fracture toughness determination and micromechanics of rock under mode I and mode II loading. Ph.D. Thesis. University of Potsdam, Germany
 31. Iqbal, M. J., & Mohanty, B. (2007). Experimental calibration of ISRM suggested fracture toughness measurement techniques in selected brittle rocks.

- Rock Mechanics and Rock Engineering, 40(5), 453-475.
32. Andersson, J. C. (2007). Rock mass response to coupled mechanical thermal loading: Äspö Pillar Stability Experiment, Sweden (Doctoral dissertation, Bygghvetenskap).
 33. Stephansson, O., Shen, B., Rinne, M., Amemiya, K., Yamashi, R., & Toguri, S. (2008, October). FRACOD modeling of rock fracturing and permeability change in excavation damaged zones. In The 12th International Conference of International Association for Computer Methods and Advances in Geomechanics (IACMAG). Goa, India.
 34. Rinne, M. (2008). Fracture mechanics and subcritical crack growth approach to model time-dependent failure in brittle rock, Doctoral Dissertation, Helsinki University of Technology, Sweden.
 35. Lin, Q., Fakhimi, A., Haggerty, M., & Labuz, J. F. (2009). Initiation of tensile and mixed-mode fracture in sandstone. *International Journal of Rock Mechanics and Mining Sciences*, 46(3), 489-497.
 36. Alkılıçgil, Ç. (2010). Development of specimen geometries for mode I fracture toughness testing with disc type rock specimens, Thesis. Middle East Technical University, Turkey.
 37. Amrollahi, H., Baghbanan, A., & Hashemolhosseini, H. (2011). Measuring fracture toughness of crystalline marbles under modes I and II and mixed mode I-II loading conditions using CCNBD and HCCD specimens. *International Journal of Rock Mechanics and Mining Sciences*, 48(7), 1123-1134.
 38. Siren, T. (2011). Fracture mechanics prediction for Posiva's Olkiluoto spalling experiment (POSE) (No. POSIVA-WR--11-23). Posiva Oy.
 39. Momber, A. W. (2015). Fracture toughness effects in geomaterial solid particle erosion. *Rock Mechanics and Rock Engineering*, 48(4), 1573-1588.
 40. Ebrahimi, R., & Hosseini, M. (2022). Experimental study of effect of number of heating-cooling cycles on mode I and mode II fracture toughness of travertine. *Theoretical and Applied Fracture Mechanics*, 117, 103185.
 41. Roy, D. G., & Singh, T. N. (2020). Predicting deformational properties of Indian coal: Soft computing and regression analysis approach. *Measurement*, 149, 106975.
 42. Yesiloglu-Gultekin, N., Gokceoglu, C., & Sezer, E. A. (2013). Prediction of uniaxial compressive strength of granitic rocks by various nonlinear tools and comparison of their performances. *International Journal of Rock Mechanics and Mining Sciences*, 62, 113-122.
 43. Sharma, L. K., Vishal, V., & Singh, T. N. (2017). Developing novel models using neural networks and fuzzy systems for the prediction of strength of rocks from key geomechanical properties. *Measurement*, 102, 158-169.
 44. Jang, J. S. R. (1992) Neuro-fuzzy modeling: architecture, analyses and applications, dissertation, department of electrical engineering and computer science, University of California, Berkeley, CA 94720.
 45. Singh, V. K., Singh, D., & Singh, T. N. (2001). Prediction of strength properties of some schistose rocks from petrographic properties using artificial neural networks. *International Journal of Rock Mechanics and Mining Sciences*, 38(2), 269-284.
 46. Rabbani, E., Sharif, F., Salooki, M. K., & Moradzadeh, A. (2012). Application of neural network technique for prediction of uniaxial compressive strength using reservoir formation properties. *International journal of rock mechanics and mining sciences*, (56), 100-111.
 47. Das, S. K. (2013). Artificial neural networks in geotechnical engineering: modeling and application issues, *Metaheuristics in water, geotechnical and transport engineering*, 231-270.
 48. Ferreira, C. (2001) Gene expression programming: a new adaptive algorithm for solving problems *Complex Systems*, 13(2), 87-129
 49. Friedman, J. H. (1991) Multivariate adaptive regression splines. *The Annals of Statistics*, 19(1), 1-67



© Author(s) 2023. This work is distributed under <https://creativecommons.org/licenses/by-sa/4.0/>



Temperature series analysis of the Hirfanli Dam Basin with the Mann-Kendall and Sequential Mann-Kendall tests

Utku Zeybekoglu *¹ 

¹Sinop University, Construction Department, Türkiye

Keywords

Hirfanli Dam Basin
Mann-Kendall Test
Sequential Mann-Kendall Test
Temperature

Research Article

DOI: 10.31127/tuje.1145716

Received: 19.07.2022

Revised: 12.09.2022

Accepted: 14.09.2022

Published: 27.02.2023



Abstract

Global warming is a result of the greenhouse effect caused by the gases released into the atmosphere; It is usually expressed as an increase in the measured average temperatures. In addition to this, extreme weather events such as droughts, floods, and severe hurricanes become more frequent, and the specified extreme events become more severe. The effects of global climate change on hydrological and meteorological variables are increasing day by day. Therefore, hydro-meteorological parameters should be examined carefully. In this study, the effects of global climate change on the Hirfanli Dam Basin temperature series were investigated using the Mann-Kendall Test and Sequential Mann-Kendall Test. The annual mean temperature series of six stations recorded between 1965 and 2017 were analyzed and evaluated. It has been determined that the annual mean temperature has increased throughout the basin and significant increases started since the 1990s. Researches analysing the effects of global climate change on hydro-meteorological parameters related to the Hirfanli Dam Basin should be increased. These studies may be the investigation of the trends of climate parameters with different methods, as well as their relations with global atmospheric indices such as the North Atlantic Oscillation and Southern Oscillation. In the Hirfanlı Dam Basin, which shows semi-arid climate characteristics, especially drought disaster should be investigated. In addition to drought detection, these studies should be conducted with an integrated disaster management perspective in order to prepare for drought disasters. With the perspective of integrated disaster management, it will be more resilience to disasters with plans in which all components in the basin are together and effective against many disasters, especially drought.

1. Introduction

Natural resources are of great importance in the rapidly developing world with the industrial revolution. The natural resources needed by industrialization started to be consumed quickly and unconsciously in this process. In addition, urbanization around the world has also accelerated by means of the industrial revolution. Subsequently, harmful gases emerged as a result of industrialization and urbanization. Considering the decreasing natural resources, this situation has caused changes in the world climate. Therefore, the causes and effects of climate change are being studied intensively by scientists.

Global climate change has become an important problem affecting civilization around the world. Global climate change manifests itself to different degrees in various geographies in Turkey. These effects were

investigated using hydro-meteorological climate parameters [1–18].

Keskin et al. [19] examined the effects of global climate change on the Eastern Anatolia region by using precipitation and temperature parameters. The increasing trend in temperature series was determined at 12 stations except for Erzurum and Bitlis, increasing trends of precipitation series were determined in Kars and Ardahan. Ulke Keskin and Ozkoca [20] investigated the changes in temperature series of the Central Black Sea Region with the Mann-Kendall (MK) Trend Test and Sen's Trend Slope Test. They stated that the temperatures in the region are in an increasing trend. Köyceğiz and Buyukyildiz [21] researched the trends of annual average temperature, maximum temperature and minimum temperature data of Konya Closed Basin, stating that more than 80% of the annual temperature series has a statistically significant increasing trend.

* Corresponding Author

^{*}(utkuz@sinop.edu.tr) ORCID ID 0000-0001-5307-8563

Cite this article

Zeybekoglu, U. (2023). Temperature series analysis of the Hirfanli Dam Basin with the Mann-Kendall and Sequential Mann-Kendall tests. Turkish Journal of Engineering, 7(4), 306-313

In this study, the annual temperature series of the Hirfanli Dam Basin, which is stated to have drought climate characteristics in the literature [22–24], were investigated using MK Test and Sequential Mann-Kendall (S-MK) Test methods.

2. Material and Method

2.1. Study area and Data

The sub-basin containing the Hirfanli Dam Basin, which is located between 33.3°E and 38.7°E longitudes and 38.3°N and 40.1°N latitudes, is within the Kizilirmak River Basin, and has a surface area of approximately 26700 km². In the basin, the altitude varies between 799 and 3880 m (Figure 1). The east part of the basin is the hilliest region of the basin, which consists of high peaks and is bordered by mountainous areas. Plateaus, wide

plains, and meadows are more common in the west part of the basin. The Hirfanli Dam, which was built on the Kizilirmak River in 1959 for flood control and hydropower purposes, has a surface area of 263 km² and reservoir volume of 5,980 hm³ at normal water surface level [22–24].

Annual temperature data of stations in the basin were procured from the Turkish State Meteorological Service (TSMS). Descriptive statistics (Minimum, maximum, mean, Std. Dev., Variation, Skewness and Kurtosis) of temperature records between 1965 and 2017 are shown in Table 1. The graphs of the temperature series for each station in the Hirfanli Dam Basin are given in Figure 2 The mean temperature is around 10.02°C and also the annual temperature decreases from the upstream to the downstream due to the increase in altitude (Figure 3) [23].

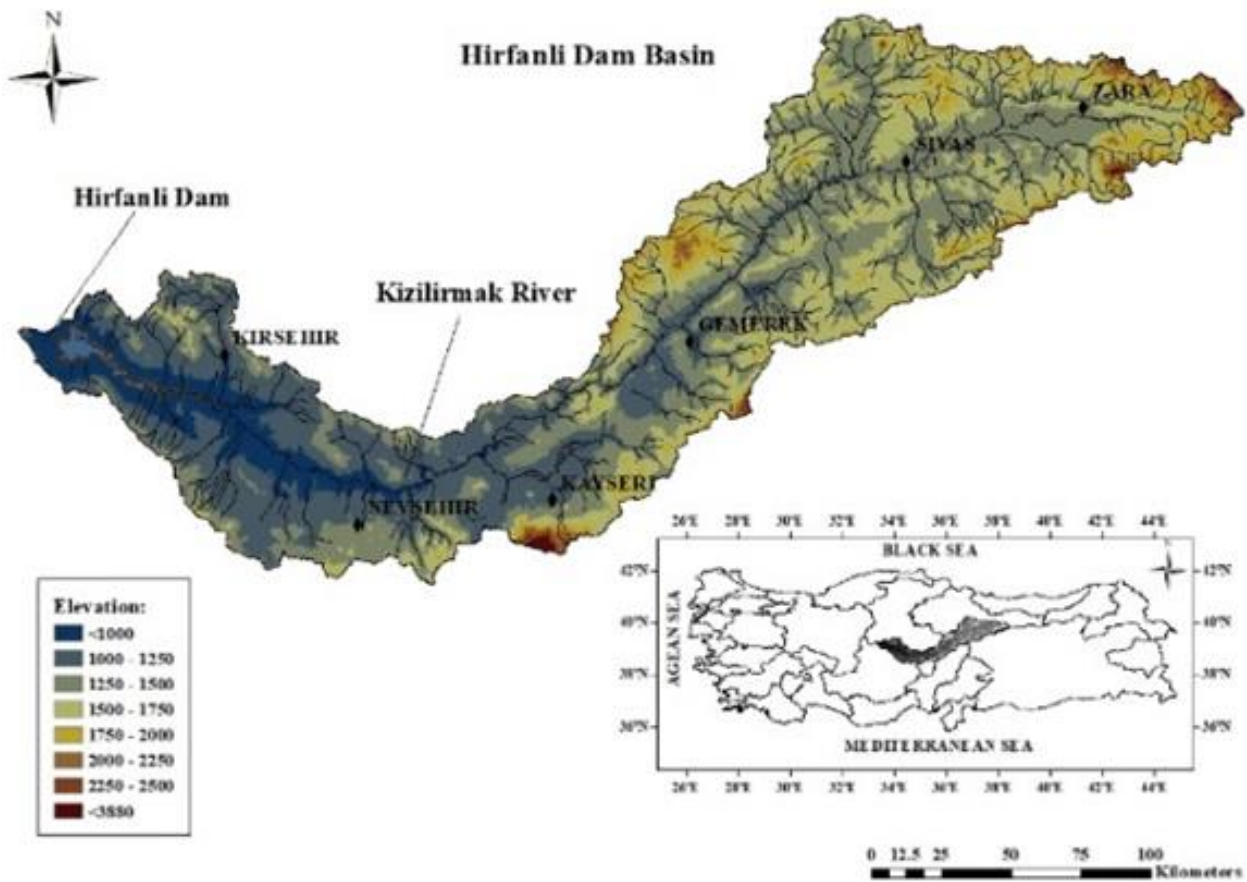


Figure 1. Geographical distributions of stations in Hirfanli Dam Basin [26]

Table 1. Descriptive statistics of temperature records of stations used in this study

°C	Gemerek	Kayseri	Kirsehir	Nevsehir	Sivas	Zara
Min.	6.94	8.41	9.43	8.49	6.64	5.94
Max.	11.77	13.23	13.78	13.64	11.99	11.27
Mean	9.63	10.52	11.46	10.69	9.17	8.63
Std. Dev.	0.96	1.03	0.84	0.98	1.04	0.96
Variation	0.92	1.06	0.71	0.97	1.07	0.92
Skewness	0.06	0.22	0.33	0.40	0.23	-0.14
Kurtosis	0.40	-0.06	0.35	0.48	0.43	0.92

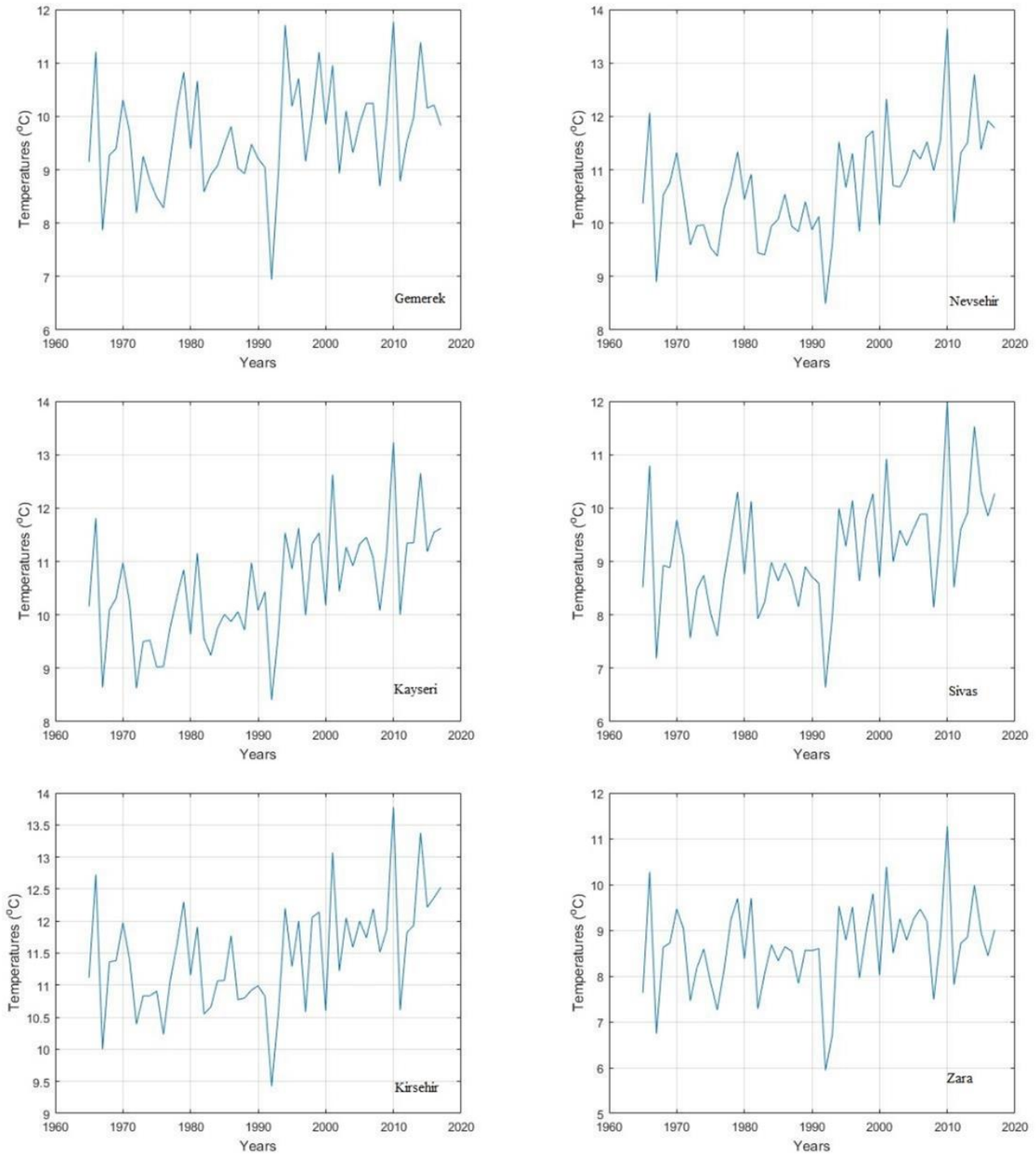


Figure 2. Temporal distribution of temperature records of station

2.2. Mann Kendall (MK)Trend Test

The MK test is independent of the distribution of variables [27-28]. Whether there is a tendency in the time series is tested by the null hypothesis (H_0 : no trend) [29-31]. The pairs x_i, x_j in the series x_1, x_2, \dots, x_n are divided into two groups. The test statistic (S) is expressed by Equation (1), where for $i < j$ the number of pairs with $x_i < x_j$ is P and the number of pairs with $x_i > x_j$ is M. Kendall correlation coefficient with Equation (2); variance is calculated by Equation (3). If there are equal values in observations in the series, the variance value is calculated using Equation (4).

$$\tau = \frac{S}{\left[\frac{n(n-1)}{2} \right]} \tag{2}$$

$$\sigma_s = \sqrt{\frac{n(n-1)(2n+5)}{18}} \tag{3}$$

$$\sigma_s = \sqrt{\frac{n(n-1)(2n+5) - \sum t_i(t_i-1)(2t_i+5)}{18}} \tag{4}$$

$$S = P - M \tag{1}$$

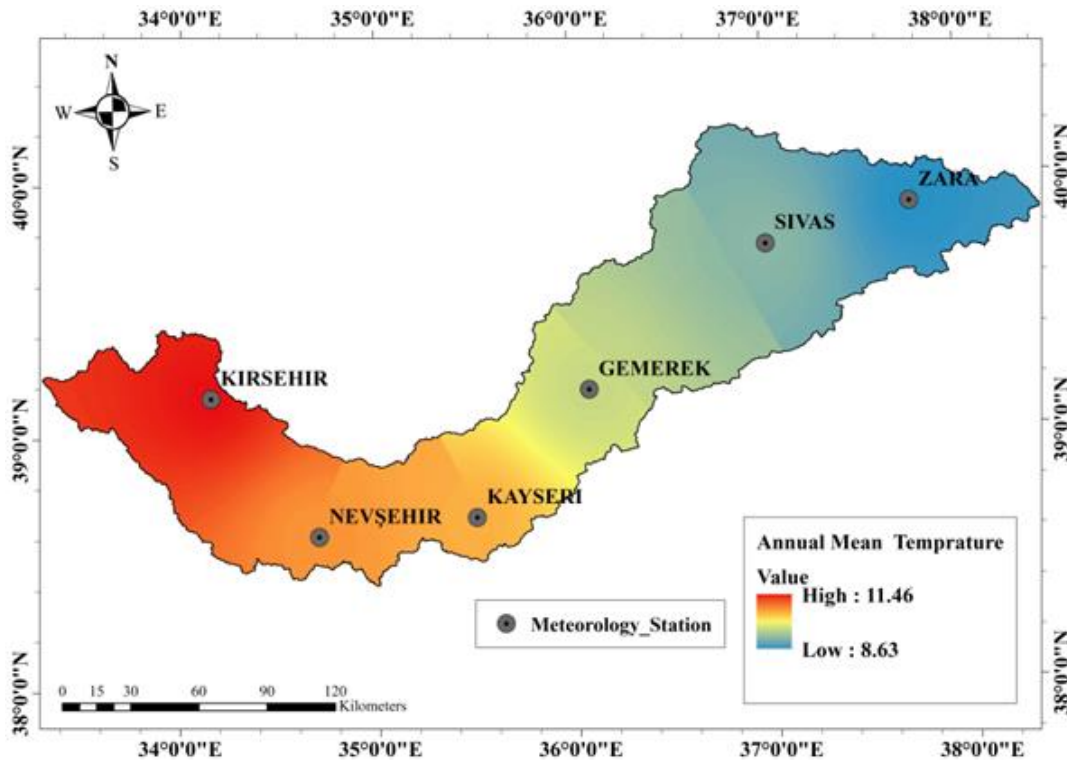


Figure 3. Spatial distribution of annual temperature series

Standardized MK test statistics are calculated by Equation (5).

$$\begin{aligned} & \frac{(S - 1)}{\sigma_s} ; S > 0 \\ & 0 ; S = 0 \\ & \frac{(S + 1)}{\sigma_s} ; S < 0 \end{aligned} \quad (5)$$

If the absolute Z obtained by Equation (5) is less than the critical Z of the normal distribution corresponding to the selected α significance level, the H_0 is accepted; otherwise, the existence of the trend is determined. Positive values indicate the presence of an increasing trend, while negative values indicate a decreasing tendency [32].

2.3. Sequential Mann Kendall (S-MK) Test

The S-MK Test is used to find out whether the series increases or decreases over time. While the test presents the results graphically, it can also determine the starting point of the trend [33].

The t value, which is the test statistic, is calculated by summing the n_i values obtained by counting the smaller ones from the previous ranks for each rank. Mean value of t's is calculated by Equation (7); variance Var(t) is calculated by Equation (8) and Test statistic u(t) is calculated by Equation (9). The backward test statistic u'(t) is calculated similarly to u(t) [34-35].

The point where u(t)-u'(t) intersect shows where the trend starts [33].

$$t = \sum_{i=1}^n n_i \quad (6)$$

$$E(t) = \frac{n(n - 1)}{4} \quad (7)$$

$$Var(t) = \frac{n(n - 1)(2n + 5)}{72} \quad (8)$$

$$u(t) = \frac{(t - E(t))}{\sqrt{Var(t)}} \quad (9)$$

3. Results and Discussion

The MK Trend Test was applied to identify the tendency in the Hirfanli Dam Basin stations recorded by TSMS in the period of 1965-2017. The results of the analyzes performed at 95% confidence levels are shown in the Table 2.

An upward trend has been determined in all stations in the basin except Zara. Upward trends in Gemerek, Kayseri, Kirsehir, Nevsehir and Sivas stations are statistically significant ($Z > Z_{Cr}$).

In order to determine the starting time of the tendency, S-MK Test was applied to the temperature time series obtained from Gemerek, Kayseri, Kirsehir, Nevsehir and Sivas stations which statistically significant trends were determined. The graphical results of the station are given in Figure 4.

It is seen that there was a fluctuation in the trend change in the first half of the 90s in Gemerek. In the u(t)-u'(t) graph, the curves intersect at two points, in 1992 and 1995. The temperature series started to decrease in 1992 and to increase in 1995. This increasing trend continues throughout the observation period after 1995.

Table 2. Results of MK Trend Test

	Z_{cr}	Z	Trend
Gemerek	± 1.96	2.43	Significant upward
Kayseri	± 1.96	4.48	Significant upward
Kirsehir	± 1.96	3.18	Significant upward
Nevsehir	± 1.96	3.82	Significant upward
Sivas	± 1.96	3.32	Significant upward
Zara	± 1.96	1.90	No trend

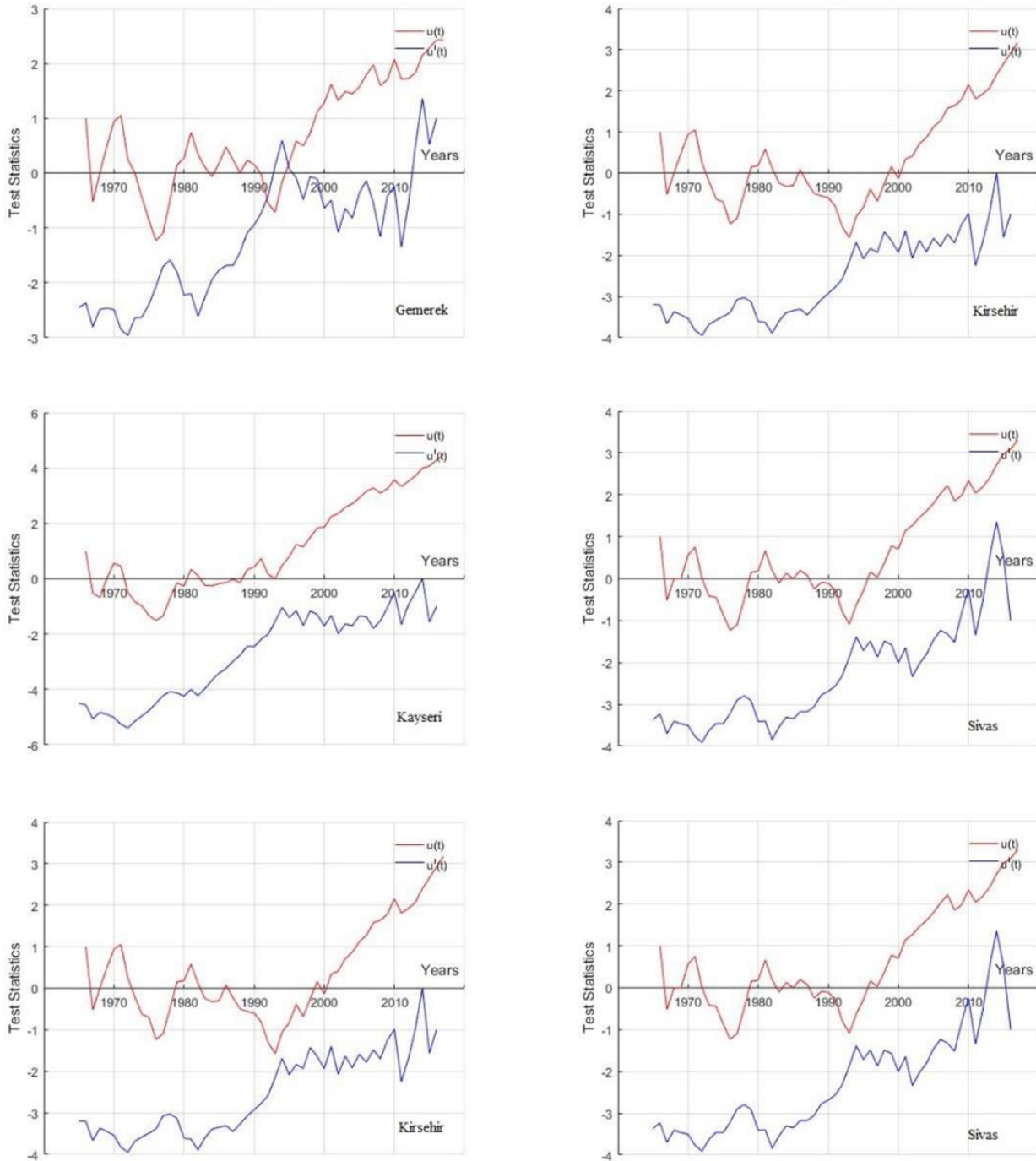


Figure 4. S-MK results of stations

From the $u(t)$ - $u'(t)$ graphs of Kayseri, Kirsehir, Nevsehir and Sivas stations, the curves do not intersect. Therefore, the starting date of the trend could not be determined. Despite this situation, it is thought that the increasing tendencies became evident in Kirsehir and Nevsehir after 1993; it becomes prominent in Kayseri and Sivas after 1994.

As can be seen in the literature, the effects of global climate change on various hydro-meteorological parameters are being investigated. It is known that the temperature series in the world show an increasing trend [35–36]. In previous studies involving this study area, increasing trends were determined in annual and seasonal temperature series for Turkey [1, 38–44].

The existence of an increasing trend in annual temperature records has been ascertained by various trend analysis methods in the Central Anatolia region and the Kizilirmak River basin [21, 25, 39, 43–48].

In addition, Doğan et al. [40] stated that 1992 was a turning point for increasing trends. Terzi and Ilker [44] determined increasing trends in Kayseri, Kirsehir, Nevsehir and Sivas as a result of the temperature records for 1980-2017. Another study was carried out by Ercan and Yüce [43] who stated that there are increasing trends for Gemerek, Kayseri, Kirsehir, Nevsehir and Sivas for the 1975-2015. As a result of this study, the increase trends determined throughout the basin, except Zara, support each other with the studies in the literature and similar study areas. The determination of increasing trends in the first half of the 90s shows parallelism with the results of the study of Doğan et al. [40].

4. Conclusion

In this study, the effect of global climate change on the temperature series in the Hirfanli Dam Basin was investigated. Hirfanli Dam basin, which is located in the semi-arid climate region where climate change can be seen due to its location. The annual mean temperature values measured by TSMS in the period 1965-2017 were used. The trend in the basin was determined using the MK test. And the S-MK test was used to determine the starting date of the tendency. An increasing trend has been determined in the temperature values throughout the basin except Zara. Statistically significant increasing trends were found in Gemerek, Kayseri, Kirsehir, Nevsehir and Sivas stations. According to the S-MK Test, the temperatures in this drought-threatened basin increased significantly, especially since the first half of the 1990s.

As a result of global climate change, drought in the basin is expected to increase even more in the future. Therefore, the following measures and activities can be carried out:

- Plans involving the community should be made against disasters caused by hydro-meteorological climate parameters [49].
- A drought-monitoring center for the basin can be established to monitor the temperature time series.
- A drought action plan should be prepared by evaluating all hydro-meteorological parameters in the basin.

- Activities related to the efficient use of water resources should be carried out.
- Information, prevention and sustention activities should be carried out against possible negative effects in agricultural activities.
- Existing urban green spaces should be protected and afforestation activities should be increased.

In the Hirfanli Dam basin, which has a semi-arid feature, it is peradventure that drought actions will be seen as a result of the temperature increase caused by global climate change. It is thought that future drought events may be severe and long-lasting. For this reason, it is of great importance to put to good use in the basin in terms of hydro-meteorological climate parameters, drought, water resources, agriculture, industry, and also civilization.

Acknowledgement

The author thanks the Turkish State Meteorological Service for the data.

Conflicts of interest

The authors declare no conflicts of interest.

References

1. Türkeş, M., Sümer, B. M., & Kılıç, G. (1995). Variations and trends in annual mean air temperatures in Turkey with respect to climatic variability. *International Journal of Climatology*, 15(5), 557-569.
2. Türkeş, M. (1996). Spatial and temporal analysis of annual rainfall variations in Turkey. *International Journal of Climatology*, 16(9), 1057-1076.
3. Cigizoglu, H. K., Bayazit, M., & Önöz, B. (2005). Trends in the maximum mean and low flows of Turkish Rivers. *Journal of Hydrometeorology*, 6(3), 280-290.
4. Bahadır, M. (2011). Kızilirmak Nehri akım değişimlerinin istatistiksel analizi. *Turkish Studies*, 6(3), 1339-1356.
5. Ay, M. & Kişi, Ö. (2016). Debi ve sediment değişkenlerinin trend analizi. *Dicle Üniversitesi Mühendislik Fakültesi Mühendislik Dergisi*, 7(2), 169-180.
6. Yenigün, K. & Ülgen, M. (2016). İklim değişikliği ekseninde maksimum akım verilerindeki trendler ve baraj güvenliğine etkisinin izlenmesi. *Dicle Üniversitesi Mühendislik Fakültesi Mühendislik Dergisi*, 7(2), 343-353.
7. Tekkanat, S. (2016). Porsuk Çayı üst kesiminde ortalama akımların Şen trend metodu kullanılarak araştırılması. *Coğrafi Bilimler Dergisi*, 15(1), 49-57.
8. Kale, S., Ejder, T., Hisar, O. & Mutlu, F. (2016). Climate change impacts on streamflow of Karamenderes River (Çanakkale, Turkey). *Marine Science and Technology Bulletin*, 5(2), 1-6.
9. Kale, S. (2017). Analysis of climatic trends in evaporation for Canakkale (Turkey). *Middle East Journal of Science*, 3(2), 69-82.

10. Kale, S. (2017). Climatic trends in the temperature of Çanakkale city, Turkey. *Natural and Engineering Sciences*, 2(3), 14-27.
11. Ülke Keskin, A., Beden, N. & Demir, V. (2018). Analysis of annual, seasonal and monthly trends of climatic data: A case study of Samsun. *Nature Sciences*, 13(3), 51-70.
12. Ceribasi, G. (2018). Analysis of meteorological and hydrological data of Iznik Lake Basin by using Innovative Sen Method. *Journal of Environmental Protection and Ecology*, 19(1), 15-24.
13. Kale, S. & Sönmez, A. (2018). Trend analysis of mean monthly, seasonally and annual streamflow of Daday Stream in Kastamonu, Turkey. *Marine Science and Technology Bulletin*, 7(2), 60-67.
14. Zeybekoğlu, U. & Karahan, H. (2018). Standart süreli yağış şiddetlerinin eğilim analizi yöntemleriyle incelenmesi. *Pamukkale Üniversitesi Mühendislik Bilimleri Dergisi*, 24(6), 974-1004.
15. Yılmaz, M. & Tosunoğlu, F. (2019). Trend assessment of annual instantaneous maximum flows in Turkey. *Hydrological Sciences Journal*, 64(7), 820-834.
16. Topuz, M., Feidas, H. & Karabulut, M. (2020). Trend analysis of precipitation data in Turkey and relations to atmospheric circulation: (1955-2013). *Italian Journal of Agrometeorology*, 2, 91-107.
17. Yılmaz, C. B., Demir, V., Sevimli, M. F., Demir, F., & Yakar. (2021). Trend Analysis of Temperature and Precipitation in Mediterranean Region. *Advanced GIS Journal*, 1(1), 15-21.
18. Yılmaz, C., Demir, V., & Sevimli, M. F. (2021). Doğu Karadeniz Bölgesi Meteorolojik Parametrelerinin Trend Analizi. *Avrupa Bilim ve Teknoloji Dergisi*, 24, 489-496.
19. Keskin, M. E., Çokta, İ., Çetin, V. & Bektaş, O. (2018). Doğu Anadolu Bölgesi yağış ve sıcaklık trend analizi. *Mühendislik Bilimleri ve Tasarım Dergisi*, 6(2), 294-300.
20. Ülke Keskin, A. & Özkoca, T. (2018). Sinop, Ordu ve Samsun illerinin sıcaklık verilerinde trend analizi. *Gümüşhane Üniversitesi Fen Bilimleri Enstitüsü Dergisi*, 8(2), 455-463.
21. Köyceğiz, C. & Büyükyıldız, M. (2020). Determination of change point and trend analysis of annual temperature data in Konya Closed Basin Turkey. *Niğde Ömer Halisdemir Üniversitesi Mühendislik Bilimleri Dergisi*, 9(1), 393-404.
22. Yildiz, O. (2009). Assessing temporal and spatial characteristics of droughts in the Hirfanli Dam Basin Turkey. *Scientific Research and Essays*, 4(4), 249-255.
23. Yildiz, O. (2014). Spatiotemporal analysis of historical droughts in the Central Anatolia Turkey. *Gazi University Journal of Science*, 27(4), 1177-1184.
24. Aktürk, G. & Yildiz, O. (2016). Assessing hydrological responses to droughts in the Hirfanli Dam Basin Turkey. *International Journal of Advances in Mechanical and Civil Engineering*, 3(5), 116-123.
25. Zeybekoglu, U. & Akturk, G. (2022). Homogeneity and Trend Analysis of Temperature Series in Hirfanli Dam Basin. *Türk Doğa ve Fen Dergisi*, 11(1), 49-58.
26. Zeybekoğlu, U., & Aktürk, G. (2021). A comparison of the China-Z index (CZI) and the standardized precipitation index (SPI) for drought assessment in the Hirfanli Dam basin in central Turkey. *Arabian Journal of Geosciences*, 14(24), 1-13.
27. Mann, H. B. (1945). Non-parametric test against trend. *Econometrika*, 13, 245-259.
28. Kendall, M. G. (1975). Rank Correlation Method, London: Charles Griffin.
29. Bayazit, M. (1996). İnşaat Mühendisliğinde Olasılık Yöntemleri, İstanbul: İTÜ İnşaat Fakültesi Matbaası.
30. Bihrat, Ö. N. Ö. Z., & Bayazit, M. (2003). The power of statistical tests for trend detection. *Turkish Journal of Engineering and Environmental Sciences*, 27(4), 247-251.
31. Partal, T. & Kahya, E. (2006). Trend analysis in Turkish precipitation data. *Hydrological Processes*, 20(9), 2011-2026.
32. Yu, S., Zou, S. & Whittemore, D. (1993). Non-parametric trend analysis of water quality data of Rivers in Kansas. *Journal of Hydrology*, 150(1), 61-80.
33. Gumus, V. & Yenigun, K. (2006). Evaluation of Lower Fırat Basin streamflow by trend analysis. 7th International Advances in Civil Engineering Conference, 11-13 October 2006, Istanbul.
34. Sneyers, R. (1990). On Statistical Analysis of Series of Observations. W.M.O., Technical Note No: 415, Geneva.
35. Arslan, O. (2017). Niğde İli'ndeki potansiyel evapotranspirasyon tahminlerinin trend analizi. *Niğde Ömer Halisdemir Üniversitesi Mühendislik Bilimleri Dergisi*, 6(2), 602-608.
36. Watson, R. T. (2001). IPCC Special Report: Climate Change 2001: Synthesis Report, Cambridge: Cambridge University Press.
37. Türkeş, M. (2007). İklim Değişikliği Nedir? Temel Kavramlar, Nedenleri, Gözlenen ve Öngörülen Değişiklikler. I. Türkiye İklim Değişikliği Kongresi, 11-13 Nisan 2007, İstanbul.
38. Kadioğlu, M. (1997). Trends in surface air temperature data over Turkey. *International Journal of Climatology: A Journal of the Royal Meteorological Society*, 17(5), 511-520.
39. Kızılelma, Y., Çelik, M. & Karabulut, M. (2015). İç Anadolu Bölgesinde sıcaklık ve yağışların trend analizi. *Türk Coğrafya Dergisi*, 64, 1-10.
40. Doğan, M., Ülke, A. & Cigizoglu, H. K. (2015). Trend direction changes of Turkish temperature series in the first half of 1990s. *Theor. Appl. Clim.*, 121(1-2), 23-39.
41. Kuyucu, H., Demir, V., Geyikli, M. S. & Citakoglu, H. (2017). Trend Analysis of Turkey Temperatures. 1st International Symposium on Multidisciplinary Studies and Innovative Technologies, 2-4 November 2017, Tokat.
42. Abbasnia, M., & Toros, H. (2020). Trend analysis of weather extremes across the coastal and non-coastal areas (case study: Turkey). *Journal of Earth System Science*, 129, 1-13.
43. Ercan, B., Yuce, M. I. (2017). Trend analysis of hydro-meteorological variables of Kızılırmak Basin. *Nevşehir Bilim ve Teknoloji Dergisi*, 6(ICOCEE 2017 Özel Sayı), 333-340.
44. Terzi, O. & Ilker, O. (2020). Trend analysis of temperature values in Kızılırmak Basin. *Süleyman*

Demirel University Journal of Natural and Applied Sciences, 24(3), 626-634.

45. Altın, T. B. (2017). Observed Changes in Annual and Seasonal Temperatures in Nevşehir (Central Anatolia, Turkey) for Period 1960-2016. *Eurasian Journal of Agricultural Research*, 1(2), 4-12.
46. İlker, A. & Terzi, Ö. (2021). Sıcaklık verilerinin trend analizi: Çankiri ve Kastamonu örneği. *Mühendislik Bilimleri ve Tasarım Dergisi*, 9(4), 1339-1347.
47. Karakuş, C. B. & Güler, Ü. A. (2022). Mann-Kendall trend analizi ile Sivas ilindeki sıcaklık ve yağış

trendlerinin belirlenmesi. *Niğde Ömer Halisdemir Üniversitesi Mühendislik Bilimleri Dergisi*, 11(3), 534-544.

48. Altın, T., Barak, B. & Altın, B. (2012). Change in Precipitation and Temperature Amounts over Three Decades in Central Anatolia, Turkey. *Atmospheric and Climate Sciences*, 2(1), 107-125.
49. Yıldırım, S. D., & Yılmaz, G. (2019). Yunanistan Attika Bölgesi Yangınının Değerlendirilmesi. *Resilience Journal*, 3(2), 201-215.



© Author(s) 2023. This work is distributed under <https://creativecommons.org/licenses/by-sa/4.0/>



A numerical study on the low-velocity impact response of hybrid composite materials

Uzay Gezer*¹, Bünyamin Demir ¹, Yusuf Kepir ¹, Alper Gunoz ¹, Memduh Kara ¹

¹Mersin University, Department of Mechanical Engineering, Türkiye

Keywords

Composites
Glass Fiber
Aramid Fiber
Low-velocity Impact
LS-DYNA

Research Article

DOI: 10.31127/tuje.1191785

Received: 19.10.2022

Revised: 06.11.2022

Accepted: 19.11.2022

Published: 27.02.2023



Abstract

Composite materials are advanced engineering materials with superior properties to traditional materials. One of the most important disadvantages is the high cost of composite materials. Therefore, producing composite materials from the first to the last stage is a very important process. Homogenization is the most important parameter in production since composites contain more than one material type in their structure. In addition, composite structures are sensitive materials against low-velocity impacts. In this study, the effect of reinforcement material combination and stacking sequence on mechanical properties used in the production of composite materials was investigated by low-velocity impact simulations using LS-DYNA software. The mass of the 12 mm diameter spherical impactor used in the analyzes was determined as 10 kg and low-velocity impact tests were applied at 20 J, 30 J and 40 J energy levels. The composite samples were modeled with 180x100mm dimensions and the contact between the impactor and the sample was made from the center of the composite structure. Numerical analyzes were performed using the Tsai-Wu damage criterion in the LS-DYNA software, and material properties were defined using the "Mat_Enhanced_Composite_Damage (MAT 055)" material card.

1. Introduction

Nowadays, instead of traditional materials such as metal, wood, polymer, composite materials that combine the excellent properties of their constituent components are used in many industries. Since the materials used in industrial production are desired to have superior properties, the need for new material types is increasing daily [1]. In line with this need, research and development studies have focused on the production of new composite materials with superior properties by changing material combinations.

While epoxy resin is generally used as matrix material in the production of fiber reinforced composite materials, glass fiber, carbon fiber, basalt fiber and aramid fiber are used extensively as reinforcement materials. In addition, hybrid composites that these fibers are used together has been increasing rapidly in recent years. The most important reasons for the widespread use of fiber-reinforced polymer composites are their high strength and modulus of elasticity.

Fiber reinforced composites can also be produced as hybrids using more than one fiber type. Hybrid composites can have better mechanical properties when comparing pure fiber composites. In hybrid composite materials, the stacking sequence can positively or negatively affect the mechanical behavior of the composite structures. For this reason, it is crucial to subject different stacking sequences hybrid composite samples to mechanical tests. In some scientific research that includes composite materials, the stacking sequence's effect on mechanical strength has been investigated [2-5].

Reinforcement materials such as glass, carbon and aramid fiber are widely used as reinforcement components in composite materials. The tensile strength of glass fibers is considerably higher than polymers. They also have a high strength-to-weight ratio [6,7]. Aramid fibers have superior characteristics such as high strength, high modulus of elasticity, high temperature resistance, high chemical corrosion resistance and high shear strength [8-11].

* Corresponding Author

* (uzaygezer@mersin.edu.tr) ORCID ID 0000-0003-3088-7610
(bd@mersin.edu.tr) ORCID ID 0000-0002-6405-4724
(ykepir@mersin.edu.tr) ORCID ID 0000-0002-3536-3931
(alpergunoz@mersin.edu.tr) ORCID ID 0000-0001-7978-6306
(memduhkara@mersin.edu.tr) ORCID ID 0000-0002-5201-5453

Cite this article

Gezer, U., Demir, B., Kepir, Y., Gunoz, A., & Kara, M. (2023). A numerical study on the low-velocity impact response of hybrid composite materials. Turkish Journal of Engineering, 7(4), 314-321

In engineering applications, besides experimental studies, there are many studies in which results are obtained with numerical analysis without the need for experimentation [12-16]. Tests are carried out to determine the mechanical strength of composite materials that cause costs in terms of both material and labor. Today, these tests can be done by physically, also can be done by numerical analysis in computers. ANSYS and LS-DYNA software are widely used in the numerical analysis of composite materials. According to the tests to be applied, the properties of the samples, which are modeled in three dimensions in the computer environment, can be defined on the material cards which in the software interface and numerical analyzes can be made. Thus these numerical analyzes, the mechanical behavior of the material planned to be produced can be tested virtually. Eventually, the numerical analysis can save labor and material costs.

Song [17] examined the tensile and bending strengths of layered composites prepared by carbon/glass and carbon/aramid fiber hybridization. Composite samples, which were formed by using six different layer numbers and stacking sequences, were produced by vacuum assisted resin transfer method. As a result of the study, it was concluded that both carbon/glass and carbon/aramid hybrid composites have much better tensile and flexural strengths of samples with carbon in the interior compared to samples with other stacking sequences.

Jaroslaw et al. [18] produced composite samples based on aluminum alloy and glass or carbon fiber reinforced laminated polymer composites and investigated their low-velocity impact behavior. They analyzed the effect of fiber stacking sequence angles by interpreting the damage and impact responses. As a result of the study, they observed that while plastic deformation creation, delamination initiation and progression were seen in samples containing glass fiber, collapse (penetration) and puncture (perforation) occurred in samples that containing carbon fiber.

Wagih et al. [19], investigated the low-velocity impact responses of carbon fiber and aramid fiber reinforced hybrid composites at different energy levels. Three-point bending tests were applied to the impact damaged samples and compared with the flexural strength of the undamaged samples. They observed that in the samples placed aramid fiber between the carbon fiber layers, no damage occurred in the lowest carbon layer as a result of low-velocity impact. They concluded that aramid reinforcement significantly increased the strength of the samples compared to pure carbon fiber reinforced and pure glass fiber reinforced composites.

Gemi et al. [20] applied low-velocity impact tests at 4 different velocities to 6 layers of glass fiber reinforced ring composites produced in 3 different diameters. It was observed that the energy absorption ability decreased with the increase of the impact velocity. As a result of the study, it was concluded that as the diameter of the samples increased, the maximum contact force and the amount of absorbed energy decreased [20].

Rezasefat et al. [21], produced 8 layers of aramid fiber and glass fiber hybrid composites and applied a low-velocity impact test. They investigated the effect of

hybridization and stacking sequence on impact resistance in samples exposed to impact at 19 J, 37 J and 72 J energy levels. As a result, it was seen that the resistance to impact increased up to the energy level of 49.5 J with hybridization, and at higher energy levels, the pure glass fiber reinforced composite performed better.

Uyaner et al. [22] investigated the impact response of 18-layer E-glass fiber reinforced composites with different sized experimentally and numerically. Numerical analyzes were performed with the MAT 055 material model using the LS-DYNA software. According to the results of the numerical and experimental, it was determined that the size of the composite materials remarkably affects the impact behavior of the materials.

Mesh density is a significant parameter in studies that includes finite element analysis. According to the mesh number determined in the analysis, the results may vary up to the optimum mesh number value, but there is no visible change in the results obtained after the optimum mesh number is reached [22]. In this work, the contact force values were determined at an element size of 2 mm, corresponding to the number of elements in one plate being 4500. Also, the impactor was created with 12096 elements.

Composite materials can be exposed to low-velocity impacts at different energy levels during their lifetime. These impacts result in different types of damages in composite structures. The researchers applied impact simulations at different energy levels to the materials which is modeled three-dimensionally in the computer environment and aimed to create predictions against impacts that could be encountered in real life with the data they obtained. In these studies, in the literature, generally 20 J and 30 J energy levels were used [23,24].

In this study, 12-layer glass fiber/epoxy, aramid fiber/epoxy composites and glass fiber/aramid fiber/epoxy hybrid composites were modeled with LS-DYNA software and the low-velocity impact test was simulated in a virtual environment. Impact energies were determined as 20 J, 30 J and 40 J in analyzes which performed on 6 different composite models. The stacking sequences of the layers forming the composites are common to all samples and the form of stacking sequences angles [0,90]₆. This study aims to predict the impact response of composite materials, which are very difficult and costly to manufacture, with a preliminary evaluation made in the computer environment.

2. Method

In this study, six different composite material designs were first carried out. Glass fiber and aramid fiber were chosen as reinforcement material and epoxy resin as matrix material. Composite structures modeled in Figure 1 are given schematically. The designed composite structures are pure aramid epoxy [A]₁₂, pure glass epoxy [C]₁₂, hybrid1 [AC]₆, hybrid2 [CA]₆, functional1 [AAAAAACCCCCC] and functional2 [CCCCCAAAAAA]. All samples are designed to be 180 × 100mm in size with 12 layers. Low-velocity impact tests were applied to the designed samples at 20 J, 30 J and 40 J energy levels. During the impact tests, the samples were modeled as free (180 mm) on both sides and embedded

(100 mm) on both sides. LS-DYNA software, which is widely used in the literature, was preferred for performing low-velocity impact tests.

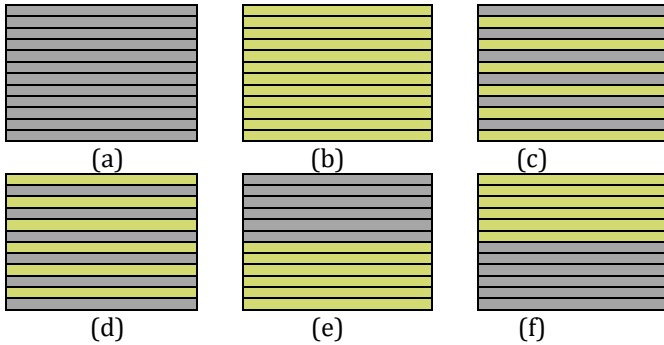


Figure 1. Designed 12-layer composite samples (a) pure glass fiber, (b) pure aramid fiber, (c) hybrid1, (d) hybrid2, (e) functional1 and (f) functional2

In order to define the layer properties of composite samples;

MAT055 (MAT_ENHANCED_COMPOSITE_DAMAGE) material card is used. The MAT 055 material card uses the Tsai-Wu damage criterion in numerical analysis, and the formula technique is given in Equation 1-3.

Tensile damage in fiber direction;

$$\left(\frac{\sigma_{11}}{X_T}\right)^2 + \beta \left(\frac{\sigma_{12}}{S_C}\right)^2 - 1 \begin{cases} \geq 0 & \text{failed} \\ \leq 0 & \text{elastic} \end{cases} \quad (1)$$

Compression damage in the fiber direction;

$$\left(\frac{\sigma_{11}}{X_C}\right)^2 - 1 \begin{cases} \geq 0 & \text{failed} \\ \leq 0 & \text{elastic} \end{cases} \quad (2)$$

Tensile and compression damages in the transverse fiber direction;

$$\left(\frac{\sigma_{22}}{Y_C Y_T}\right)^2 + \left(\frac{\sigma_{12}}{S_C}\right)^2 + \left(\frac{\sigma_{22}(Y_C - Y_T)}{Y_C Y_T}\right) - 1 \begin{cases} \geq 0 & \text{failed} \\ \leq 0 & \text{elastic} \end{cases} \quad (3)$$

calculated using the formulas. The subscript “1” denotes the fiber array direction, and the “2” denotes the transverse fiber direction (the normal of the fiber). σ_{11} is the normal stress in the fiber direction, σ_{12} is the in-plane shear stress, σ_{22} is the transverse normal stress in the fiber direction, and β is the weight factor in the shear stress. S_C corresponds to interlayer shear strength, X_C longitudinal compression strength, X_T longitudinal tensile strength, Y_T cross-sectional tensile strength and Y_C cross-sectional compression strength values.

Composite samples were modeled as 12 different layers, and aramid/epoxy and glass/epoxy layer properties were defined for each layer using the Part Composite material card. The layers are connected to each other using with the Contact Automatic_One_Way_Surface_To_Surface_Tiebreak material card. In accordance with the literature, the glass/epoxy layer thickness is 0.2125 mm and the aramid/epoxy layer thickness is 0.3875 mm [22]. The material properties of aramid/epoxy layers are given in Table 1, and the material properties of glass/epoxy layers are given in Table 2.

Table 1. Material properties of aramid/epoxy ply [25]

LS-DYNA Flag	Value	Unit
E ₁₁	40300	MPa
E ₂₂	10300	MPa
G ₁₂	2500	MPa
V ₁₂	0.23	-
X _T	743	MPa
X _C	249.6	MPa
Y _T	59.4	MPa
Y _C	87.6	MPa
S _C	34.5	MPa
DFAILT	0.0184	-
DFAILC	0.0062	-
DFAILM	0.0058	-
DFAILS	0.0138	-

Table 2. Material properties of glass fiber/epoxy ply [22]

LS-DYNA Flag	Value	Unit
E ₁₁	42000	MPa
E ₂₂	9500	MPa
G ₁₂	3500	MPa
V ₁₂	0.34	-
X _T	690	MPa
X _C	300	MPa
Y _T	66	MPa
Y _C	147	MPa
S _C	56	MPa
DFAILT	0.0164	-
DFAILC	0.0071	-
DFAILM	0.0069	-
DFAILS	0.0160	-

The impactor properties used in the numerical analysis are given in Table 3. Impact material properties, modeled as solid spherical and 12 mm in diameter, were defined using the MAT_020 Rigid material card. The MAT_020 material card has been used in many low-velocity impact studies in the scientific studies [26]. The impactor was defined as having a mass of 10 kg and its density was determined as 1.112885 kg/m³. The connection between the impactor and the composite sample was established with the CONTACT_AUTOMATIC_NODES_TO_SURFACE material card and numerical analysis was performed [27].

Table 3. Material properties of impactor [23]

Material	Density, ρ	Modulus of elasticity, E	Poisson's ratio
Steel	1.112885 kg/m ³	207000 MPa	0.3

3. Results

In low-velocity impact tests using LS-DYNA software, 20 J, 30 J and 40 J impact energy levels were preferred. Low-velocity impact tests with the specified properties were applied to the modeled samples by making 6 different combinations, force-time and force-displacement graphs were created.

In Figure 2a force-time and Figure 2b force-displacement graphs of 12-layer glass fiber composite samples at different energy levels are given.

Figure 3 shows (a) force-time and (b) force-displacement histories of 12-layer aramid fiber composite sample at different energy levels.

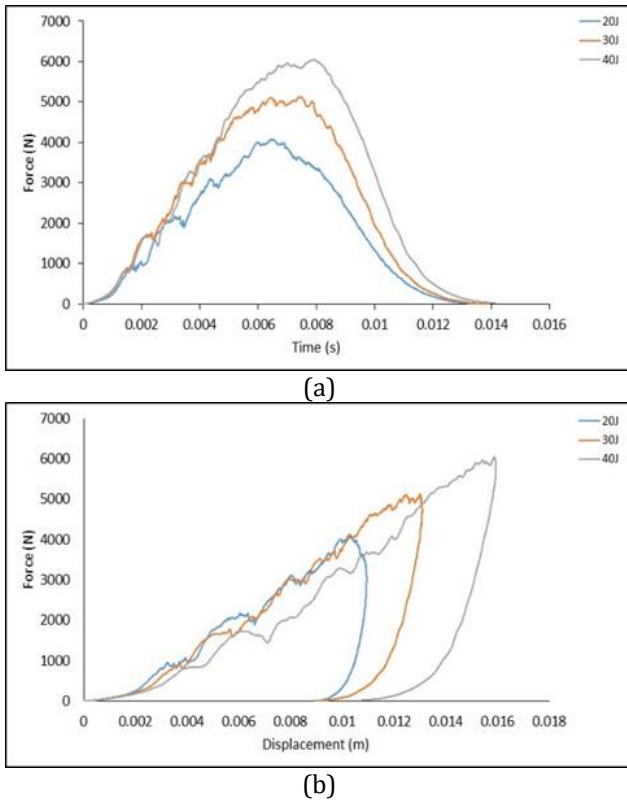


Figure 2. The graphs of (a) force-time and (b) force-displacement for 12-layer glass fiber composite sample at different energy levels

When the force-time histories given in Figure 2a are examined, it is seen that the contact force increases rapidly as the impactor contacts the sample and starts to decrease after reaching a certain value. Since the impactor rebound from the sample surface, the contact force value decreased to 0 at all energy levels. It is seen that the force-time changes are in the form of a bell-shaped curve for all energy levels. Vibrations occurring especially in the part where the force increases, indicate that the composite samples are damaged [28]. As the impact energy level increases, the maximum contact force value also increases. In Figure 2b, the force-displacement changes for different energy levels are given together. The slope in the increasing part of the force-displacement change is called bending rigidity in the scientific research due to the resistance of the sample against the impact load [22]. While the bending rigidity value was nearly same at 20 J and 30 J energy levels, it decreased at 40 J energy level. This indicates that the resistance of the glass fiber/epoxy composite sample decreases somewhat with the increase in the energy level. As the impact energy increases, sample's displacement increases. The area under the force-displacement curve gives the amount of energy absorbed by the material during the impact. It is clearly seen from the graphs that the amount of energy absorbed increases with the increase of the impact energy.

When the force-time changes given in Figure 3a are examined, it is seen that the force increases rapidly with the contact of the impactor to the sample, similar to the glass fiber/epoxy sample, and decreases to 0 after reaching a certain value. The highest contact force values obtained for the same energy levels were higher in

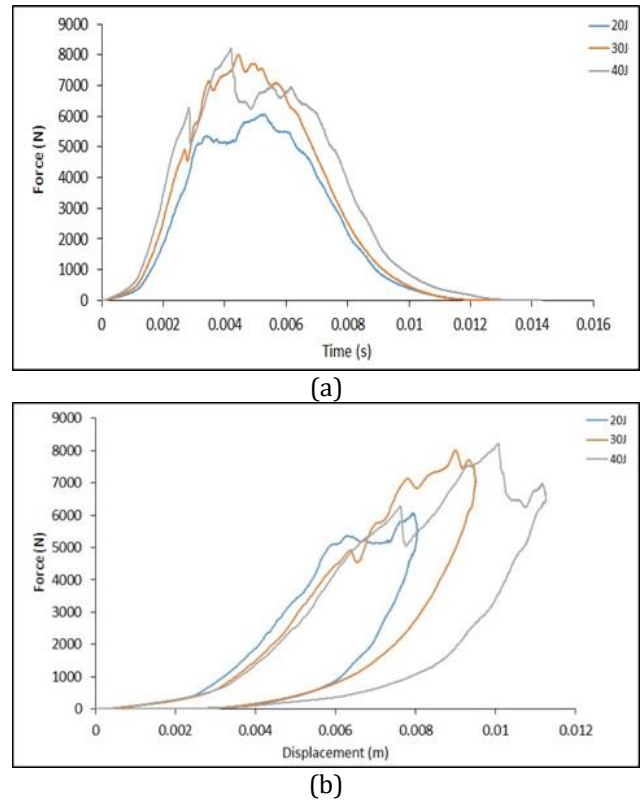


Figure 3. The graphs of (a) force-time and (b) force-displacement for 12-layer aramid fiber composite sample at different energy levels

aramid fiber/epoxy samples. The most important reason for this is that aramid fiber behaves more rigidly than glass fiber. As the stiffness of the specimen increased, the maximum contact force value also increased. Figure 3b shows the force-displacement changes of the aramid fiber/epoxy composite sample for different energy levels. When the graph is examined, it is seen that the bending rigidity value for the 20 J energy level is higher than the others. The bending rigidity values at 30 J and 40 J energy levels were nearly same. For the same energy level, it is seen that the largest displacement value in the samples is lower than the glass fiber/epoxy composite samples.

In Figure 4, 12-layer hybrid1 and in Figure 5, 12 layer hybrid2 glass and aramid fiber reinforced composite samples' (a) force-time and (b) force-displacement graphs are given.

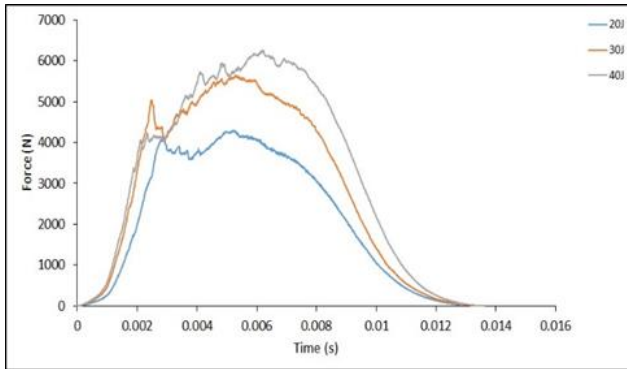
When the force-time changes given for the hybrid1 sample in Figure 4a and for the hybrid2 sample in Figure 5a are examined, they are characteristically similar to the graphs obtained from pure glass and pure aramid composite samples. The highest contact force values obtained from hybrid1 and hybrid2 composite samples were found to be higher than pure glass sample and lower than pure aramid sample for the same energy level. When the hybrid1 and hybrid2 samples were evaluated within themselves, it was seen that the highest contact force value obtained from the hybrid2 sample was higher for the 20 J energy level. The maximum contact force values were nearly the same for 30 J and 40 J energy levels. The impacted surface in the hybrid2 sample is the aramid surface and has a higher stiffness value. This resulted in a higher contact force for the 20 J energy level.

Since the damage to the samples will increase at other energy levels, the impact response was similar.

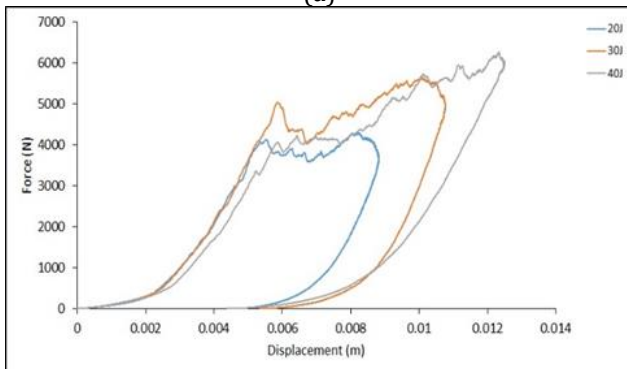
Force-displacement graphs at different energy levels are given for the hybrid1 sample in Figure 4b, and for the hybrid2 sample in Figure 5b. When the graphs are examined, the bending stiffness values of the hybrid1 sample impacted from the glass surface were nearly the same for 20 J and 30 J energy levels, but decreased at 40 J energy level. This variation is similar to a pure glass sample. On the other hand, bending rigidity values at 30 J and 40 J energy levels were nearly same in hybrid2 sample, which was impacted by the aramid surface, while

bending stiffness was higher at 20 J energy level. This change was similar to the force-displacement changes obtained from the pure aramid sample. When the maximum displacement values for the same energy level are examined, it is seen that nearly same displacement values are reached in hybrid1 and hybrid2 samples.

In Figure 6a and Figure 7a force-time, Figure 6b and Figure 7b force-displacement graphs of 12-layer functional1 and 12-layer functional2 glass and aramid fiber reinforced composite samples are given at different energy levels.



(a)

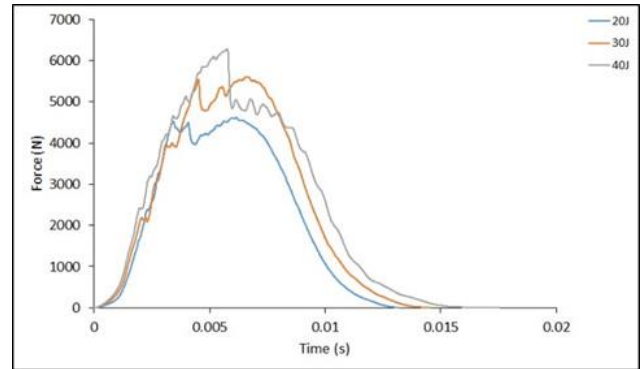


(b)

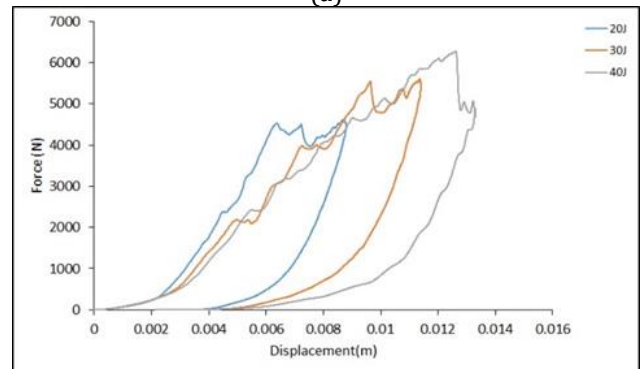
Figure 4. The graphs of (a) force-time and (b) force-displacement for 12-layer hybrid1 glass and aramid fiber reinforced composite sample at different energy levels

When the force-time changes given for the functional1 sample in Figure 6a and for the functional2 sample in Figure 7a are examined, the maximum contact force values obtained from the same energy levels were lower than the previous samples. When the functional1 and functional2 composite samples were evaluated within themselves, lower force values were obtained for the same energy level than the functional1 sample. Obtaining lower force values by producing the samples functionally indicates that the samples' stiffness has decreased. Otherwise, raw material of the impacted surface for functional samples is extremely important in impact responses.

Force-displacement graphs at different energy levels are given for the functional1 sample in Figure 6b and for the functional2 sample in Figure 7b. For the same energy levels, higher displacement values were obtained from the functional2 sample compared to the functional1 sample. When the bending rigidity values in force-displacement changes are examined, different values



(a)



(b)

Figure 5. The graphs of (a) force-time and (b) force-displacement for 12-layer hybrid2 glass and aramid fiber reinforced composite sample at different energy levels

occur at different energy levels in the functional1 sample, while nearly same bending rigidity values are obtained in the functional2 sample.

4. Conclusion

Composite materials are frequently used in aviation, space, automotive and defense industry sectors due to their superior properties such as high strength/weight ratio, high wear and corrosion resistance. The most disadvantageous features of composite materials are their sensitivity to impact loading and their high cost. For this reason, predicting the damages that will occur with impact load in composite materials and designing them accordingly will make a significant contribution to reducing the cost. In this study, the low-velocity impact response of 180x100mm glass, aramid and hybrid composite materials at 20 J, 30 J and 40 J energy levels was investigated using LS-Dyna software. The results obtained from the study are presented below;

- When the force-time histories of all test samples at different energy levels were examined, it was determined that the maximum contact force increased with the increase of the impact energy. It was observed that the oscillations indicating damage also increased with the increase of the impact energy.
- In the force-displacement curves of the 12-layer glass fiber composite sample, the bending rigidity value was nearly same for 20 J and 30 J, but decreased slightly at the 40 J energy level.
- In the force-displacement curves of the 12-layer aramid fiber composite sample, the bending rigidity value was found to be higher at 20 J energy levels than the other energy levels, and nearly same at 30 J and 40 J energy levels.
- In the force-displacement curves of the hybrid1 sample, it was observed that the bending rigidity values at 20 J and 30 J energy levels were nearly same,

but decreased at 40 J energy level. On the other hand, for the hybrid 2 composite sample, while the bending rigidity value was nearly same at 30 J and 40 J energy levels, but it was higher at 20 J energy level.

- Force-displacement curves of the functional1 sample show that different bending rigidities occur at different energy levels; The graphs of the functional 2 sample show that nearly same bending rigidities occur at different energy levels.
- The area under the force-displacement curves gives the amount of absorbed energy by the sample during the impact. For all test samples, as the impact energy increased, the amount of absorbed energy also increased.
- Since this study examines the low-velocity impact responses of aramid and glass fiber reinforced composites at different energy levels, it will lead to future studies on this subject.

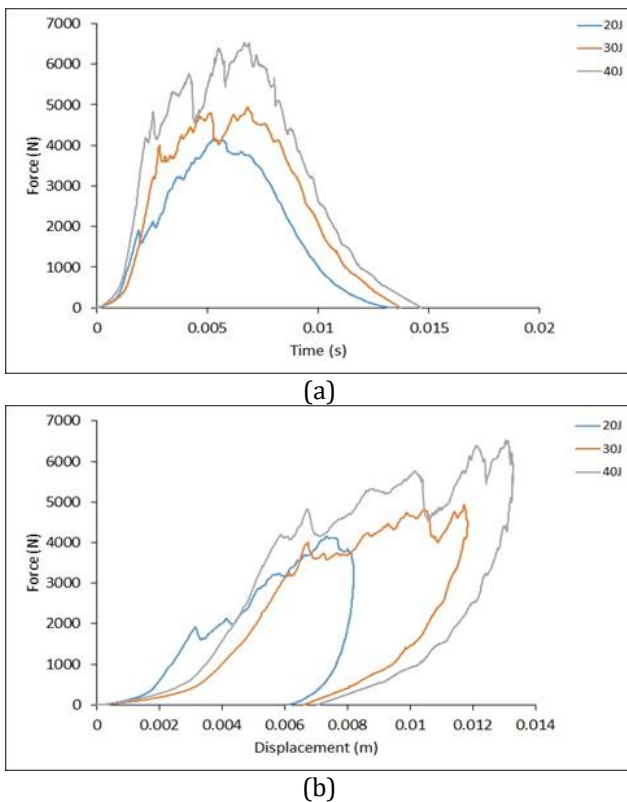


Figure 6. The graphs of (a) force-time and (b) force-displacement for 12-layer functionally graded glass and aramid fiber reinforced functional1 composite sample at different energy levels

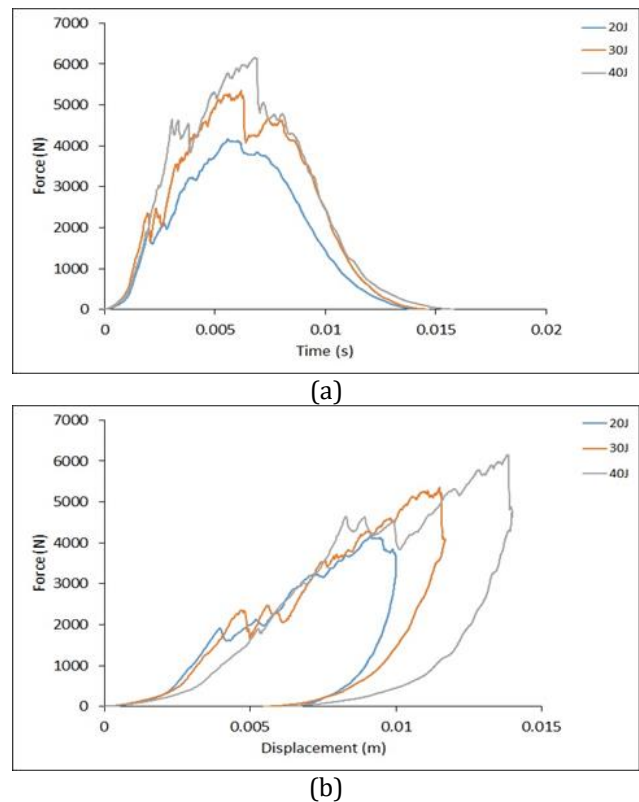


Figure 7. The graphs of (a) force-time and (b) force-displacement for 12-layer functionally graded glass and aramid fiber reinforced functional2 composite sample at different energy levels

Acknowledgement

We would like to thank Erzurum Atatürk University for the LS-DYNA software which is used in the numerical analysis in this study.

Author contributions

Uzay Gezer: Investigation, Methodology, Software, Writing-Original draft preparation. **Bünyamin Demir:** Conceptualization, Methodology, Data curation, Validation. **Yusuf Kepir:** Investigation, Software,

Writing-Reviewing and Editing. **Alper Günöz:** Software, Visualization and Editing. **Memduh Kara:** Conceptualization, Visualization, Writing-Reviewing and Editing.

Conflicts of interest

The authors declare no conflicts of interest.

References

1. Naqvi, S. R., Prabhakara, H. M., Bramer, E. A., Dierkes, W., Akkerman, R., & Brem, G. (2018). A critical review on recycling of end-of-life carbon fibre/glass fibre reinforced composites waste using pyrolysis towards a circular economy. *Resources, conservation and recycling*, 136, 118-129.
2. Lin, S., & Waas, A. M. (2021). The effect of stacking sequence on the LVI damage of laminated composites; experiments and analysis. *Composites Part A: Applied Science and Manufacturing*, 145, 106377.
3. Kazemi, M. E., Shanmugam, L., Dadashi, A., Shakouri, M., Lu, D., Du, Z., ... & Yang, J. (2021). Investigating the roles of fiber, resin, and stacking sequence on the low-velocity impact response of novel hybrid thermoplastic composites. *Composites Part B: Engineering*, 207, 108554.
4. Supian, A. B. M., Sapuan, S. M., Jawaid, M., Zuhri, M. Y. M., Ilyas, R. A., & Syamsir, A. (2022). Crashworthiness response of filament wound kenaf/glass fibre-reinforced epoxy composite tubes with influence of stacking sequence under intermediate-velocity impact load. *Fibers and Polymers*, 23(1), 222-233.
5. Garouge, S. E., Tarfaoui, M., Hassoon, O. H., Minor, H. E., & Bendarma, A. (2022). Effect of stacking sequence on the mechanical performance of the composite structure under slamming impact. *Materials Today: Proceedings*, 52, 29-39.
6. Goh, G. D., Dikshit, V., Nagalingam, A. P., Goh, G. L., Agarwala, S., Sing, S. L., ... & Yeong, W. Y. (2018). Characterization of mechanical properties and fracture mode of additively manufactured carbon fiber and glass fiber reinforced thermoplastics. *Materials & Design*, 137, 79-89.
7. Günöz, A., Kepir, Y. & Kara, M. (2022). The investigation of hardness and density properties of GFRP composite pipes under seawater conditions. *Turkish Journal of Engineering*, 6 (1), 34-39 .
8. Yang, G., Park, M., & Park, S. J. (2019). Recent progresses of fabrication and characterization of fibers-reinforced composites: A review. *Composites Communications*, 14, 34-42.
9. Lertwassana, W., Parnklang, T., Mora, P., Jubsilp, C., & Rimdusit, S. (2019). High performance aramid pulp/carbon fiber-reinforced polybenzoxazine composites as friction materials. *Composites Part B: Engineering*, 177, 107280.
10. Qi, G., Zhang, B., Du, S., & Yu, Y. (2017). Estimation of aramid fiber/epoxy interfacial properties by fiber bundle tests and multiscale modeling considering the fiber skin/core structure. *Composite Structures*, 167, 1-10.
11. Raphael, N., Namratha, K., Chandrashekar, B. N., Sadasivuni, K. K., Ponnamma, D., Smitha, A. S., ... & Byrappa, K. J. P. I. C. G. (2018). Surface modification and grafting of carbon fibers: A route to better interface. *Progress in Crystal Growth and Characterization of Materials*, 64(3), 75-101.
12. Akan, A. E., & Ünal, F. (2020). Thin-Layer Drying Modeling in the Hot Oil-Heated Stenter. *International Journal of Thermophysics*, 41(8), 1-27.
13. Carrera, E., & Pagani, A. (2014). Free vibration analysis of civil engineering structures by component-wise models. *Journal of Sound and Vibration*, 333(19), 4597-4620.
14. Yilmaz, H. M., Aktan, N., Çolak, A., & Alptekin, A. (2022). Modelling Ozancık village (Aksaray) in computer environment using UAV photogrammetry. *Mersin Photogrammetry Journal*, 4(1), 32-36.
15. Kip, M., & Goren, A. (2022). Güneş Enerjili Hafif Aracın Arka Salıncak Kolunun Topoloji Optimizasyonu Çalışması. *Journal of Science, Technology and Engineering Research*, 3(2), 42-49.
16. Beyazit, N. I., Unal, F., & Bulut, H. (2020). Modeling of the hourly horizontal solar diffuse radiation in Sanliurfa, Turkey. *Thermal Science*, 24(2 Part A), 939-950.
17. Song, J. H. (2015). Pairing effect and tensile properties of laminated high-performance hybrid composites prepared using carbon/glass and carbon/aramid fibers. *Composites Part B: Engineering*, 79, 61-66.
18. Jaroslaw, B., Barbara, S., & Patryk, J. (2016). The comparison of low-velocity impact resistance of aluminum/carbon and glass fiber metal laminates. *Polymer Composites*, 37(4), 1056-1063.
19. Wagih, A., Sebaey, T. A., Yudhanto, A., & Lubineau, G. (2020). Post-impact flexural behavior of carbon-aramid/epoxy hybrid composites. *Composite Structures*, 239, 112022.
20. Gemi, D. S., Şahin, Ö. S., & Gemi, L. (2021). Experimental investigation of the effect of diameter upon low velocity impact response of glass fiber reinforced composite pipes. *Composite Structures*, 275, 114428.
21. Rezasefat, M., Gonzalez-Jimenez, A., Ma, D., Vescovini, A., Lomazzi, L., da Silva, A. A., ... & Manes, A. (2022). Experimental study on the low-velocity impact response of inter-ply S2-glass/aramid woven fabric hybrid laminates. *Thin-Walled Structures*, 177, 109458.
22. Uyaner, M., Kara, M., Kepir, Y., & Gunoz, A. (2022). Virtual Testing of Laminated Composites Subjected to Low-Velocity Impact. *Iranian Journal of Science and Technology, Transactions of Mechanical Engineering*, 1-16.
23. Berk, B., Karakuzu, R., Murat Icten, B., Arikan, V., Arman, Y., Atas, C., & Goren, A. (2016). An experimental and numerical investigation on low velocity impact behavior of composite plates. *Journal of Composite Materials*, 50(25), 3551-3559.
24. Maghsoudlou, M. A., Barbaz Isfahani, R., Saber-Samandari, S., & Sadighi, M. (2021). The response of GFRP nanocomposites reinforced with functionalized SWCNT under low velocity impact: experimental and LS-DYNA simulation investigations. *Iranian Journal of Materials Science and Engineering*, 18(2), 1-11.
25. Sayer, M. (2009). Hibrit kompozitlerin darbe davranışlarının incelenmesi. (PHD Thesis), Pamukkale University.
26. Alkhatib, F., Mahdi, E., & Dean, A. (2020). Crushing response of CFRP and KFRP composite corrugated tubes to quasi-static slipping axial loading:

- experimental investigation and numerical simulation. *Composite Structures*, 246, 112370.
27. Singh, N. K., & Singh, K. K. (2015). Review on impact analysis of FRP composites validated by LS-DYNA. *Polymer Composites*, 36(10), 1786-1798.
28. Uyaner, M., & Kara, M. (2007). Dynamic response of laminated composites subjected to low-velocity impact. *Journal of Composite materials*, 41(24), 2877-2896.



© Author(s) 2023. This work is distributed under <https://creativecommons.org/licenses/by-sa/4.0/>



Machine learning-based lung cancer diagnosis

Mahmut Dirik *¹ 

¹Sirnak University, Computer Engineering Department, Türkiye

Keywords

Lung cancer
Early diagnosis
Machine learning
Classification

Research Article

DOI: 10.31127/tuje.1180931

Received: 27.09.2022

Revised: 22.12.2022

Accepted: 27.12.2022

Published: 27.02.2023



Abstract

Cancer is one of the leading health problems, occurring in various organs and tissues of the body, and its incidence is increasing worldwide. Lung cancer is one of the deadliest types of cancer. Due to its worldwide prevalence, increasing number of cases, and deadly consequences, early detection of lung cancer, as with all other cancers, greatly increases the chances of survival. As with all other diseases, the diagnosis of cancer is only possible after the appearance of various symptoms and an examination by specialists. Known symptoms of lung cancer are shortness of breath, coughing, wheezing, jaundice in the fingers, chest pain, and difficulty swallowing. The diagnosis is made by an expert on site based on these symptoms and additional tests. The aim of this study is to detect the disease at an earlier stage based on the symptoms present, to assess more cases with less time and cost, and to achieve results in new situations that are as successful or even faster than those of human experts by deriving them from existing data using different algorithms. The aim is to develop an automated model that can detect early-stage lung cancer based on machine learning methods. The developed model includes nine different machine learning algorithms (NB, LR, DT, RF, GB, and SVM). The success of the classification algorithms used was evaluated using the metrics of accuracy, sensitivity, and precision calculated using the parameters of the confusion matrix. The results obtained show that the proposed model can detect cancer with a maximum accuracy of 91%.

1. Introduction

Lung cancer is the formation of a mass (tumor) in the lung by cells that are structurally normal lung tissue but that multiply uncontrollably. The mass formed here first grows around itself and, in later stages, spreads via the blood to surrounding tissue or distant sites (liver, bones, brain, etc.) and causes damage. This spread is called metastasis. Lung cancer is responsible for the largest proportion of deaths from malignant diseases worldwide [1-6]. The International Agency for Research on Cancer (IARC) provides estimates of incidence and mortality rates for 36 specific cancers in 185 countries and for all cancers combined for the year 2020, according to its latest estimates of the global cancer burden as of December 15, 2020 [6-7]. Worldwide, the total number of cancer patients still alive within 5 years of cancer diagnosis (5-year prevalence) is estimated at 50.6 million. The most common cancer worldwide is breast cancer in women (11.7%), followed by lung cancer (11.4%), colorectal cancer (10.0%), prostate cancer

(7.3%), and stomach cancer (5.6%) [6]. The causes of cancer are diverse and range from behavioral characteristics such as high body mass index, tobacco, and alcohol use to physical carcinogens such as exposure to ultraviolet rays and radiation, including certain biological and genetic carcinogens [8]. Malaise, fatigue, nausea, a persistent cough, difficulty breathing, weight loss, muscle pain, and bleeding and bruising are among the most common cancer symptoms [3, 9, 10]. Again, none of these symptoms are cancer-specific, and not every patient has them all. Without a comprehensive diagnostic examination such as a computed tomography scan (CT) [11], magnetic resonance imaging (MRI) [12, 13], positron emission tomography (PET) [14], ultrasound, or a biopsy, it is impossible to detect the presence of cancer. In the early stages, those affected often show few or no symptoms. As with all other malignancies, timely and early detection of lung cancer is critical due to its prevalence, high mortality rate, and increasing incidence. Clinicians want to know the actual relationship between observations, interventions, and

* Corresponding Author

(scai.journal@gmail.com) ORCID ID 0000-0003-1718-5075

Cite this article

Dirik, M. (2023). Machine learning-based lung cancer diagnosis. Turkish Journal of Engineering, 7(4), 322-330

outcomes (outputs). In other words, they need a model to detect, classify, or predict disease. Currently, this information is based on clinical trials and clinicians' experience. Reviewing medical records to determine the best treatment options for patients is also very time-consuming. A good estimation and classification model simplifies the whole process.

The diagnosis of cancer is made by doctors who are experts in the field by interpreting the observable symptoms and the results of examinations. Intensive studies in the field of artificial intelligence [15–17], together with rapidly developing technology, have paved the way for machines to make the right decisions in many areas, just like human experts. The branch of artificial intelligence that enables predictions about new situations by using correlations obtained from data by interpreting the data of the current situation is called machine learning (ML) [18–20]. It is a set of techniques that enable rapid and accurate decisions to be made for new and different situations by learning from data that has been studied in a particular subject area. These techniques have enabled successful applications in healthcare [18, 19] and many other fields. ML has a wide range of applications, from disease detection in pathology to intelligent systems that can prescribe conventional drugs when evaluated based on the patient's symptoms [21]. When provided with high quality and sufficient data, it can deliver results that are as accurate as those of human experts, even faster and more powerful.

When it comes to methods of diagnosing disease, computer technology and artificial intelligence have shown incredible potential in the diagnostic industry, offering a powerful alternative to traditional diagnostic methods. Diagnosing a particular disease requires taking a sample from a patient, running a series of tests on those samples, converting the results into an interpretable form, and finally having a trained person make a decision

based on those results. If the samples taken from a patient are digital or have been digitized in some way, they can be analyzed by machines. They can then be provided with a dataset containing decisions about similar situations in the past. In machine learning, making decisions based on information obtained from past scenarios is called "supervised learning" [22]. Over the last three decades, many supervised learning algorithms have been developed that are ideal for working with biomedical data. By using biomedical data [23], artificial intelligence can offer a new dimension in the field of medical diagnosis [24] and is increasingly becoming a viable alternative to traditional diagnostic methods. Although AI models appear promising on paper and in controlled experiments, they are not yet reliable enough to be trusted with life-changing decisions. Of course, some simple diagnostic procedures are only performed by machines with little or no human intervention. Yet AI methods often still struggle in practice. These challenges are being overcome by collecting more practical data, developing new and improved learning algorithms, and rigorously testing new models.

In this study, we developed a ML-based classification model based on a performance comparison of algorithms that can diagnose lung cancer. The results showed that the model is able to classify associated lung cancer with high reliability. In the following sections, we describe this approach to cancer diagnosis and provide the necessary graphs, tables, charts, and other drawings to facilitate interpretation.

The rest of the article is structured as follows: Chapter 2 explains the principles of the methods and techniques required to build this model. This section explains the dataset, the machine learning algorithm, and the performance evaluation metrics used. Finally, chapter 3 presents the results and discussion.

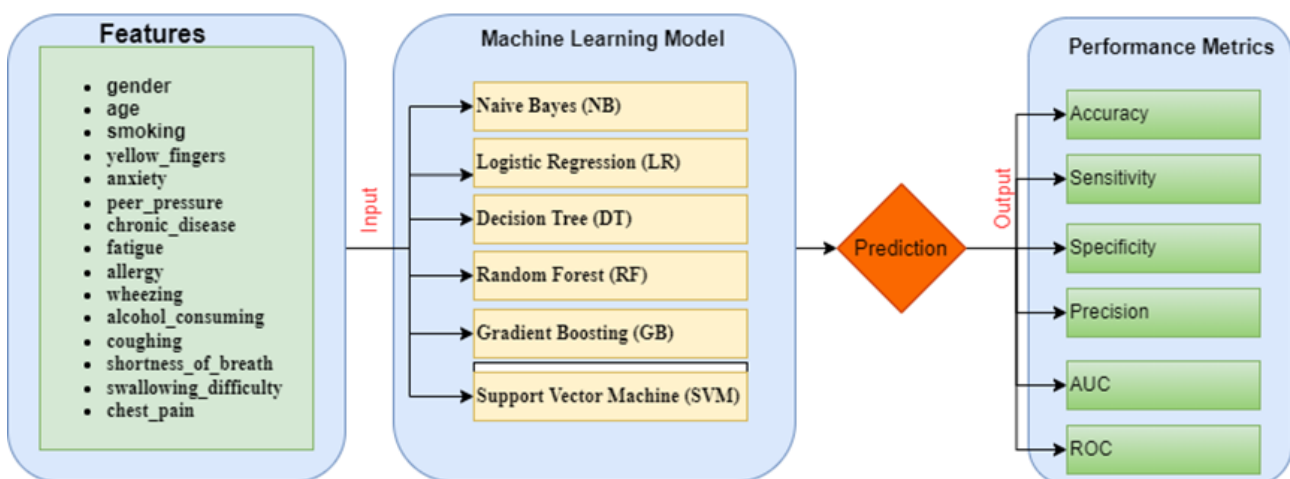


Figure 1. Flowchart of the process for machine learning based lung cancer diagnosis

2. Method

Early detection of lung cancer is thought to increase survival rates and reduce cancer-related deaths worldwide. People at high risk often undergo annual radiological screening by computed tomography, the current method of clinical lung cancer diagnosis. The

performance of CT screening is not satisfactory due to its high cost and high prevalence of false-positive results [25]. In this study, the predictive biomarkers for the diagnosis of lung cancer were a persistent or worsening cough, blood or bloody sputum when coughing, chest pain that worsens when coughing or laughing while breathing deeply, loss of appetite, weakness, fatigue,

weight loss, hoarseness, shortness of breath, and recurrent or persistent lung infections such as bronchitis or pneumonia. These data are combined using machine learning techniques to find diagnostic indicators of early-stage lung cancer. Figure 1 shows the overall framework of the proposed architecture.

2.1. Dataset

The effectiveness of the cancer prediction system helps people know their cancer risk at a low cost and helps them make the right decision based on their cancer risk status. The data used in this study [25] consists of responses from 309 different people from a lung cancer survey conducted in 2013. In addition to the basic information about the individuals in the dataset, there are several observable anomalies about their harmful habits and health. The dataset contains information on 15 characteristics. Depending on these features, a label is

generated indicating whether lung cancer was diagnosed in the returns of the same individuals. The features in the dataset and the correlation between them are listed below. The 16th feature in the dataset was obtained as feedback from participants. A study was conducted to estimate the 16th feature using the first 15 features related to lung cancer in the dataset. Figure 2 shows a diagram of the general distribution of the data.

The statistical method used to determine whether a linear relationship exists between numerical measurements of data in a data set and, if so, the direction and strength of that relationship, is called correlation. If the correlation coefficient is negative, there is an inverse relationship between the two variables. If the correlation coefficient is positive, there is a correct relationship between the two variables, i.e., "if one variable increases, so does the other." Table 1 shows the correlation of the data used.

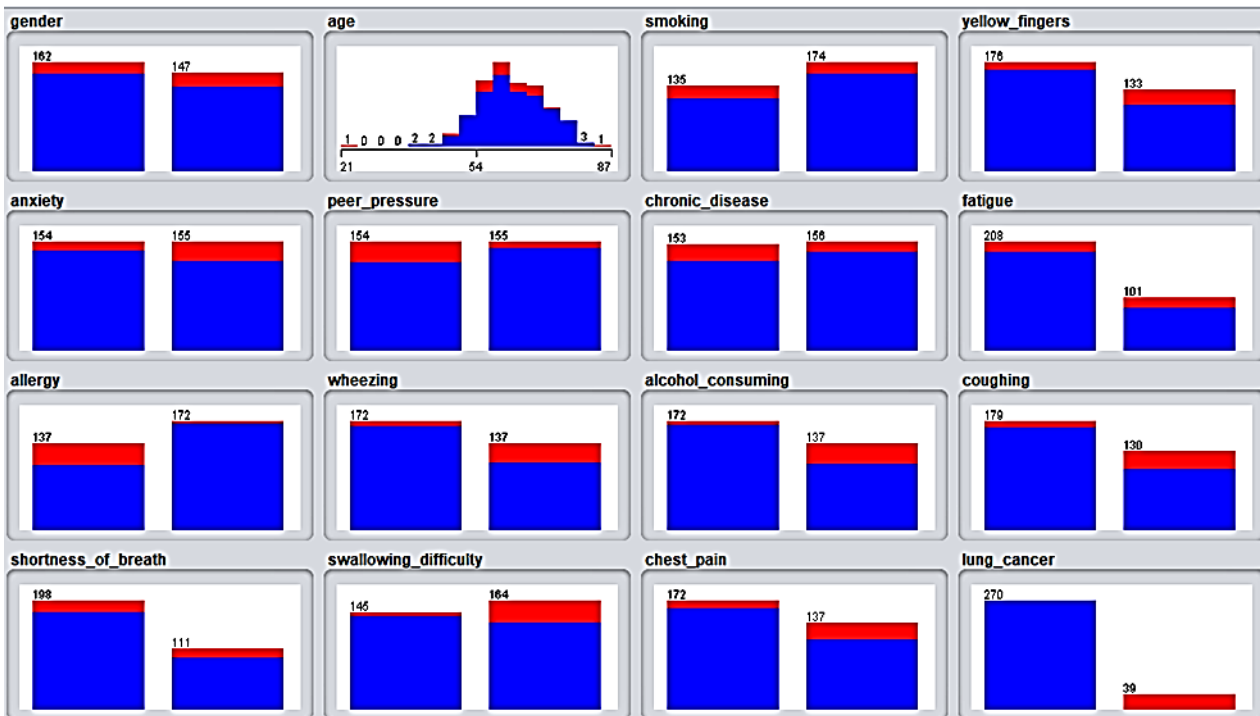


Figure 2. Visualize All attributes

Table 1. Lung cancer data correlation table

Attributes	age	alcohol...	allergy ...	anxiety ...	chest_p...	chronic...	coughin...	fatigue ...	gender ...	lung_ca...	peer_pr...	shortne...	smokin...	swallo...	wheezi...	yellow_...
age	1	0.059	0.028	-0.053	-0.018	-0.013	0.170	0.013	0.021	0.089	0.019	-0.018	-0.084	0.001	0.055	0.005
alcohol_co...	0.059	1	0.344	0.166	0.331	0.002	0.203	-0.191	0.454	0.289	-0.160	-0.179	-0.051	0.009	0.266	-0.289
allergy = yes	0.028	0.344	1	0.166	0.239	0.106	0.190	0.003	0.154	0.328	-0.082	-0.030	0.002	0.062	0.174	-0.144
anxiety = no	-0.053	0.166	0.166	1	0.114	0.010	0.226	0.189	0.152	-0.145	-0.217	0.144	-0.160	0.489	0.192	-0.566
chest_pain ...	-0.018	0.331	0.239	0.114	1	-0.037	0.084	-0.011	0.363	0.190	-0.095	0.024	0.120	-0.069	0.148	-0.105
chronic_dis...	-0.013	0.002	0.106	0.010	-0.037	1	-0.175	-0.111	-0.205	0.111	0.049	-0.026	-0.142	-0.075	-0.050	0.041
coughing = ...	0.170	0.203	0.190	0.226	0.084	-0.175	1	0.147	0.133	0.249	-0.089	0.277	-0.129	0.158	0.374	-0.013
fatigue = yes	0.013	-0.191	0.003	0.189	-0.011	-0.111	0.147	1	-0.084	0.151	0.078	0.442	-0.030	0.133	0.142	-0.118
gender = m...	0.021	0.454	0.154	0.152	0.363	-0.205	0.133	-0.084	1	0.067	-0.276	-0.065	0.036	0.078	0.141	-0.213
lung_cance...	0.089	0.289	0.328	-0.145	0.190	0.111	0.249	0.151	0.067	1	0.186	0.061	0.058	-0.260	0.249	0.181
peer_press...	0.019	-0.160	-0.082	-0.217	-0.095	0.049	-0.089	0.078	-0.276	0.186	1	-0.220	-0.043	-0.367	-0.069	0.323
shortness_...	-0.018	-0.179	-0.030	0.144	0.024	-0.026	0.277	0.442	-0.065	0.061	-0.220	1	0.061	0.161	0.038	-0.106
smoking = ...	-0.084	-0.051	0.002	-0.160	0.120	-0.142	-0.129	-0.030	0.036	0.058	-0.043	0.061	1	-0.031	-0.129	-0.015
swallowing...	0.001	0.009	0.062	0.489	-0.069	-0.075	0.158	0.133	0.078	-0.260	-0.367	0.161	-0.031	1	-0.069	-0.346
wheezing = ...	0.055	0.266	0.174	0.192	0.148	-0.050	0.374	0.142	0.141	0.249	-0.069	0.038	-0.129	-0.069	1	-0.079
yellow_fing...	0.005	-0.289	-0.144	-0.566	-0.105	0.041	-0.013	-0.118	-0.213	0.181	0.323	-0.106	-0.015	-0.346	-0.079	1

2.2. Machine Learning Classifiers

Machine learning (ML) [26–28] is the process of instructing computers to use data more efficiently and effectively through reinforcement learning. It refers to the supervised learning process used in classification, whereby the software learns from incoming data and then applies this knowledge to categorize future observations. Classification techniques are used to determine the classification of the data. Similar to the regression model, the categorization model predicts future outcomes. In this study on ML-based lung cancer detection, we used the following algorithms: Naive Bayes, Logistic Regression, Fast Large Margin, Decision Tree, Random Forest, Gradient Boosting, and Support Vector Machin.

2.2.1. Naive Bayes (NB)

Naive Bayes is a simple learning procedure developed by Thomas Bayes [29] that applies Bayes' rule and makes a strong assumption about the conditional independence of features with respect to class. Naive Bayes is widely used in practice because of its computational efficiency and several other advantageous properties. The quantitative component of the Bayesian network consists of three basic components: probability theory, Bayes' theorem, and conditional probability functions. Bayes' theorem starts from the premise that the conditional probability is proportional to the probability of events occurring. This makes it easy to represent the probability distribution in graphical models as conditional dependence or independence [30, 31].

2.2.2. Logistic Regression (LR)

Logistic regression (LR) is a simpler and more accurate method for dealing with binary and linear classification problems, i.e., modelling the probability of a discrete outcome as a function of an input variable. It is a basic classification model that works effectively for classes that can be linearly separated [32].

2.2.3. Decision Tree (DT)

The decision tree method is a supervised learning technique that can handle categorical and numerical data under supervision and corresponds to the ideal node and edge tree for classification problems. Each node in the tree indicates the class of the problem, while each edge reflects the result of the analysis. This classifier is a predictive machine learning model that illustrates the relationship between the values of the dataset and the features. The goal of decision-making is to determine the best option considering the entire probability distribution. Each branch of the decision tree represents the possible value of a different category. The nodes are determined based on entropy measurements of the features in the dataset. The root node is the feature with the highest entropy [33–35].

2.2.4. Random Forest (RF)

Random Forest was developed by Leo Breiman [36] to create a community of estimators by generating a set of decision trees in randomly selected data subdomains, where each tree has the same value and depends on the values of an independently generated random vector. Random forests, also known as random choice forests, are a type of ensemble learning technique used to solve classification, regression, and other problems that require training a large number of decision trees. The output of the random forest is the class of the classification problem that is chosen by the majority of the trees [37, 38].

2.2.5. Gradient Boosting (GB)

The method was developed by combining the concepts of gradient descent and boosting, improves the results of decision trees using the gradient descent algorithm. Splitting the dataset into multiple sub-datasets as in a Random Forest is not done in this approach. A decision tree is created from the existing dataset and a new decision tree is created based on its errors [39–41].

2.2.6. Support Vector Machine (SVM)

Support Vector Machine (SVM) is a supervised machine learning algorithm that can be used for classification or regression problems. However, it is mainly used for classification problems. Draws a line to separate points that lie on a plane [42–44]. The objective is that this line has the maximum distance between the points of the two classes. SVM was developed by Vapnik et al [45].

2.3. Performance Metrics

The purpose of the performance evaluation is to analyze the effectiveness of the algorithms used and show the usability of the system. The output values are compared with the actual values to validate a classification approach. In this study, the confusion matrix [46] was used to measure the classification success of the proposed approach, and six different performance measures were used, namely accuracy, area under the curve (AUC), precision, F-measure, sensitivity, and specificity. The corresponding calculation formulas can be found in Table 2. In the table, TP (True Positive) represents the number of correctly classified positive data, FP (False Positive) represents the number of misclassified positive data, TN (True Negative) represents the number of correctly classified negative data, and FN (False Negative) represents the number of misclassified negative data [46].

The Receiver Operating Characteristic Curve (ROC) is characterized by the AUC. AUC is a graphical representation of the false-positive rate (FPR) and the true-positive rate (TPR) at different confidence levels. Since AUC is not based on a discontinuity number, it is a more reliable measure of overall performance than accuracy [51].

Table 2. Performance metrics

Description	Formula	References
Accuracy	$ACC = \frac{TP + TN}{TP + FP + TN + FN}$	[47] [48], [49]
Sensitivity (Recall)	$RCL = \frac{TP}{TP + FN}$	[48], [49]
Specificity	$SPC = \frac{TN}{FP + TN}$	[48], [49]
Precision	$PRE = \frac{TP}{TP + FP}$	[48], [49]
F-1 Score	$FSC = 2 * \frac{PRE * RCL}{PRE + RCL}$	[48], [49]
Area Under the Curve	$AUC = \frac{1}{2} * (RCL + SPC)$	[50]

3. Results and Discussion

Lung cancer is one of the cancers that causes the most deaths among cancers because it is not diagnosed until the late stages. For this reason, it is very important to detect lung cancer at an early stage. As in many other fields, machine learning is now delivering successful results in health research. The use of computer-aided diagnosis systems in the early detection of lung cancer can lead to more accurate and faster results. The classification system implemented in this study is able to provide a practical assessment of the risk status of lung cancer based on the information provided by the individuals themselves. In this study, Naive NB, LR, DT, RF, GB, and SVM were classified by six different machine learning methods to accurately diagnose critical disease-related features of lung cancer.

In the study on evaluating the performance of machine learning classifiers, we present the results of the metrics obtained based on the complexity matrix of the case with the highest average classification success. The values ACC, RCL, SPC, PRE, FSC, AUC, and ROC of the classifiers used are shown in Figures 3–10.

4. Conclusion

A summary graph of the accuracy rates achieved as a result of the classification process can be found in Figure 3. Although all six methods showed high success in classifying the data, it was found that the most successful methods were NB and SVM, with a rate of 91%.

The ROC curves of each classifier are shown in Figure 10. The ROC curve is one of the most commonly used metrics to evaluate the performance of machine learning algorithms. It explains how good the model is at prediction. One of the most commonly used metrics is the AUC curve. AUC stands for "Area Under the ROC Curve." The area of this field is AUC. The larger the area covered; the better machine learning models can distinguish between certain classes. The ideal value for AUC is 1. The classification system implemented in this study is able to provide a practical assessment of the risk status of lung cancer based on the information provided by the people themselves. In this way, it guides people to take the necessary precautions in time. Due to the methods used, high diagnostic accuracy is aimed for. In addition, this study will help doctors who will use the system to provide initial information for the diagnosis of lung cancer. Methods with high accuracy are necessary to achieve developments in such matters. This study focuses on effective decision-support systems that can help them diagnose more easily and accurately. In this context, the effectiveness and accuracy of expert systems and various artificial intelligence techniques were evaluated. As a result of this evaluation, NB and SVM showed high predictive performance in the problem of diagnosing lung diseases. In conclusion, NB and SVM methods can be successfully used in the diagnosis of lung diseases and are preferred by physicians to make decisions about the disease.

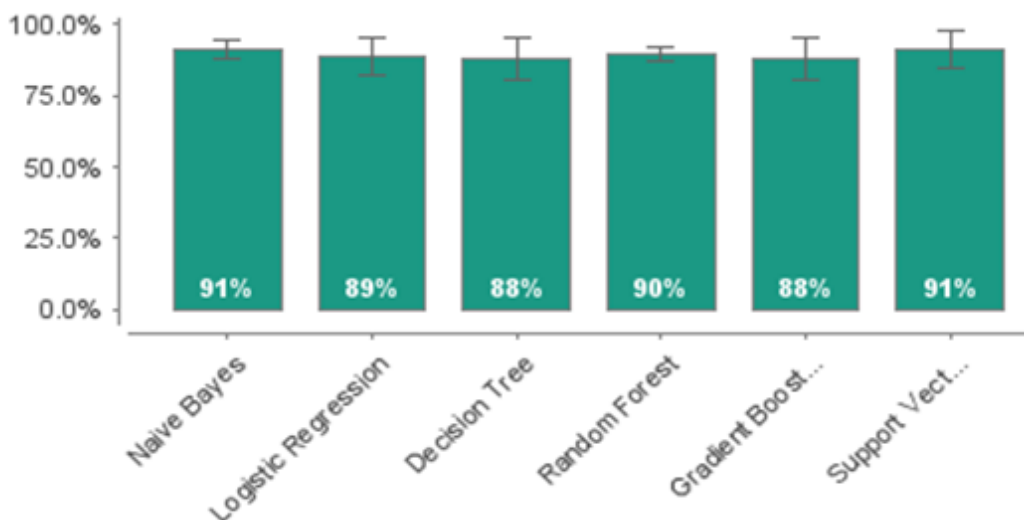


Figure 3. Accuracy (ACC) of machine learning-based lung cancer diagnosis

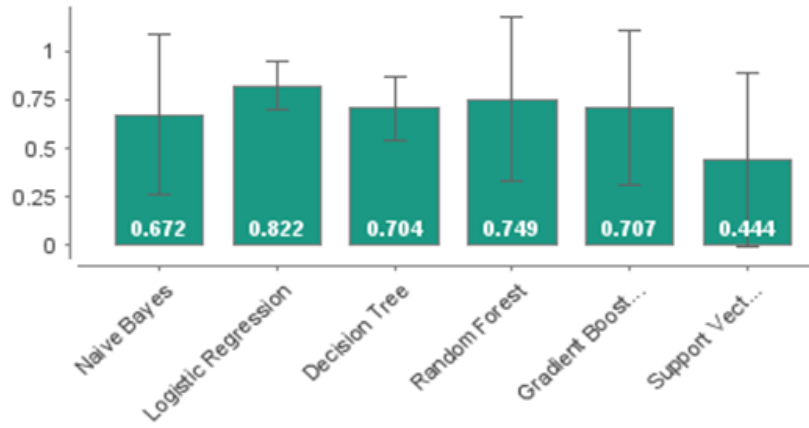


Figure 4. Area Under the Curve (AUC) of machine learning-based lung cancer diagnosis

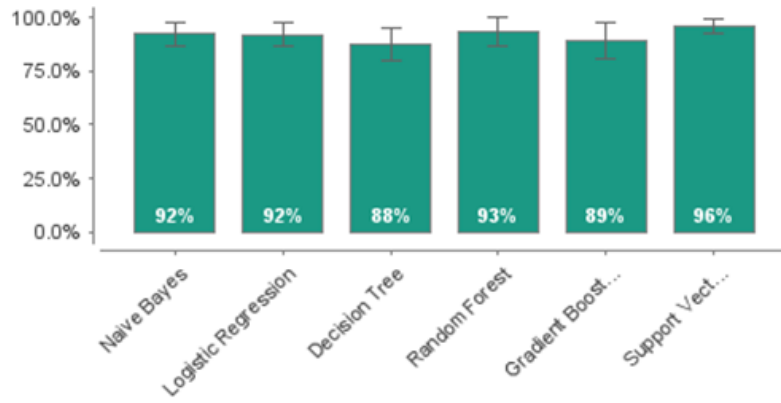


Figure 5. Precision of machine learning-based lung cancer diagnosis

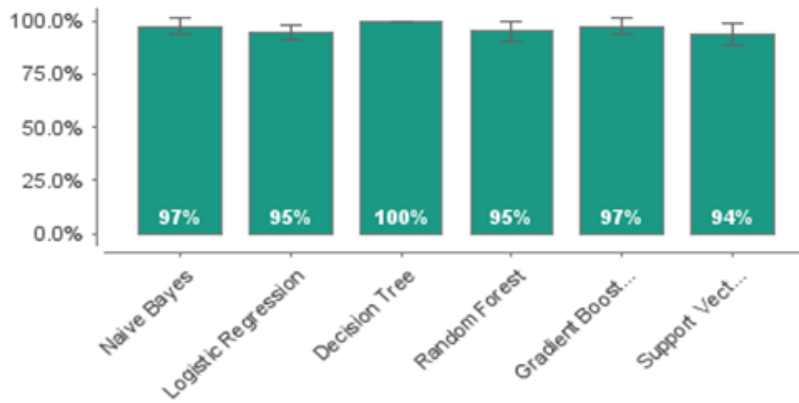


Figure 6. Sensitivity/Recall of machine learning-based lung cancer diagnosis

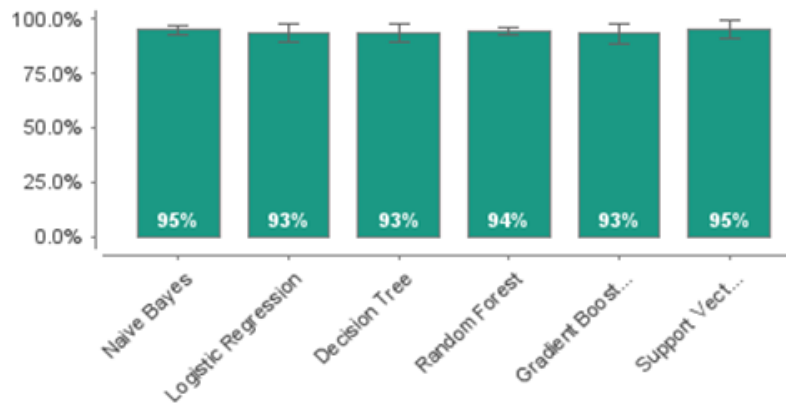


Figure 7. F Measure of machine learning-based lung cancer diagnosis

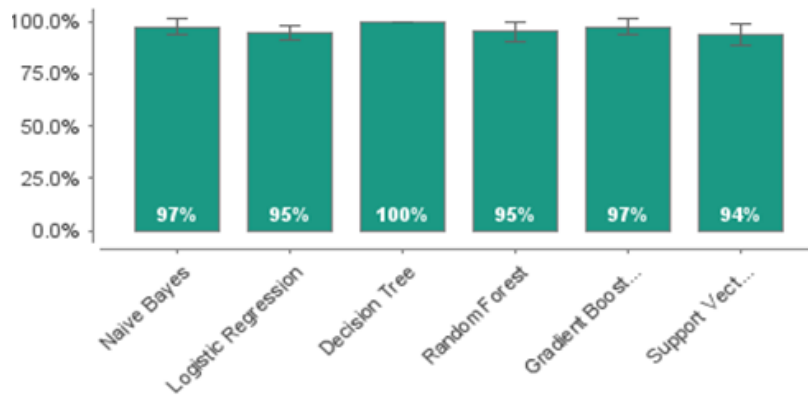


Figure 8. Sensitivity of machine learning-based lung cancer diagnosis

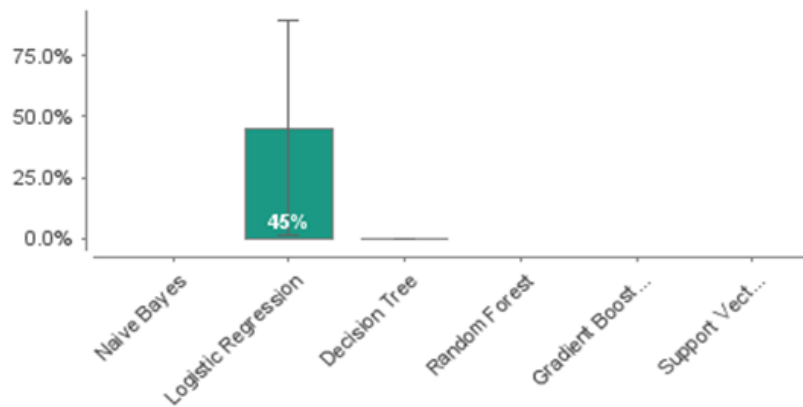


Figure 9. Specificity of machine learning-based lung cancer diagnosis

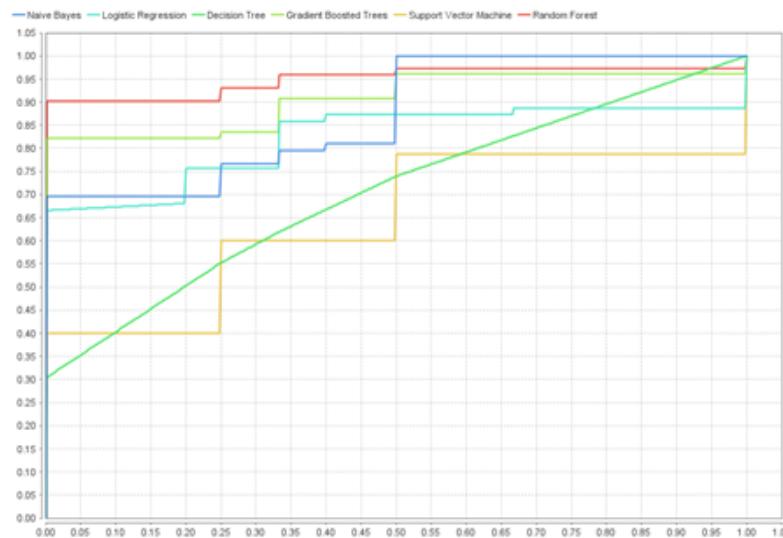


Figure 10. ROC Comparison of machine learning-based lung cancer diagnosis

Conflicts of interest

The authors declare no conflicts of interest.

References

- Xie, Y., Meng, W. Y., Li, R. Z., Wang, Y. W., Qian, X., Chan, C., ... & Leung, E. L. H. (2021). Early lung cancer diagnostic biomarker discovery by machine learning methods. *Translational oncology*, 14(1), 100907. <https://doi.org/10.1016/j.tranon.2020.100907>
- Chiu, H. Y., Chao, H. S., & Chen, Y. M. (2022). Application of artificial intelligence in lung cancer. *Cancers*, 14(6), 1370. <https://doi.org/10.3390/cancers14061370>
- Masud, M., Sikder, N., Nahid, A. A., Bairagi, A. K., & AlZain, M. A. (2021). A machine learning approach to diagnosing lung and colon cancer using a deep learning-based classification framework. *Sensors*, 21(3), 748. <https://doi.org/10.3390/s21030748>
- <https://www.mohw.gov.tw/cp-4650-50697-2.html>
- <https://www.who.int/news-room/fact-sheets/detail/cancer>
- Sung, H., Ferlay, J., Siegel, R. L., Laversanne, M., Soerjomataram, I., Jemal, A., & Bray, F. (2021). Global

- cancer statistics 2020: GLOBOCAN estimates of incidence and mortality worldwide for 36 cancers in 185 countries. *CA: a cancer journal for clinicians*, 71(3), 209-249. <https://doi.org/10.3322/CAAC.21660>
7. <https://gco.iarc.fr/>
 8. <https://www.who.int/news-room/fact-sheets/detail/cancer>
 9. Rock, C. L., Thomson, C., Gansler, T., Gapstur, S. M., McCullough, M. L., Patel, A. V., ... & Doyle, C. (2020). American Cancer Society guideline for diet and physical activity for cancer prevention. *CA: a cancer journal for clinicians*, 70(4), 245-271. <https://doi.org/10.3322/CAAC.21591>
 10. Shakeel, P. M., Tolba, A., Al-Makhadmeh, Z., & Jaber, M. M. (2020). Automatic detection of lung cancer from biomedical data set using discrete AdaBoost optimized ensemble learning generalized neural networks. *Neural Computing and Applications*, 32, 777-790. <https://doi.org/10.1007/S00521-018-03972-2/FIGURES/8>
 11. Bruno, F., Granata, V., Cobianchi Bellisari, F., Sgalambro, F., Tommasino, E., Palumbo, P., ... & Barile, A. (2022). Advanced Magnetic Resonance Imaging (MRI) Techniques: Technical Principles and Applications in Nanomedicine. *Cancers*, 14(7), 1626. <https://doi.org/10.3390/CANCERS14071626>
 12. Zhang, Y., Wang, R., Hu, J., Qin, X., Chen, A., & Li, X. (2022). Magnetic resonance imaging (MRI) and computed topography (CT) analysis of Schatzker type IV tibial plateau fracture revealed possible mechanisms of injury beyond varus deforming force. *Injury*, 53(2), 683-690. <https://doi.org/10.1016/J.INJURY.2021.09.041>
 13. Grootjans, W., Rietbergen, D. D., & van Velden, F. H. (2022, May). Added value of respiratory gating in positron emission tomography for the clinical management of lung cancer patients. In *Seminars in Nuclear Medicine*. WB Saunders. <https://doi.org/10.1053/J.SEMNUCLMED.2022.04.006>
 14. Kooli, C., & Al Muftah, H. (2022). Artificial intelligence in healthcare: a comprehensive review of its ethical concerns. *Technological Sustainability*, 1(2), 121-131. <https://doi.org/10.1108/TECHS-12-2021-0029>
 15. Sun, L., Gupta, R. K., & Sharma, A. (2022). Review and potential for artificial intelligence in healthcare. *International Journal of System Assurance Engineering and Management*, 13(Suppl 1), 54-62. <https://doi.org/10.1007/S13198-021-01221-9/FIGURES/6>
 16. Sanchez, P., Voisey, J. P., Xia, T., Watson, H. I., O'Neil, A. Q., & Tsaftaris, S. A. (2022). Causal machine learning for healthcare and precision medicine. *Royal Society Open Science*, 9(8), 220638. <https://doi.org/10.1098/RSOS.220638>
 17. Rastogi, M., Vijarana, D., & Goel, D. (2022). Role of Machine Learning in Healthcare Sector. *Neha, Role of Machine Learning in Healthcare Sector (August 20, 2022)*. <https://doi.org/10.2139/SSRN.4195384>
 18. Lawson, C. E., Martí, J. M., Radivojevic, T., Jonnalagadda, S. V. R., Gentz, R., Hillson, N. J., ... & Martin, H. G. (2021). Machine learning for metabolic engineering: A review. *Metabolic Engineering*, 63, 34-60. <https://doi.org/10.1016/J.YMBEN.2020.10.005>
 19. Das, S., Biswas, S., Paul, A., & Dey, A. (2018). AI Doctor: An intelligent approach for medical diagnosis. In *Industry Interactive Innovations in Science, Engineering and Technology: Proceedings of the International Conference, I3SET 2016* (pp. 173-183). Springer Singapore. https://doi.org/10.1007/978-981-10-3953-9_17/COVER
 20. Bukhari, S. U. K., Syed, A., Bokhari, S. K. A., Hussain, S. S., Armaghan, S. U., & Shah, S. S. H. (2020). The histological diagnosis of colonic adenocarcinoma by applying partial self supervised learning. *MedRxiv*, 2020-08. <https://doi.org/10.1101/2020.08.15.20175760>
 21. Shakeel, P. M., Tolba, A., Al-Makhadmeh, Z., & Jaber, M. M. (2020). Automatic detection of lung cancer from biomedical data set using discrete AdaBoost optimized ensemble learning generalized neural networks. *Neural Computing and Applications*, 32, 777-790. <https://doi.org/10.1007/S00521-018-03972-2/FIGURES/8>
 22. Das, S., Biswas, S., Paul, A., & Dey, A. (2018). AI Doctor: An intelligent approach for medical diagnosis. In *Industry Interactive Innovations in Science, Engineering and Technology: Proceedings of the International Conference, I3SET 2016* (pp. 173-183). Springer Singapore. https://doi.org/10.1007/978-981-10-3953-9_17/COVER
 23. Zhao, W., Yang, J., Sun, Y., Li, C., Wu, W., Jin, L., ... & Li, M. (2018). 3D deep learning from CT scans predicts tumor invasiveness of subcentimeter pulmonary adenocarcinomas. *Cancer research*, 78(24), 6881-6889. <https://doi.org/10.1158/0008-5472.CAN-18-0696>
 24. <https://data.world/josh-nbu/lung-cancer/workspace/file?filename=survey+lung+cancer+%281%29.csv>
 25. Alanazi, A. (2022). Using machine learning for healthcare challenges and opportunities. *Informatics in Medicine Unlocked*, 100924. <https://doi.org/10.1016/J.IMU.2022.100924>
 26. Mohammadi, F. G., Shenavarmasouleh, F., & Arabnia, H. R. (2022). Applications of machine learning in healthcare and internet of things (IOT): a comprehensive review. *arXiv preprint arXiv:2202.02868*. <https://doi.org/10.48550/arxiv.2202.02868>
 27. Subasi, A. (2020). *Practical machine learning for data analysis using python*. Academic Press. <https://doi.org/10.1016/B978-0-12-821379-7.00003-5>
 28. Bellhouse, D. R. (2004). The Reverend Thomas Bayes, FRS: a biography to celebrate the tercentenary of his birth. <https://doi.org/10.1214/088342304000000189>
 29. Itoo, F., & Singh, S. (2021). Comparison and analysis of logistic regression, Naïve Bayes and KNN machine learning algorithms for credit card fraud detection. *International Journal of Information Technology*, 13, 1503-1511. <https://doi.org/10.1007/s41870-020-00430-y>

30. Frank, E., Trigg, L., Holmes, G., & Witten, I. H. (2000). Naive Bayes for regression. *Machine Learning*, 41, 5-25.
31. LaValley, M. P. (2008). Logistic regression. *Circulation*, 117(18), 2395-2399. <https://doi.org/10.1161/CIRCULATIONAHA.106.682658>
32. Senan, E. M., Al-Adhaileh, M. H., Alsaade, F. W., Aldhyani, T. H., Alqarni, A. A., Alsharif, N., ... & Alzahrani, M. Y. (2021). Diagnosis of chronic kidney disease using effective classification algorithms and recursive feature elimination techniques. *Journal of Healthcare Engineering*, 2021. <https://doi.org/10.1155/2021/1004767>
33. Aggrawal, R., & Pal, S. (2020). Sequential feature selection and machine learning algorithm-based patient's death events prediction and diagnosis in heart disease. *SN Computer Science*, 1(6), 344. <https://doi.org/10.1007/S42979-020-00370-1/TABLES/5>
34. Ayon, S. I., Islam, M. M., & Hossain, M. R. (2022). Coronary artery heart disease prediction: a comparative study of computational intelligence techniques. *IETE Journal of Research*, 68(4), 2488-2507. <https://doi.org/10.1080/03772063.2020.1713916>
35. Cutler, D. R., Edwards Jr, T. C., Beard, K. H., Cutler, A., Hess, K. T., Gibson, J., & Lawler, J. J. (2007). Random forests for classification in ecology. *Ecology*, 88(11), 2783-2792. <https://doi.org/10.1890/07-0539.1>
36. Biau, G. (2012). Analysis of a random forests model. *The Journal of Machine Learning Research*, 13(1), 1063-1095.
37. Lingwal, S., Bhatia, K. K., & Tomer, M. S. (2021). Image-based wheat grain classification using convolutional neural network. *Multimedia Tools and Applications*, 80, 35441-35465. <https://doi.org/10.1007/s11042-020-10174-3>
38. Biau, G., Cadre, B., & Rouvière, L. (2019). Accelerated gradient boosting. *Machine learning*, 108, 971-992. <https://doi.org/10.1007/S10994-019-05787-1/TABLES/5>
39. Friedman, J. H. (2002). Stochastic gradient boosting. *Computational statistics & data analysis*, 38(4), 367-378. [https://doi.org/10.1016/S0167-9473\(01\)00065-2](https://doi.org/10.1016/S0167-9473(01)00065-2)
40. Natekin, A., & Knoll, A. (2013). Gradient boosting machines, a tutorial. *Frontiers in neurorobotics*, 7, 21. <https://doi.org/10.3389/FNBOT.2013.00021/XML/NLM>
41. Cristianini, N., & Shawe-Taylor, J. (2000). *An introduction to support vector machines and other kernel-based learning methods*. Cambridge university press. <https://doi.org/10.1017/CBO9780511801389>
42. Auria, L., & Moro, R. A. (2008). Support vector machines (SVM) as a technique for solvency analysis. *SSRN Electronic Journal*. <https://doi.org/10.2139/SSRN.1424949>
43. Rivas-Perea, P., Cota-Ruiz, J., Chaparro, D. G., Venzor, J. A. P., Carreón, A. Q., & Rosiles, J. G. (2012). Support vector machines for regression: a succinct review of large-scale and linear programming formulations. *International Journal of Intelligence Science*, 03(01), 5-14. <https://doi.org/10.4236/ijis.2013.31002>
44. Cortes, C., & Vapnik, V. (1995). Support-vector networks. *Machine learning*, 20, 273-297.
45. <https://devopedia.org/confusion-matrix>
46. Isabella, S. J., Srinivasan, S., & Suseendran, G. (2020). An efficient study of fraud detection system using ML techniques. *Intelligent Computing and Innovation on Data Science*, 59-67. https://doi.org/10.1007/978-981-15-3284-9_8
47. Taha, A. A., & Malebary, S. J. (2020). An intelligent approach to credit card fraud detection using an optimized light gradient boosting machine. *IEEE Access*, 8, 25579-25587. <https://doi.org/10.1109/ACCESS.2020.2971354>
48. Awoyemi, J. O., Adetunmbi, A. O., & Oluwadare, S. A. (2017, October). Credit card fraud detection using machine learning techniques: A comparative analysis. In *2017 international conference on computing networking and informatics (ICCNi)* (pp. 1-9). IEEE. <https://doi.org/10.1109/ICCNi.2017.8123782>
49. Dirik, M., & Gül, M. (2021). Dynamic optimal ANFIS parameters tuning with particle swarm optimization. *Avrupa Bilim ve Teknoloji Dergisi*, (28), 1083-1092. <https://doi.org/10.31590/ejosat.1012888>
50. Lin, T. H., & Jiang, J. R. (2021). Credit card fraud detection with autoencoder and probabilistic random forest. *Mathematics*, 9(21), 2683. <https://doi.org/10.3390/math9212683>
51. Xie, Y., Zhu, C., Zhou, W., Li, Z., Liu, X., & Tu, M. (2018). Evaluation of machine learning methods for formation lithology identification: A comparison of tuning processes and model performances. *Journal of Petroleum Science and Engineering*, 160, 182-193. <https://doi.org/10.1016/j.petrol.2017.10.028>





Modeling of daily groundwater level using deep learning neural networks

Mohammed Moatasem Othman *¹ 

¹Atilim University, Department of Civil Engineering, Turkiye

Keywords

Artificial Intelligence
CNN-biLSTM
Groundwater
Neural Network

Research Article

DOI: 10.31127/tuje.1169908

Received: 01.09.2022

Revised: 05.10.2022

Accepted: 12.10.2022

Published: 27.02.2023



Abstract

Groundwater is an essential water source, becoming more vital due to shortages in available surface water resources. Hence, monitoring groundwater levels can show the amount of water available to extract and use for various purposes. However, the groundwater system is naturally complex, and we need models to simulate it. Therefore, we employed a deep learning model called CNN-biLSTM neural networks for modeling groundwater, and the data was obtained from USGS. The data included daily groundwater levels from 2002 to 2021, and the data was divided into 95% for training and 5% for testing. Besides, three deep CNN-biLSTM models were employed using three different algorithms (SGDM, ADAM, and RMSprop). Also, Bayesian optimization was used to optimize parameters such as the number of biLSTM layers and the number of biLSTM units. The model's performance was based on Spearman's Rank-Order Correlation (r), and the model with SGDM showed the best results compared to other models in this study. Finally, the CNN model with LSTM can simulate time series data effectively.

1. Introduction

Groundwater refers to the gravitational water in the more subordinate soil layer [1]. It is an essential provider of freshwater that can assist in solving problems related to the shortages in freshwater supplies. Therefore, frequent groundwater level monitoring is necessary for practical groundwater resource management [2] because precise and trustworthy groundwater level (GWL) predictions give fundamental details on groundwater availability [3]. Besides, the plunge in water levels implies that the resources are consumed significantly in some areas [4]. Thus, assessing the known groundwater resource in a more practical technique is required and developing the best consumption objectives [5].

The GWL is part of the natural groundwater system, which is exceptionally complicated. Therefore, there is a necessity for simplification in managing groundwater resources. A model, such as the groundwater model, is an approach that can be used to simulate and understand the natural groundwater system. Besides, modeling groundwater is meant to imitate the aquifer's physical

variables [5]. Thangarajan [5] showed that the groundwater models could be classified into physical, analog, and mathematical Models. Physical models were employed from the 1930s to the 1950s to analyze groundwater problems; for instance, the physical groundwater model called the sand tank model, a basic laboratory-scale standard with proper aquifer features, is scaled down to simulate the field conditions [5]. The mathematical model includes the exact details of the conceptual model but is described as controllable equations with analytical and numerical explanations [6-9]. The analog model considers a similarity between 1D groundwater steady flow expressed by Darcy's law and the constant flow of electrical waves by Ohm's law [9]. It is essential to mention that the details of these models are out of the scope of this study.

Various studies were employed broadly to study GWL using the literature mentioned above models (physical, analog, and mathematical models). Faulkner et al. [10] used a laboratory analog model to imitate groundwater flow and solute transport in an aquifer and showed that the analog model could provide the hydraulic head distribution. Gholami et al. [11]

* Corresponding Author

(memedosman471@gmail.com) ORCID ID 0000-0002-1717-8601

Cite this article

Othman, M. M. (2023). Modeling of daily groundwater level using deep learning neural networks. Turkish Journal of Engineering, 7(4), 331-337

constructed a laboratory approach to investigate the influence of the GWL change on internal air pressure. Boyraz et al. [12] performed analytical, experimental, and numerical solutions to describe the GWL distribution. Lee et al. [13] employed numerical and sandy tank models to study the increase of GWL due to underground obstructions in the coastal aquifer. They showed that the sandy tank experiment offered details of the hydraulic features of groundwater systems such as GWL in the coastal aquifer with an obstacle like a seawall. Xu et al. [14] conducted a sequence of laboratory experiments to examine the differences in GWL during dewatering. Kagabu et al. [15] designed a three-stage tank model to imitate GWL changes before the earthquake and then apply it to the same case for the post-earthquake duration. They showed that their model could represent GWL differences due to earthquake events. Ansarifar et al. [16] employed MODFLOW mathematical approach to simulate the groundwater level in a coastal aquifer. Akter and Ahmed [17] used MODFLOW 2005 mathematical model to study water level drawdown and groundwater modeling. They showed that mathematical models could show pertinent details and save money and time. Armanuos et al. [18] used MODFLOW to study the effects of the rising pumping on the GWL in the aquifer. Yang et al. [19] employed an analytical model to study the GWL over height varying with multi-tidal circumstances.

The improvement of soft computing applications such as artificial intelligence (AI) has recently encouraged researchers to adopt it to study various engineering problems [20-27]. One of the AI applications is deep learning (DL), as shown in Figure (1) [27], and is established on the algorithms created and inspired by the biological neuron system of humans to calculate or approximate functions by solving many inputs into a target output [28]. Besides, DL boosts computer technology to create outcomes established on the earlier known data [29-30]. DL has changed conventional industries and is increasingly employed in many scientific fields [31] and water resource engineering. For example, AI models were used to show the potential to handle investigations on relations between input and important system variables [32].

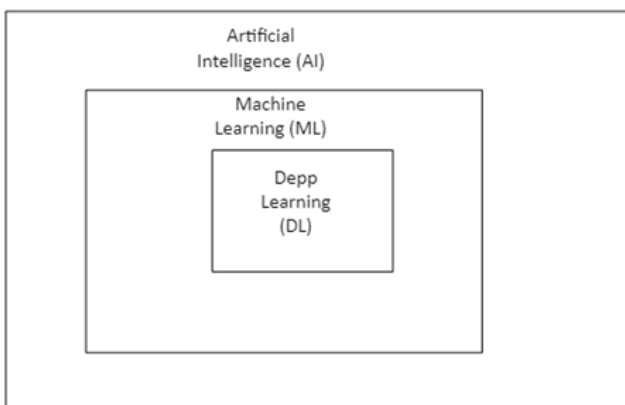


Figure 1. Artificial Intelligence models [27]

Moreover, Rajae et al. [33] reviewed 67 papers for applications of machine learning approaches such as artificial neural networks, adaptive neuro-fuzzy

inference systems, genetic programming, and support vector machine in GWL modeling from 2001 to 2018. They showed that artificial intelligence techniques could be employed to forecast the GWL time series in various aquifers. Nevertheless, the deep learning approaches grew slowly initially [31] but are to succeed in water resources engineering [32]. It is recommended to read published studies in the literature for more details on DL models, which can be found in [34-36].

Long short-term memory (LSTM) neural network is one of the deep learning applications, and it has been applied in various studies [37-40], and the employment of LSTM in GWL modeling is also increasing. Zhang et al. [41] created a two-layer LSTM model for forecasting GWL and trained the LSTM model with monthly water diversion, evaporation, precipitation, temperature, and time as input parameters. They showed that The LSTM offers a good performance for GWL simulating. Huang et al. [42] applied the LSTM model to estimate groundwater recharge according to GWL change. They compared the performance of the LSTM model with multi-layer perception (MLP) and linear regression models and found that LSTM demonstrated better results than the two models. Shin et al. [43] employed LSTM to forecast the GWL due to pumping wells in the locations close to observing wells. They showed that the GWL forecast by the LSTM model was extremely high. Vu et al. [44] used the LSTM model to rebuild GWL missed data of piezometers employed to observe water changes in a regional karstic aquifer. They showed that LSTM is proper for rebuilding the GWL changes with acceptable precision. Solgi et al. [45] employed LSTM to forecast GWL for short and long periods compared to a simple neural network. They showed that the LSTM exceeded the accurate GW level prediction of the simple neural network. Yokoo et al. [46] employed the LSTM model for GWL modeling and demonstrated that the model could simulate GWL in acceptable agreement with the measured data. Besides, a convolutional neural network (CNN) is another deep learning model used for various problems in civil engineering, such as groundwater problems. Ali et al. [47] one of few studies that used groundwater level as the only input for training the AI model, used a hybrid CNN-BI LSTM neural network to model hourly groundwater levels. They showed that CNN-biLSTM could handle modeling hourly groundwater levels, and this model can be used for time series data.

AI techniques have been utilized to emulate GWL by engaging data like rainfall, temperature, humidity, evaporation, and extraction rates. Nonetheless, few pieces of research were used to predict the groundwater level based on the measured groundwater level as the only input to the AI model [45]. Hence, this study aims to employ daily groundwater level data to train CNN-bi LSTM models with Bayesian optimization to simulate GWL using only the GWL time series data as input to the models. The first section of the article contains a brief introduction to recent studies of GWL using various modeling approaches. The second section shows the study area and the deep learning models. The third section illustrates the results. Finally, the discussion with recommendations for further study.

2. Method

2.1. Study Area

The daily groundwater data were collected from The United States Geological Survey (USGS) for a city called Camdenton, a municipality in the middle of Camden County, Missouri, USA. The data consist of groundwater daily measurements from Jan 2002 – Oct 2021, as shown in Figure 2. The total number of measures was 7242; 0.95% of data was selected for training the AI model, and 0.5% for testing the AI model.

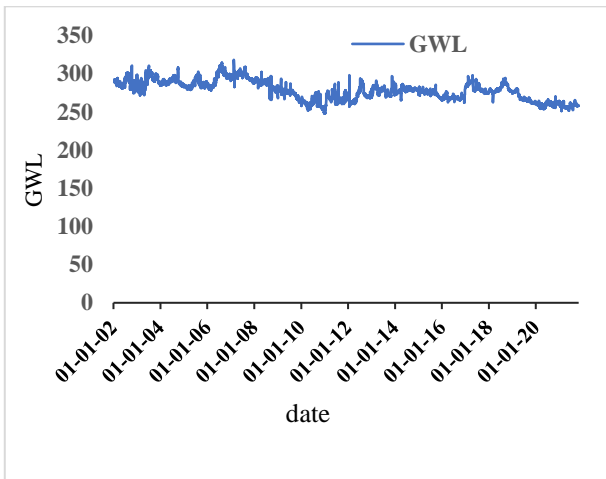


Figure 2. Daily groundwater measurements

2.2. CNN-biLSTM Model

Bidirectional -LSTM (BiLSTM) is a distinct network of the traditional long-term short-memory neural network (LSTM), which includes forward and backward LSTM, supplying entry to the long-range context in both directions. Furthermore, LSTM is developed to fix the vanishing gradients problem using a unique gating process [48]. Besides, biLSTMs improve the quantity of data attainable to the AI model (Chiu and Nichols, 2016). Thus, the biLSTM permits for incorporation of the prior and following data [49]. The traditional LSTM contains multiple memory cells or blocks. Memory blocks include many memory units and three gates. The first one, the input gate, seeks to determine the required latest data and convert it to the cell form. The second one, called forget gate, manages to extract the details that are not important anymore. In contrast, the output gate determines what type of essential details in the cell should be considered as the outcome [49].

As biLSTM is a particular type of recurrent neural network (RNN), it converts the different activations into dependent activations procedures by delivering all the neural network layers with the same weights and biases and specifying earlier outcomes to give the subsequent hidden layer as input. For illustration, in a precise RNN method, per iteration, t , the hidden layer endures a hidden form, h_t , updates and accelerates it based on the layer input, x_t , and earlier hidden form, h_{t-1} , employing the Equation 1 [50].

$$h_t = \sigma_h(Wx_t + Vh_{t-1} - b_h) \quad (1)$$

W is the weight matrix delivered via the input to the hidden layer, V is the weight matrix between two hidden serial states (h_{t-1} and h_t), b_h is the bias vector for the hidden layer, and σ_h is the activation function to generate the hidden structure. The model result can represent as Equation 2 [50]:

$$y_t = \sigma_y(Uh_t + b_y) \quad (2)$$

U is the weight matrix from the hidden converted to the output layer, and σ_y is the activation function of the result layer. Finally, the hidden layer supplies the outcome y_t . The LSTM layers procedure series data unidirectionally and modify it to capture the randomness. Nonetheless, a backward LSTM layer can deliver bidirectionally into the model. Thus, developing a Bi LSTM layer, including a forward LSTM layer and a backward LSTM layer, processes series data with two particular hidden layers and merges them into the same result layer [51].

Convolutional Neural Network (CNN) is a multi-layer artificial intelligence model founded on convolution calculation. CNN model has been widely used in numerous areas. It is presented by Y. LeCun et al. [52] and is a feed-forward neural network. CNN's local perception and weight sharing can remarkably reduce the parameters; thus, models can be executed to foretell time-series data. Besides, the typical CNN model provides a standard network configuration for the CNNs, primarily including convolutional layers, pooling layers, and fully connected layers, as shown in Figure 2. The mechanism of CNN is that each layer retains a majority of convolution kernels and pulls the data characteristic. Its calculation is as Equation (3):

$$l_t = \tanh(x_t * k_t + b_t) \quad (3)$$

Where l_t is the result value after convolution, \tanh is the activation function, x_t is the input vector, k_t is the weight of the convolution kernel, and b_t is the bias of the convolution kernel [53].

A CNN-biLSTM standard model, as illustrated in Figure 3, incorporates CNN layers that carry the characteristic from input data and biLSTMs layers to deliver sequel projections. It is employed for activity recognition. Their specific attributes utilize optical time series projection problems [54]. biLSTM with CNN layers has been used for encoding spatiotemporal elements for varied objectives, like precipitation estimation [55]. Still, the applications of CNN-biLSTM approaches in hydrology have not been exploited to unravel problems [56]. The component for both CNN and Bi LSTM models is presented in the publications extensively.

In this study, three CNN-biLSTM models were developed to model the daily groundwater level, and these models were optimized with Bayesian optimization to determine the best performance. Table 1 shows the hyperparameters parameters for the three models. The three models were trained with 350 epochs, 60 iterations, 32 batch sizes, and a factor for dropping rate equal to 0.5. Moreover, each model was trained with three different algorithms to update the weights, as shown in Table 2. The first model was trained with

stochastic gradient descent with momentum (SGDM), the second one with RMSprop, and the last one with root mean squared propagation (ADAM).

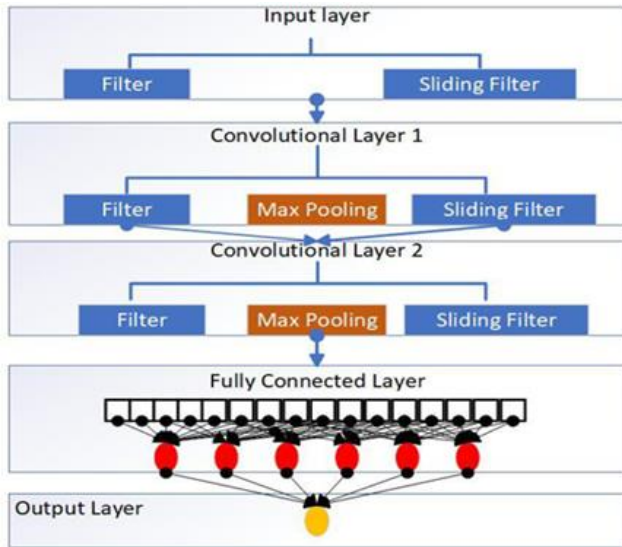


Figure 3. CNN model [57]

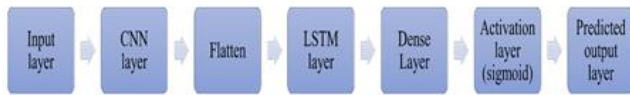


Figure 4. CNN-biLSTM model [57]

Besides, the performance of models was assessed based on Spearman's Rank-Order Correlation:

$$\rho = 1 - \frac{6 \sum d_i^2}{n(n^2 - 1)} \quad (4)$$

Where ρ is Spearman's rank correlation coefficient, is the distinction between the two classes per observation, and n is the number of data.

Table 1. Hyperparameters parameters

Number of LSTM Layer	1 to 4
Number of BI-LSTM Units	75 to 200
Learning Rate	0.001 to 1
L2Regularization Rate	0.0000000001 to 0.001

Table 2. CNN-biLSTM models

Model	Training algorithm
Model 1	SGDM
Model 2	RMSprop
Model 3	ADAM

3. Results

The results showed that the first model is the best among CNN-biLSTM models developed for modeling daily groundwater levels. Model 1 showed a high correlation coefficient (R) equal to 0.9896 for training

and 0.9633 for the testing stage, as illustrated in Figures 5 and 6. Furthermore, Bessie, Bayesian optimization showed the best parameters for training model 1, as shown in Table 3.

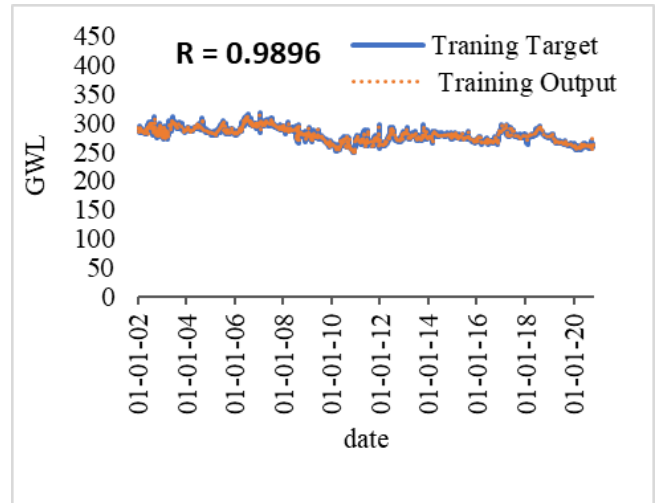


Figure 5. Training stage for model 1

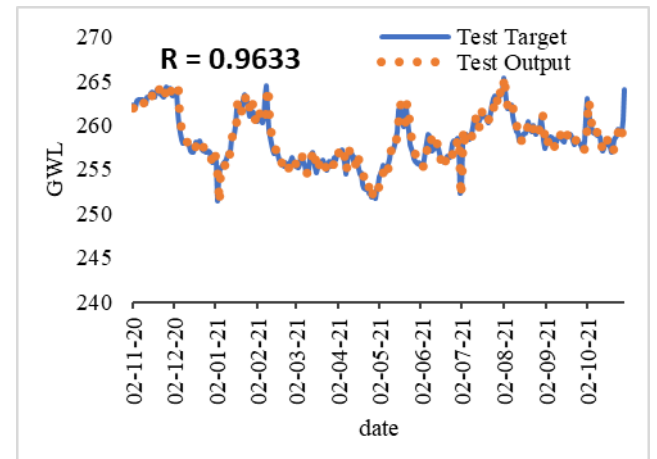


Figure 6. Testing stage for model 1

Table 3. Optimized parameters for model1

Number of BI-LSTM Layer	1
Number of BI-LSTM Units	171
Initial Learning Rate	0.021642
L2Regularization Rate	2.8×10^{-10}

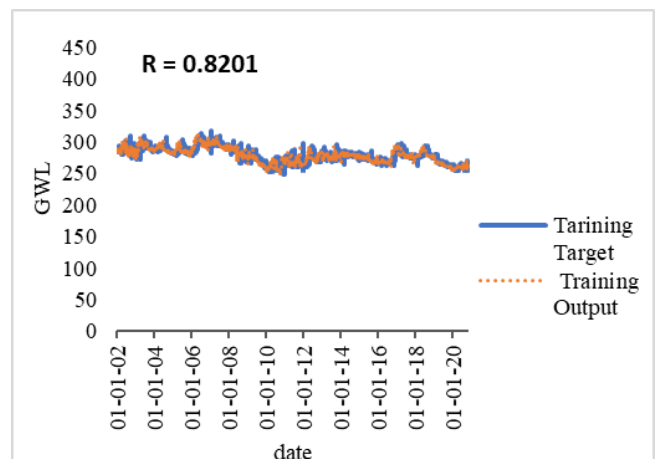


Figure 7. Training stage for model 2

Meanwhile, the second model showed a good correlation coefficient (R) equal to 0.8201 in the training stage but a better correlation in the testing stage equal to 0.9027, as shown in Figures 7 and 8. Besides, Table 4 shows the optimized parameter for model 2.

Finally, the last model, model 3, showed the worse performance, with a correlation coefficient (R) equal to 0.8128 in training and 0.8811 in testing stages, as shown in Figures 9 and 10, respectively. Besides, Table 5 shows the optimized parameter for model 3.

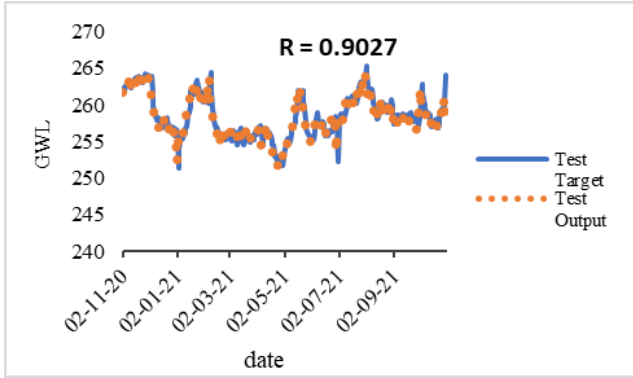


Figure 8. Testing stage for model 2

Table 4. Optimized parameters for model 2

Number of BI-LSTM Layer	2
Number of BI-LSTM Units	94
Initial Learning Rate	0.010901
L2Regularization Rate	$1.7 \times e^{-5}$

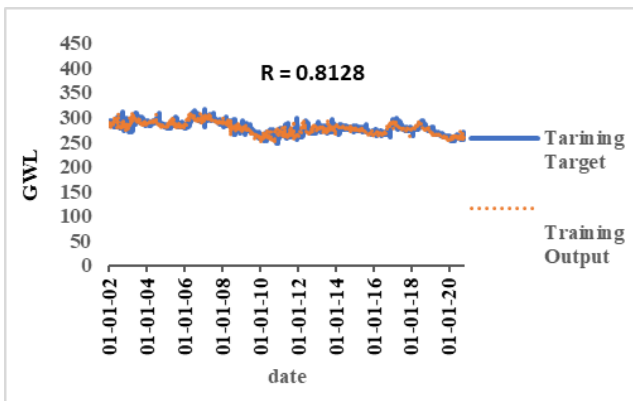


Figure 9. Training stage for model 3

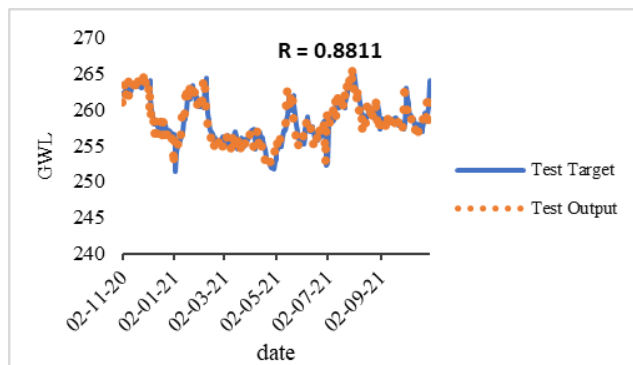


Figure 10. Testing stage for model 3

Table 5. Optimized parameters for model 3

Number of BI-LSTM Layer	2
Number of BI-LSTM Units	84
Initial Learning Rate	0.010009
L2Regularization Rate	0.00015

4. Conclusion

The groundwater level is a vital detail that can be influenced due to environmental divergence. For instance, an investigation of climate deviation shows that decreasing rainfalls and temperature growths lead to problems such as finding available water resources [50-60]. Besides, research on the groundwater level is critical for providing details on the availability of groundwater resources. Thus, a hybrid CNN-biLSTM was utilized, which integrates CNN and biLSTM networks. The results showed that the three models showed good outcomes based on the coefficient correlation (R), especially the model trained with the SGDM training algorithm. Besides, the CNN-bi LSTM showed it could handle time series data related to hydrology problems like modeling daily groundwater data. Finally, Bayesian optimization was employed to locate the most acceptable hyperparameter parameters, including the number of LSTM layers, the number of LSTM units, the learning rate, and the L2regularization rate. The limitation of the current study is that the model is trained with only daily groundwater level, and it is recommended that the model trained with monthly groundwater level to show the ability of model for simulating various time steps.

Conflicts of interest

The authors declare no conflicts of interest.

References

1. Ao, C., Zeng, W., Wu, L., Qian, L., Srivastava, A. K., & Gaiser, T. (2021). Time-delayed machine learning models for estimating groundwater depth in the Hetao Irrigation District, China. *Agricultural Water Management*, 255, 107032.
2. Taylor, C. J., & Alley, W. M. (2001). *Ground-water-level monitoring and the importance of long-term water-level data* (Vol. 1217). Denver, CO, USA: US Geological Survey.
3. Wunsch, A., Liesch, T., & Broda, S. (2020). Groundwater Level Forecasting with Artificial Neural Networks: A Comparison of LSTM, CNN and NARX. *Hydrology and Earth System Sciences Discussions*, 2020, 1-23.
4. Ebrahimi, S., & Khorram, M. (2021). Variability effect of hydrological regime on river quality pattern and its uncertainties: case study of Zarjoob River in Iran. *Journal of Hydroinformatics*, 23(5), 1146-1164.
5. Thangarajan, M. (2007). Groundwater models and their role in assessment and management of groundwater resources and pollution. In *groundwater* (pp. 189-236). Springer, Dordrecht.
6. Bear, J., Beljin, M. S., & Ross, R. R. (1992). *Fundamentals of groundwater modeling*. Ground-water issue (No. PB-92-232354/XAB; EPA-540/S-92/005). Environmental Protection Agency, Ada, OK (United States). Robert S. Kerr Environmental Research Lab.
7. Anderson, M. P., Woessner, W. W., & Hunt, R. J. (2015). Introduction. *Applied Groundwater Modeling*, 3-25. <https://doi.org/10.1016/b978-0-08-091638-5.00001-8>

8. Alasta, M. S., Ali, A. S. A., Ebrahimi, S., Ashiq, M. M., Dheyab, A. S., AlMasri, A., Alqatanani, A., & Khorram, M. Modeling of Local Scour Depth Around Bridge Pier Using FLOW 3D.
9. Prickett, T. A. (1975). Modeling techniques for groundwater evaluation. In *Advances in hydrosience* (Vol. 10, pp. 1-143). Elsevier.
10. Faulkner, J., Hu, B. X., Kish, S., & Hua, F. (2009). Laboratory analog and numerical study of groundwater flow and solute transport in a karst aquifer with conduit and matrix domains. *Journal of contaminant hydrology*, 110(1-2), 34-44.
11. Gholami, V. C. K. W., Chau, K. W., Fadaee, F., Torkaman, J., & Ghaffari, A. (2015). Modeling of groundwater level fluctuations using dendrochronology in alluvial aquifers. *Journal of hydrology*, 529, 1060-1069.
12. Boyraz, U., & Kazezyilmaz-Alhan, C. M. (2018). Solutions for groundwater flow with sloping stream boundary: analytical, numerical and experimental models. *Hydrology Research*, 49(4), 1120-1130.
13. Lee, W. D., Yoo, Y. J., Jeong, Y. M., & Hur, D. S. (2019). Experimental and numerical analysis on hydraulic characteristics of coastal aquifers with seawall. *Water*, 11(11), 2343.
14. Xu, Y. S., Yan, X. X., Shen, S. L., & Zhou, A. N. (2019). Experimental investigation on the blocking of groundwater seepage from a waterproof curtain during pumped dewatering in an excavation. *Hydrogeology Journal*, 27(7), 2659-2672.
15. Kagabu, M., Ide, K., Hosono, T., Nakagawa, K., & Shimada, J. (2020). Describing coseismic groundwater level rise using tank model in volcanic aquifers, Kumamoto, southern Japan. *Journal of Hydrology*, 582, 124464.
16. Ansarifar, M. M., Salarijazi, M., Ghorbani, K., & Kaboli, A. R. (2020). Simulation of groundwater level in a coastal aquifer. *Marine Georesources & Geotechnology*, 38(3), 257-265.
17. Akter, A., & Ahmed, S. (2021). Modeling of groundwater level changes in an urban area. *Sustainable Water Resources Management*, 7(1), 1-2018.
18. Armanuos, A., Ahmed, K., Shiru, M. S., & Jamei, M. (2021). Impact of Increasing Pumping Discharge on Groundwater Level in the Nile Delta Aquifer, Egypt. *Knowledge-Based Engineering and Sciences*, 2(2), 13-23.
19. Yang, M., Liu, H., & Meng, W. (2021). An analytical solution of the tide-induced groundwater table overheight under a three-dimensional kinematic boundary condition. *Journal of Hydrology*, 595, 125986.
20. Melesse, A. M., & Hanley, R. S. (2005). Artificial neural network application for multi-ecosystem carbon flux simulation. *Ecological Modelling*, 189(3-4), 305-314.
21. Ali, A. S. A., & Günal, M. (2021). Artificial neural network for estimation of local scour depth around bridge piers. *Archives of Hydro-Engineering and Environmental Mechanics*, 68(2), 87-101.
22. Pérez-Pérez, E. J., López-Estrada, F. R., Valencia-Palomo, G., Torres, L., Puig, V., & Mina-Antonio, J. D. (2021). Leak diagnosis in pipelines using a combined artificial neural network approach. *Control Engineering Practice*, 107, 104677.
23. Pan, L., Novák, L., Lehký, D., Novák, D., & Cao, M. (2021). Neural network ensemble-based sensitivity analysis in structural engineering: Comparison of selected methods and the influence of statistical correlation. *Computers & Structures*, 242, 106376.
24. Wu, D., & Wang, G. G. (2021). Causal artificial neural network and its applications in engineering design. *Engineering Applications of Artificial Intelligence*, 97, 104089.
25. Azari, B., Hassan, K., Pierce, J., & Ebrahimi, S. (2022). Evaluation of machine learning methods application in temperature prediction. *Transactions of Civil and Environmental Engineering*, 8, 1-12.
26. Kashani, A. R., Camp, C. V., Akhani, M., & Ebrahimi, S. (2022). Optimum design of combined footings using swarm intelligence-based algorithms. *Advances in Engineering Software*, 169, 103140.
27. Ali, A. S. A. (2021). Republic of Turkey Gaziantep University Graduate School of Natural & Applied Sciences.
28. Bengio, Y., Goodfellow, I., & Courville, A. (2017). *Deep learning* (Vol. 1). Massachusetts, USA: MIT press.
29. Goh, G. B., Hodas, N. O., & Vishnu, A. (2017). Deep learning for computational chemistry. *Journal of Computational Chemistry*, 38(16), 1291-1307. <https://doi.org/10.1002/jcc.24764>.
30. Bashar, A. (2019). Survey on evolving deep learning neural network architectures. *Journal of Artificial Intelligence*, 1(02), 73-82.
31. Shreyas, N., Venkatraman, M., Malini, S., & Chandrakala, S. (2020). Trends of sound event recognition in audio surveillance: a recent review and study. *The Cognitive Approach in Cloud Computing and Internet of Things Technologies for Surveillance Tracking Systems*, 95-106.
32. Shen, C. (2018). A transdisciplinary review of deep learning research and its relevance for water resources scientists. *Water Resources Research*, 54(11), 8558-8593.
33. Wunsch, A., Liesch, T., & Broda, S. (2021). Groundwater level forecasting with artificial neural networks: a comparison of long short-term memory (LSTM), convolutional neural networks (CNNs), and non-linear autoregressive networks with exogenous input (NARX). *Hydrology and Earth System Sciences*, 25(3), 1671-1687.
34. Rajaei, T., Ebrahimi, H., & Nourani, V. (2019). A review of the artificial intelligence methods in groundwater level modeling. *Journal of hydrology*, 572, 336-351.
35. Schmidhuber, J. (2015). Deep learning in neural networks: An overview. *Neural Networks*, 61, 85-117. <https://doi.org/10.1016/j.neunet.2014.09.003>.
36. Samudrala, S. (2019). *Machine Intelligence: Demystifying Machine Learning, Neural Networks and Deep Learning*. Notion Press.

37. Goodfellow, I., Bengio, Y., & Courville, A. (2016). *Deep learning*. MIT press.
38. Sahoo, B. B., Jha, R., Singh, A., & Kumar, D. (2019). Long short-term memory (LSTM) recurrent neural network for low-flow hydrological time series forecasting. *Acta Geophysica*, 67(5), 1471-1481.
39. Lees, T., Buechel, M., Anderson, B., Slater, L., Reece, S., Coxon, G., & Dadson, S. J. (2021). Benchmarking Data-Driven Rainfall-Runoff Models in Great Britain: A comparison of LSTM-based models with four lumped conceptual models. *Hydrology and Earth System Sciences*.
40. Ayzel, G., Kurochkina, L., Abramov, D., & Zhuravlev, S. (2021). Development of a Regional Gridded Runoff Dataset Using Long Short-Term Memory (LSTM) Networks. *Hydrology*, 8(1), 6.
41. Heindel, L., Hantschke, P., & Kästner, M. (2021). A Virtual Sensing approach for approximating nonlinear dynamical systems using LSTM networks. *PAMM*, 21(1), e202100119.
42. Zhang, J., Zhu, Y., Zhang, X., Ye, M., & Yang, J. (2018). Developing a Long Short-Term Memory (LSTM) based model for predicting water table depth in agricultural areas. *Journal of hydrology*, 561, 918-929.
43. Huang, X., Gao, L., Crosbie, R. S., Zhang, N., Fu, G., & Doble, R. (2019). Groundwater recharge prediction using linear regression, multi-layer perception network, and deep learning. *Water*, 11(9), 1879.
44. Shin, M. J., Moon, S. H., Kang, K. G., Moon, D. C., & Koh, H. J. (2020). Analysis of Groundwater Level Variations Caused by the Changes in Groundwater Withdrawals Using Long Short-Term Memory Network. *Hydrology*, 7(3), 64.
45. Vu, M. T., Jardani, A., Massei, N., & Fournier, M. (2021). Reconstruction of missing groundwater level data by using Long Short-Term Memory (LSTM) deep neural network. *Journal of Hydrology*, 597, 125776.
46. Solgi, R., Loaiciga, H. A., & Kram, M. (2021). Long short-term memory neural network (LSTM-NN) for aquifer level time series forecasting using in-situ piezometric observations. *Journal of Hydrology*, 601, 126800.
47. Yokoo, K., Ishida, K., Nagasato, T., Kawagoshi, Y., & Ito, H. (2021, October). Reconstruction of groundwater level at Kumamoto, Japan by means of deep learning to evaluate its increase by the 2016 earthquake. In *IOP Conference Series: Earth and Environmental Science* (Vol. 851, No. 1, p. 012032). IOP Publishing
48. Ali, A. S. A., Ebrahimi, S., Ashiq, M. M., Alasta, M. S., & Azari, B. (2022). CNN-Bi LSTM neural network for simulating groundwater level. *CRPASE: Transactions of Civil and Environmental Engineering*, 8, 1-7.
49. Guo, X. (2020, November). Prediction of taxi demand based on CNN-BiLSTM-attention neural network. In *International Conference on Neural Information Processing* (pp. 331-342). Springer, Cham.
50. Tao, Y., Sun, H., & Cai, Y. (2022). Predictions of Deep Excavation Responses Considering Model Uncertainty: Integrating BiLSTM Neural Networks with Bayesian Updating. *International Journal of Geomechanics*, 22(1), 04021250.
51. Dey, S., Dey, A. K., & Mall, R. K. (2021). Modeling long-term groundwater levels by exploring deep bidirectional long short-term memory using hydro-climatic data. *Water Resources Management*, 35(10), 3395-3410.
52. Cui, Z., Ke, R., Pu, Z., & Wang, Y. (2018). Deep bidirectional and unidirectional LSTM recurrent neural network for network-wide traffic speed prediction. *arXiv preprint arXiv:1801.02143*.
53. LeCun, Y., Bottou, L., Bengio, Y., & Haffner, P. (1998). Gradient-based learning applied to document recognition. *Proceedings of the IEEE*, 86(11), 2278-2324.
54. Lu, W., Li, J., Wang, J., & Qin, L. (2021). A CNN-BiLSTM-AM method for stock price prediction. *Neural Computing and Applications*, 33(10), 4741-4753.
55. Donahue, J., Anne Hendricks, L., Guadarrama, S., Rohrbach, M., Venugopalan, S., Saenko, K., & Darrell, T. (2015). Long-term recurrent convolutional networks for visual recognition and description. In *Proceedings of the IEEE conference on computer vision and pattern recognition* (pp. 2625-2634).
56. Shi, X., Chen, Z., Wang, H., Yeung, D. Y., Wong, W. K., & Woo, W. C. (2015). Convolutional LSTM network: A machine learning approach for precipitation nowcasting. *Advances in neural information processing systems*, 28.
57. Anderson, S., & Radic, V. (2021). Evaluation and interpretation of convolutional-recurrent networks for regional hydrological modelling. *Hydrology and Earth System Sciences*. <https://doi.org/10.5194/hess-2021-113>, in review.
58. Yerima, S. Y., Alzaylae, M. K., & Shajan, A. (2021). Deep learning techniques for android botnet detection. *Electronics*, 10(4), 519
59. Azizi, K., Kashani, A. R., Ebrahimi, S., & Jazaei, F. (2022). Application of a multi-objective optimization model for the design of piano key weirs with a fixed dam height. *Canadian Journal of Civil Engineering*, (ja).
60. Ashiq, M. M., Jazaei, F., Ali, A. S., & Bakhshae, A. (2022, December). Investigation and Identification of the Microplastics Presence in the Soil. In *Fall Meeting 2022. AGU*.





Bentonite and polymeric support fluids used for stabilization in excavations

Muhammad Shahbaz Akhtar *¹ 

¹Forman Christian College (A Chartered University), Department of Environmental Sciences, Lahore, Pakistan

Keywords

Bentonite
Excavation support fluids
Natural & synthetic polymers
Partially hydrolyzed
Polyacrylamides (PHAPS)

Review Article

DOI: 10.31127/tuje.1118896

Received: 19.05.2022

Revised: 10.09.2022

Accepted: 14.09.2022

Published: 01.03.2023



Abstract

Bentonite is a natural and finite mineral resource. Dilute suspensions of sodium montmorillonite clay in water represents bentonite slurries. Suspension and orientation of colloidal clay particles define rheological properties in bentonite slurry (BS). The BS has been used about seventy years to temporarily support the excavations. More recently, polymer support fluids (PSF) gained much popularity and are widely used compared to bentonite support fluids. The PSF are categorized into natural (pure) and synthetic polymers. Physico-chemical properties of PSF are different than BS irrespective of the quite similarity in the mode of action. Synthetic polymer fluids are molecularly engineered fluids that can be a popular alternative of conventional BS deployed as excavation support fluids in different foundation applications such as diaphragm wall panels and pile bores. The synthetically engineered fluids of polymers (water-soluble) are different from conventional BS. The PSF offer additional benefits because their use is cost effective, eco-friendly, and these polymers need smaller site footprint as well as easy preparation, mixing, handling, management and ultimately the final disposal. Nevertheless, synthetic polymers have advantage over bentonite, however, foundation engineers and scientists have also certain concerns about their use because of their performance related issues. For an efficient use of polymers, specific properties and *in situ* behavior of polymers as well as their sorption onto the soils must be recognized because the polymer concentration in the solution is decreased with time during their use. The present manuscript reviewed the relative performance of excavation support fluids and displayed an arranged marriage of physicochemical and rheological properties of natural and synthetic excavation support fluids used in the foundation industry. This information will be highly useful to scientific community for their future ventures and will lay a foundation to understand the mechanisms of stabilization in open and deep excavations.

1. Introduction

Support fluids (sometimes termed as muds or slurries) are referred to the resultant compounds of admixture of manufactured materials and water and that support the sides of open and deep excavations prior to filling of these excavations. Supporting fluids are generally based on bentonite clay (BC), natural or synthetically produced polymers or blending of both bentonite and polymers. Use of excavation support fluids (ESF) in diverse geotechnical and civil engineering operations such as drilling, piling, tunneling (slurry), diaphragm walling, and investigation boreholes (drilling) for stabilizing the excavation until the installment of a permanent element (e.g., liming,

concrete etc.) is a common practice in many countries of the world [1].

Bentonite denotes the clays having characteristics of swelling and gel formation upon hydration and dispersion in water. The name 'bentonite' was denoted to such clay (natural sodium bentonite in nature) after its discovery in the 19th century near Fort Benton, USA [2]. Since the trendsetting results reported by Veder [3], bentonite support fluids (BSF) such as bentonite clay (BC) has been widely used for supporting side walls of excavations in permeable and unstable strata prior to concreting while constructing board piles and diaphragm walls [4-5]. Due to distinctive bentonite characteristics (better expansion on hydration, high viscosity, and ability for gel-slurry formation), the BC

* Corresponding Author

^{*}(lithosoil@gmail.com) ORCID ID 0000-0001-5495-1934

Cite this article

Akhtar, M. S. (2023). Bentonite and polymeric support fluids used for stabilization in excavations. Turkish Journal of Engineering, 7(4), 338-348

(e.g., aluminum silicate clay) is commonly applied for making drilling fluid in mud rotary drilling process of water wells. During well development, use of low-quality BC can clog the aquifer due to formation of thick wall cake that can be difficult to remove compared to the wall cake formed by high quality bentonite because such cake can be easily removed.

Similarly, polymer support fluids (PSF) have also gained tremendous success in the foundation industry since their use form early 1990s [6]. Polymers can be categorized as naturally occurring polymers and synthetically produced polymers. Natural polymers are naturally the derived products whereas synthetic polymers are the blending products of different polymers. These polymer fluids are more ecological and operational friendly due to their easy mixing, easy handling, and low cost compared to BSF [1, 7-9]. Nevertheless, polymer use is associated with pile bore stability and soft toe risk at the pile base due to less particle holding capacity and fast settling compared to BC

[10]. Although, both bentonite (mineral) and polymer (synthetic) slurry function in almost similar mode/fashion and same testing procedures such as pH, viscosity, density, and sand contents are applicable on both ESF, however, synthetic slurries have advantage due to lack of gel strength. Although, both fluids function in a similar way by exerting a hydrostatic pressure on the excavation side walls to ensure its stability; however, their composition and characteristics are quite different. The present manuscript will review the excavation support fluids used in civil and geotechnical applications and will provide valuable information to the engineers and scientist community working in the foundation industry.

2. Types of excavation support fluids

Two types of excavation support fluids are commonly used in many applications. Figure 1 depicts these two types of supporting fluids used in excavations.

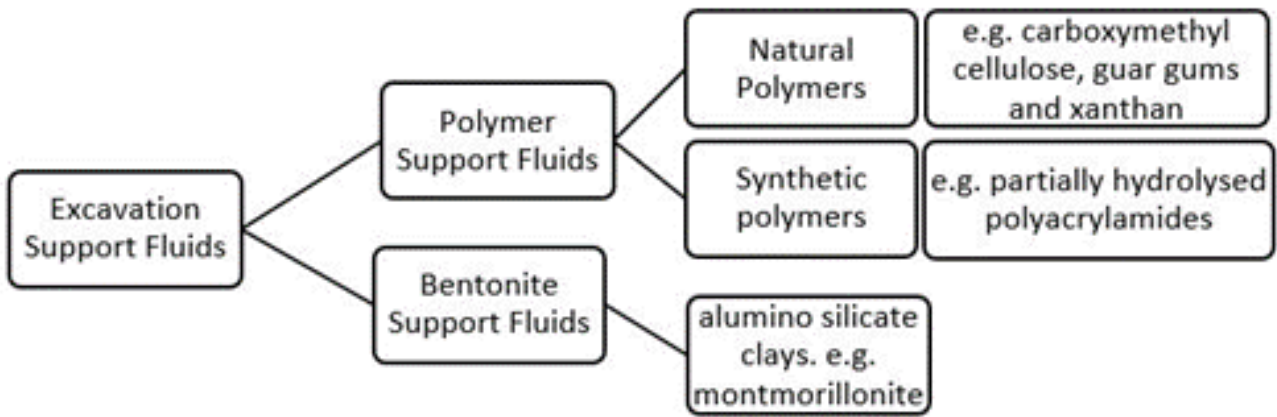


Figure 1. Types of excavation support fluids used in different operations

2.1. Bentonite support fluids

The BSF are broadly used in different engineering applications such as (i) panel excavations sides for diaphragm walls are supported by producing a barrier or a filter cake (FC) on the sides to avoid/prevent fluid loss into the ground, and by providing a surface mat to resist external pressures, (ii) for constructing large diameter bored piles, (iii) for making boreholes of small diameter for site

Investigation activities in unstable strata, (iv) for constructing cut-off walls below ground to generate barriers to groundwater. Bentonite slurry (BS) has been used for more than six to seven decades to support the excavations temporarily such as bored piles and diaphragm walls.

The excavation concept by deploying BS to form a continuous structural wall was advanced by Veder [11-12] in well drilling by using supporting muds known from earlier times [1]. Hajnal et al. [13] reported that relatively smooth diaphragm walls were obtained in 1950 and concrete diaphragm wall concept was established by the late 1950s. In earlier applications, excavation support was carried out by the fluids of clay nature, particularly montmorillonite (bentonite) clay of

swelling form enriched with high sodium (Na). Types of silicates and bentonites are represented in Figure 2. The BC is a special clay originating from weathered ash that can swell approximately ten times higher than its original volume upon complete mixing with water or when fully hydrated.

Most bentonites available on commercial scale are hydrated alumino silicates containing the predominant mineral montmorillonite i.e., derived from a clay type discovered near Montmorillon in France. Most common types of bentonites include (i) natural Na-bentonite, (ii) natural Ca-bentonite, (iii) Na-activated bentonite. The cation exchange capacity (CEC) of these bentonites is much higher than other clays e.g., ball clays, china clay, and attapulgite. Although expensive, natural Na-bentonite has high swelling capacity than natural Ca-bentonite. To overcome the cost factor, with similar characteristics of Na-bentonite, Na-activated bentonite is produced by replacing Ca ions with Na ions in natural Ca-bentonite with the addition of soluble Na₂CO₃. Today, Na-activated bentonites are widely used in foundation industry. Nevertheless, in case of bentonite applications, large ancillary plant is needed for different process steps such as mixing, cleaning etc.

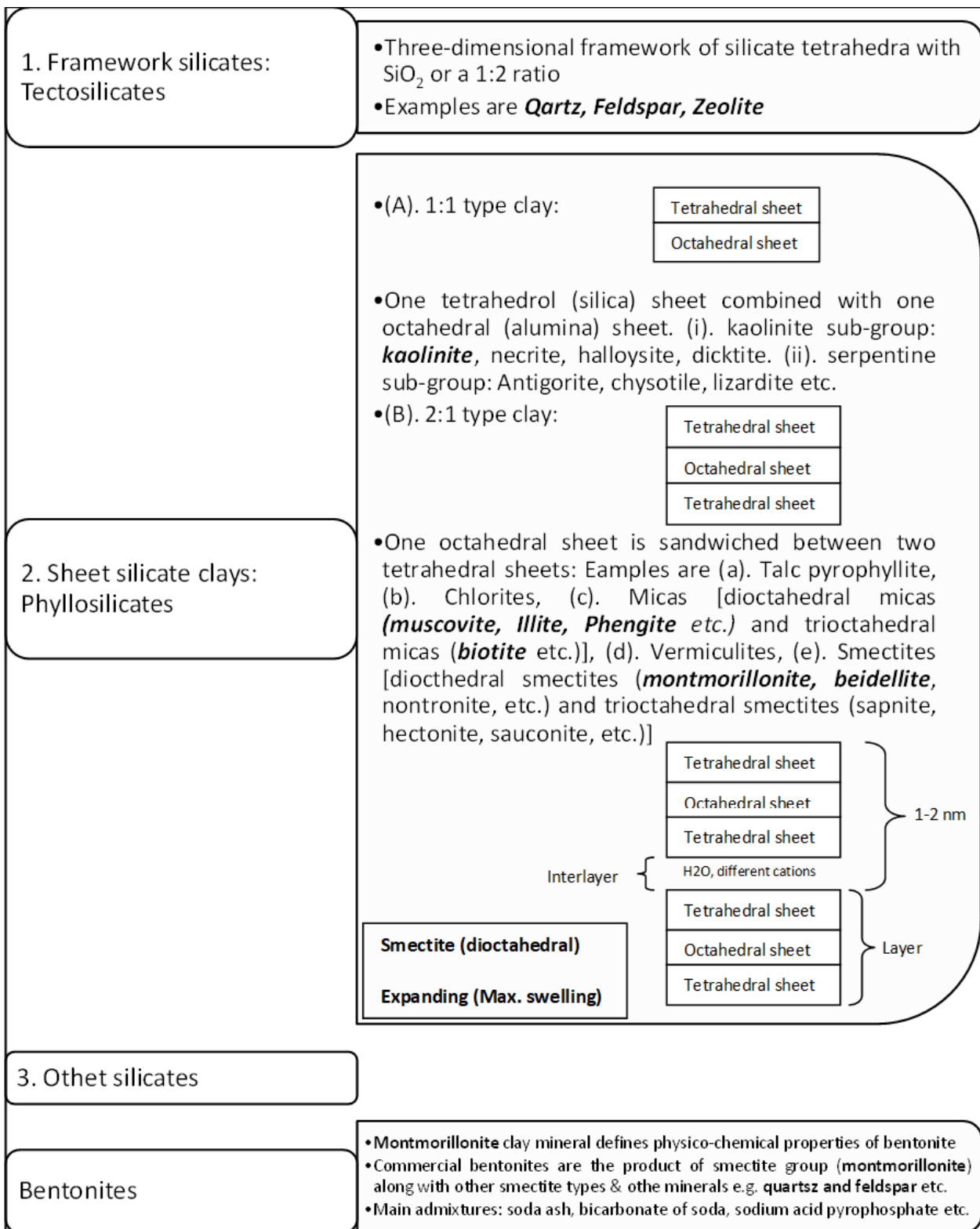


Figure 2. Types of silicates and bentonites

2.2. Polymer support fluids

With the passage of time, polymer modification of bentonites has been emerged to meet the requirements of geotechnical and civil engineering industry and many bentonites that are significantly polymer modified are available today. With polymer modification, properties of moderately active bentonites can be developed to use in excavation supports and with high rheological properties

(e.g., viscosity and gel). Addition of polymers to BC can be carried out during their production or at the time of their use. Polymer addition to bentonite at the time of using the polymer/bentonite system should be done by keeping in view the slurry formulations; otherwise, their effectiveness is questionable. Imprudent mixing of bentonite/polymer in the field does not give the desired results. Furthermore, for effective use of these polymers, their use is warranted with specification as well as with

an expert’s advice. Polymer fluids have advantages in terms of smaller site footprint, easy mixing of fluids, and better concrete-sand interface resistance [5, 7, 14].

2.2.1. Natural polymers and natural modified polymers

Earlier used polymers are termed as pure polymers that are naturally derived products e.g., guar gums, hydroxypropyl guar (HPG- gum derivatives), xanthan gum (additive), carboxymethyl cellulose (CMC), polyanionic cellulose (PAC) lignite, hydroxyethylcellulose (HEC) [1, 15-20]. The CMC in the form of its Na salt is used to modify the rheological properties of aqueous liquids. Natural polymers were used sporadically since four to five decades. These pure polymers were used alone or in combination with bentonite and/or natural clay dispersed into the slurry from the excavated formation. As natural polymers are biodegradable, therefore, their use is limited only to those processes/operations in the construction industry where biodegradation is desirable such as in permeable reactive barriers and deep drainage trenches [21]. Due to biodegradable nature of naturally derived polymers, these materials should be used generally with biocide. In addition, dispersion of fine clays (clays into excavation) is not inhibited by natural polymers like bentonite, thus, necessary cleaning is required prior to their re-use.

2.2.2. Synthetic polymers

Advanced development of fluid systems has been achieved with the invention of synthetic polymers by blending of different types of polymers. Many synthetic polymers used in the construction or foundation and geotechnical industry are simply partially hydrolyzed

polyacrylamides (PHPAs). The PHPAs bring the breakthrough in deep foundation construction industry in the early 1990s. Earlier, PHPAs have been used in oil and gas industry as bentonite additives for inhibition of swelling of water-sensitive shales and reduction of fluid loss in permeable formations [22-24]. The PHPAs fluids gain popularity by replacing BS in civil engineering due to less site requirement for fluid management and easy and readily operation of excavation. The PHPAs are water soluble synthetic polymers of high molecular weight typically between 12 and 17 million g/mol [25] with negatively charged molecules and can form non-Newtonian solution when dissolved in water [24]. The density of these high-molecular-weight polymers is almost similar to water, but their viscosity is much higher than water. Unlike bentonite, these polymer fluids are gel less when these fluids are not disturbed (nonthixotropic), display low yield stress and high viscosity (10^5 MPa · s) when shear rates are low [24, 26]. If proper slurry management is done, then synthetic polymers can be repeatedly reused till the completion of the operation. Nevertheless, the addition of fresh polymer is required because the polymer concentration is decreased with time due to their potential sorption onto soil surfaces. Due to resistant nature of synthetic polymers to biodegradation, these materials can be used without biocide [1].

3. Testing protocols for support fluids

Properties of support fluids are interdependent and require a range of tests rather than a single test. Serial simple tests reflecting the rheological properties are conducted because on site rheological properties are rarely measured. Different support fluids are listed in Table 1.

Table 1. Testing protocols for supporting fluids

Parameter	Unit/Basis	Instrument /Protocol
Density (ρ)	g/ml	Mud balance or protocol for precision weighing
Sand content	% vol.	Protocol for sand content measurement
Rheological characteristics-	s/qt	Fann viscometer (hand cranked and electrically driven viscometers), flow cones-Marsh funnel
Viscosity		Shearometer
Gel strength	lb/100 ft ² (N/m ²)	pH meters or litmus or pH papers
pH		American Petroleum Institute standard fluid loss protocol
Filtration/fluid loss	ml after 0.5 hr	American Petroleum Institute standard fluid loss protocol
Thickness of filter cake	mm after 0.5 hr	

4. Formation of bentonite slurry and its reuse

Figure 3 represents the layout of BSF in terms of bentonite types, slurry formation, characteristics, functions, and reuse of BS. The BS is prepared from bentonite powder by achieving maximum hydration. The use of salt water or water containing Ca or Mg should be avoided otherwise the desired dispersion will be inhibited. However, the Ca can be removed as a precipitate of CaCO₃ by using an appropriate amount of Na₂CO₃, and Mg can be removed with an alkali such as NaOH. The amount of bentonite powder to make slurry depends on the bentonite quality and desired viscosity of the slurry. Generally, concentrations between 4 to 6% on weight basis are used in many applications [2]. Swelling

of bentonite particles takes place by absorbing water after dispersion phenomenon. Viscosity and gel strength of the slurry is linearly related to the mixing and agitation. The slurry should be stored at least 12 hours prior to its use; however, it can be immediately used even after mixing if the properties are suitable for its use. Important parameters need to be tested for BS includes rheology, density, sand contents, pH, and segregation processes of slurry such as filtrate loss (fluid loss), settlement, bleed (separation of water from solids) and syneresis.

By careful monitoring and controlling the characteristics of BS, it can be reused. Whatever system of the excavation is used, loss of slurry will be occurred. The lost slurry should be replaced and blended with fresh

slurry. Accumulation of clay and silt sized particles can increase the density and Marsh viscosity (measured viscosity with marsh funnel). The pH of slurry can be changed due to contamination with cement, acids, or acidic groundwater. To adjust the properties, bentonite powder can be added to the slurry or admixtures and pH can be readjusted by the addition of NaHCO_3 (if pH ↓) or Na_2CO_3 (if pH ↑), viscosity and flocculation can be

corrected by organic thinners or polyphosphates, and fluid loss can be reduced by using CMC. At completion of the operation, the BS can be disposed of safely in an appropriate landfill because bentonite is a non-hazardous waste. Nevertheless, care should be taken into account so that BS should not be released into an aquatic environment, otherwise, it could be highly polluting for aquatic biodiversity.

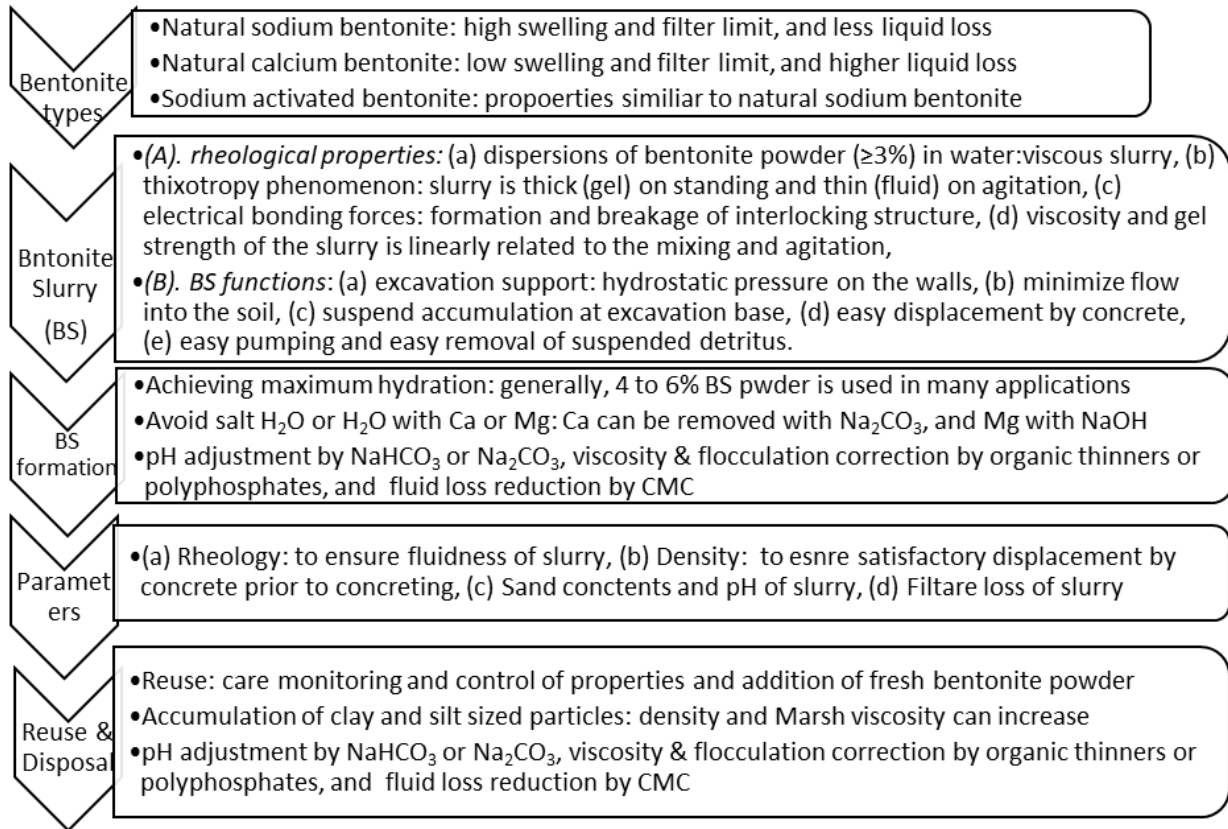


Figure 3. Bentonite support fluids: bentonite types, slurry formation, characteristics, functions, and reuse of BS

Formation of a filter cake (FC) on the side walls as a stabilizing mechanism in permeable soils (gravel and sand) is a well-documented phenomenon in pertinent literature. For stability of coarse unconsolidated soils, the slurry induced hydrostatic pressure is applied against a barrier/membrane created by the slurry [27]. The slurry penetration into ground until the gel strength of the slurry acting over the penetrated area of soil particles is enough to prevent further slurry penetration that can be ascribed to FC assisted by rheological blocking [5]. Bentonite slurries should have characteristics to perform functions such as (a) exert hydrostatic pressure on the walls to support the excavation, (b) minimize flow into the soil, (c) suspend accumulation at the base of excavation (d) easy displacement by concrete, (e) easy pumping and easy removal of suspended detritus. In permeable soils, formation of BFC with bentonite slurry is important for stabilizing the excavation because bentonite platelets create viscosity and gel strength and shingle off to form BFC. Low permeability of BFC results in the reduction of fluid loss into the ground and stabilizes the excavation by

providing a membrane/barrier against the applied hydrostatic slurry pressure [28].

The rheological properties of bentonites define their fitness for use in different engineering applications. Upon dispersion in water, natural Na bentonite and Na-activated bentonite formed minute plate-like particles with positive charges on the surfaces and negative charges on the edges. Dispersion of bentonite powder ($\geq 3\%$) in water results in the formation of viscous slurry displaying thixotropic phenomenon (i.e., slurry is thick on standing and thin on agitation) due to plate like particle orientation in the slurry. Formation and breakage of interlocking structure due to electrical bonding forces results in the formation of gel from slurry (on standing) and fluid from slurry (on agitation), respectively [2]. Nevertheless, constant buildup of BFC with time can be a concern in terms of skin friction and load bearing capacity of the shaft.

In BS, bentonite concentration generally ranges between 2.5 to 5% on weight basis with fluid density ranges between 1.014 and 1.028 g/cm^3 , while the concentrations of synthetic polymers in mix water ranges between 0.05 to 0.2% on weight basis with ρ

(density) of a clean polymer fluid is effectively the same as that of water because of low polymer concentration used [1, 5]. Contrarily, long molecular chains in synthetic slurry produce viscosity in water with little to no gel strength and gel membranes are created in and near borehole pores [27]. Solid surfaces absorb the segments of long molecular chains and chemical net is created due to bridge formation across the soil's grains. Highly viscous solution is produced by synthetic polymers (mainly PHAPs) due to the interaction of molecules of high molecular weight having functional side groups with ionic charges through hydrodynamic and electrostatic forces that bind soil particles. However, molecular induced viscosity is sensitive to different external influencing factors such as ground contaminants, shearing of pumping, and *in situ* physico-chemical interactions [9, 29-31]. Synthetic slurry gel membrane is broken easily with high alkalinity and CaCO₃ contents of cement [27]. Cement can displace synthetic slurry in the shaft and slurry can be pumped for reuse after proper testing.

5. Rheological characteristics of PHPAS polymer support fluids (PSF)

Rheological properties of BSF are reported in pertinent literature [32-34], but Rheological properties of PSF are scarcely documented [24]. The rheological characteristics of PSF might also affect the fluid loss from the excavation and influence its stability. Although, the mode of action of both supporting fluids (i.e., BSF and PSF) is quite similar and both fluids exert pressure for stabilization against the side walls and base of the excavating structure, however, they display differential impacts on the excavating structure and completed foundation element primarily due to their differential rheological properties. During excavation, BS forms a FC layer on soil surface that is exposed while PSF do not form a FC layer, rather than PSF fluids flow continuously into surrounding soil formations because of pressure head difference of >15 kPa between groundwater and the surrounding soil formations [24, 26]. The fluid flow rate is dependent on PSF shear viscosity [35]. Because soil particles settling velocity in fluid depends on viscosity and elasticity, therefore, reasonable amount of detritus accumulation takes place at the basal part of excavation or at the upper (top) part of fresh concretion as it is termed into the hole [36-37]. Sedimentation of soil particles occurs in creeping flow regime (Reynolds number, $R < 1$) without influencing by fluid elasticity in agreeing with [38] who also reported no effect of fluid elasticity on the particle drag when Deborah number (De) < 0.1. The De number defines the ratio between fluid's characteristic time of and process's characteristic time. For steady state flows, $De = 0$. Although, settling of the large sized particles occurs with high R and De numbers and fluid elasticity has an influence on the dragging force that tends to increase it. Nevertheless, settling process of the large sized particles is fast and the sediment removal is easier prior to concretion. Therefore, in case of soil sedimentation process, steady state viscosity is more important than the fluid transient

viscoelasticity. Lam et al., [24] also investigated these parameters (steady shear viscosity and transient viscoelasticity) of a PSF by performing serial oscillatory tests and reported that the viscoelastic characteristics of PSF are quite different from the counterpart BSF. These authors reported that PSF used in construction showed non-Newtonian activity at shear rates relevant to the construction work and recommended that the obtained results are useful to investigate the related issues during excavation such as sedimentation of particles in fluids and soil liquefaction mitigation.

6. Wise use and misuse of polymers: advantages and drawbacks

Advantages/benefits through proper use and failures/drawbacks through abuse of polymers are depicted in Figure 4. Polymer use within the specification of manufacturers and suppliers gives the satisfactory results. Polymers display their full effectiveness if they use within specifications and as per instructions of the expert's advice. Furthermore, in case of bentonite/polymer mixture use, imprudent mixing or injudicious use in the field does give satisfactory results.

7. Polymer chemistry: sorption mechanisms, flipping effect, and residual concentrations

Generally, the world polymer refers to molecules with repeating structural units such as rubber, plastics, DNA etc. In foundation industry, polymer is used for synthetic polymers commonly known as partially hydrolyzed polyacrylamides (PHPAs) (repeating units of acrylamides and acrylates belonging to family of acrylamide copolymers) or their derivatives [25]. The general formula of PHPAs is $[-(\text{CH}_2\text{CHCONH}_2)_x - (\text{CH}_2\text{CHCOOH})_y -]_n$, where, subscript x = proportion of the acrylamide, subscript y = proportion of acrylic acid, and n = number of repeating units in a polymer molecule. In addition, certain additives are also used to improve the functions of the system such as fast settling of suspended soil particles, control of fluid loss, and fluid weighting for enhancing stability of the excavation. Fluid loss additives or modified additives resistant to high temperature such as 2-acrylamido-2-methylpropane sulfonic acid (AMPS) multi-copolymers are preferable choice in drilling fluid deployed for deep foundations (e.g., oil and gas exploration) because they contain more aromatic units in their structure [39-42]. Different aromatic polymers available as commercial polymers include polyesters, aromatic polyamides, heterocyclic polymers, polyimides, polysulfones [43-46]. Furthermore, synthetic polymers as fluid loss additives can improve interaction between polymer and bentonite via adsorption group ($-\text{CONH}_2$, $-\text{SiOH}$, $-\text{OH}$, other cationic groups) and can enhance dispersive properties of bentonite via hydration groups ($-\text{COO}^-$ and $-\text{SO}_3^-$) [47-48]. Traditionally, PHPAs have been effectively used in different applications such as drilling of oil well, stabilization of soil for erosion control and treatment of water. Recently, these are also effectively deployed in geoenvironmental and geotechnical applications.

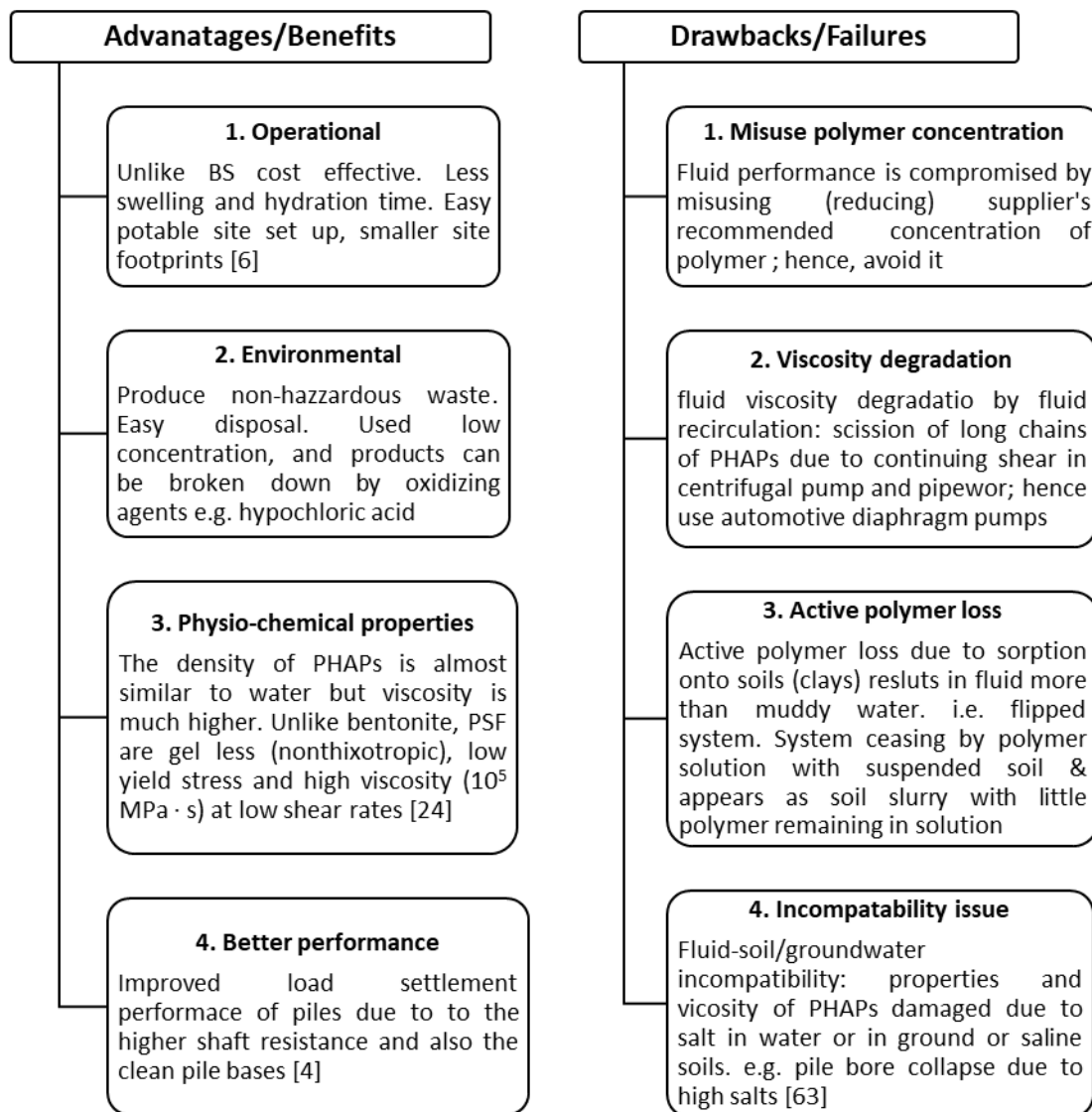


Figure 4. Advantages/benefits through proper use and failures/drawbacks through misuse of polymers

In a polymer supported excavation, polymer soil interactions are generally ignored and lacking detailed information about this subject. After repeated use, polymer fluids contain substantial amounts of suspended soil with no or polymer residual concentration in solution that can be ascribed to the action of digging equipment that can bring *in-situ* soils into fluid suspension. This is due to the relative settling velocity rates i.e., the fast-settling rate of larger particles compared to the slow settling rates of smaller particles (< coarse silt particles) that tend to remain in the fluid relatively for longer time periods due to high fluid viscosity.

In addition, surfaces of soils especially clay soils display sorption sites where sorption of polymer molecules can take place and the functional groups of these polymer chains can aggravate this sorption mechanism. The binding ability of the polymer molecules to soil particles is one of the important characteristics of the polymer fluids that allows interaction between molecules and soils at the excavation side walls and tend to reduce the swelling amount in clay soils or slaking in argillaceous rocks [49-51]. The interface shear strength between soil and foundation element seems to be not

affected because there is no formation of FC during the process [30, 52-53]. The cut soil can be encapsulated as lumps by polymer molecules to prevent disintegration into smaller pieces apart from the coating effect. Therefore, the cut soil can fall out of suspension more rapidly so that the polymer fluids can remain relatively free of suspended soil [5, 54]. Because of polymer removal from the solution due to sorption onto the soils, their functions (the soil-binding & side-wall coating) can be reduced or even lost unless the suspended soil particles are removed, and fluid is reconditioned after its use by supplying the fresh polymer [55]. Fluid properties can be maintained by using sedimentation tanks and addition of the desired amount of new polymer materials to ensure that the cut soil settles without dispersing into the slurry. Nevertheless, fluid's filtration capacity can be improved by the addition of fluid loss additives [42, 56-58].

If the above stated steps are neglected, a mixture of water and native soil with no active polymer (absence of free polymer for development of solution properties including bonding to soil particles) will be formed. This phenomenon is referred as 'flipping effect' and the exhausted polymer fluid system is referred as a 'flipped'

system [54]. When the fluid becomes flipped, then polymer becomes nonfunctional. Hence, a soft native soil FC can be formed in permeable soils and the slurry needs more efforts for functions as well as additional equipment are required for completion of the operation. Reversal of flipping fluid system is cost expensive and dispersion of soil cutting will take place. In such system, much more amount of polymer is required to satisfy the exposed bonding sites compared to a non-flipping fluid system (system with coarser lumps) [55]. Therefore, by considering the above scenario, there is a dire need for functional and practical methods/protocols for determination of residual polymer concentration (RPC) to access the flipping risk.

Polymer sorption onto the soil particles is an important phenomenon influencing their functional ability [59]. In this context, with the passage of time, different methods have been developed for estimating RPC after soil-polymer interactions. Taylor and Nasr-El-Din [60] reported seventeen different testing protocols/methods such as turbidimetry (simple) and electron spin resonance spectroscopy (advanced) techniques for measuring RPC. Bae and Inyang [61] used thermogravimetric analysis successfully for estimating RPC. However, these testing protocols have substantial variations in terms of accuracy of the results and complexity and equipment requirements. Jefferis & Lam [62] suggested the criteria for a testing protocol to satisfy the requirements of the industry. The authors reported that the testing procedure should be compatible with different polymer chemistries ranging from basic to complex polymer blends, avoid hazardous and radioactive materials, the equipment used in process should be the electrical dependent and potable, perform analysis in minimum time, and procedure should display the tolerance against the contaminants entering the polymer fluids from the excavation ground. The authors also tested three candidate techniques out of seventeen methods reported by Taylor and Nasr-El-Din [60] that were thematically based on total organic carbon content, fluid viscosity and absorption of ultraviolet light. Among these methods, technique based on the viscosity and density measurements showed the superior performance for polymer loss detection by sorption compared to other two methods. However, mud balance device used for onsite density measurements gives poor resolution, especially this device is not suitable for polymer fluid concentration control for both freshly prepared and/or re-used polymer concentrations [63], hence; more precise methods are needed for onsite density measurements. Nevertheless, new approaches for steady state flow (also based on modeling) are direly needed to describe the stabilizing mechanism of PSF. Mechanics and industrial processing of PSF can be robustly and accurately simulated by improved constitutive modeling [64].

7. Conclusion

Application of excavation support fluids (ESF) in the construction of deep bored piles and diaphragm walls is a well-known practice around the globe. Bentonite slurry (BS) is in practice around 60 to 70 years to temporarily

support the excavations such as bored piles and diaphragm walls. Due to distinctive bentonite characteristics such as better expansion on hydration, high viscosity and ability for gel-slurry formation, bentonite clay (alumino silicate clays e.g., swelling type montmorillonite clay enriched with high Na) is commonly applied for making drilling fluid in mud rotary drilling process of water wells. In permeable soils, formation of bentonite filter cake with bentonite slurry is important for stabilizing the excavation because bentonite platelets create viscosity and gel strength. Viscous slurry is formed due to dispersion of bentonite powder in water by displaying thixotropic phenomenon. Gel viscosity and strength has linear relationship with mixing and agitation. Bentonite properties can be readjusted such change in pH by NaHCO_3 or Na_2CO_3 , viscosity and flocculation by organic thinners or polyphosphates, and fluid loss by CMC.

The physico-chemical properties of modern polymer support fluids (PSF) are quite distinct from BSF irrespective of the similar mode of action displayed by both polymer fluids and bentonite slurries. Use of PSF has both advantages and drawbacks. The PSF could be the possible alternative for BS especially in case of site space limitations. Advantages recommend their use due to simplicity of site operations, minimum environmental disturbance (eco-friendly) and improvement in foundation performance. Drawbacks impel our attention on the altered (reduced) fluid characteristics due to continued shear in re-circulating system, sorption of polymers onto soils and altered (lost) properties in saline soils/salty water. To combat the alterations in fluid properties and to minimize significant degradation in fluid performance, fresh polymer should be regularly augmented. Further research is needed for complete understanding of soil-polymer interactions, on site density measurements, direct measurement of residual polymer concentrations in solution, and to identify the mechanisms that determine the preferential use of PSF over BS. New approaches/protocols (that also include modeling) based on steady-state flow are direly needed to explain the stabilizing mechanism of PSF.

Conflicts of interest

The authors declare no conflicts of interest.

References

1. Jefferis, S., Troughton, V., & Lam, C. (2011). Polymer systems for fluid supported excavations. In: Proceedings of 2nd Conference on Geotechnical Issues in Construction, London, CIRIA Report X513, 7–12.
2. FPS (Federation of Piling Specialists). (2006). Bentonite Support Fluids in Civil Engineering. 2nd Edn. Federation of Piling Specialists, Kent, U.K.
3. Veder, C. (1953). Method for the construction of impermeable diaphragms at great depth by means of thixotropic muds. (in French). In: Proceedings of 3rd International Conference on Soil Mechanics and Foundation Engineering, 91–94.

4. Lam, C., Jefferis, S. A., & Martin, C. M. (2014). Effects of polymer and bentonite support fluids on concrete-sand interface shear strength. *Géotechnique*, 64(1), 28–39. <https://doi.org/10.1680/geot.13.p.012>
5. Lam, C. (2011). Properties and Applications of Polymer Support Fluids in Geotechnical Engineering. *DPhil Thesis*, University of Oxford, UK.
6. Lam, C., Jefferis, S. A., Suckling, T. P., & Troughton, V. M. (2015). Effects of polymer and bentonite support fluids on the performance of bored piles. *Soils and Foundations*, 55(6), 1487–1500. <https://doi.org/10.1016/j.sandf.2015.10.013>
7. Lennon, D. J., Ritchie, D., Parry, G. O., & Suckling, T. P. (2006). Piling projects constructed with vinyl polymer support fluid in Glasgow, Scotland”, Proc., 10th International Conference on Piling and Deep Foundations, Deep Foundations Institute, Hawthorne, NJ., 499–506.
8. Schünmann, D. (2004). Fisherman's friend. *Ground Engineering*, 37(12), 17.
9. Jefferis, S. A., & Lam, C. (2013). Polymer support fluids: use and misuse of innovative fluids in geotechnical works. In: Proceedings of 18th International Conference on Soil Mechanics and Geotechnical Engineering, Paris, 3219–3222.
10. Fleming, K., Weltman, A., Randolph, M., & Elson, K. (2009). Piling Engineering. 3rd Ed., Taylor & Francis, Abingdon, UK.
11. Veder, C. (1963). The excavation of trenches in the presence of bentonite suspensions for the construction of impermeable and load bearing diaphragms. In: Proceedings of Grouts and Drilling Muds in Engineering Practice, Symposium of the British National Society on Soil Mechanics and Foundations Engineering. Institution of Civil Engineers, London, 181-188.
12. Xanthakos, P. P. (1979). Slurry Waifs. McGraw Hill Publishers, London.
13. Hajnai, I., Marton, J., & Regele, Z. (1984). Construction of Diaphragm Walls. John Wiley & Sons, USA.
14. Wheeler, P. (2003). Piles unlock polymer potential. *Ground Engineering*, 36, 8–9.
15. Kelessidis, V. C., Zografou, M., & Chatzistamou, V. (2013). Optimization of drilling fluid rheological and fluid loss properties utilizing PHPA polymer. In: Proceedings of SPE Middle East Oil and Gas Show and Conference, Society of Petroleum Engineers, TX, 1–9.
16. Lin, L., & Luo, P. (2014). Amphoteric hydrolyzed poly (acrylamide/dimethyl diallyl ammonium chloride) as a filtration reducer under high temperatures and high salinities. *Journal of Applied Polymer Science*, 132(10), n/a–n/a. <https://doi.org/10.1002/app.41581>
17. Lin, L., & Luo, P. (2018). Effect of polyampholyte-bentonite interactions on the properties of saltwater mud. *Applied Clay Science*, 163, 10–19. <https://doi.org/10.1016/j.clay.2018.07.012>
18. Li, M.-C., Wu, Q., Song, K., Qing, Y., & Wu, Y. (2015). Cellulose nanoparticles as modifiers for rheology and fluid loss in bentonite water-based fluids. *ACS Applied Materials & Interfaces*, 7(8), 5006–5016. <https://doi.org/10.1021/acsami.5b00498>
19. Dias, F. T. G., Souza, R. R., & Lucas, E. F. (2015). Influence of modified starches composition on their performance as fluid loss additives in invert-emulsion drilling fluids. *Fuel*, 140, 711–716. <https://doi.org/10.1016/j.fuel.2014.09.074>
20. Darson-Balleur, S., Harnan, C., Admiraal, B., et al. (2019). Guide to Support Fluids to Deep Foundations. Joint EFFC/DFI Support Fluid Task Group.
21. Day, S. (1999). Geotechnical techniques for the construction of reactive barriers.” *Journal of Hazardous Materials*, 67(3), 285–297. [https://doi.org/10.1016/s0304-3894\(99\)00044-8](https://doi.org/10.1016/s0304-3894(99)00044-8)
22. Kadaster, A. G., Guild, G. J., Hanni, G. L., & Schmidt, D. D. (1992). Field applications of PHPA muds. *SPE Drilling Engineering*, 7(03), 191–199. <https://doi.org/10.2118/19531-pa>
23. Kelessidis, V. C., Tsamantaki, C., Michalakis, A., Christidis, G. E., Makri, P., Papanicolaou, K., & Foscolos, A. (2007). Greek lignites as additives for controlling filtration properties of water-bentonite suspensions at high temperatures. *Fuel*, 86(7-8), 1112–1121. <https://doi.org/10.1016/j.fuel.2006.10.009>
24. Lam, C., Martin, P. J., & Jefferis, S. A. (2015). Rheological properties of PHPA polymer support fluids. *Journal of Materials in Civil Engineering*, 27(11), 04015021. [https://doi.org/10.1061/\(asce\)mt.1943-5533.0001252](https://doi.org/10.1061/(asce)mt.1943-5533.0001252)
25. O'Neill, M. W., & Reese, L. C. (1999). Drilled Shafts: Construction Procedures and Design Methods. Publ. No. FHWA-IF-99-025, Federal Highway Administration, U.S. Department of Transportation, Washington, D.C.
26. Lam, C., & Jefferis, S. A. (2016). Performance of bored piles constructed using polymer fluids: lessons from european experience. *Journal of Performance of Constructed Facilities*, 30(2), 04015024. [https://doi.org/10.1061/\(asce\)cf.1943-5509.0000756](https://doi.org/10.1061/(asce)cf.1943-5509.0000756)
27. Dugan, G. (2013). Drilling Fluids: Choose Bentonite or Synthetic Slurry as the Job Demands. <https://www.nationaldriller.com/articles/88767-drilling-fluids-choose-bentonite-or-synthetic-slurry-as-the-job-demands>.
28. Nash, K. L. (1974). Stability of trenches filled with fluids. *Journal of the Construction Division*, 100(4), 533–542. <https://doi.org/10.1061/jceaz.0000456>
29. Majano, R. E., O'Neill, M. W., & Hassan, K. M. (1994). Perimeter load transfer in model drilled shafts formed under slurry. *Journal of Geotechnical Engineering*, 120(12), 2136–2154. [https://doi.org/10.1061/\(asce\)0733-9410\(1994\)120:12\(2136\)](https://doi.org/10.1061/(asce)0733-9410(1994)120:12(2136))
30. Lam, C., Jefferis, S. A., & Goodhue, Jr., K. G. (2010). Observations on viscosity reduction of PHPA polymer support fluids. *Deep Foundations and Geotechnical in Situ Testing*. [https://doi.org/10.1061/41106\(379\)23](https://doi.org/10.1061/41106(379)23)
31. Lam, C., & Jefferis, S. A. (2014). Interpretation of viscometer test results for polymer support fluids. *Tunneling and Underground Construction*. <https://doi.org/10.1061/9780784413449.043>
32. Santagata, M., Dalmazzo, D., & Santagata, E. (2008). Deformation behavior of clay-water suspensions from rheological tests. In: Proceedings of 4th

- International Symposium on Deformation Characteristics of Geomaterials, Vol. 1, IOS Press, Amsterdam, Netherlands, 453–459.
33. Speers, R. A., Holme, K. R., Tung, M. A., & Williamson, W. T. (1987). Drilling fluid shear stress overshoot behavior. *Rheologica Acta*, 26(5), 447–452. <https://doi.org/10.1007/bf01333845>
 34. Alderman, N. J., Meeten, G. H., & Sherwood, J. D. (1991). Vane rheometry of bentonite gels. *Journal of Non-Newtonian Fluid Mechanics*, 39(3), 291–310. [https://doi.org/10.1016/0377-0257\(91\)80019-g](https://doi.org/10.1016/0377-0257(91)80019-g)
 35. Lesemann, H., & Vogt, N. (2012). Investigations into hydraulic support using polymeric solutions (in German). *Geotechnik*, 35(1), 11–21.
 36. Majano, R. E., & O'Neill, M. W. (1993). Effect of mineral and polymer slurries on perimeter load transfer in drilled shafts. Rep. No. UHCE-93-1, Dept. of Civil and Environmental Engineering, Univ. of Houston, Houston.
 37. Lam, C., Jefferis, S. A., & Suckling, T. P. (2014c). Construction techniques for bored piling in sand using polymer fluids. In: *Proceedings of the Institution of Civil Engineers-Geotechnical Engineering*, 167(6), 565–573. <https://doi.org/10.1680/geng.13.00128>
 38. McKinley, G. H. (2002). Steady and transient motion of spherical particles in viscoelastic liquids. In: *Transport Processes in Bubbles, Drops, and Particles*. Kee, D.De., and Chhabra, R.P. (Eds), Taylor & Francis, New York, 338–375.
 39. Mohamed, N. A. (1994). Novel wholly aromatic polyamide-hydrazides. Part V: Structure-molecular-weight-thermal-stability relationships. *Polymer Degradation and Stability*, 44(1), 33–42. [https://doi.org/10.1016/0141-3910\(94\)90029-9](https://doi.org/10.1016/0141-3910(94)90029-9)
 40. Kim, S. I., Ree, M., Shin, T. J., & Jung, J. C. (1999). Synthesis of new aromatic polyimides with various side chains containing a biphenyl mesogen unit and their abilities to control liquid-crystal alignments on the rubbed surface. *Journal of Polymer Science. Part A: Polymer Chemistry*, 37, 2909–2921. [https://doi.org/10.1002/\(sici\)1099-0518\(19990801\)37:15<2909::aid-pola24>3.0.co;2-b](https://doi.org/10.1002/(sici)1099-0518(19990801)37:15<2909::aid-pola24>3.0.co;2-b)
 41. Ahmad, H. M., Kamal, M. S., & Al-Harhi, M. A. (2018). High molecular weight copolymers as rheology modifier and fluid loss additive for water-based drilling fluids. *Journal of Molecular Liquids*, 252, 133–143. <https://doi.org/10.1016/j.molliq.2017.12.135>
 42. Chu, Q., & Lin, L. (2019). Effect of molecular flexibility on the rheological and filtration properties of synthetic polymers used as fluid loss additives in water-based drilling fluid. *RSC Advances*, 9(15), 8608–8619. <https://doi.org/10.1039/c9ra00038k>
 43. Chen, T.-A., Jen, A. K.-Y., & Cai, Y. (1995). Facile approach to nonlinear optical side-chain aromatic polyimides with large second-order nonlinearity and thermal stability. *Journal of the American Chemical Society*, 117(27), 7295–7296. <https://doi.org/10.1021/ja00132a050>
 44. Liaw, D.-J., Chang, F.-C., Leung, M., Chou, M.-Y., & Muellen, K. (2005). High thermal stability and rigid rod of novel organo soluble polyimides and polyamides based on bulky and noncoplanar naphthalene-biphenyldiamine. *Macromolecules*, 38(9), 4024–4029. <https://doi.org/10.1021/ma048559x>
 45. Varganici, C.-D., Rosu, D., Barbu-Mic, C., Rosu, L., Popovici, D., Hulubei, C., & Simionescu, B. C. (2015). On the thermal stability of some aromatic-aliphatic polyimides. *Journal of Analytical and Applied Pyrolysis*, 113, 390–401. <https://doi.org/10.1016/j.jaap.2015.02.031>
 46. Gu, Y., Sun, Z., Gong, S., Zhang, H., Gong, Q., Liu, L., & Wang, Y. (2015). Synthesis and characterization of soluble and thermally stable triphenylpyridine-containing aromatic polyimides. *Journal of Materials Science*, 50(20), 6552–6558. <https://doi.org/10.1007/s10853-015-9186-7>
 47. Cao, J., Meng, L., Yang, Y., Zhu, Y., Wang, X., Yao, C. Y., Sun, M. B., & Zhong, H. (2017). Novel acrylamide/2-acrylamide-2-methylpropanesulfonic acid/4-vinylpyridine terpolymer as an anti-calcium contamination fluid-loss additive for water-based drilling fluids. *Energy & Fuels*, 31(11), 11963–11970. <https://doi.org/10.1021/acs.energyfuels.7b02354>
 48. Plank, J., Brandl, A., & Lummer, N. R. (2007). Effect of different anchor groups on adsorption behavior and effectiveness of poly (N, N-dimethylacrylamide-co-Ca 2-acrylamido-2-methylpropanesulfonate) as cement fluid loss additive in presence of acetone-formaldehyde-sulfite dispersant. *Journal of Applied Polymer Science*, 106(6), 3889–3894. <https://doi.org/10.1002/app.26897>
 49. Likos, W. J., Akunuri, K., & Loehr, J. E. (2005). Performance of PHPA Polymer slurries for applications in Missouri shale. In: *Proceedings of Sessions of the Geo-Frontiers 2005 Congress*, Geotechnical Special Publication No. 132, ASCE, Reston, VA, 665–676.
 50. Inyang, H. I., Bae, S., Mbamalu, G., & Park, S.-W. (2007). Aqueous polymer effects on volumetric swelling of Na-montmorillonite. *Journal of Materials in Civil Engineering*, 19(1), 84–90. doi:10.1061/(asce)0899-1561(2007)19:1(84)
 51. Brown D., & Axtell, P. J. (2010). Design and Construction Challenges at the kcICON Bridge. *Deep Foundation*, 73–76.
 52. Chaney, R., Demars, K., Ata, A., & O'Neill, M. (2000). The physiochemical interaction between PHPA polymer slurry and cement mortar. *Geotechnical Testing Journal*, 23(2), 225–235. <https://doi.org/10.1520/gtj11047j>
 53. Lam, C., Troughton, V., Jefferis, S., & Suckling, T. (2010b). Effect of Support Fluids on Pile Performance – A Field Trial in East London. *Ground Engineering*, 43(10), 28–31.
 54. Lam, C., Martin, P. J., Jefferis, S. A., & Goodhue, K. G. (2014b). Determination of residual concentration of active polymer in a polymeric support fluid. *Geotechnical Testing Journal*, 37(1), 20130019. <https://doi.org/10.1520/gtj20130019>
 55. KB Technologies. (2002). A Slurry and Earth Stabilization System for the New Millennium: A Technical Discussion and Historical Overview. Trade Literature, KB Technologies, Chattanooga, Tenn.

56. Quan, H., Li, H., Huang, Z., Zhang, T., & Dai, S. (2014). Copolymer SJ-1 as a fluid loss additive for drilling fluid with high content of salt and calcium. *International Journal of Polymer Science*, 2014, 1–7. <https://doi.org/10.1155/2014/201301>
57. Wu, Y.-M., Zhang, B.-Q., Wu, T., & Zhang, C.-G. (2001). Properties of the forpolymer of N -vinylpyrrolidone with itaconic acid, acrylamide and 2-acrylamido-2-methyl-1-propane sulfonic acid as a fluid-loss reducer for drilling fluid at high temperatures. *Colloid & Polymer Science*, 279(9), 836–842. <https://doi.org/10.1007/s003960100494>
58. Falode, O. A., Ehinola, O. A., & Nebeife, P. C. (2008). “Evaluation of local bentonitic clay as oil well drilling fluids in Nigeria. *Applied Clay Science*, 39(1-2), 19–27. <https://doi.org/10.1016/j.clay.2007.04.011>
59. Lam, C., & Jefferis, S. A. (2020). Effect of sorption on the active concentration of polymer support fluids. *Géotechnique Letters*, 11, 36-41. <https://doi.org/10.1680/jgele.20.00062>
60. Taylor, K. C., & Nasr-El-Din, H. A. (1994). Acrylamide copolymers: A review of methods for the determination of concentration and degree of hydrolysis. *Journal of Petroleum Science and Engineering*, 12(1), 9–23. [https://doi.org/10.1016/0920-4105\(94\)90003-5](https://doi.org/10.1016/0920-4105(94)90003-5)
61. Bae, S., & Inyang, H. I. (2006). Confirmation of aqueous polymer sorption on contaminant barrier clay using TGA. *Journal of Materials in Civil Engineering*, 18(2), 307–310. [https://doi.org/10.1061/\(asce\)0899-1561\(2006\)18:2\(307\)](https://doi.org/10.1061/(asce)0899-1561(2006)18:2(307))
62. Jefferis, S., & Lam, C. (2017). Using density to determine the solids content of construction slurries. In: *Proceedings of International Conference Soil Mechanics and Geotechnical Engineering*, Seoul, 1695-1698.
63. Larson, R. G., & Desai, P. S. (2015). Modeling the rheology of polymer melts and solutions. *Annual Review of Fluid Mechanics*, 47(1), 47–65. [doi:10.1146/annurev-fluid-010814-014612](https://doi.org/10.1146/annurev-fluid-010814-014612)
64. Schwarz, J., & Lange, U. (2004). Brücken Gründung mit 70 m tiefen flüssigkeitsgestützten gebohrten Pfählen in Benin/Afrika. (in German). In: *Proceedings of 19th Christian Veder Kolloquium*, Graz, Austria, 73–89.



© Author(s) 2023. This work is distributed under <https://creativecommons.org/licenses/by-sa/4.0/>



Laboratory modeling and analysis of slopes of different geometry under the effect of precipitation

Mert Takci¹, Inci Develioglu¹, Hasan Firat Pulat^{*1}, Hasan Emre Demirci¹

¹Izmir Katip Celebi University, Department of Civil Engineering, Türkiye

Keywords

Laboratory model
Plaxis 2D
Precipitation
Slope angle
Slope stability

Research Article

DOI: 10.31127/tuje.1191246

Received: 18.10.2022

Revised: 04.03.2022

Accepted: 07.03.2022

Published: 24.04.2023



Abstract

Back stability analysis, in-lab testing, and field tests may all be used to assess the behavior of stability of slopes. Each of these approaches has benefits and drawbacks compared to one another. Amongst these approaches, laboratory modeling stands out with its ability to prepare identical samples, keep external conditions under control, and measure deformations precisely. In this study, laboratory-based slope models at 1(Horizontal)/1(Vertical), 2/3, and 1/3 angles including the effects of precipitation and external loading were created. The results of these models were compared with those of the Plaxis 2D software. First, models were built using highly permeable cohesionless coarse-grained soils, and mixtures containing high plasticity clay (bentonite) at different rates were then prepared to investigate the effect of fine-grained soils on stability. Laboratory tests such as sieve analysis, specific gravity, consistency limits, Standard Proctor, and direct shear were used to assess the geotechnical index and mechanical properties of soils. Incremental surcharge loads were placed on the slope models and surface deformations, and local and general collapses under the effect of precipitation were observed. Laboratory model results highlighted that the fines content had a non-negligible effect on stability. When the slope behaviors were examined, it was observed that the models with a 1/3 slope had more severe local fractures and collapses. The stability of the slope is negatively affected when bentonite content in soil mixtures rises. The results of Plaxis 2D analysis are compatible with those of laboratory model tests and the factor of safety values obtained from Plaxis 2D range from 0.98 to 11.4.

1. Introduction

Geological formations, historical natural disasters, and climatic factors should all be considered while choosing the new construction location. Engineers are being forced to defy nature, though, due to population increase and a lack of appropriate development locations. Slope stability issue is one of the most common problems in geotechnical engineering [1-2]. Uncontrolled excavations and fillings, heavy rains, and pore water pressure variation, poor engineering properties of debris adversely affect the stability of slopes [3-5]. When the mechanism is thoroughly explored, it is seen that it depends on many more parameters than anticipated, such as soil class and density, fine and organic matter content, rainfall intensity-duration, surcharge load and location, slope height, and slope angle.

Precipitation, which increases the water content, degree of saturation, and total body weight of the soil and decreases the negative pore water pressures for unsaturated soil, adversely affects the stability of the slope [6-10]. Rainwater infiltration produces wet front formation, an increase in groundwater level, and a consequent increase in pore water pressure. This causes the soil to lose its shear strength and even causes the slope to collapse. There are many numerical and experimental studies on the effect of precipitation infiltration on slope stability [11-14]. Genc [11] mixed kaolin and bentonite clays in certain ratios (95/5, 90/10, 85/15, 80/20, 75/25, 70/30) and determined the geotechnical index and swelling properties of the obtained mixtures. According to the experimental results, it was determined that the swelling percentage increased as the bentonite ratio increased. It was also observed that the swelling index decreased with

* Corresponding Author

(merttakci@hotmail.com) ORCID ID 0000-0002-2261-3524
(inci.develioglu@ikcu.edu.tr) ORCID ID 0000-0001-6594-8095
(hfirat.pulat@ikcu.edu.tr) ORCID ID 0000-0002-8298-7106
(hasanemre.demirci@ikcu.edu.tr) ORCID ID 0000-0001-6455-9100

Cite this article

Takci, M., Develioglu, İ., Pulat, H. F., & Demirci, H. E. (2023). Laboratory modeling and analysis of slopes of different geometry under the effect of precipitation. Turkish Journal of Engineering, 7(4), 349-357

increasing water content. It was observed that as the amount of bentonite increased, the liquid limit and plasticity index increased linearly, and the percentage of swelling increased as the bentonite ratio increased [11].

In this study, it was determined that the bentonite ratio, the swelling percentage in the ground and the liquid limit values were increased. In this study, the effect of this relationship on slope stability was examined.

Pınarlık et al. [12] conducted seepage analyses for the most comprehensive slope stability and steady-unsteady flow conditions of slopes, embankments, dams, and retaining walls with different soil properties with Slide V6 balance software. The program helps to determine the effects of individual variables in slope stability on the factor of safety (FS) of slope. In the study, samples with and without geotextiles with the same slope angles were analyzed by the limit equilibrium method. Soil deformations and safety coefficients occurring in both analyzes were compared. The contribution of geotextiles to the increase of soil-bearing capacity has been examined. As a result of the study, it was interpreted that the FS increased as the cohesion and the internal friction angle value increased, and it was reported that the FS of the slopes reinforced with geosynthetics reached to the safe side.

Ün [13] performed pile analysis, and modeling, on drained and undrained soils with Plaxis 2D software. According to the findings of the analysis, the FS reduced as slope height and load rose, whereas it increased when soil strength parameters increased. Additionally, it was shown that the FS rose in the model built with two-layered soil as the layer height of the soil with high shear strength grew.

Zhao et al. [14] have modeled and analyzed the excavation process of high and steeply inclined slopes in Plaxis 2D software. It has been determined that the inner rock mass affected by the excavation creates tensile stress in some areas, which is reflected in the stress distribution. Considering the unloading effect of the excavated place, it was determined that the FS of the slope gradually decreased due to the increase in the excavation depth. For this reason, it was suggested that numerical simulation should adequately account for the degradation of the rock mass caused by the excavation.

In this study, the behavior of slopes in different geometries under the influence of precipitation and surcharge loading was examined. Besides, slope stability analyses were executed by considering laboratory modeling and obtained results were compared. Observations were made about the movement mechanisms of the slopes under the influence of precipitation. It was determined to what extent the percentage of fines, angle of slope, and the amount of external loading affected the stability.

2. Material and Method

2.1. Sand

The sand used in this study was obtained from a private company and its geotechnical and mechanical

properties are shown in Table 1. After considering the geotechnical properties, the soil is classified as poorly graded silty and gravelly sand according to the Unified Soil Classification System (USCS).

Table 1. Geotechnical and mechanical properties of sand

Parameter	Unit	Value
Specific gravity (G_s)	-	2.77
Plastic limit (PL)	%	NP
Optimum water content (w_{opt})	%	10.6
Maximum dry density ($\gamma_{d,max}$)	kN/m ³	19.8
Internal friction angle (ϕ)	°	31
Cohesion (c)	kPa	11.3
Soil classification (USCS)	-	SP

2.2. Bentonite

The bentonite is convenient in terms of API 13A Part 9 specifications used in the study provided by Karben Company. It has a high swelling capacity since it contains sodium and at least 90% montmorillonite. It complies with TS EN 13500 Part 9 [15] bentonite specification and TS 977 Type-1 [16] standards. When mixed with water, it disperses easily and does not clump. The physical and chemical properties of bentonite are listed in Table 2.

Table 2. Physical and chemical properties of bentonite

Parameter	Unit	Value
Filtration	ml	15
Humidity	%	10
Yield point plastic viscosity ratio	-	3.0
SiO ₂	%	61.28
Al ₂ O ₃	%	17.79
Fe ₂ O ₃	%	3.01
CaO	%	4.54
Na ₂ O	%	2.7
MgO	%	2.10
K ₂ O	%	1.24

2.3. Slope modeling system with precipitation effect

The box in which the slope model was created was composed of transparent tempered glass so that the deformations and movements that took place throughout the experiment could be observed. For this purpose, 6 mm thick tempered glass was placed in an aluminum frame and the box was formed. The connection points of the frame have been strengthened so that the system is not damaged during the placement and compaction processes. Water was transferred to the system with a flexible pipe and adjustable nozzles were used to equalize the rainfall intensity. Nozzles and flexible pipes were fixed to the metal frame on the system. In order to observe deformations and movements more accurately, 20 mm x 20 mm grids were formed on the front glass of the boxes. Moreover, red beads were located at the corner points of the slope model to determine the movement. The box was 116 cm in length, 60 cm in width, and 80 cm in height (H). The slope stability behavior observation system under the influence of precipitation and surcharge has been shown in Figure 1.

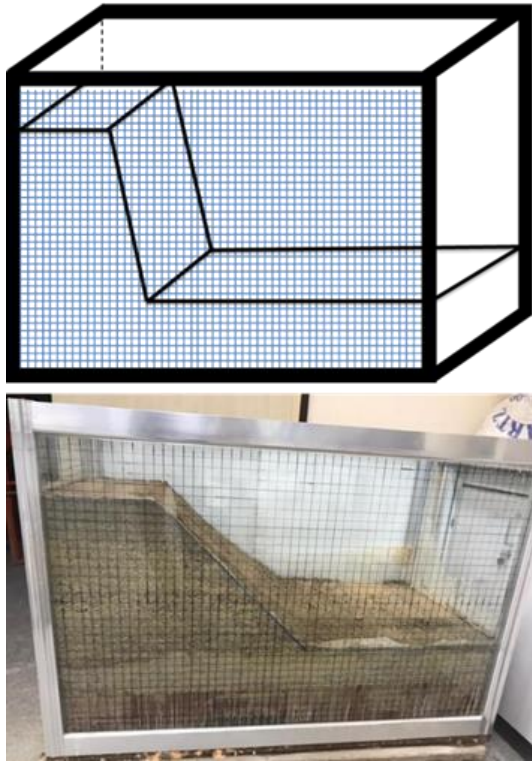


Figure 1. Slope stability behavior observation system

In the slope modeling system, the precipitation effect was created using the sprinkling method. This approach was chosen because it would provide the same quantity of water to the slope without creating deformation, as opposed to allowing droplets to develop on the surface of the slope. Instead of the physical effects of rain, it was intended to observe the impact of rainwater pressure. In this system, 4 nozzles were connected on the same flexible pipe, and water was sprayed toward the slope surface. With this system, water was supplied to the slope with a flow rate of 0.5 l/min ($7.7 \times 10^{-3} \text{ cm}^3/\text{s}$). This precipitation system has been shown in Figure 2.



Figure 2. Precipitation mechanism

2.4. Geotechnical index properties experiments

The grain size distribution of sand and sand-bentonite mixtures were obtained using wet sieve analysis in accordance with ASTM D422 [17] and ASTM D6913 [18]. The liquid limit was measured by the fall cone method (BS1377-1:2016) [19]. The plastic limit test was conducted by following the ASTM D4318 [20]. The soil samples were classified using consistency limits and

grain size analyses according to ASTM D2487 [21]. The specific gravity (G_s) of samples was defined according to ASTM D854 [22]. The optimum water content and maximum dry unit weight of samples were determined with the Standard Proctor test according to ASTM D698 [23]. To determine shear strength parameters, the consolidated drained (CD) direct shear tests were conducted according to ASTM D3080/D3080M [24]. The samples were prepared at optimum water content and maximum dry unit weight. The specimens were tested in saturated conditions at three various normal stresses of 49 kPa, 98 kPa, and 196 kPa, respectively [25-27]. The test samples were sheared at a speed of 0.1 mm/min to prevent the generation of excess pore water.

2.5. Slope modelling experiments

The optimum water content and 85% of the maximum dry unit weight were used while forming the slope models. The optimum water content was added to the sample, which was completely dried in an oven at 105°C for 24 hours and mixed in the concrete mixer until a homogeneous mixture was obtained. It was then compacted in layers to a thickness of 5 cm using a Standard Proctor hammer and a wooden block. The wooden block used is 58 cm long and 15 cm wide. As a result of the trial and error method, the soil placement and compaction process were performed as follows. During the compaction process, a total of 27 blows were made at 3 different points of the wooden block, with 9 blows to each point. Side and top views of the compaction process have been shown in Figure 3.

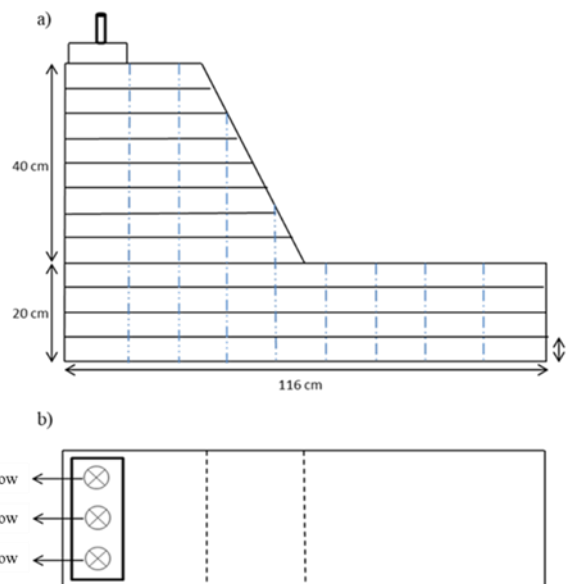


Figure 3. a) Side view of the compaction process, b) top view of the compaction process

While the sprinkler system was being installed, the annual average precipitation amount of 2021 (490 mm/m²) in the Izmir Cigli district Balatcik region was taken into consideration. These values have been obtained from the valley bulletin of the General Directorate of Agriculture and Forestry for many years [28]. By trial and error method, it was determined that while the water coming from the tap was at the maximum

level, the amount of water supplied to the system by 4 nozzles was compatible with the annual precipitation amount. A concrete block was made in the laboratory environment to transmit the surcharge load to the determined areas of the slope. These concrete blocks have dimensions of B=15 cm, L=58 cm, and H=12.5 cm. The 0.0725 m² surface of this concrete block (H x L), whose weight is adjusted as 200 N, is called the narrow area where it contacts the soil surface and the wide area when it comes into contact with its 0.087 m² surface (B x L). The surcharge load to be given to the slope was adjusted by using narrow and wide areas. The pressure values transmitted to the slope according to the narrow and large surface area have been listed in Table 3. These specified weights were loaded 6 times in total every 45 minutes and weights in the laboratory were used. The amount of bentonite in the soil was another experiment-related variable that altered. The overall goal of each experiment was to monitor the collapse state of slopes by starting with the natural soil and applying the slope's maximum effect (limited area, 1/3 slope angle, and maximum weight). Additionally, different bentonite-soil combinations of 10, 15, 20, 30, 40, and 50% were employed to compare their strengths while altering the soil's characteristics.

Table 3. Slope loading steps

No	N (kg)	Higher stress		Lower stress	
		A (m ²)	P (kN/m ²)	A (m ²)	P (kN/m ²)
1	35.5		5		4.2
2	71		10		8.3
3	142	0.0725	20	0.087	16.7
4	213	(Narrow loading area)	30	(Wide loading area)	25.0
5	284		40		33.3
6	355		50		41.6

Slope model experiments were carried out under many different geometric properties. The slope geometries used in the experiments and the names given to these models are shown in Figure 4.

2.6. Plaxis 2D slope modelling analysis

In order to compare the results obtained from laboratory modeling experiments with numerical analyzes, Plaxis 2D software was used for the analysis of the experiments performed in the laboratory [29]. The same geometry, dimensions, and boundary conditions were used to compare the results of the experiments with the numerical analysis. An example of the model used in the software is shown in Figure 5.

In the experiments, the soil was compressed and limited according to the optimum water content values, but a continuous sprinkler effect system was given. It is known that when the collapse state is observed, it is between the soil liquid limit and the plastic limit value. While measuring these requirements in this program, 3 analyzes were made according to the plastic limit of the soils, the liquid limit, and the water content in the optimum water content.

Mohr-Coulomb soil model was used in Plaxis 2D analysis. The values in Table 4 were used as soil parameters and were modeled as drained.

The displacement and FS values were compared by modeling and analyzing the experiments carried out in the laboratory in Plaxis 2D program. In the experiments, the soil was placed by compacting according to the optimum water content values, but the sprinkler effect was given to the system continuously. When the collapse condition is observed, it is known that the soil is between the liquid limit and the plastic limit value. For this reason, while modeling in Plaxis 2D, three different analyzes were made according to the plastic limit, liquid limit, and optimum water content of the soils.

The surcharge load given to the system in Plaxis 2D is the same as the load when the collapse condition is observed in the modeling experiment. For this reason, the results of the experiments made in the laboratory environment and the results of the analysis made in Plaxis 2D were compared.

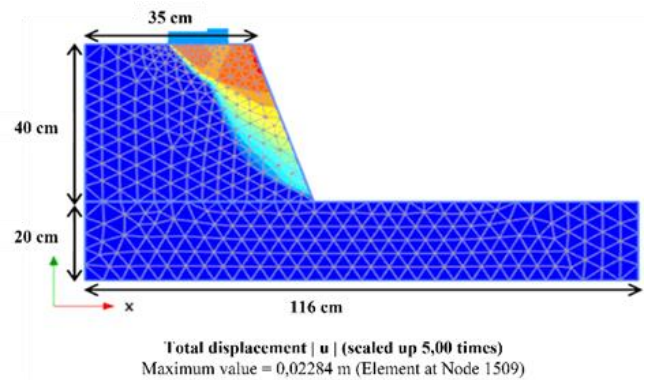


Figure 5. Slope model of the Plaxis 2D analysis

3. Results

3.1. Results of geotechnical index properties

The geotechnical index properties of sand and sand/bentonite mixtures are listed in Table 4. The soil classification was made according to the Unified Soil Classification System (USCS) [21].

3.2. Results of slope modelling experiments

In order to examine the stability behavior in detail and systematically, the parameters that will negatively affect the stability have been examined in different tests. Scenarios that will trigger instability such as increasing the angle of slope, surcharge stress, and fine-grained soil ratio have been tested in combination. As a result of many successful or unsuccessful laboratory models and examination of video recordings, slope instabilities were divided into three different classes which are punching, local deformation, and general failure. Punching deformations are comparatively smaller deformations. Although the deformations are visible to the naked eye, the raft-representative concrete block can still carry the loading plates. Local failure can be defined as a situation where significant deformations occur and the concrete plate representing the raft cannot carry the loading plates. In this case of failure, it is possible to observe a

clear slip surface, even if it is not curvilinear or circular. General failure is defined as the situation in which the greatest deformations are observed, and the concrete plate (slab) completely loses its bearing capacity. As a result of this failure, it is possible to define one or more

failure surfaces. 19 slope model experiments under various conditions such as different slope geometry and bentonite ratios were performed. Table 5 summarizes the results of slope model experiments.

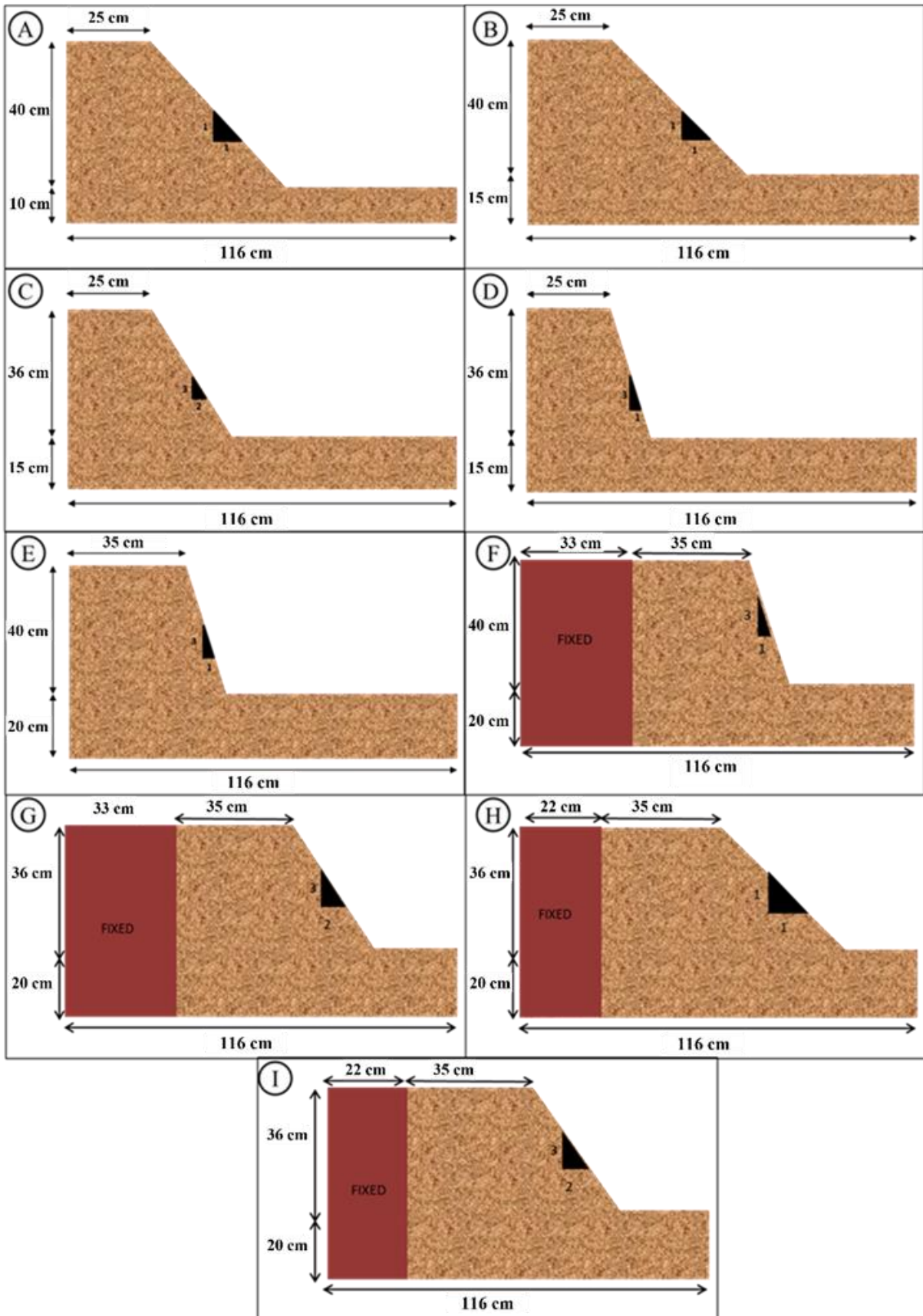


Figure 4. Geometries of slope models

Table 4. Geotechnical index properties of sand and sand/bentonite mixtures

Geotechnical index properties	Sand	90S	85S	80S	70S	60S	50S
		10B	15B	20B	30B	40B	50B
Max. dry unit weight, γ_{drymax} (kN/m ³)	19.1	18.6	18.4	18.1	17.5	17.5	17.4
Optimum water content, w_{opt} (%)	10.6	10.9	11.3	13.6	14.5	15.0	15.8
Liquid limit, LL (%)	16	43	80	92	98	118	142
The plastic limit, PL, (%)	NP	17	20	28	33	41	47
Specific gravity, G_s	2.77	2.68	2.63	2.56	2.55	2.55	2.55
D_{10} (mm)	0.12	-	-	-	-	-	-
D_{30} (mm)	1.6	1.4	1.2	1.3	0.27	-	-
D_{60} (mm)	3.5	3.5	3.4	3.2	2.2	2.1	1.8
Coefficient of uniformity, C_u	29.2	-	-	-	-	-	-
Coefficient of curvature, C_c	6.1	-	-	-	-	-	-
Soil classification, USCS	SW	SP	SC	SC	SC	SC	SC
Cohesion, c (kPa)	11.3	25.9	30.9	38.3	48.9	54.0	55.2
Internal friction angle, ϕ (°)	31.0	25.7	21.8	16.6	12.4	10.2	10.0

Table 5. Results of slope modelling experiments

Test No	Slope model	Slope angle (H/V)	Bentonite ratio (%)	Failure status	Failure Stress (kN/m ²)	Failure type
1	A	1/1	-	-	-	Punching
2	A	1/1	-	-	-	Punching
3	A	1/1	-	-	-	Punching
4	B	1/1	-	-	-	Punching
5	C	2/3	-	-	-	Punching
6	D	1/3	-	-	-	Local deformation
7	D	1/3	10	-	-	Local deformation
8	D	1/3	15	-	-	Local deformation
9	D	1/3	20	-	-	Local deformation
10	E	1/3	20	Failure	39.4	General failure
11	F	1/3	20	Failure	40.8	General failure
12	F	1/3	20	Failure	35.2	General failure
13	F	1/3	30	Failure	33.8	General failure
14	F	1/3	40	Failure	32.4	General failure
15	G	2/3	40	Failure	36.6	General failure
16	H	1/1	40	-	-	Local deformation
17	I	2/3	30	-	-	Local deformation
18	H	1/1	50	-	-	Local deformation
19	I	2/3	50	Failure	35.2	General failure

In experiment No 1, the contact area of the surcharge at the top of the slope was 0.087 m². As a result of this experiment, no collapse was observed in the slope model. However, small punching deformations were observed under the concrete mass (Figure 6).

In experiment No 10, the angle of inclination was kept constant at 1/3 and 20% bentonite and 80% sand were used. The experiment was carried out by keeping the slope angle, precipitation intensity, loading intervals, and total load constant. The collapse was observed after approximately 3 hours and under a load of 280 kg (40 kPa) with the 80/20 sand–bentonite mixture. General failure was observed in this experiment (Figure 7). In experiment No 11, the experiment was repeated, keeping all conditions constant to check the repeatability. The results were extremely similar to the previous experiment and the modeling process proved to be reproducible.

A general failure was observed in experiment No. 12, which aimed to observe the effect of the loading period and precipitation intensity. For this reason, the rain intensity of 0.5 l/min was adjusted to 0.25 l/min. Also, loads increased every 45 minutes instead of 90 minutes.

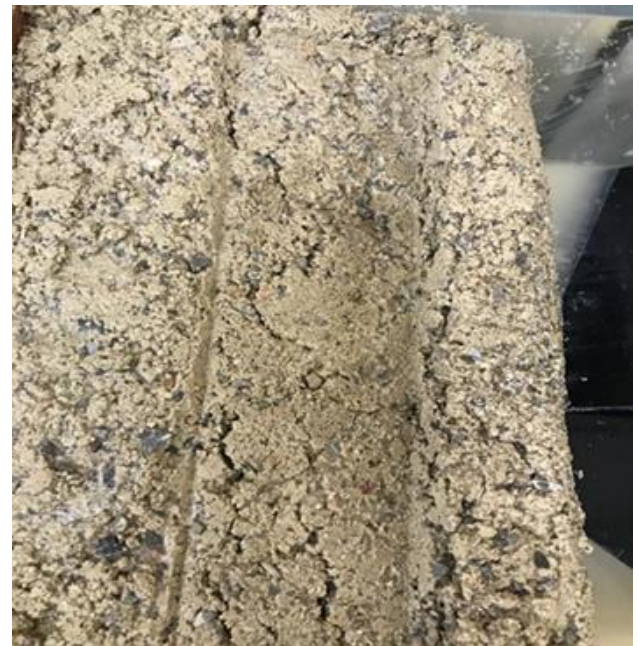


Figure 6. Small deformations under the concrete mass in experiments No 1

In experiments no 13 and 14, the bentonite ratio was 30% and 40% respectively and general failures were observed. Large deformations occurred at failure stresses between 32.4 kN/m² and 33.8 kN/m².

In experiment No. 15, the geometry was changed (G) and the angle of the slope became 2/3. General failure was observed under failure stress of 36.6 kN/m² (Figure 8). This experiment proved that a slope body that contained the same soil compositions can carry 13% more stress when the slope angle decreased from 1/3 to 2/3.



Figure 7. General failure in experiment No 10



Figure 8. General failure in experiment No 15

Soil composition did not change for experiment 16 but the slope was modeled as 1/1. Although the general failure was not observed due to the comparatively soft slope surface large deformations occurred and raft representative concrete plate did not safely carry the loading plates. In other experiments slope behavior was investigated by changing soil compositions and slope models (No.17, 18, 19). Experiments in which general failure was not observed but the concrete plate representing the raft foundation could not carry the load were defined as local failure. When the test results are compared with the literature studies, many compatible results stand out [11-13].

According to study of Genç [11], the test results showed that the swelling percentage increased as the bentonite ratio increased. It was observed that as the amount of bentonite increased, the liquid limit and

plasticity index increased linearly, and the percentage of swelling increased as the bentonite ratio increased. Therefore, indirectly, as the swelling index increases, the stability of the slope decreases [11].

3.3. Results of Plaxis 2D modelling analysis

Modeling and analysis of the experiments carried out in the laboratory were run with Plaxis 2D software, and the FS values were compared. In the experiments, the soil was compacted according to the optimum water content, but the precipitation effect was constantly given to the system. Therefore, when the collapse condition is observed, the soil may have a water content between the plastic limit and the liquid limit. For this reason, while modeling with Plaxis 2D software, three different analyzes were made according to the plastic limit, liquid limit, and optimum water content of the soils. Experiments were made in the laboratory with these different water contents and the internal friction angles and cohesion values were found in the results of these experiments. These values were entered into the Plaxis 2D program and the results were obtained. The surcharge load input given to the system in Plaxis 2D is the load obtained in the case of failure in the modeling experiment. Thus, the results of the experiments made in the laboratory and the results of the analysis made in Plaxis 2D could be compared. The FS values of the optimum water content, plastic limit, and liquid limit values in the analyzes of experiments No. 10, 13, 14, and 19, which were observed in the laboratory experiments, were shown in Figure 9. Although the FS value depends on the water content, it decreases as the water content increases. This shows the effect of the infiltration effect on the soil strength. But the suction values were not used during the modelling study.

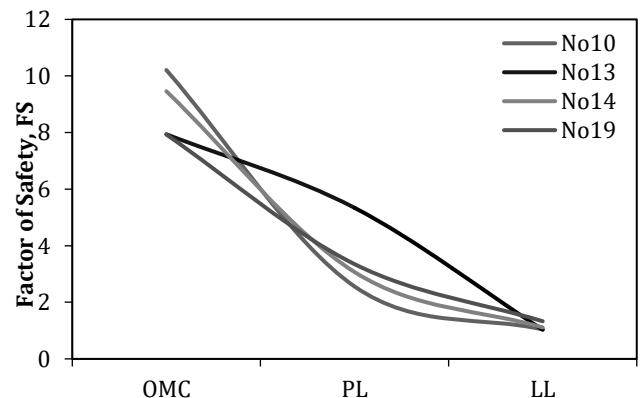


Figure 9. The FS values of the No. 10, 13, 14, and 19 experiments

The FS values of the optimum water content, plastic limit, and liquid limit values in the analyzes of experiments No 16, 17, and 18, which were not observed in the experiments performed in the laboratory, in the Plaxis 2D software, are shown in Figure 10. As mentioned above, although the FS value depends on the water content, it decreases as the water content increases.

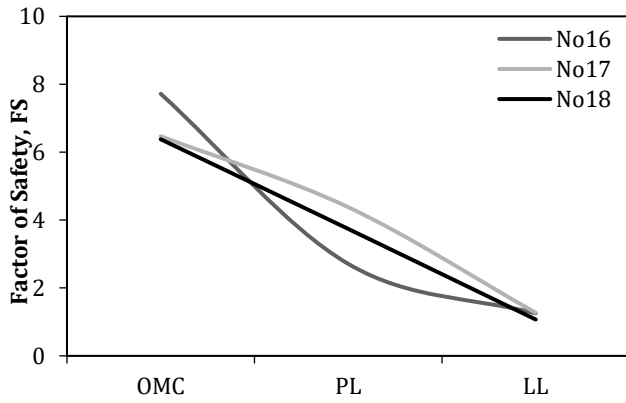


Figure 10. The FS values of the No. 16, 17, and 18 experiments

4. Conclusion

This study investigated the behavior of the slope under the influence of various parameters as well as the impact of surcharge loads. Mixtures with various bentonite contents were made to investigate the effect of the fine soil ratio on the stability of the slope. Between each experiment, the slope angle was gradually changed according to the program and the slope behavior in each experiment was investigated. A sprinkler was applied along the slope surface with the fogging method at a constant flow rate to create a precipitation effect in all experiments. The findings of the study are as follows:

- Incremental surcharge loads were applied to the top of the slope at regular intervals. It is observed that as these loads increase, local deformations become more pronounced or the slope collapses.
- In slopes with the same conditions and geometry, as the bentonite ratio of the soil mixture increased, the stability of the slope was adversely affected, and the collapse of the slope became more likely.
- The collapse of the slope was observed more clearly due to the swelling property of bentonite due to the index parameters. The reason for this is that fine-grained clays have higher water retention capacity, therefore the weight of the slope body increases, and the FS decreases.
- In models under the same conditions, the weight of the slope with a small angle is greater in case of collapse. It was observed that the load at the time of failure increased by 13% when the slope angle was reduced from 2/3 to 1/3.
- When the rain intensity and loading rate are reduced by 50%, the total load in the collapsed state is 16%.
- The analysis results made in the Plaxis 2D software are consistent with the model experiments carried out in the laboratory.
- According to the analysis results obtained from the Plaxis 2D, the displacement values at the apex of the slope are approximately 9-10 times higher than the displacement values at the heel point.
- According to the analysis results obtained from the Plaxis 2D, the displacement values are the lowest in the modeling made at the optimum water content for the

same point, while the displacement value is the highest in the models made at the liquid limit water content.

- According to the graphics obtained from the Plaxis 2D, the FS value decreases as the slope angle increases, the water content of the soil increases, and the amount of bentonite in the soil increases.

Acknowledgement

The authors greatly acknowledge the support of the Scientific Research Project of Izmir Kâtip Celebi University (2022-TYL-FEBE-0011).

Author contributions

Mert Takci: Conceived and designed the analysis, Collected the data, Performed the analysis, writing original draft preparation; **Inci Develioglu:** Writing original draft preparation; **Hasan Firat Pulat:** Conceived and designed the analysis, Performed the analysis, writing original draft preparation; **Hasan Emre Demirci:** Contributed data or analysis tools, Performed the analysis

Conflicts of interest

The authors declare no conflicts of interest.

References

1. Das, B. M. (1994). Principles of Geotechnical Engineering. Cengage.
2. Pulat, H. F., & Yükselen Aksoy, Y. (2017). Investigation of Shear Strength and Slope Stability of Turkish Municipal Solid Waste Composition. *Teknik Dergi*, 28(1), 7703-7724
3. Yamak, S. (2017). *Karayolu şevlerinde boşluk suyu basınç değişikliklerinin şev stabilitesine etkisinin incelenmesi* (Yüksek lisans tezi, Fen Bilimleri Enstitüsü, Gazi Üniversitesi, Ankara, Türkiye).
4. Collins, B. D., & Znidarcic, D. (2004). Stability analyses of rainfall induced landslides. *Journal of geotechnical and geoenvironmental engineering*, 130(4), 362-372.
5. Griffiths, D. V., & Lane, P. A. (1999). Slope Stability Analysis by finite elements. *Geotechnique*, 49(3), 387-403.
6. Aslan Fidan, A. (2017). *Doğgun olmayan koşullarda yağış infiltrasyonu etkisindeki şevlerin stabilite analizi* (Yüksek lisans tezi, Fen Bilimleri Enstitüsü, Dicle Üniversitesi, Diyarbakır, Türkiye).
7. Fourie, A. B., Rowe, D. & Blight, G. E. (1999). The effect of infiltration on the stability of the slopes of a dry ash dump. *Geotechnique*, 49(1), 1-13.
8. Gasmu, J. M., Rahardjo, H., & Leong, E. C. (2000). Infiltration effects on stability of a residual soil slope. *Computers and Geotechnics*, 26, 145-165.
9. Wersin, P., Curti, E., & Appelo, C. A. J. (2004). Modelling bentonite-water interactions at high solid/liquid ratios: swelling and diffuse double layer effects. *Applied clay science*, 26, 249-257.

10. Rocscience. (2004). A New Era in Slope Stability Analysis: Shear Strength Reduction Finite Element Technique.
11. Genç, S. (2009). Şişen zeminler ve bentonit kaolin karışımlarının şişme özellikleri, (Yüksek lisans tezi, Fen bilimleri enstitüsü, İstanbul Teknik Üniversitesi, İstanbul, Türkiye).
12. Pınarlık, M., Kardoğan, P., & Demircan, R. (2017) Şev stabilitesine zemin özelliklerinin etkisinin limit denge yöntemi ile irdelenmesi. Mühendislik Bilimleri ve Tasarım Dergisi, 5(3), 675 – 684.
13. Ün, B. (2019). Şev stabilitesi ve şev hareketlerine karşı alınacak önlemler (Yüksek lisans tezi, Fen Bilimleri Enstitüsü, Çukurova Üniversitesi, Adana, Türkiye).
14. Zhao, C., Jiang, L., Li, X., & Luo, S. (2020). Stability analysis of a rocky slope considering excavation unloading effect. The Civil Engineering Journal, 2, 170-181.
15. TS EN ISO 13500: (2006). Petroleum and natural gas industries - Drilling fluid materials - Specifications and tests. Turkish Standards.
16. TS 977 (1993). Bentonite as drilling fluid material.
17. ASTM D 422 (2020). Standard Test Method for Particle-Size Analysis of Soils ASTM International, West Conshohocken, PA, ASTM International.
18. ASTM D6913 – 04 (2009). Standard Test Methods for Particle-Size Distribution (Gradation) of Soils Using Sieve Analysis, ASTM International, West Conshohocken, PA, USA.
19. BS 1377 – 1 (2016). Methods of test for soils for civil engineering purposes. British Standard Institution, London, UK.
20. ASTM D4318 – 17e1 (2017). Standard test methods for liquid limit, plastic limit, and plasticity index of soils, ASTM International, West Conshohocken, PA, USA.
21. ASTM D2487 – 11 (2011). Standard Practice for Classification of Soils for Engineering Purposes (Unified Soil Classification System). ASTM International, West Conshohocken, PA, USA.
22. ASTM D854/D854 – 14 (2014). Standard Test Methods for Specific Gravity of Soil Solids by Water Pycnometer. ASTM International, West Conshohocken, PA, USA.
23. ASTM D698 – 12 (2021). Standard Test Methods for Laboratory Compaction Characteristics of Soil Using Standard Effort (12,400 ft-lbf/ft³ (600 kN-m/m³)). ASTM International, West Conshohocken, PA, USA.
24. ASTM D3080/3080M – 11 (2011). Standard Test Method for Direct Shear Test of Soils Under Consolidated Drained Conditions. ASTM International, West Conshohocken, PA, USA.
25. Yano, K., Suzuki, M., & Nakai, T. (1997). Undrained shear and creep behavior of stiff natural clay. Conference, Japan in Deformation and Progressive Failure in Geomechanics, '97, Nagoya, 205–210.
26. Shah, K., & Shah, D. L. (2015). Interface friction between soil and geosynthetics. Proceedings of the 5th Indian Young Geotechnical Engineers Conference, March 14-15, Vadodara, Italy, 81-82.
27. Angelim, R. R., Cunha, R. P., & Sales, M. M. (2016). Determining the elastic deformation modulus from a compacted earth embankment via laboratory and Ménard pressuremeter tests. Soils Rocks, São Paulo 39(3), 285–300.
28. T.C. Çevre, Şehircilik ve İklim Değişikliği Bakanlığı, Meteoroloji Genel Müdürlüğü (2023). <https://mgm.gov.tr/>
29. Manual, T. (2016). PLAXIS 2D. Delft University of Technology & PLAXIS, Netherlands.



© Author(s) 2023. This work is distributed under <https://creativecommons.org/licenses/by-sa/4.0/>



Comparison of commodity prices by using machine learning models in the COVID-19 era

Sena Alparslan¹, Tamer Uçar^{*2}

¹Bahçeşehir University, Graduate School, Big Data Analytics and Management, Türkiye

²Bahçeşehir University, Faculty of Engineering and Natural Sciences, Software Engineering Department, Türkiye

Keywords

Machine Learning
Price Prediction
Commodities
Time Series

Research Article

DOI: 10.31127/tuje.1196296

Received: 29.10.2022

Revised: 22.03.2023

Accepted: 24.03.2023

Published: 24.04.2023



Abstract

Commodity products such as gold, silver, and metal have been seen as safe havens in past economic crises. This situation increases the interest in commodity products. Due to the COVID-19 pandemic, quarantine decisions and precautions have caused an economic slowdown in stock markets and consumer activities. This inactivity in the economy has led to the COVID-19 recession that started in February 2020. Because of the increase in the number of COVID-19 cases, the difficulty of physical buying-selling transactions has shown that commodity products can be a safe investment tool. Based on the fact that machine learning approaches gained importance in commodity price prediction, the main goal of this study is to understand whether machine learning methods are meaningful for commodity price prediction even in extraordinary situations. To measure commodities' price volatility, a data set obtained from Borsa İstanbul is separated into pre-COVID-19 and COVID-19 periods. Daily prices for gold and silver commodities, from July 2018, which is before the ongoing COVID-19 recession, to October 2021 are used. The performances of the machine learning models were compared with MAE, MAPE, and RMSE metrics. The findings of this study point out that the LSTM model has more accurate predictions, especially in the pre-COVID-19 period. When considering the COVID-19 period only, SVR produces the best prediction results for the gold commodity and LSTM has the best prediction results for the silver commodity.

1. Introduction

The commodity market allows buying, selling, and exchanging of raw materials or primary products [1]. In the commodity market, everything can be changed suddenly because the market has large price fluctuations due to different types of players such as investors, brokers, and traders who anticipate each other's actions. Besides that, players or investors should prepare themselves for unexpected effects like COVID-19 [2]. Normally, when negative developments happen in the financial area such as interest rates, inflation, etc., commodities, especially gold and silver prices inevitably increase. However, the recent crisis is not related to the financial area but is stemmed from the health field. According to the risk and volatility indicators, the COVID-19 pandemic is considered the most substantial global phenomenon [3]. In such circumstances, gold and silver commodities come into prominence. Gold is already known as a safe harbor for investors, known for keeping

its value. According to [4], the role of gold as a hedging tool consists of two theoretical mechanisms. One of them is, that when volatility increases, this provides the risk-averse investor to move away from other financial markets. This behavior creates a peak in demand for gold, then causes gold prices up and increases investors' wealth. The other mechanism is due to the biased behavior related to gold's history; gold becomes preferable to other assets. In addition to this, with the COVID-19 era, silver's demand increased. Both commodities are preferred by the concerned investors and other economic actors when market predictability diminishes.

Commodity prices, especially gold and silver have importance to investors, suppliers, governments, etc. If the prediction of commodity price is obtained with the best result, it will help people such as experts and other parties using and forecasting commodities prices while planning budgets or similar needs. This situation prompts academic research and agents of the market to

* Corresponding Author

(senasualan@hotmail.com) ORCID ID 0000-0002-4466-4840
(tameru@gmail.com) ORCID ID 0000-0002-9397-6656

Cite this article

Alparslan, S., & Uçar, T. (2023). Comparison of commodity prices by using machine learning models in the COVID-19 era. Turkish Journal of Engineering, 7(4), 358-368

start studies on predicting economic and financial crises and crashes such as Global Financial Crisis (2008), Eurozone Debt Crisis (2010–2012), and the novel COVID-19 pandemic [5].

From this point of view, machine learning methods have gained importance recently, and deep learning has become very popular, especially for commodity price prediction. In 2020, one of the black swan events took place during the COVID-19 pandemic in Turkey and around the world. During that period, commodity prices were more volatile, and it became more difficult to forecast. For this reason, measurement of the performance of prediction models gained great importance.

Machine learning is an application of artificial intelligence, which stems from the theory claiming that machines are capable of learning from data, pinpointing patterns, and making decisions with an insignificant amount of human interaction. It provides a wide variety of applications including portfolio optimization, image and speech recognition, weather forecasting, and many more. In today's data world, machine learning is of great importance due to its amount of learning potential [1].

In recent years, machine learning has been the first thing that comes to mind in solving many problems in computer science. It made analyses easier, more innovative, and more effective when working with an enormous amount of data. Machine learning can be categorized into three groups which are unsupervised, supervised, and reinforcement learning. For the price prediction of commodities or currencies based on historical data, existing machine learning systems generally use deep or supervised learning approaches to help investors with decision-making and risk calculation needs. Besides that, by using deep reinforcement learning, trading decisions can be made without human intervention [1].

In this study, data sets containing gold and silver commodity prices for the period before the COVID-19 pandemic and during the COVID-19 pandemic were analyzed. The analyzed data sets were obtained from Borsa İstanbul. Different prediction models were built using Long Short-Term Memory (LSTM), Random Forest (RF) and Support Vector Regression (SVR). To find the best prediction model, the performances of the models were compared using various evaluation metrics. The main goal is to find out whether machine learning methods are meaningful and useful for commodity price prediction even in unprecedented circumstances.

2. Literature review

There are many publications in the literature on the field of price prediction. In this study, a literature review process has been conducted based on the following steps:

- a. The main research question of this study is stated as “How meaningful and accurate are machine learning methods for gold and silver commodity price prediction even in extreme situations?”.
- b. Academic databases including ScienceDirect, IEEE Xplore, and Google Scholar were used.

- c. 15 different search keywords were defined considering the study's main research question. These keywords are “commodity market”, “commodity trading” “stock market”, “stock price”, “time series data”, “COVID-19”, “pandemics”, “machine learning”, “deep learning”, “SVR”, “LSTM”, “random forest”, “regression”, “price prediction”, and “predictive models”.

- d. A time range covering the past five years was set to review recent studies.

- e. The most relevant and most cited papers were selected during the literature review process.

- f. Studies without any citations were excluded.

Based on this elimination and filtering methodology, the selected studies on price prediction are briefly mentioned below.

Ramakrishnan et al. [6] focused on predicting commodity prices and exchange rates in Malaysia. Gold commodities, rubber, palm oil, and crude oil were included in the study. For the predictions, Support Vector Machine (SVM), Neural Networks (NN), and RF machine learning algorithms were utilized. The following evaluation techniques were applied: Relative Absolute Error (RAE), Root Mean Squared Error (RMSE), Relative Squared Error (RSE), and Mean Absolute Error (MAE). The authors reached the conclusion that RF has better performance for accuracy and performance compared to the NN and SVM models.

Akin et al. [7] focused on forecasting the raisin commodity price index of Turkey using Decision Tree (DT), Artificial Neural Networks (ANN), and SVM methods. Researchers considered accuracy and f-measure scores to compare the model performances. Daily historical data for explanatory variables such as gold price, oil price, and political and social issues that occurred in Turkey were included. The results of the study showed that the accuracy performance of the SVM method performed better compared to other methods.

Yadav et al. [8] aimed on analyzing the forecasting models to predict the Bombay Stock Exchange (BSE) SENSEX, which is a parameter of the stock market of India. To find the best prediction model to forecast, the authors made a comparison of mean errors. R tool was used in the study. Research data was collected from BSE's official website. The researchers converted the data set into time series. Following that, output from the time-series data was used as a newly created time-series object. It is stated that data is very volatile, therefore the authors transformed the data set for the Box-Jenkins approach to increase the accuracy of the forecast. Augmented Dickey-Fuller (ADF) Test and Ljung-Box Test were also applied. Autoregressive Integrated Moving Average (ARIMA) Model, Exponential Smoothing Forecast (ESF), BoxCox Transformation (BT), Mean Forecast (MF), Seasonal Naive Forecast (SNF) and NN were used and compared to find the best prediction result. For evaluation criteria, several metrics including MAE, MAPE (Mean Absolute Percentage Error), and RMSE were taken into account. According to the results of the study, NN and ESF methods gave the best outcomes.

Štifanić et al. [9] analyzed COVID-19's impact on three stock indexes in the US: NASDAQ Composite, S&P 500, DJI, and also in crude oil prices. The authors proposed a

system for predicting the integration of commodity and stock prices. Stationary Wavelet Transform (SWT) and Bidirectional Long Short-Term Memory (BDLSTM) networks were used in the prediction. To achieve low-performance measure values and high-quality regression, three main system configurations were examined. RMSE and MAE scores were taken as evaluation criteria. It was stated that the proposed system has successful results in forecasts of five-day crude oil prices.

Luo [10] conducted a study on forecasting Bitcoin price trends and return rates by comparing the performances of DT, RF, AdaBoost, and SVM algorithms. Prediction models used different historical data sets including Bitcoin exchange data, Bitcoin exchange & COVID-19 (recovery, confirmed, death) data, Bitcoin exchange & Twitter data, and Bitcoin exchange & COVID-19 (recovery, confirmed, death) & Twitter data. Researchers used RMSE and accuracy scores as evaluation criteria. Luo (2020) observed that the performance of the models is improved when Twitter data is included. On the other hand, SVM does not provide good performance in price trends or Bitcoin return predictions, and no improvement is achieved in the predictions with the usage of COVID-19 data.

Amin [11] aimed to predict commodity prices by using machine learning algorithms. Different kinds of daily commodities were included in the study which are wheat, avocado, and dairy foods. The data sets were gathered from Kaggle, Bangladesh Agricultural Research Council, and wheat prices were gathered from the Humanitarian Data Exchange. Researchers applied SVM, RF, Bagging, AdaBoost, GradientBoost, XGBoost, and LightGBM models. To evaluate the performance of the models, Mean Squared Error (MSE), MAE, and R2 evaluation metrics were used. The authors found that ensemble methods performed better for medium-to-large data sets compared to the base SVM model.

Ruan et al. [12] analyzed prediction models to estimate stock prices under unexpected circumstances like the COVID-19 pandemic situation. Stock prices were determined by using the top five stocks of each industry. The data set was collected from Yahoo Finance. 100 stocks from 20 industries were acquired. Researchers compared the methods which are parametric and non-parametric and forecasted stock prices under unpredicted conditions. Long Short-Term Memory (LSTM) and ARIMA models were applied at the single-stock level, industry level, and general market level respectively. It is observed that the LSTM model performed better than the ARIMA model in following the stock price trends and time complexity.

Ghosh [13] used a different approach to predict future prices. A novel hybrid granular ensemble of ensembles forecasting framework was studied. Crude oil, gold, copper, silver, and natural gas commodities' closing price values were taken into account. The framework included two separate methodologies on time series decomposition which are Singular Spectrum Analysis (SSA) and Ensemble Empirical Mode Decomposition (EEMD). The researchers concluded that their framework has high quality and had better results on all

commodity forecasts compared with the other competitive five models.

Kamdem et al. [2] aimed to forecast the prices of exported commodities of African countries by using deep learning techniques. Researchers also explored the effect of COVID-19 on the market volatility of these commodities. The West Texas Intermediate crude oil, Brent oil, wheat, and silver were examined. Researchers applied the LSTM model for predicting commodity prices. For training, data was split into two parts. 80% of the data set was used for training and 20% was used for testing. Model scores including MAPE and RMSE were used as evaluation criteria. It was stated that the LSTM model has good accuracy scores for forecasting commodities prices.

Ly et al. [14] studied predicting cotton and oil prices by LSTM, ARIMA, and a combination of methods named the forecast averaging method. The authors gathered data from the World Bank commodity prices data set. The data set was split into 70% as training and 30% as testing. When the ARIMA and the LSTM model performances were compared, the ARIMA model performed better in predicting the prices for commodities. When comparing results with the proposed forecast averaging method, the authors stated that the new method gave better results in the prediction of commodity prices.

Mahdi et al. [15] focused on forecasting cryptocurrency returns. The authors considered the daily returns of Bitcoin, Ethereum, Ripple, Binance Coin, Cardano, and Dogecoin before and during the COVID-19 pandemic. SVM was used as the main predictor. The data set was split into 75% for training and 25% for testing. The best-performing model selection was based on the minimization of MAPE and RMSE. This study showed that the SVM model is a robust algorithm for the predictability of cryptocurrencies.

Vora et al. [16] studied predicting stock prices by historic prices of stock behavior. Researchers used the stock's closing price for further predictions and applied Google Colab for programming models. Authors utilized algorithms such as Linear Regression (LR), RF, DT, and LSTM. Model outputs were compared with the original closing values. It was founded that the Recurrent Neural Network (RNN) type of algorithm such as LSTM shows the best accuracy compared to other models.

Chandra and He [17] studied stock price predictor models' performances during the COVID-19 pandemic. Researchers also investigated if the pre-COVID-19 pandemic data sets would be useful for stock price forecasting during the COVID-19 pandemic. It was found that it is more challenging to provide forecasting because of the high volatility of stock prices during the pandemic. It was also stated that Bayesian NN could provide reasonable predictions in uncertain conditions.

Niu and Zhou [18] aimed to forecast daily prices and seven-day volatility of WTI crude oil and Brent oil. The data set contained 2000 daily observations for Brent oil and WTI oil gathered from the Energy Information Administration (EIA). The data set was divided into two subsets which are 80% training and 20% testing set. To forecast the volatility, researchers proposed a hybrid decomposition-ensemble forecasting model which is

based on variational mode decomposition (VMD) and Kernel Extreme Learning Machine (KELM). In the proposed model, the VMD method was employed to separate the series into subseries with several frequencies, followed by forecasting subseries by KELM. The VMD-KELM model showed better prediction ability and performance with low evaluation criteria values when compared to other models. The authors stated that the decomposition-ensemble strategy is demonstrated by the point that hybrid models have significantly higher prediction accuracies compared to those of single models.

Depren et al. [3] analyzed the influential factors on the gold prices in Turkey during the COVID-19 pandemic by employing machine learning algorithms. Data that belong to the year 2020 were collected from the Ministry of Health of Turkey, Bloomberg, and the Central Bank of the Republic of Turkey. The collected data was split into pre-pandemic and pandemic periods. The researchers analyzed data by using Box and Whisker Plot, RF, K-Nearest Neighbors (KNN), and SVM algorithms. The model performances were assessed with R2, RMSE, and MAE evaluation criteria. It was found that the RF algorithm generated higher prediction accuracy.

Olubusoye et al. [19] focused on energy prices. Researchers analyzed how energy prices are affected during the COVID-19 pandemic under uncertainties. For the uncertainty measurements, the authors preferred to use Economic Policy Uncertainty (EPU), Volatility Index (VIX), Global Fear Index (GFI), COVID-Induced Uncertainty (CIU), and Misinformation Index of Uncertainty (MIU). The Multivariate Adaptive Regression Spline (MARS) algorithm was used. Eight energy price values which are for gasoline, diesel, kerosene, heating oil, natural gas, Brent oil, WTI oil, and propane was included. The study showed that EPU affects most types of energy prices during the COVID-19 pandemic within all examined uncertainty measurements. It was also emphasized that CIU, VIX, and MIU have forecast potential for global energy sources.

In this study, the gold and silver commodity price data set that was obtained from Borsa İstanbul was used for building price-prediction models. The data set was analyzed considering both before and during the COVID-19 pandemic period.

The main research question of this study is “How meaningful and accurate are machine learning methods for gold and silver commodity price prediction even in extreme situations?”. To address this research question, our study uses and analyzes a novel data set obtained from Borsa İstanbul for gold and silver commodities. This data set is not used or analyzed in any other previous studies.

The main contribution of this study is to provide guidance to future machine learning studies by showing which prediction models are more accurate for price predictions in unprecedented circumstances such as the COVID-19 era. The result of this study will help investors, decision-makers, and other related stakeholders to make quicker decisions in unexpected situations.

3. Method

This section provides a detailed explanation of the data set and methods used in this study. Python is used as the primary implementation language in collaboration with Google Colab. Scikit-learn library is used for building machine learning models [20]. NumPy is used for scientific calculations [21]. Pandas is used for analyzing the data set [22]. For deep learning and additional machine learning processes, TensorFlow is included in the implementation [23].

3.1. Data set

Price values of gold and silver commodities from a past time period are used in this study. Since gold and silver are the most preferred commodities with the highest trading volume, the data used in this study only includes these commodities. Others were excluded from the data set.

Precious Metals and Diamond Market’s historical data set covering a time frame between July 2018 and October 2021 is acquired from Borsa İstanbul DataStore. The attributes and their data types are given in Table 1.

The obtained data set is divided into two sets: pre-COVID-19 and COVID-19 pandemic data. The pre-COVID-19 data set covers instances until February 2021. The other set, which is the COVID-19 pandemic data covers values from March 2021 to November 2021.

Both sets are split into testing and training subsets. The COVID-19 period includes 333 silver and 409 gold observations whereas the pre-COVID-19 period includes 272 silver and 413 gold observations. Testing and training set sizes are given in the following Table 2.

Table 1. Attributes of the data set

#	Name	Type
1	Date	Alphanumeric
2	Instrument Code	Alphanumeric
3	Market	Alphabetical
4	Market Segment	Alphabetical
5	Instrument Group	Alphabetical
6	Instrument Type	Alphabetical
7	Instrument Class	Alphabetical
8	Metal Type	Alphabetical
9	Metal Bar Type	Alphabetical
10	Price Unit/Weight	Decimal, Numerical
11	Fineness	Decimal, Numerical
12	Weight	Decimal, Numerical
13	Vault Location	Alphanumeric
14	Settlement Date	Alphanumeric
15	Previous Close Price	Decimal, Numerical
16	Opening Price	Decimal, Numerical
17	Minimum Price	Decimal, Numerical
18	Maximum Price	Decimal, Numerical
19	Close Price	Decimal, Numerical
20	Weighted Average Price	Decimal, Numerical
21	Total Gross Weight	Decimal, Numerical
22	Total Traded Value	Decimal, Numerical
23	Total Traded Quantity	Decimal, Numerical
24	Total Number of Deals	Decimal, Numerical

Table 2. Testing and training set sizes

Commodity Name	Subsets of Data	# of instances (Pre-COVID-19)	# of instances (COVID-19)
Gold	Train	250	300
Gold	Test	22	33
Silver	Train	350	350
Silver	Test	63	59

3.2. The Data processing

The prediction process includes six phases. Figure 1 depicts each of these steps.

The first phase of the prediction process begins with data collection. Data sets containing gold and silver commodity prices are acquired using the source described in the previous section. The second phase is data preprocessing. The entire data preprocessing consists of the following steps:

Data discretization: Continuous quantitative data is converted into intervals.

Data transformation: Min-max normalization method is applied.

Data cleaning: Other commodities such as palladium and platinum are eliminated. Then, duplicated rows are dropped. Rows with missing values are deleted.

Data imputation: Duplicate records for each day are removed.

Data integration: The monthly data sets are combined.

After applying the preprocessing steps, the data set is split into training and testing sets.

The third phase of the process includes building prediction models. The data set is again split into two subsets, one containing values for the pre-COVID-19 pandemic period and the other one including values about the COVID-19 pandemic period observations. SVM, RF, and LSTM prediction models are built based on these two data sets.

The fourth phase includes the execution of SVM, RF, and LSTM models for forecasting commodity price values. To obtain the forecast of the next day’s price, the last input window length (w) is fed into the model. The next day’s forecasted price was used as an input, and it is re-fed into the model. This process is repeated up until reaching the prediction window length.

After completing the forecasting phase, the fifth phase includes evaluating model performances. MAPE, MAE, and RMSE scores are computed for each model to compare prediction performances.

In the final phase, gathered results obtained from the models using both pre-COVID-19 pandemic and COVID-19 pandemic data were compiled.

In the data preprocessing phase of this study, the Moving Average (MA) method is implemented. MA is a basic technical analysis tool used to smooth out the price data by establishing a continuously updated average price value. The average is taken for a specific period such as one month, one week, and so on. Strategies based on the MA tool are used widely and have the capability to be adapted to any time frame, which makes it appropriate both for long and short-term traders [24]. In this study, moving average prices and closing prices of gold and silver commodities are compared in time series. The results are shown in Figure 2 and Figure 3.

3.3. Model building

To analyze time series data set, machine learning methods are increasingly being preferred recently. Especially in the case of complex and non-linear data structures, machine learning methods can determine the relationship between the dependent and independent variables more precisely [3]. In accordance with the literature review, LSTM, RF and SVR are used as the most preferred algorithms for price forecast problems.

Considering such information, the following machine learning methods were used in this study for gold and silver price prediction.

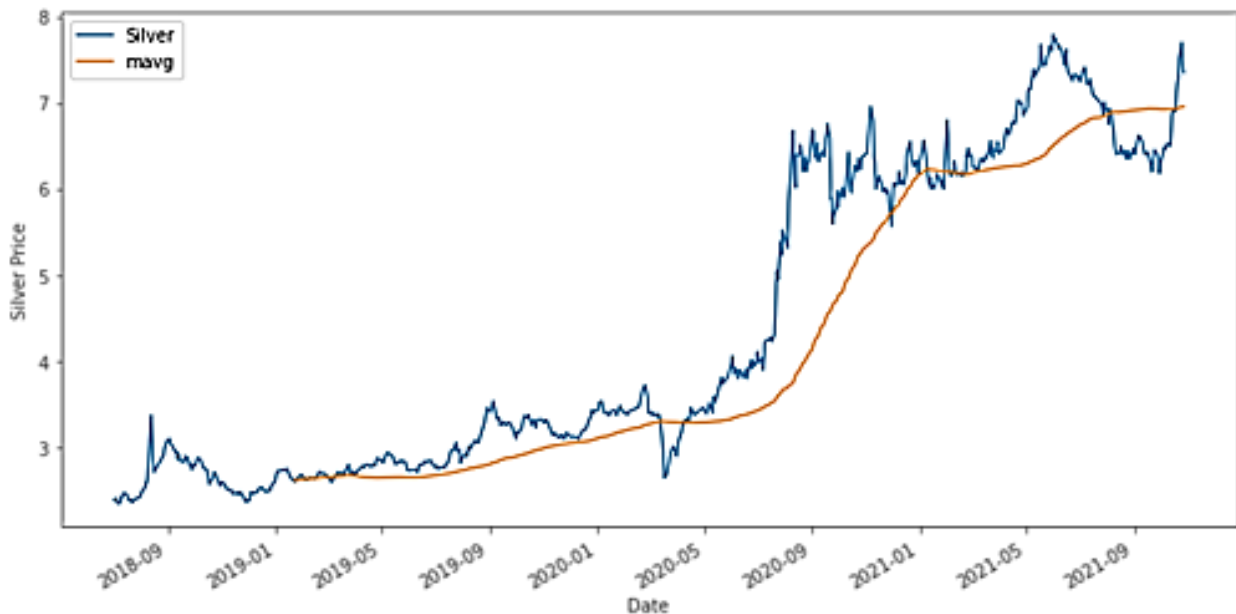


Figure 2. Silver closing prices with moving average prices

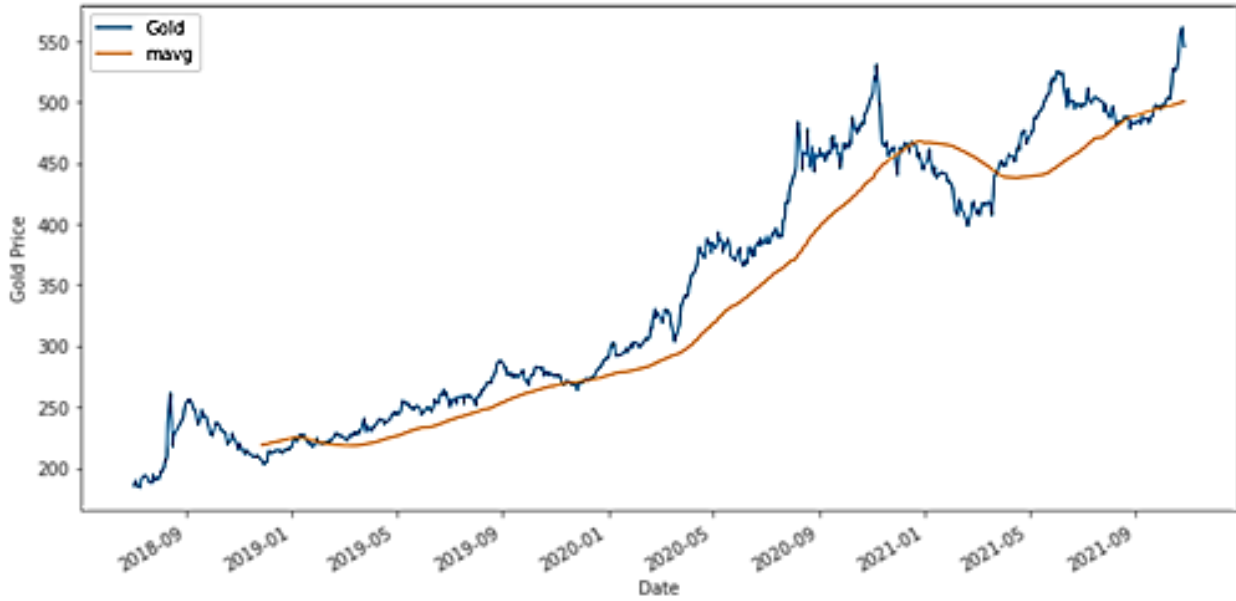


Figure 3. Gold closing prices with moving average prices

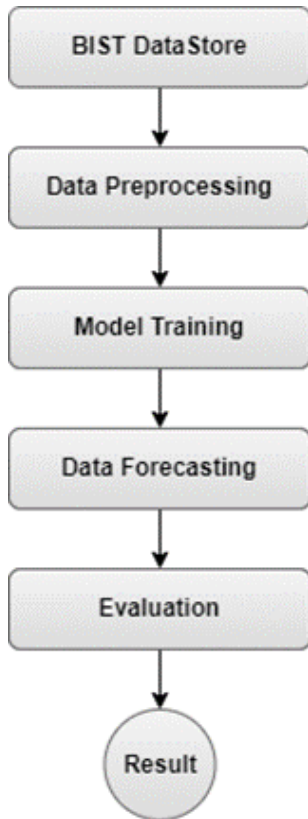


Figure 1. The prediction processes

3.3.1. Random Forest (RF)

RF model is introduced by Breiman [25]. Although it can be used in different areas, it is known as one of the most successful classification methods. In this algorithm, the decision trees examine randomly selected subsets at each node and are divided into branches.

RF is an ensemble method that is a combination of multiple models to create an optimal predictive model. RF works by building multiple decision trees during the training phase. Ensemble methods using slightly different data while building each tree increases the variety of models. Taking an average of the outcomes of several trees together diminishes the overfitting risk. Moreover, more accurate predictions are provided by multiple trees compared to a single tree [11].

The RF model used in this study is based on the TensorFlow machine learning framework [26]. The six parameters in Table 3 are crucial when building the model. The selected values are n_estimators = 300, max_depth = 5, min_samples_split = 2, min_samples_leaf = 1, bootstrap = True, random_state = 0. These selected values are picked by using the grid search method. Grid search is a brute-force approach for hyperparameter tuning. The model is trained and evaluated for each combination. The hyperparameters that result in the best performance are then selected.

Table 3. RF model parameters

Parameter	Description
n_estimators	refers to the number of trees in the forest
max_depth	refers to the maximum depth in a tree
min_samples_split	refers to the minimum number of data points prior to the splitting of the sample
min_samples_leaf	refers to the minimum number of leaf nodes that are required to be sampled
bootstrap	sampling for data points, true or false
random_state	generated random numbers for the random forest.

3.3.2. Long Short-Term Memory (LSTM)

Long-term short-term memory is considered one of the most successful RNN architectures. Long-term short-

term memory is a memory cell, which is a processing unit that replaces conventional artificial neurons in the hidden layer of the network. These memory cells allow networks to efficiently allocate and remotely insert

memory over time to dynamically record the data structure over time with high predictable capacity.

The main goal of RNN is to handle data sets whose inputs and outputs are sequences. The architecture of RNNs is adopted from artificial neural networks. The primary variance is that RNNs can reach both current and historical sequences to predict the results in the same step or current time sequence. This gives RNNs a substantial advantage while predicting time series data which can be categorized under time-sensitive sequential data [14].

An important shortcoming of RNN is its deficient ability to contend with long-term dependencies. This commonly occurs with a problem of vanishing gradients [14].

It is apparent that lots of complex financial indicators exist, and the fluctuation of the stock markets is overly aggressive. On the other hand, with the advances in technology, the chance to achieve a steady income in stock markets is expanded. This can also help experts to discover the best indicators to make better predictions.

At this phase, our data is inputted into the neural network and is trained for forecasts by assigning random weights and biases. Our LSTM model is built with 50 neurons and 4 hidden layers based on our previous experience. Lastly, one neuron was assigned to the output layer for predicting the normalized commodity close price. We also utilize the Adam stochastic gradient descent optimizer and the mean squared error. This model is based on Keras deep learning framework [26].

3.3.3. Support Vector Regression (SVR):

To be used in the Support Vector Machine (SVM) model, sub-algorithms of Support Vector Classification (SVC) and SVR algorithms should be used together. To implement the SVC model, the model needed to be separated in terms of kernel parameters as linear, sigmoid, and polynomial. The most suitable parameters are determined by changing the cache size and cost parameters of these three linear, sigmoid, and polynomial sub-models for the sub-algorithms.

Nu Support Vector Regression (NuSVR) is one of the sub-algorithms determined for SVR. To reach the best model, nu (upper limit of the training error rate and lower limit of the support vectors) value, cost, cache size, and other parameters such as degree is constantly tried during the performing of NuSVR. In addition to that, a radial basis function (RBF) kernel is applied to implement NuSVR.

Like the NuSVR, degree parameters, cache size, and cost are applied and tried to find the best model in the EpsilonSVR algorithm. Moreover, a linear kernel model is implemented in this algorithm.

The SVR model is based on the Scikit-learn machine learning framework [20].

SVR Scikit-learn library is defined as a class of the Support Vector Machine module. While training the model, it is applied for three different kernel parameters, and it is seen that the radial basis function kernel gives the best result.

3.4. Model accuracy assessment

The best-fit model is assessed based on higher accuracy and the least error scores. Regarding the measurement of performance results, the root mean square error measures the error between two data sets, the mean absolute error stands for the average of absolute values of all the differences in a set, and the mean absolute percentage error is considered in forecasting to compare the predicted results with LSTM, RF and SVR models.

3.4.1. Mean Absolute Percentage Error (MAPE)

MAPE is a type of measurement in statistics, used to predict the accuracy of a forecasting method, such as trend estimation. Another term used for MAPE is mean absolute percentage deviation (MAPD) [27].

3.4.2. Mean Absolute Error (MAE)

MAE is an expression referring to the average of absolute values of differences between measured values and actual values in a set. It measures the accuracy of the magnitude of errors and continuous variables without considering their direction [28].

3.4.3. Root Mean Square Error (RMSE)

RMSE compares a predicted value that is predicted by a model with the observed value. RMSE measures the magnitude of errors between two data sets [29].

4. Results

The prediction results of the models are visualized in Figures 4, 5, 6, 7, 8, and 9.

After the time series object is plotted with the information from the data set, it was seen that it can be analyzed on different components such as seasonality, trend, heteroskedasticity, and stationarity. To test the stationarity of the data set, the Augmented Dickey-Fuller Test and Kwiatkowski-Phillips-Schmidt-Shin Test are executed. The results of the tests are included and shown in Tables 4, 5, 6, and 7. According to these results of the applied tests, it is observed that the values of close price variables do not change over time.

LSTM, RF, and SVR methods are used to predict commodity prices and measure the effectiveness of using machine learning models during the COVID-19 recession. Table 8 lists the evaluated model results for gold and silver commodities. Results are given based on MAPE, MAE, and RMSE scores. The obtained findings are discussed in detail in the following section.

5. Discussion and Conclusion

This study compares LSTM, RF, and SVR methods to predict commodity prices and measure the effect of the economic crisis factor caused by the COVID-19 recession. The findings of this study point out that the LSTM model has more accurate predictions, especially in the pre-COVID-19 period. The reason for better LSTM model

performance in predicting COVID-19 outcomes is likely due to the sequential nature of the data, which is well-suited for LSTMs. LSTMs are a type of RNN that can capture patterns in sequential data by processing information through hidden states that are passed from one-time step to the next. However, during the COVID-19 period, it could not give the most effective result for the gold commodity. Time series data typically exhibit temporal dependencies, where the value at a given time step is influenced by past values. Due to the fact that the bagging ensemble of decision trees used by RF could not capture the temporal relationships between observations for time series data, it could not provide efficient model performance in the pre-COVID-19 period for the gold commodity.

When considering the COVID-19 period only, SVR produces the best prediction results for the gold commodity and LSTM has the best prediction results for the silver commodity. With the COVID-19 recession, it is observed that uncertainties such as changes in market

trends and prices caused by uncertainty and fear among investors, increased volatility and unpredictability in the financial markets, widespread job losses, reduced consumer spending, supply chain disruptions, and similar factors in the markets reflected a negative impact on the prediction models. It should also be highlighted that using a hybrid prediction model such as combining LSTM and SVR for commodity price prediction could provide better results even in extraordinary situations. For this reason, this study can provide a foundation to make emergency decisions even more precise and pragmatic for future machine learning studies. On the other hand, the main limitation of the study is the scope being narrowed down to Borsa Istanbul dataset for gold and silver commodities. Therefore, the obtained results depend on this cluster only. To eliminate this limitation, a future study may include testing LSTM, RF, and SVR methods with different datasets other than Borsa Istanbul.

Table 4. Stationarity test results for gold (COVID-19)

Augmented Dickey-Fuller Test		Kwiatkowski-Phillips-Schmidt-Shin Test	
Dickey-Fuller:	-1.8285878399555700	X-squared:	1.3232240371964543
Lag order:	0	Df:	17
p-value:	0.366363806384533	p-value:	0.01
	10%: -2.5714292194077513		10% : 0.347
Alternative hypothesis:	5%: -2.8702852297358983	Alternative hypothesis:	5% : 0.463
	1%: -3.4502011472639724		1% : 0.739

Table 5. Stationarity test results for gold (Pre-COVID-19)

Augmented Dickey-Fuller Test		Kwiatkowski-Phillips-Schmidt-Shin Test	
Dickey-Fuller:	-1.3903018258267308	X-squared:	1.3580822772797543
Lag order:	1	Df:	16
p-value:	0.5869166127306464	p-value:	0.01
	10%: -2.572506310013717		10% : 0.347
Alternative hypothesis:	5%: -2.872304928618605	Alternative hypothesis:	5% : 0.463
	1%: -3.4548039258751206		1% : 0.739

Table 6. Stationarity test results for silver (COVID-19)

Augmented Dickey-Fuller Test		Kwiatkowski-Phillips-Schmidt-Shin Test	
Dickey-Fuller:	-1.5465256906310958	X-squared:	1.5050727639465018
Lag order:	0	Df:	18
p-value:	0.5103831897872779	p-value:	0.01
	10%: -2.5705574627547096		10% : 0.347
Alternative hypothesis:	5%: -2.8686500930967354	Alternative hypothesis:	5% : 0.463
	1%: -3.446479704252724		1% : 0.739

Table 7. Stationarity test results for silver (Pre-COVID-19)

Augmented Dickey-Fuller Test		Kwiatkowski-Phillips-Schmidt-Shin Test	
Dickey-Fuller:	-0.5549123365711701	X-squared:	2.0040231470182444
Lag order:	2	Df:	18
p-value:	0.8808480575502857	p-value:	0.01
	10% : -2.5705		10% : 0.347
Alternative hypothesis:	5% : -2.8686	Alternative hypothesis:	5% : 0.463
	1% : -3.4464		1% : 0.739

Table 8. Evaluated model results

Commodity Name	Evaluating Indicators	LSTM (Pre-COVID-19)	LSTM (COVID-19)	RF (Pre-COVID-19)	RF (COVID-19)	SVR (Pre-COVID-19)	SVR (COVID-19)
Gold	MAPE	0.0182	0.0387	0.0608	0.0148	0.0386	0.0149
Gold	MAE	0.0647	0.2694	0.2123	0.1021	0.1350	0.1025
Gold	RMSE	0.0979	0.3620	0.2293	0.1434	0.1488	0.1180
Silver	MAPE	0.0216	0.0173	0.0361	0.0677	0.1718	0.0922
Silver	MAE	6.5359	8.9148	18.6405	20.6489	52.1202	46.7167
Silver	RMSE	8.4863	12.9622	27.9628	24.7679	55.1280	51.4302

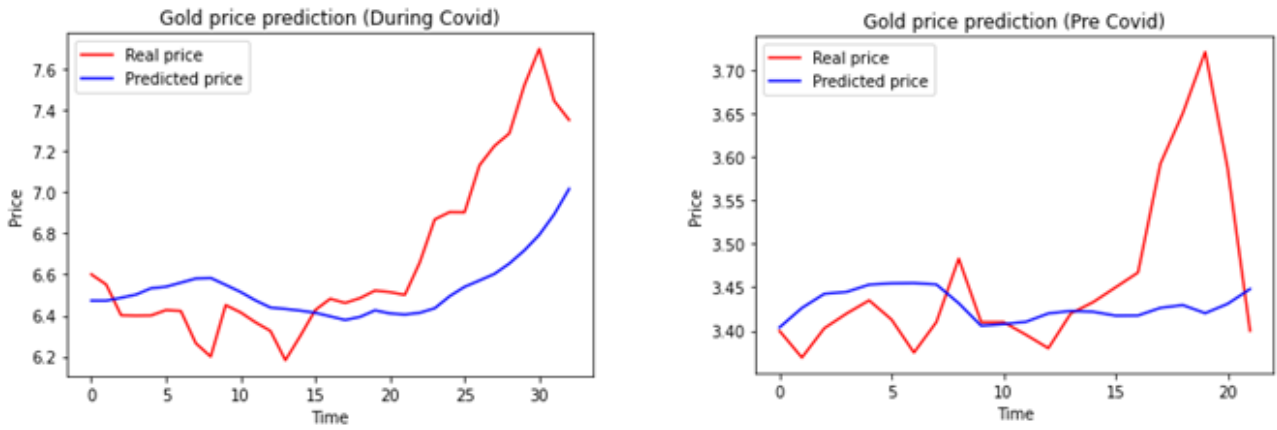


Figure 4. Gold price predictions using LSTM (left: COVID-19, right: Pre-COVID-19)

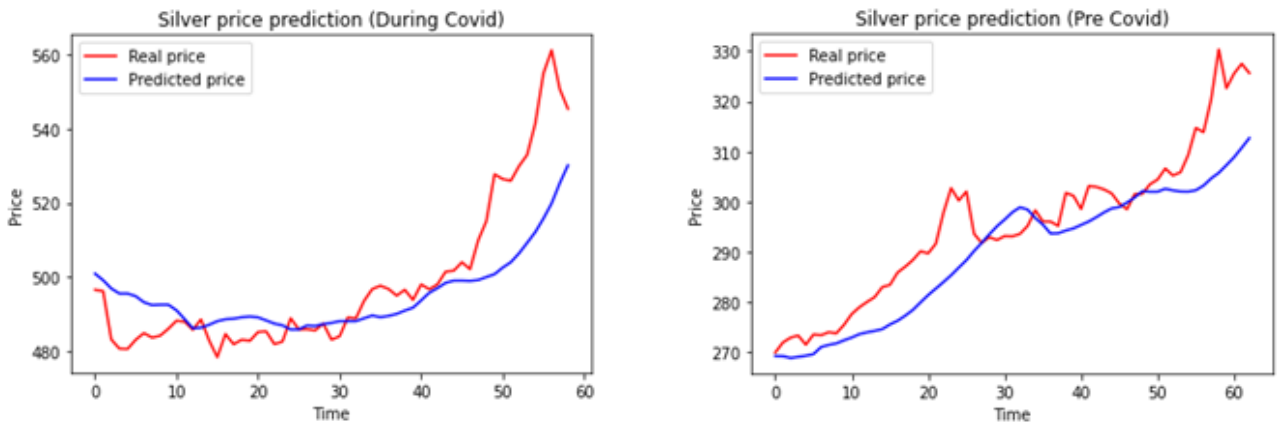


Figure 5. Silver price predictions using LSTM (left: COVID-19, right: Pre-COVID-19)

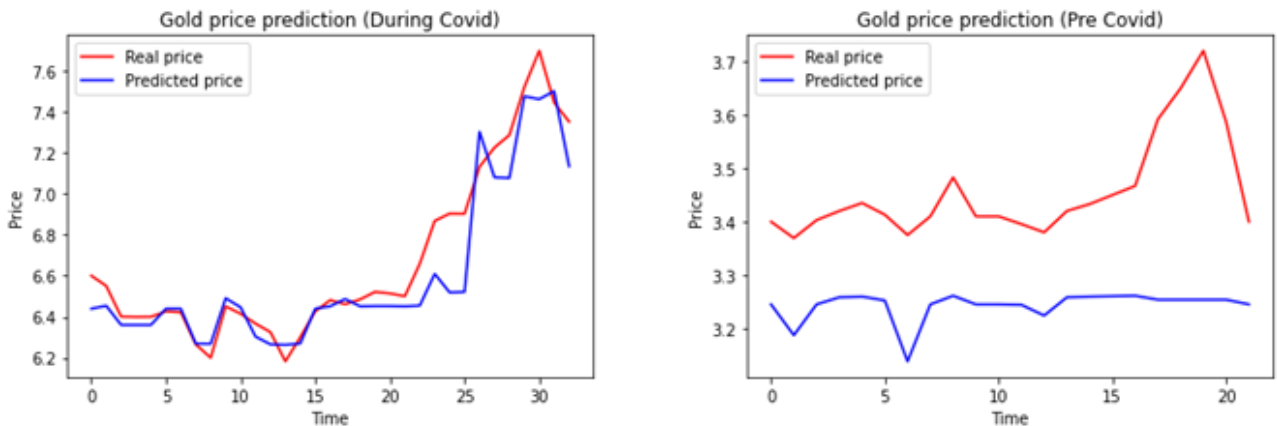


Figure 6. Gold price predictions using RF (left: COVID-19, right: Pre-COVID-19)

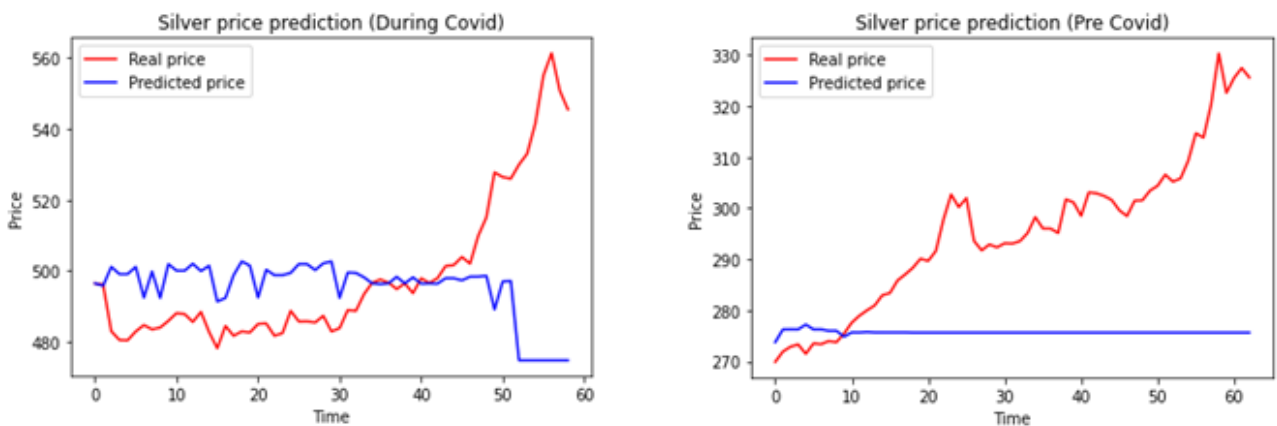


Figure 7. Silver price predictions using RF (left: COVID-19, right: Pre-COVID-19)

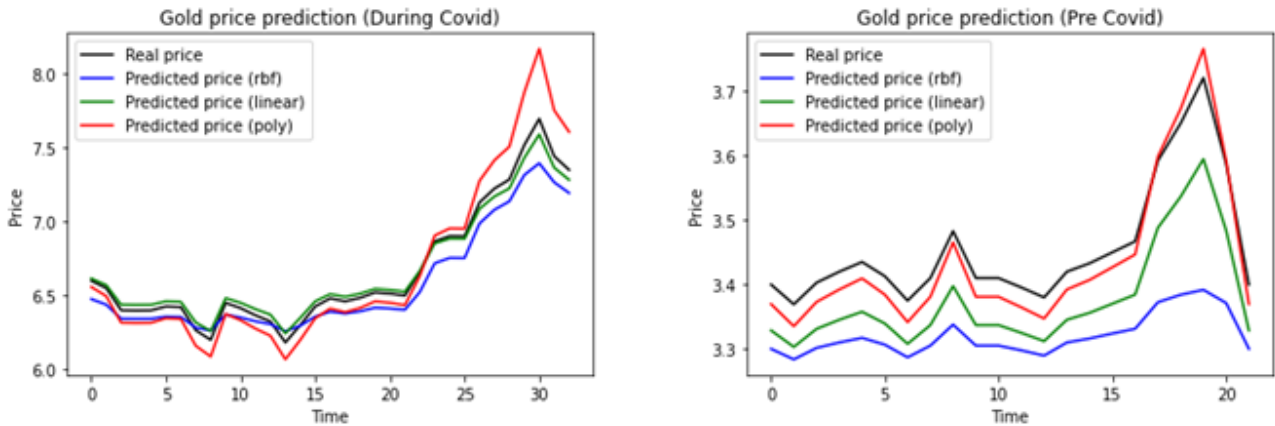


Figure 8. Gold price predictions using SVR (left: COVID-19, right: Pre-COVID-19)

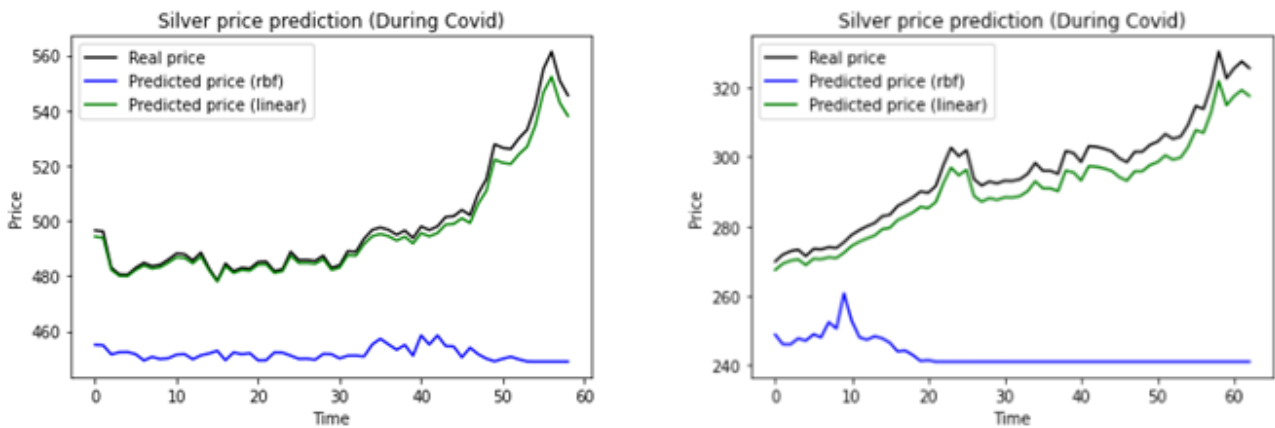


Figure 9. Silver price predictions using SVR (left: COVID-19, right: Pre-COVID-19)

Author contributions

Sena Alparslan: Conceptualization, Software, Writing
Tamer Uçar: Methodology, Reviewing, Editing

Conflicts of interest

The authors declare no conflicts of interest.

References

1. Usha, B. A., Manjunath, T. N., & Mudunuri, T. (2019, March). Commodity and Forex trade automation using deep reinforcement learning. In 2019 1st International Conference on Advanced Technologies in Intelligent Control, Environment, Computing & Communication Engineering (ICATIECE) (pp. 27-31). IEEE.
2. Kamdem, J. S., Essomba, R. B., & Berinyuy, J. N. (2020). Deep learning models for forecasting and analyzing the implications of COVID-19 spread on some commodities markets volatilities. *Chaos, Solitons & Fractals*, 140, 110215.
3. Depren, Ö., Kartal, M. T., & Depren, S. K. (2021). Changes of gold prices in COVID-19 pandemic: Daily evidence from Turkey's monetary policy measures with selected determinants. *Technological Forecasting and Social Change*, 170, 120884.

4. Elgammal, M. M., Ahmed, W. M., & Alshami, A. (2021). Price and volatility spillovers between global equity, gold, and energy markets prior to and during the COVID-19 pandemic. *Resources Policy*, 74, 102334.
5. Jabeur, S. B., Khalfaoui, R., & Arfi, W. B. (2021). The effect of green energy, global environmental indexes, and stock markets in predicting oil price crashes: Evidence from explainable machine learning. *Journal of Environmental Management*, 298, 113511.
6. Ramakrishnan, S., Butt, S., Chohan, M. A., & Ahmad, H. (2017, July). Forecasting Malaysian exchange rate using machine learning techniques based on commodities prices. In 2017 International Conference on Research and Innovation in Information Systems (ICRIIS) (pp. 1-5). IEEE.
7. Akın, B., Dizbay, İ. E., Gümüsoğlu, Ş., & Güdücü, E. (2018). Forecasting the Direction of Agricultural Commodity Price Index through ANN, SVM and Decision Tree: Evidence from Raisin. *Ege Academic Review*, 18(4), 579-588.
8. Yadav, S., & Sharma, K. P. (2018, December). Statistical analysis and forecasting models for stock market. In 2018 First International Conference on Secure Cyber Computing and Communication (ICSCCC) (pp. 117-121). IEEE.
9. Štifanić, D., Musulin, J., Miočević, A., Baressi Šegota, S., Šubić, R., & Car, Z. (2020). Impact of COVID-19 on forecasting stock prices: an integration of stationary

- wavelet transform and bidirectional long short-term memory. *Complexity*, 2020.
10. Luo, J. (2020, December). Bitcoin price prediction in the time of COVID-19. In *2020 Management Science Informatization and Economic Innovation Development Conference (MSIEID)* (pp. 243-247). IEEE.
 11. Amin, M. N. (2020, December). Predicting Price of Daily Commodities using Machine Learning. In *2020 International Conference on Innovation and Intelligence for Informatics, Computing and Technologies (3ICT)* (pp. 1-6). IEEE.
 12. Ruan, J., Wu, W., & Luo, J. (2020, December). Stock Price Prediction Under Anomalous Circumstances. In *2020 IEEE International Conference on Big Data (Big Data)* (pp. 4787-4794). IEEE.
 13. Ghosh, I., Sanyal, M. K., & Jana, R. K. (2020, February). An ensemble of ensembles framework for predictive analytics of commodity market. In *2020 4th International Conference on Computational Intelligence and Networks (CINE)* (pp. 1-6). IEEE.
 14. Ly, R., Traore, F., & Dia, K. (2021). Forecasting commodity prices using long-short-term memory neural networks (Vol. 2000). *Intl Food Policy Res Inst.*
 15. Mahdi, E., Leiva, V., Mara'Beh, S., & Martin-Barreiro, C. (2021). A new approach to predicting cryptocurrency returns based on the gold prices with support vector machines during the COVID-19 pandemic using sensor-related data. *Sensors*, 21(18), 6319.
 16. Vora, C., Sheth, D., Shah, B., & Shah, N. B. (2021, June). Stock Price Analysis and Prediction. In *2021 International Conference on Communication information and Computing Technology (ICCICT)* (pp. 1-7). IEEE.
 17. Chandra, R., & He, Y. (2021). Bayesian neural networks for stock price forecasting before and during COVID-19 pandemic. *Plos one*, 16(7), e0253217.
 18. Niu, H., & Zhao, Y. (2021). Crude oil prices and volatility prediction by a hybrid model based on kernel extreme learning machine. *Mathematical Biosciences and Engineering*, 18(6), 8096-8122.
 19. Olubusoye, O. E., Akintande, O. J., Yaya, O. S., Ogbonna, A. E., & Adenikinju, A. F. (2021). Energy pricing during the COVID-19 pandemic: Predictive information-based uncertainty indexes with machine learning algorithm. *Intelligent Systems with Applications*, 12, 200050.
 20. Garreta, R., & Moncecchi, G. (2013). *Learning scikit-learn: machine learning in python*. Packt Publishing Ltd.
 21. Bressert, E. (2012). *SciPy and NumPy: an overview for developers*.
 22. McKinney, W., (2011). *Pandas: a foundational Python library for data analysis and statistics. Python for high performance and scientific computing*, 14(9), 1-9.
 23. Abadi, M., Barham, P., Chen, J., Chen, Z., Davis, A., Dean, J., ... & Zheng, X. (2016). TensorFlow: a system for Large-Scale machine learning. In *12th USENIX symposium on operating systems design and implementation (OSDI 16)* (pp. 265-283).
 24. Hansun, S. (2013, November). A new approach of moving average method in time series analysis. In *2013 conference on new media studies (CoNMedia)* (pp. 1-4). IEEE.
 25. Breiman, L. (2001). Random forests. *Machine learning*, 45(1), 5-32.
 26. Géron, A. (2022). *Hands-on machine learning with Scikit-Learn, Keras, and TensorFlow*. " O'Reilly Media, Inc."
 27. De Myttenaere, A., Golden, B., Le Grand, B., & Rossi, F. (2016). Mean absolute percentage error for regression models. *Neurocomputing*, 192, 38-48.
 28. Sammut, C., & Webb, G. I. (2010). Mean absolute error. *Encyclopedia of Machine Learning*, 652.
 29. Nevitt, J., & Hancock, G. R. (2000). Improving the root mean square error of approximation for nonnormal conditions in structural equation modeling. *The Journal of experimental education*, 68(3), 251-268.



© Author(s) 2023. This work is distributed under <https://creativecommons.org/licenses/by-sa/4.0/>